INTERFACE ENGINNERING AND INTERFACIAL CHARGE TRANSFER DYNAMICS IN QUANTUM DOT SOLAR CELLS AND PEROVSKITE SOLAR CELLS

By

Chao Ding

SEPTEMBER, 2018

THE UNIVERSITY OF ELECTRO-COMMUNICATIONS

Interface Engineering and Interfacial Charge Transfer Dynamics in Quantum Dot Solar Cells and Perovskite Solar Cells

Chao Ding

Doctor of Philosophy

THE UNIVERSITY OF ELECTRO-COMMUNICATIONS

SEPTEMBER 2018

Interface Engineering and Interfacial Charge Transfer Dynamics in Quantum Dot Solar Cells and Perovskite Solar Cells

APPROVED BY THE SUPERVISPRY COMMITTEE:

CHAIRPERSON: Prof. Qing Shen

MEMBER: Prof. Koji Abe

MEMBER: Prof. Tsuyoshi Okuno

MEMBER: Prof. Takashi Hirano

MEMBER: Prof. Taro Toyoda

量子ドット太陽電池とペロブスカイト太陽電池における界面エンジニアリングと界面電荷移動ダイナミクス

和文要旨

現在ますます深刻になってきた環境問題とエネルギー問題を解決するために、無尽蔵で再生可能エネルギー源である太陽光の活用が強く望まれている。しかし、太陽エネルギーは大きな可能性があるにも関わらず、現在ごくわずかしか利用されていない。その原因は、太陽電池の作製コストがまだ高く、かつ変換効率が十分には高くないことにある。最近、コロイド量子ドット太陽電池とペロブスカイト太陽電池は安価な溶液法で作製可能であることと理論変換効率は高いため、安価・高効率な次世代太陽電池として注目されている。しかし、これらの次世代太陽電池を実用化させるためには、さらなる高効率化と安定化の向上とそれらのメカニズムの解明に関する基礎研究は重要かつ不可欠である。特にこれらの太陽電池の各界面における①界面エンジニアリングと②界面電荷移動ダイナミクスおよび③これらの界面制御と電荷移動電荷ダイナミクスと太陽電池の光電変換特性および安定化との関連を明らかにすることは鍵となる。

そこで本研究では、PbS コロイド量子ドット太陽電池とペロブスカイト太陽電池を作製し、各界面に対して異なる界面エンジニアリングを行い、変換効率の向上と安定化の向上に成功した。さらに、過渡吸収分光法と開放電圧の過渡応答測定法などを用いて、界面電荷移動（電荷分離と再結合）ダイナミクスを解明し、界面エンジニアリングによるこれらの電荷移動ダイナミクスの変化と効率向上との関連性を明らかにした。具体的に以下の 3 つの内容である。

（１）PbS 量子ドット光吸収層のエネルギーレベルアライメント（energy level alignment）による電荷分離の向上と電荷再結合の抑制について研究を行った。PbS 量子ドット太陽電池のデバイス構造は透明電極(FTO)/TiO_2/PbS 量子ドット層/Au 電極である。PbS 量子ドット層については、異なる粒径の 4 種類の PbS 量子ドット（M: 3.6 nm; S1: 3.3 nm; S2: 2.9 nm; S3: 2.6 nm）を用いて、PbS 量子ドット層/Au 電極の界面におけるエネルギーレベルアライメントを行った。具体的に、以下の 4 種類の PbS 量子ドット光吸収層（ (I) M-PbS 量子ドット (~300 nm thick)；(II) M-PbS (~260 nm) + S2-PbS (~40 nm)；(III) M-PbS (~220 nm) + S1-PbS (~40 nm) + S2-PbS (~40 nm)と（IV）M-PbS (~180 nm) + S1-PbS (~40 nm) + S2-PbS (~40 nm) + S3-PbS (~40 nm)）を用いて太陽電池を作製した。これらの PbS 量子ドット光吸収層の違いによる PbS 量子ドット層の光吸収スペクトルの変化、PbS 量子ドット/Au 界面でのエネルギー準位の変化、太陽電池の光電変換特性の変化について詳しく調べた。さらに、レーザー分光測定によりこれらの PbS 量子ドット太陽電池における電荷分離と電荷再結合

過程は PbS 量子ドット層のエネルギーレベルアライメントに強く依存することを明らかにした。その結果、最適な PbS 量子ドット光吸収層構造（構造 III）により電荷分離の向上と再結合の抑制が実現できた。これらの結果により、適切な量子ドット層のエネルギーレベルアライメントを確立できれば、さらなる高効率化である PbS 量子ドット太陽電池の構築ができることが判明した。また、これらの PbS 量子ドット太陽電池は空気中で 150 日以上保存しても安定であることを実証した。

（２）PbS 量子ドット太陽電池の界面制御による界面電荷移動ダイナミクスの変化と高効率化について研究を行った。本研究では、PbS 量子ドット太陽電池の透明電極(FTO)と PbS 量子ドット層の間での電子輸送層におけるエネルギー準位と光・電子物性の制御を行った。溶液法により ZnO に Mg をドーピングすることで $Zn_{1-x}Mg_xO$（x = 0, 0.05, 0.1, 0.15, 0.2）の電子輸送層を形成した。x の増加に伴い、$Zn_{1-x}Mg_xO$ 膜の光吸収特性、発光特性、電子物性、エネルギー準位が顕著に変化しすることが分かった。$Zn_{1-x}Mg_xO$ 膜を電子輸送層とする PbS 量子ドット太陽電池の光電変換特性は x に強く依存して変化することを見出した。特に、最適な x である $Zn_{1-x}Mg_xO$ 膜(x=0.1)が存在するが判明した。それを用いた場合では、太陽電池の開放電圧と短絡電流の向上に伴い、エネルギー変換効率は 10.6%に達成できた。そのメカニズムを解明するために、開放電圧の時間応答と過渡吸収スペクトルの測定を行った。その結果より、$Zn_{1-x}Mg_xO$ 膜/PbS 量子ドットの界面における conduction band offset(CBO）によるバンド構造の変化と $Zn_{1-x}Mg_xO$ 膜の電子物性の変化が電荷再結合と光電変換特性に強く影響することを明らかになった。

（３）ペロブスカイト太陽電池の界面制御による電荷再結合の抑制と高効率化について研究を行った。ペロブスカイト太陽電池は最近の 5 年間で大変注目され、盛んに研究されている。ペロブスカイト太陽電池の各界面の制御はさらなる高効率化と安定化の鍵の一つである。そこで本研究では、上記の（２）で研究していた $Zn_{1-x}Mg_xO$（x = 0, 0.05, 0.1, 0.15, 0.2）の電子輸送層をペロブスカイト太陽電池に適用し、界面電荷再結合と光電変換特性への影響について検討した。その結果、量子ドット太陽電池と同じく、ペロブスカイト層と電子輸送層 $Zn_{1-x}Mg_xO$ の界面における電荷再結合と光電変換特性は x に強く依存することを見出した。その中で、$Zn_{0.9}Mg_{0.1}O$ 電子輸送層を用いた場合では、ペロブスカイト太陽電池の変換効率は 15.6%に達成し、ZnO 電子輸送層を用いた場合(11.2%)より著しく向上したことが分かった。その原因は $Zn_{0.9}Mg_{0.1}O$ 電子輸送層により界面での再結合が抑制されたためでさる。

以上の３つの研究内容の結果より、今後量子ドット太陽電池とペロブスカイト太陽電池のさらなる高効率化と安定化の実現に重要な知見を与えることが明らかになった。

Interface Engineering and Interfacial Charge Transfer Dynamics in Quantum Dot Solar Cells and Perovskite Solar Cells

Abstract

Solar photovoltaics (PV) propose a direct and practical solution to the daunting challenges of facing the energy crisis and environmental pollution in the world. Although traditional solar cells have been commercialized for many years, their inherent shortcomings, e.g., high production costs and high pollution have slowed down its implementation worldwide. Recently, colloidal quantum dot solar cells (CQDSC) and perovskite solar cells (PSC) have rapidly become new stars in the solar cell field and are considered to be promising candidates for low-cost and high-efficiency solar energy. This is due to its low cost. Solution-based technology and high theoretical power conversion efficiency. However, the current research on these both types of emerging solar cells is mainly focused on the device fabrication and materials control, the dynamics of carriers (i.e., carrier transport and recombination) at the interface still lacks systematical study, which is favorable to the understanding of the factors that limit their performance. The central aim of this thesis is that to understand the influence of interface engineering on of carrier dynamics of CQDSCs and PSCs, and on this base to obtain a more efficient solar cell.

This thesis will systematically investigate the effects of the interface engineering on the performance of CQD DHSCs, especially for carrier transmission and recombination, and use energy level control to modify the interface of CQDSCs and PSCs to enhance the charge collection in CQDSCs and PSCs.

In this thesis, I explore the development of air atmosphere solution-processed TiO_2/PbS QDs/Au QDHSCs by engineering the energy-level alignment (ELA) of the active layer via the use of a sorted order of differently sized QD layers (four QD sizes). We find that introduce the ELA structure at the PbS QDs/Au interface can enhance J_{sc} greatly. In comparison to an ungraded device (without the ELA), the optimized graded architecture (containing the ELA) solar cells exhibited a great increase (21.4%) in J_{sc}. A J_{sc} value greater than 30 mA/cm^2 has been realized in the PbS QDHSCs, and a high efficiency of 7.25% has been achieved. We have investigated the mechanism through characterization of V_{oc} decay and light-intensity dependences of V_{oc} and J_{sc}. We have clearly demonstrated that enhancement of J_{sc} in the QDHSCs results from reducing the recombination at both the QD active layer and the interface using the ELA structure.

I also explore a method to enhance the charge collection efficiency in CQDSCs by tunning conduction band offset (CBO) between the electron-transport layer and the PbS QDs. It is generally believed that the conduction band minimum (CBM) of the ETL

should be lower than that of the QDs to enable efficient charge transfer from the QDs to the collection electrode (here, FTO) through the ETL. However, by employing Mg-doped ZnO ($Zn_{1-x}Mg_xO$) as a model ETL in PbS QDHSCs, we found that an ETL with a lower CBM is not necessary to realize efficient charge transfer in QDHSCs. The existence of shallow defect states in the $Zn_{1-x}Mg_xO$ ETL can serve as additional charge-transfer pathways. In addition, the CBO between the ETL and the QD absorber has been, for the first time, revealed to significantly affect interfacial recombination in QDHSCs. We demonstrate that a spike in the band structure at the ETL/QD interface is useful for suppressing interfacial recombination and improving the open-circuit voltage. By varying the Mg doping level in ZnO, we were able to tune the CBM, defect distribution and carrier concentration in the ETL, which play key roles in charge transfer and recombination and therefore the device performance. PbS QDHSCs based on the optimized $Zn_{1-x}Mg_xO$ ETL exhibited a high-power conversion efficiency of 10.6%. Our findings provide important guidance for enhancing the photovoltaic performance of QD-based solar cells.

I also systematically investigated the effects of the CBO between the ESL and the perovskite layer in planar-heterojunction perovskite solar cells. I found that the charge recombination at the interface between the ESL and the perovskite is strongly dependent on the CBO values. A favorable CBO would be reducing charge recombination at the ESL/perovskite interface and hence improves device performance. In addition, we found an appropriate amount of Mg doping in ZnO can also reduce the carrier concentration and improve the carrier mobility of ZMO, and thereby enhancing the charge collection efficiency of the photoexcited electrons by the FTO electrode and subsequently, the short-circuit current density (J_{sc}). The mechanism for this improved performance is discussed in detail through characterization of photoluminescence (PL) spectra, carrier lifetimes, charge injection and charge recombination through fluorescence spectroscopy, transient photovoltage (TPV) decay measurement, and ultrafast transient absorption (TA) spectroscopy.

The purpose of above studies is to improve the understanding of charge carrier dynamics in CQDSCs and PSCs, so that more efficient designing and optimizing the interfaces, and ultimately the solar cell efficiency can be further improved.

Table of Contents

Chapter 1: Introduction and Motivation

1.1 The Research Significance of Photovoltaics

Currently, in the rapidly improving economic and social conditions, a growth in energy demand is spurred by increasing population and prosperity. Notably, the world continues to electrify, with electricity consumption growing actively. Almost 70% of the increase in primary energy (e.g., coal, oil, gas, solar, wind) is used to generate electricity, with electric power consumption growing three times more rapidly than that of other energy sources.[1] The share of fossil fuel (e.g., coal, oil and natural gas) in the primary energy that is used for power generation is still over 70%, and It is estimated that by 2040 these energy sources will continue to account for approximately 60% of the total electricity generation (Figure 1-1(a)).[2] However, the energy crisis and environmental pollution (i.e., the threats of global warming and climate change) that are caused by fossil fuel utilization are highlighted as critical global problems in the 21st century. To meet the increased energy consumption needs and phase down environmental pollution, the share of renewable energy will need to exceed 40% for power generation by 2050.[3] According to a new report, namely, "BP Energy Outlook-2018", renewable energy accounts for approximately 50% of the increase in power, and its share of total power generation will increase from its current level of 7% to approximately 25% by 2040.[2] The strong growth in renewable energy is due to the growing competitiveness of wind and solar power. The sun offers a vast resource that generates clean and sustainable electricity without toxic pollution or global warming discharges. It is projected that global solar power usage in 2022 will be more than 150% higher than in the base case of the 2015 Energy Outlook (Figure 1-1(b)). This difference reflects that solar costs are falling faster than anticipated, with solar energy now projected to be widely competitive by the 2020s.[4]

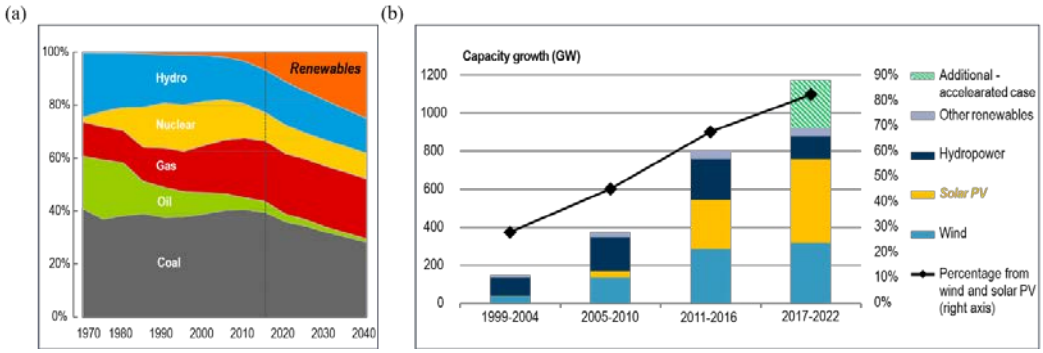

Figure 1-1. (a) Primary energy consumption in power generation. (b) Renewable electricity capacity growth by technology.[2]

These beautiful visions are primarily the results of booming solar photovoltaic (PV) deployment around the world, which is driven by continued research and development of inexpensive photovoltaic technologies and policy support. Currently, limited by PV

technologies and materials, the solar energy that is utilized by photovoltaic power generation has yet to reach its enormous potential. Moreover, the cost of solar power is not less than that of fossil fuels, which is a significant obstacle to the widespread installation of photovoltaic equipment. This work focuses on photovoltaic technology. We investigate solar cells in terms of the internal mechanism and study the potential for improving their photoelectric conversion capability.

1.2 History and Types of Photovoltaics

In 1839, the basic science of photovoltaics, i.e., *the photovoltaic effect*, was first discovered by French scientist Edmond Becquerel. Experimenting with metal electrodes and electrolytes, he observed the production of an electric current when they were exposed to light.[5] In the next few decades, with the discovery of the *photoelectric effect* of selenium, the first solar cell, which was based on selenium wafers, was invented by American inventor Charles Fritts in 1883.[6] Although the estimated power conversion efficiencies of selenium solar cells were less than 1%, they proved that a solid material could convert light into electricity without heat or with any moving parts, which was an essential milestone for technological development. However, it was not until the 1920s that scientists achieved a better understanding of photo-electricity based on a seminal paper of Albert Einstein in 1905 on the photoelectric effect[7], combined with the discovery of the electron (1898).[8] Daryl Chapin (Bell Labs) found that photo-excited carriers can produce an efficient separation in the P-N junction that is formed by combining n-doped and p-doped silicon. Then, the first practical photovoltaic cells, with a power conversion efficiency (PCE) of 6%, were developed in 1954.[9] This development laid the foundation for future solar cell designs. At this point, the photovoltaic technology and industry entered a new era of vigorous growth.

From the 1950s to the present, solar cell technologies have made tremendous progress. They are typically divided into three generations: As the first-generation photovoltaic devices, crystalline-silicon-based solar cells advanced substantially in the past half-century, and their efficiency has grown from 6% to 27.6%.[10] Silicon-based solar cells still dominate today's PV market (share of over 90%).[11] It is necessary to grow highly pure and crystalline silicon to produce highly efficient silicon cells. However, building large crystals of pure silicon is difficult because it requires high-temperature and dust-free processing under rigorous process-controlled conditions. In addition, silicon is an indirect-bandgap semiconductor and is limited by its optical bandgap (Eg=1.1 eV) that does not optimally match the solar spectrum; therefore, a thick(~200 μm) silicon layer is necessary to allow photons with photon energies that exceed the bandgap to be absorbed as thoroughly as possible.[12] The performance of silicon solar cells is easily affected by the ambient temperature. When the temperature exceeds 25 °C, the device loses efficiency, which imposes requirements for the installation of silicon panels.[13] These factors result in silicon panels that are heavy, bulky, inflexible, and high in cost. The production cost of this type of panel has historically been the highest of all solar panels types.

The disadvantages (e.g., high cost and unwieldy panels) of silicon cells have prompted researchers to investigate the potential of other materials to replace silicon. These investigations resulted in the second-generation photovoltaics, which use less material and have a lower-cost manufacturing processes. Because they have much thinner active layers (below one micrometer) than silicon cells, they are also called thin-film solar cells. Thin-film solar cells are typically based on direct-bandgap materials: amorphous silicon (a-Si), cadmium telluride (CdTe), and copper indium gallium selenide (CIGS). Their absorbing layer can be prepared on lightweight glass and flexible substrates, which led to an enlarged range of possible applications (e.g., mobile and wearable) compared with first-generation photovoltaics. Second-generation cells are relatively lower in efficiency than crystal silicon cells: the record efficiencies for a-Si, CdTe, and CIGS devices are 21.2%,[14] 22.1%,[15] and 23.3%,[16] respectively. However, the PCE of commercial thin-film PV modules has historically lagged below the PCE of silicon modules. As of 2016, the market share of thin-film PV products was only 6%, and the installed capacity of photovoltaic devices was nearly 4.9 GWp (Figure 1-2). Recently, the thin-film PV modules have achieved a significant breakthrough in efficiency: the CdTe and CIGS modules reached 18.6% and 19.2% efficiency, respectively, which is very close to that of polycrystalline silicon modules (19.9%).[17] However, the production of thin-film solar cells always requires vacuum and high-temperature conditions; thus, the production of these cells still results in significant energy consumption. In addition, the rare elements (indium and gallium in CIGS cells; tellurium in CdTe) may also limit cost. Therefore, thin-film PV technology requires further study.

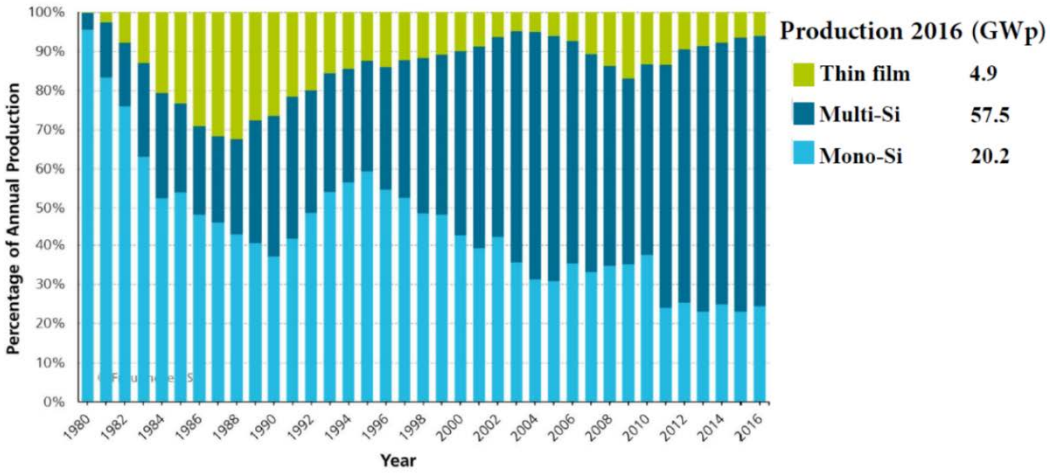

Figure 1-2. Percentage of global annual production of PV production by technology.[17]

Based on the second-generation PV technologies, the third-generation photovoltaics are intended to achieve higher efficiency and lower costs through improved material utilization (i.e., the use of inexpensive, plentiful and environmentally friendly materials) and fabrication technology (i.e., economical and scalable manufacturing technology), and balancing of system costs. Large-area fabrication, flexibility, and light weight are

also among the goals of this generation of solar cells. At present, the primary exploration frontier is PV that is made of solution-processable materials, which allows for high-throughput fabrication techniques to be used, such as flexographic printing, spray coating, blade coating and spin coating. The scalability of third-generation photovoltaic devices provides competition with traditional PV technology on a commercial level, even if the current efficiency is not higher. Figure 1-3 shows plots of the highest authenticated conversion efficiencies for a wide variety of research solar cells from 1976 to the present, which were provided by the National Renewable Energy Laboratory (NREL).[18] The emergence of PV technologies is related to the development of solution processing fabrication techniques. These PV technologies include dye-sensitized solar cells, various organic-based cells, inorganic cells (i.e., $Cu_2ZnSn(S, Se)_4$), quantum dot cells and perovskite cells. Dye-sensitized solar cells (DSSCs) were initially investigated in 1991 by Michael Gratzel and Brian O'Regan and opened up a new field and rapidly advanced PV technology into the era of the third-generation solar cells.[19] Unlike a traditional P-N junction solar cell, a DSSC consists of a transparent conductive substrate, a high-surface-area n-type semiconductor (usually TiO_2), a dye (sensitizers) that absorbs light and an electrolyte that contains a redox mediator and a counter electrode.[20] The DSSCs provides comparable PCE (the device PCE rapidly increased from 7.1% in 1991 to 13% in 2014) at low material and manufacturing costs, at a level that is suitable for commercial use.[21] In addition, DSSCs outperform Si solar cells under indoor conditions and in the utilization of flexible substrates for colorful and transparent devices.[22] However, the use of liquid electrolyte in DSSCs causes serious problems such as temperature sensitivity (i.e., they are not stable at varying temperatures), potential instability, and higher packaging requirements.[23] Organic solar cells (OSCs), as another cost-effective possible third-generation photovoltaic technology, have attracted considerable attention, thanks to their advantages of low cost and large-area fabrication (e.g., roll-to-roll or printing, spin coating, spraying, and vaporization), environmental friendliness and use of abundant materials, mechanical light weight and flexibility.[24] Although the PCE of OSCs has improved from 2.9% in 1995 to 11.5% in 2014, it is insufficient to compete with more-mature solar cells.[25] Moreover, the long-term use of OSCs are not satisfactorily. Therefore, the current challenge is to continue the progress in improving their efficiency and increase their stability.[26] Inorganic solar cells, namely, $Cu_2ZnSn(S, Se)_4$ (CZTSSe), were introduced in 1997 as the most promising candidate to replace the second-generation photovoltaics because of their dual advantage of being made with readily available materials and using an inexpensive ink-based process.[27] After 20 years of development, the CZTSSe solar cell achieved a conversion efficiency of 12.6% by non-vacuum solution deposition methods.[28] Hence, the CZTSSe PV attracted potential commercial interest.

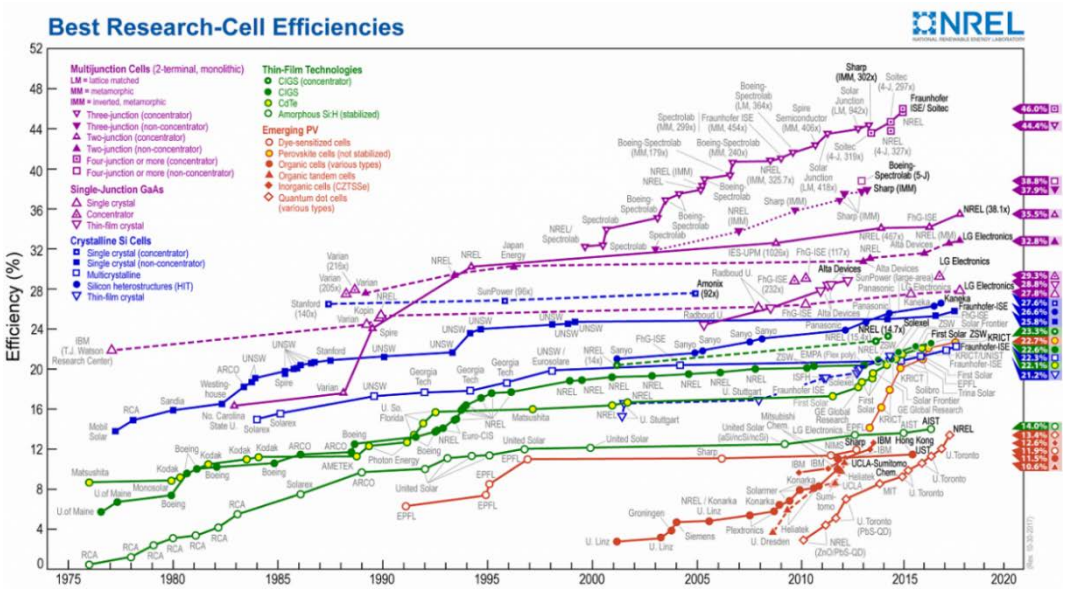

Figure 1-3. Gradually increase the efficiency of the recording cell according to the type of solar cell. This plot is provided by the National Renewable Energy Laboratory, Golden, CO.[18]

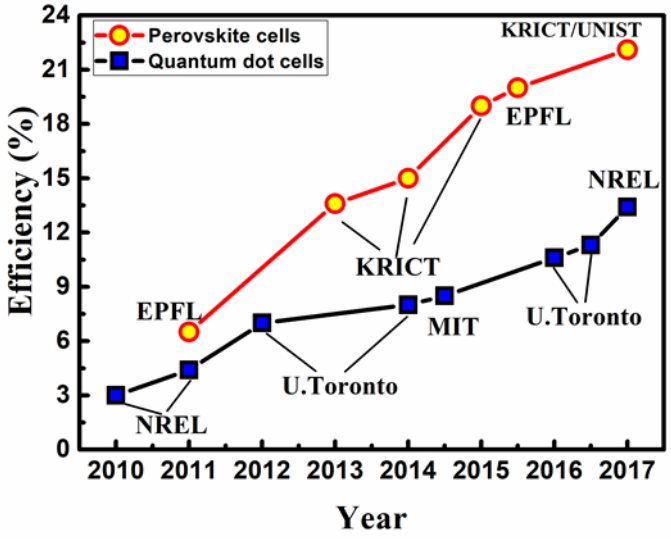

Figure 1-4. Timeline for perovskite cells and quantum dot cells technologies from Figure 1-3.

Other emerging PVs, namely, quantum dots solar cells (QDSCs) and perovskite solar cells (PSCs), are the topic of this thesis. QDSCs have been considered a desirable option for the third generation of photovoltaic devices, which benefit from the multifold and unique advantages of QDs, e.g., quantum-sized effect bandgap tunability, broader hot carrier lifetimes, multiple exciton generation (MEG), and facile solution processing.[29-31] Since 1998, their PCE grew significantly from far below 1% to over 13% to date (Figure 1-4), owing to significant efforts from numerous researchers.[32-33] First reported in 2009, metal halide perovskite materials (e.g., $CH_3NH_3PbI_3$ and $CH_3NH_3PbBr_3$

nanocrystals) were used as dyes in DSSCs and generates 3.8% of solar energy conversion efficiency,[34] which demonstrated for the first time the ability of perovskite materials to act as light-harvesting materials. Since then, research on perovskite-based SCs has been booming. Notably, since their introduction just eight years ago, their PCE has undergone impressively rapid development – it increased from 3.8 to 22.7% (the most recently reported certified value) (Figure 1-4) at a speed that exceeds those of other types of solar cells throughout history.[35] Moreover, PSCs share benefits with QDSCs, such as low-cost fabrication process. As a result, they soon became a new star in the field of solar cells and are now considered as emerging candidates for low-cost and high-efficiency solar cells. In the next section, a thorough introduction to QDSCs and PSCs will be given.

1.3 Quantum Dot Photovoltaics

1.3.1. Physical Fundamental of Quantum Dot

Quantum dots (QDs) are a semiconducting material with diameters in the range of few nanometers. They have attracted substantial attention since they were first discovered in 1980[36] because they have a variety of potential applications, e.g., biological imaging,[37] photovoltaic devices,[38] LEDs[39] and sensor materials.[40] The application potential of QDs in these fields is mainly attributed to their unique and tunable electronic and optical properties, which result from their nanoscale size due to the quantum confinement effect. Generally, when the diameter of a nanocrystal is close to or smaller than the Bohr radius, i.e., electrons and holes are being squeezed into a dimension-critical quantum measurement of the bulk semiconductor, then the electronic and optical properties show size dependence. The Bohr radius is the electron-hole separation.[41] Table 1-1 shows examples of exciton Bohr radii for various semiconductors.

Table 1-1. Exciton ball radius and bandgap energy of some common semiconductors.[41]

Semiconductor Structure	Exciton Bohr Radius (nm)	Bandgap Energy (eV)
PbSe	46.0	0.28
PbS	18.0	0.37
CdTe	15.0	1.50
CdSe	10.6	1.74
ZnSe	8.4	2.58
CdS	5.6	2.53

The electrons and holes move freely in bulk semiconductor crystals, i.e., carriers are free to move in 3 dimensions; thus, they have continuous energy states and energy bands are formed by the energy levels that are close to each other. Besides, the density of states (DOS) is often used to describe the number of states per interval of energy level that are available to be occupied by electrons. As shown in Figure 1-5, the DOS in bulk materials is proportional to $\sqrt{\mathrm{E}}$ (3 degrees of freedom). When the physical size of crystals is tiny (within a few nanoscales), the DOS becomes discrete and depends on the size and shape of the nanocrystals. In the quantum well, electrons and holes are confined in one dimension (2 degrees of freedom) and thus possess a DOS that is independent of energy. In a quantum wire, electrons and holes are confined in two dimensions (1 degree of freedom); thus, DOS is proportional to $1/\sqrt{E}$. A quantum dot is a zero-dimensional (0-D) material in which electrons and holes are confined in three dimensions. Therefore, quantum dots have the atomic-like DOS mathematically described by $\triangle$E.[42]

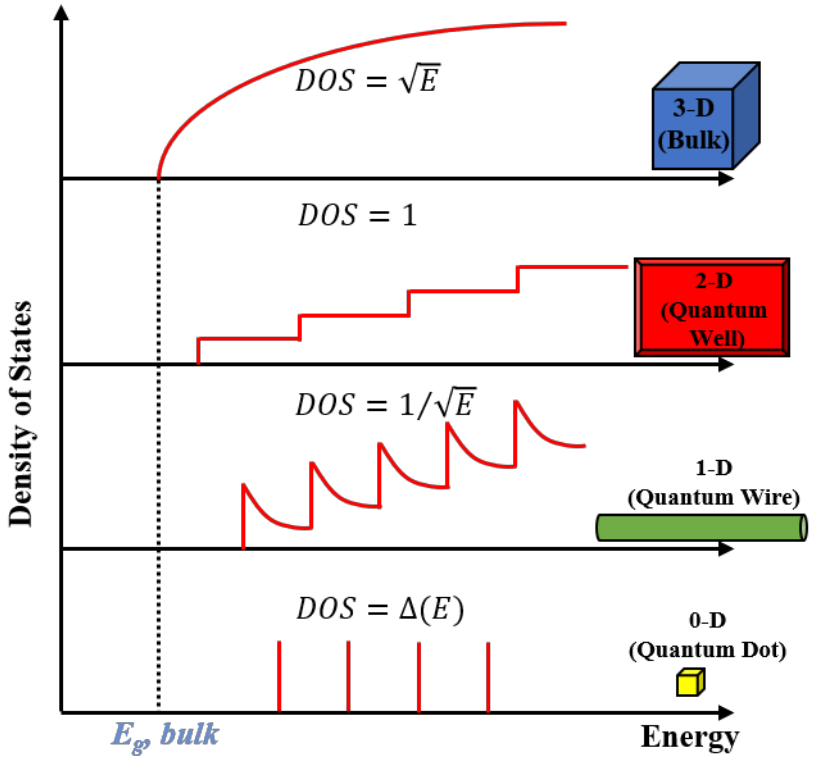

Figure 1-5. Schematic of the density of states (DOS) in the bulk and ideal quantum confined systems predicted by the simplified particle.[42]

To obtain the energy eigenvalues of electrons and holes in a QD, the boundary conditions for solving the Schrödinger equations must be modified. Here, a QD is imagined as a quantum box (a box with side dimensions L_x=L_y= L_z=L), and the size (L)-related energy eigenvalues E_n can be written as:

$$E_n = \frac{\pi^2 h^2}{2mL^2}\left(n_x^2 + n_y^2 + n_z^2\right) = \frac{\pi^2 h^2}{2mL^2} n^2 \qquad (1\text{-}1)$$

where h is Planck's constant, and m is an effective mass. Moreover, the ground-state energy in a QD is higher than that in bulk. For the spherical shape of a QD with radius r, based on the effective mass model that was reported by Louis Brus[43] for colloidal QDs, the bandgap ($E_{g,\,QD}$) of a QD can be described by:

$$E_{g,QD} = E_{g,bulk} + \frac{\pi^2 h^2}{2r^2}\left(\frac{1}{m_e} + \frac{1}{m_h}\right) - \frac{1.8e^2}{4\pi\varepsilon\varepsilon_0 r} \qquad (1\text{-}2)$$

where m_e and m_h are the effective masses of an electron and a hole, respectively, ε is the relative permittivity, and ε_0 = 8.85410^{-14} F.cm^{-1} is the permittivity of free space. The third item details the Coulomb attraction between electrons and holes (excitons). The third term in equation (1-2) corresponds to the Coulomb attraction of the exciton (electron-hole pair). From this equation (8), we found that $E_{g,\,QD}$ strongly depends on the quantum dot size, e.g., $E_{g,\,QD}$ increases as the size of the QDs decreases.

Quantum confinement effects are the physical basis for all characteristics of QDs and were first demonstrated experimentally in research on growing crystalline CuCl clusters: a blueshift of up to 0.1 eV of the absorption spectrum relative to the bulk is observed when the size of the cluster decreases.[44] Figure 1-6 shows the calculated energy bandgap for semiconductor QDs of various sizes using the useful mass approximation model.

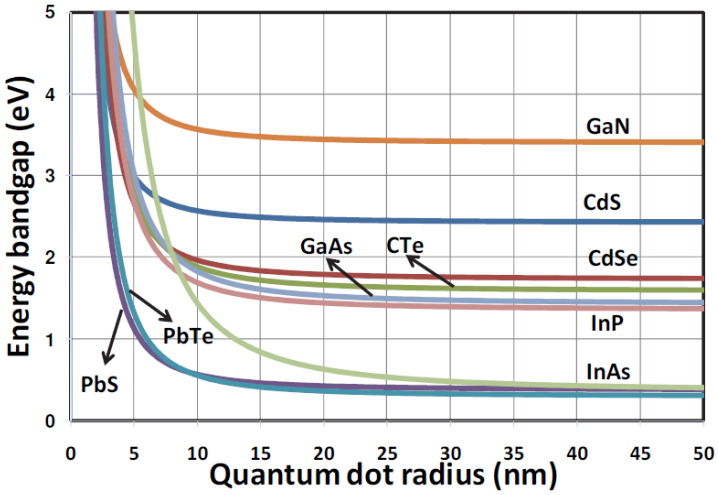

Figure 1-6. Calculating energy gaps of some semiconductor quantum dots using an effective mass-approximation model.[44]

Here, one of the most important advantages of QDs is shown: broad tunability of bandgaps. Figure 1-7 shows the absorption spectra of lead sulfide (PbS) quantum dots of various sizes that were prepared in our laboratory. A quantum dot bandgap is readily tunable by adjusting QD sizes – the smaller the QD size, the larger the bandgap. This is because the smaller the size of the QD, the higher the energy required to confine an

exciton within its volume. At the same time, the energy level increases and further expands, resulting in a blue shift of exciton absorption peaks. This feature optimizes traditional single junction solar cells by optimizing the quantum dot band gap. Moreover, this feature enables the simple construction of multi-junction solar cells that can potentially absorb most of the solar spectrum (insert of Figure 1-7). In addition to the primary characteristic of bandgap tunability, QDs possess other advantages for the application of PV. In the next section, I will discuss in detail the other unique advantages of QDs.

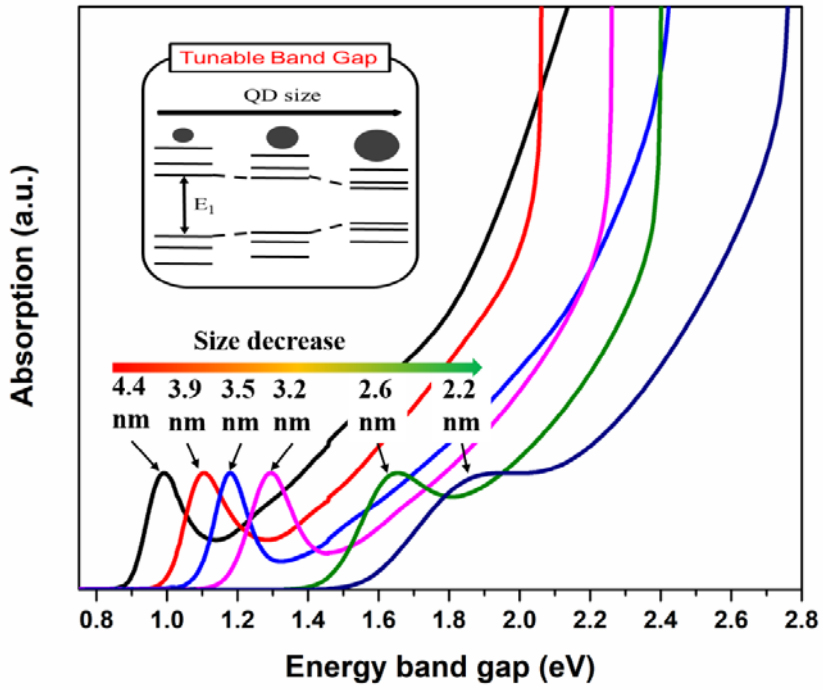

Figure 1-7. Absorbance spectrum of different size of PbS QDS dispersed in octane.

1.3.2. Advantages of QDs in photovoltaics

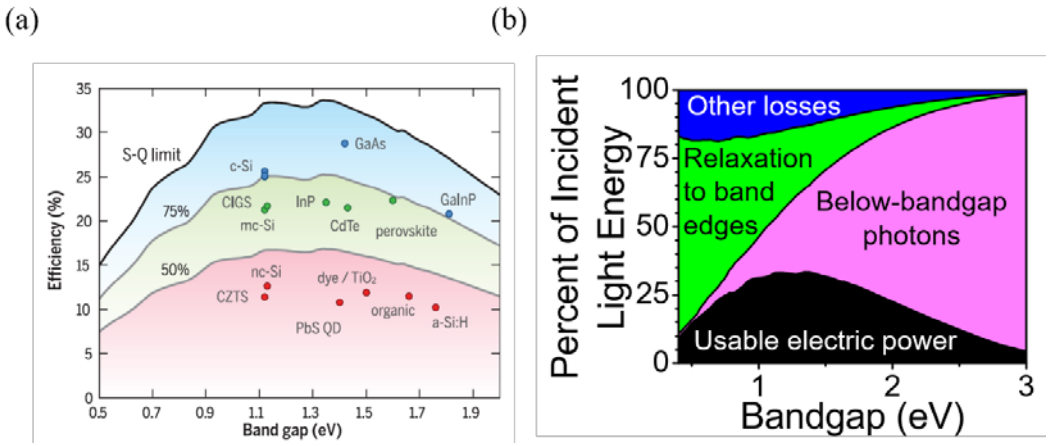

Figure 1-8. (a) The theoretical maximum efficiency of a single-junction solar cell as a function of bandgap energy calculated by the Shockley–Queisser model and 75% and 50%of the limit (gray lines).[45] The record efficiencies for different materials are plotted for the corresponding band gaps. (b) Breakdown of the causes for the Shockley-Queisser limit.[46]

1. Breakthrough in efficiency limits of solar cell-- Multiple Exciton Generation

The Shockley–Queisser limit, which is one of the fundamental concepts for guiding the development of photovoltaic cells, was reported in 1960.[47] The restriction is that the maximum PCE is limited to ~33.7% for a single P-N junction photovoltaic cell with a bandgap of 1.4 eV (using an AM 1.5 solar spectrum). Figure 1-8 (a) shows the maximum PCE as a function of the bandgap energy in a single-junction solar cell, which was calculated by the Shockley–Queisser model (assuming the incident solar spectrum is a 6000 K blackbody spectrum). To calculate the limit, it is assumed that one photon of incoming sunlight excites one electron-hole pair. Figure 1-8 (b) shows the reasons for the limits of solar cell efficiency in the Shockley–Queisser model: (1) Blackbody radiation (green height): the energy that is lost from a cell is converted into heat when hot photogenerated electron hole pairs relax to the band edges and represents approximately 7% of the available incoming energy of a cell at room temperature; (2) Recombination (blue height): the energy loss from a cell is mainly due to radiative-recombination-induced voltage deficiency; (3) Spectrum losses (pink height): the energy that is lost is the energy of below-bandgap photons because only photons with more energy than the bandgap energy will produce an electron-hole pair (as shown in Figure 1-9(a); the dashed black line corresponds to the bandgap of Si).[47] The remaining energy after these energy losses (black height) is the energy that a single solar cell is able to use efficiently in the Shockley-Queisser model. Therefore, to break through the Shockley-Queisser limit, one or more of these three loss processes must be overcome.

A part of the energy loss of blackbody radiation is the energy of incident photons with energy that exceeds the semiconductor bandgap energy, which decreases the

amount of current that can be generated. Hot carriers that are generated by this part of the energy relax via electron-phonon scattering. Then, phonon dissipation as heat (i.e., thermalization of charge carriers) decreases the energy conversion efficiency (Figure 1-9(b)). Although the blue-light energy is rough twice the energy of red light, no additional energy is converted to electrical energy by a single P-N junction device.[48] As shown in Figure 1-9(a), for semiconductors with a bandgap of 1.1 to 1.4 eV, if the cell is operated at a voltage that corresponds to the bandgap energy and a current that corresponds to full capture of all photons with energy that exceeds the bandgap, there is a theoretical conversion efficiency limit of approximately 48% (ignoring all other factors).[45]

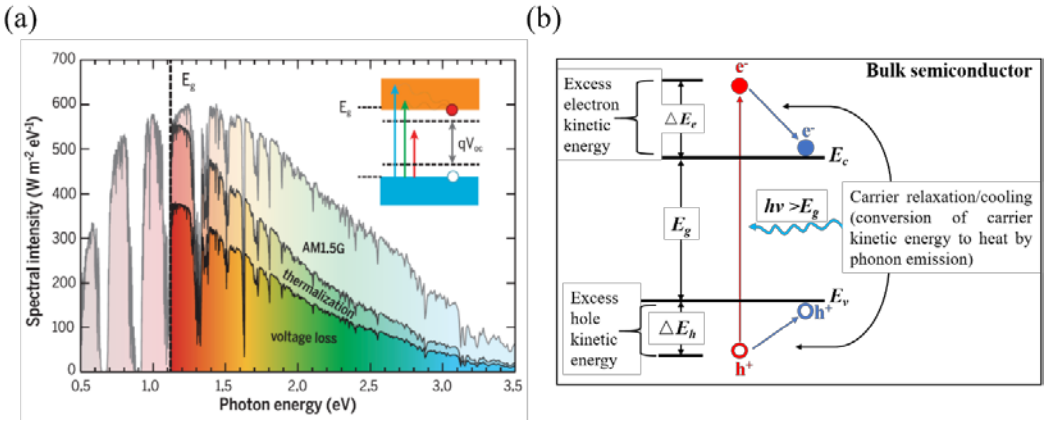

Figure 1-9. (a) AM1.5 solar spectrum has a significant decrease due to the absorption of molecules in the earth's atmosphere.[45] (b) Hot carrier energy loss due to relaxation/cooling via electron–phonon scattering.[48]

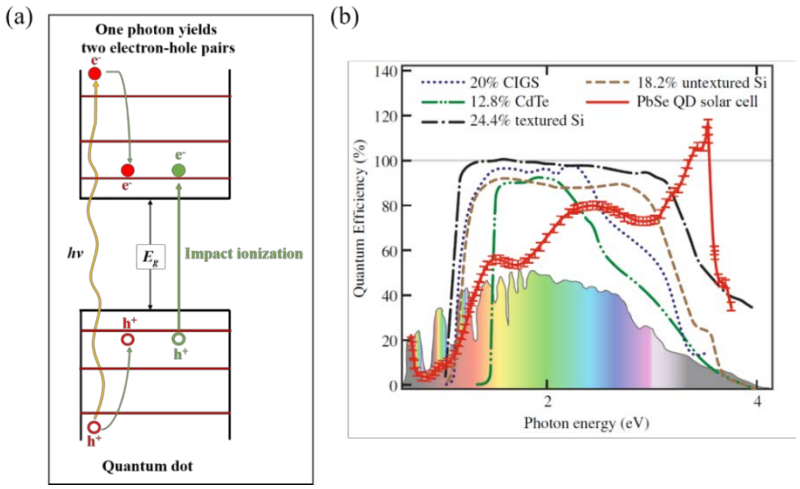

Figure 1-10. (a) Absorbed single photons generate multiple excitons (MEG) in quantum dots.[49] (b) External quantum efficiency (corrected for reflection) for PV PbSe QD solar cell and for standard bulk Si, CdTe and CIGS solar cells as a function of incident photon energy.[48] Only the QD solar cell shows QYs exceeding 100% due to MEG; MEG occurs within the solar spectrum from 3 to 3.5 eV. MEG onset is at about 2.6Eg.

As the above analysis, the significant energy loss (~50%) of absorbed photons results from the excess kinetic energy of hot carriers being converted into heat. One approach uses QDs to reduce or avoid this energy loss thanks to an advantage of QDs: multiple exciton generation (MEG).[50-51] As shown in Figure 1-10 (a), in QDs, the excess kinetic energy of photogenerated hot electron-hole pairs is used to produce additional (or secondary) electron-hole pairs at the band edges. Then, relaxed electron-hole pairs are cooled to the lattice temperature (from 3000 K to 300 K).[48] A similar process occurs in bulk semiconductors (impact ionization); however, higher energy photon excitations are required to generate multiple excitons, e.g., in silicon, one photon with 7 eV (180 nm) can produce one extra carrier and, thus, its influence on solar cells is negligible.[51] MEG was first investigated by the Nozik group and has also been experimentally demonstrated in PbSe QDs through the ultrafast transient absorption technique.[48, 52] As shown in Figure 1-10 (b), the external quantum efficiency (EQE) of the PbSe QD solar cell exceeded 100% for photon energies of more than 2.6 Eg, thus, it was demonstrated that the quantum confinement can significantly increase the energy conversion efficiency of the primary conversion step from high-energy photons to multiple charge carriers.[48] Thereby, QD solar cells with multiple-exciton generation have the potential to reach a new solar conversion efficiency limit.

2. The facile solution processing

Colloidal quantum dot (CQD) synthesis

Semiconductor QDs that are synthesized by a solution method are called colloidal quantum dots. They are cost-effective, which makes them promising candidates for applications in solar cells. Since the solution-based synthesis of CQDs was first reported in 1993, various synthetic methods have been developed, e.g., sol-gel processing, hydrothermal/solvothermal synthesis,[53] coprecipitation,[54] microemulsions and hot injection.[55] To synthesize high-quality and size-controllable CQDs, the hot-injection method is the mainstream route. In this approach, metal-organic precursors are injected into coordinating/non-coordinating solvents at expected temperatures in a nitrogen- and moisture-free atmosphere, which is usually provided by the Schlenk line, as shown in Figure 1-11 (a).[56] As shown in Figure 1-11(b), the CQD formation process can be divided into five steps based on a model that was developed by LaMer[57]: Step I consists of the reaction of CQD precursors, which results in the desired monomers (e.g., metal-organic monomers) with a concentration that exceeds the threshold for nucleation. Then, cluster or monomer growth by these monomers is initiated (step II). Notably, steps I and II are reversible since the growth threshold of the cluster has not yet been reached. Once this threshold has been reached, i.e., the cluster reaches a critical dimension (step III), the process becomes irreversible. Then, the nanocrystal size can be controlled with the aid of ligands as stabilizers (larger molecules) until it becomes monodispersed (step IV). The surface of the CQD is surrounded by organic ligands, so that the quantum dots are stably dispersed in the organic solvent while passivating their surfaces. (inset of Figure 1-1.11(a)).[58] The final size, morphology, and composition of

the CQDs can be controlled by the injection temperature, concentration of precursors, organic ligands and the duration of the maturity phase.

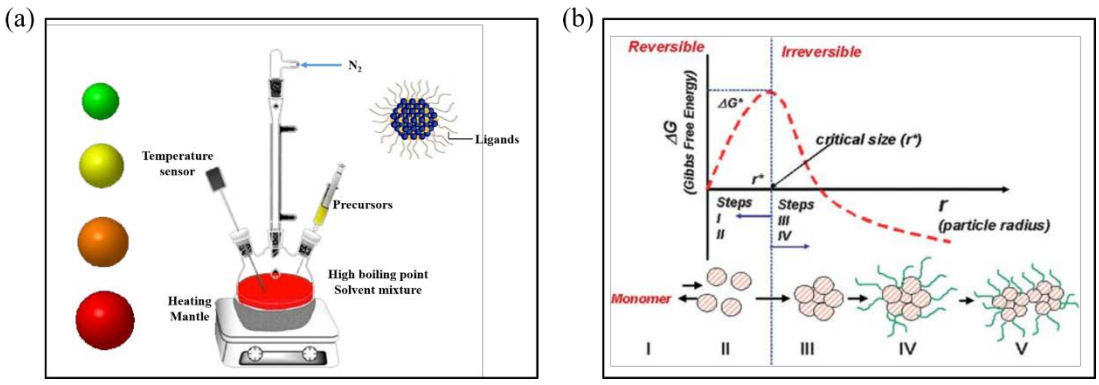

Figure 1-11. (a) a typical " hot-injection " set-up to achieve the burst nucleation. (b) Schematic of the LaMer model.[58] This model describes the nucleation and growth of nanocrystals over time.

CQD Film Formation

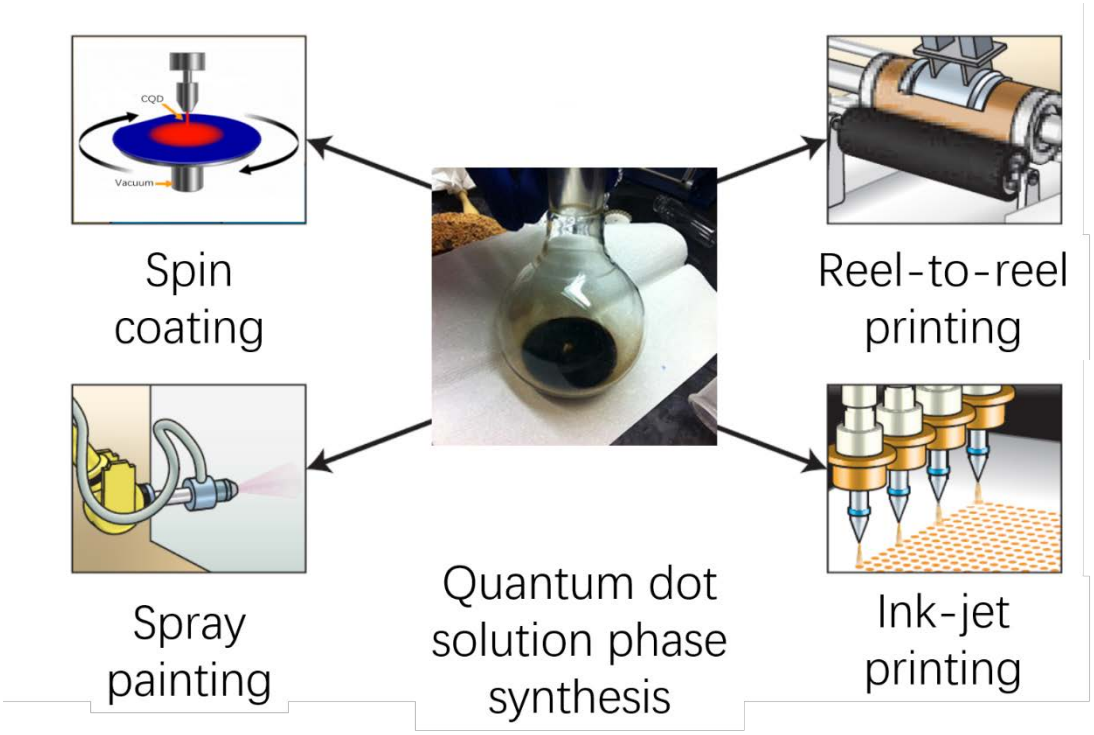

Figure 1-12. After synthesis, colloidal quantum dots are deposited on the substrate at low temperatures. Process technologies used to achieve this include spin coating, spray coating, roll-to-roll printing, and inkjet printing.[59]

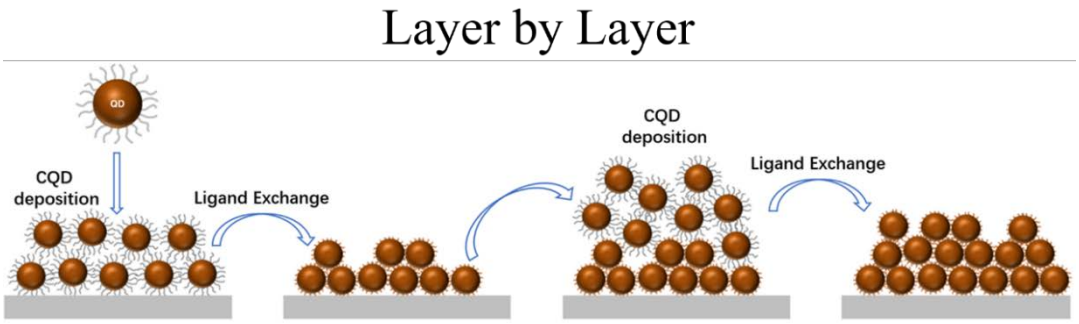

Figure 1-13. Layer-by layer deposition of QD films.[60]

To achieve the goal of low-cost third-generation solar cells, in addition to CQD synthesis, CQD film formation is significant. Because CQDs are usually dispersed in solution (e.g., octane, toluene, or hexane), CQD films can be deposited on various substrates (e.g., flexible substrates) by a variety of low-temperature deposition methods and large-area films can even be prepared (Figure 1-12).[61] Furthermore, a photovoltaic device that is based on a flexible and lightweight substrate can realize lower solar module weight, which reduces installation costs. Compared with other film forming techniques such as drop casting and dip coating, spin coating is a mainstream method for producing high quality CQD films. This method is used in this paper.[62-63] This is due to obtaining a uniform film thickness through a constant rotation speed and promoting evaporation of the solvent during rotation of the substrate. From the "CQD synthesis" section, we know that CQDs have long-chain organic ligands (e.g., oleic acid) on their surface, which ensure the stable dispersion of CQDs in organic solutions. The presence of these long-chain ligands in the CQD film makes the distance between two adjacent CQDs very large, thereby making it difficult for carrier transport to occur between adjacent CQDs. Therefore, after a CQD film has been formed, the long-chain ligands on the surface of the CQDs must be replaced by smaller-sized and short-chain ligands (e.g., ethanedithiol or halide ion) through a process of ligand exchange to reduce the distance between adjacent QDs; then, better performance of the CQD film can be obtained. As shown in Figure 1-13, the process is named layer-by-layer deposition (LBL). The LBL process involves the deposition of CQD solutions and ligand exchange. This process is repeated until the desired film thickness is reached.[60]

1.3.3. Colloidal PbS QDs solar cell

Advantages of PbS CQDs

Many CQD materials have been studied for photovoltaic applications, such as perovskite CQDs ($CsPbI_3$, $CsSnPbI_3$),[64] II-VI materials (CdS, CdSe, CdTe),[65] III-V materials (InAs, InP),[66] and IV-VI materials (PbS, PbSe, PbTe).[67-68] Lead chalcogenide CQDs (i.e., lead sulfide) have attracted the most attention due to their fast efficiency growth from 3% to near 12% within seven years.[69-70] In particular, lead sulfide CQDs

(PbS) have emerged as a leading material for the fabrication of CQD solar cells and are the focus of this thesis. As shown in Figure 1-14 (a), PbS exhibits a cubic rock-salt crystal structure with a lattice constant of 5.93 Å.[71] Since PbS has a small bulk bandgap (0.37 eV) and a large Bohr radius (18 nm),[72] when the size of PbS QD is less than 10 nm, the excitons in PbS all enter the extreme quantum confinement regime, which gives it a sufficiently large spectral range (300~1600) for light harvesting and photodetection. As a superior QD material, PbS CQDs certainly have the characteristic of tunable bandgap, i.e., the bandgap of PbS CQDs can be shifted at will by carefully controlling the QD size (2.5-10 nm), as shown in Figure 1-14(b). In addition, the precise adjustment of the electronic properties and energy-level positions (e.g., the positions of the conduction band energy level and the valence band energy level) of PbS CQD film can also be achieved by modifying the surfaces of QDs with various ligands, as shown in Figure 1-14(c).[73] In this way, the bandgap energy level can be used as a universally adjustable parameter in the performance improvement of QD PV devices, or as an advantageous element in the optimization of tandem solar cells..

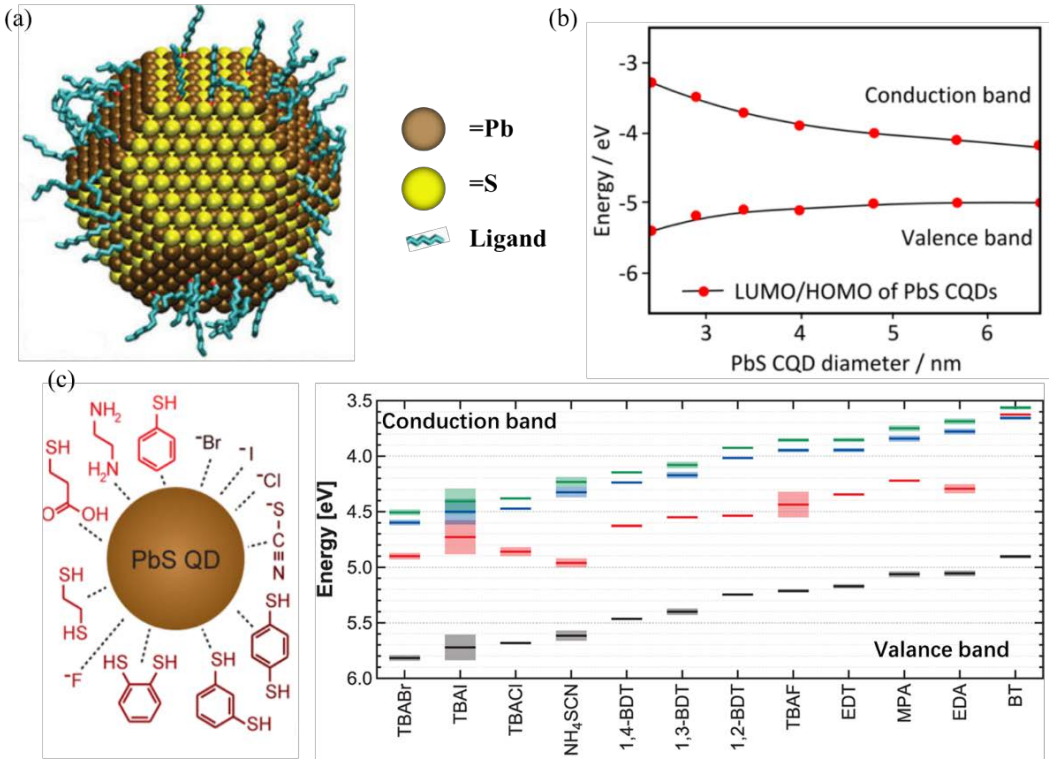

Figure 1-15. (a) Complete atomistic model of colloidal lead sulfide (PbS) nanoparticle with surface passivation by oleic acid, oleyl and hydroxyl groups.[74] (b) Quantum confinement effect for PbS CQDs with its conduction and valence bands.[73] (c) Complete energy level diagrams of PbS CQDs exchanged with the ligands.[75]

Progress in PbS CQD solar cells

In recent years, PbS CQD solar cells have developed rapidly. The significant improvements have mainly been achieved due to the design and improvement of device

architectures and interface engineering. In the development of PbS CQD-based solar cells, a variety of device architectures have been explored to enhance solar cell photon-to-electron conversion efficiency.

Architecture of Devices

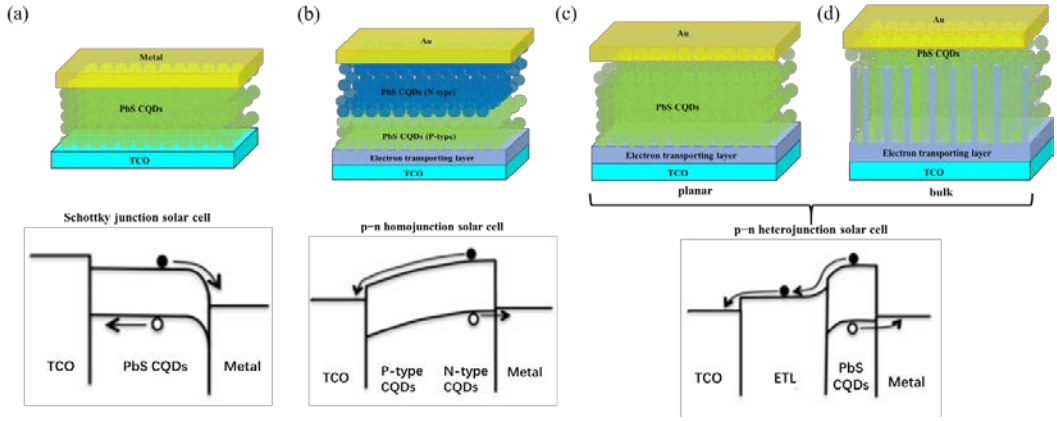

Figure 1-15. Device configuration and energy band diagram for PbS CQD solar cells: (a) Schottky junction solar cell, (b) p−n homojunction solar cell (c) planar heterojunction solar cell and (d) bulk heterojunction solar cell.

Here, we focus on four classes of QD-based solar cell devices (Figure 1-15). PbS CQDs were first applied to solar cells that were based on the Schottky junction by Nozik's group in 2008.[76] As shown in Figure 1-15(a), the structure of a Schottky solar cell is simple: the PbS CQD layer is sandwiched between an ohmic contact transparent electrode (e.g., indium doped tin oxide (ITO)) and a low work function metal electrode (e.g., aluminum (Al)) to form a Schottky junction, as shown in Figure 1-15 (a). In general, the Schottky junction created by the metal with PbS CQD creates a depletion region and a built-in field that separates electron-hole pairs and drives free carriers. Then, the ITO electrode collects the majority carrier, whereas the Al electrode collects the minority carrier. The Schottky structure resulted in fewer interfaces and ease of fabrication during the development of early PbS CQD solar cells. Thus, the optimization and demonstration of the photovoltaic properties (e.g., developing ligand strategies and extending the response to the infrared range) of CQDs film were based on Schottky structures. With these advances, the efficiency of solar cells of this type eventually reached 4.5% in 2011,[77]; this was once the highest efficiency among all types of CQD solar cells. However, this architecture suffers various limitations: When the thickness of the absorbing layer (PbS CQDs) exceeds the width of the depletion region, minority carriers that are generated on the illumination side and diffuse to the metal electrode must cross a quasi-neutral region, which significantly increases the probability of minority carrier recombination. In addition, V_{oc} is generally limited by the Fermi level pinning, the upper limit is only about half of the band gap of PbS quantum dots. Therefore, the PCE of the Schottky solar cell has been limited to sub-6%

values.[78]

The P-N homojunction CQD solar cells were developed on the basis of the simple structure of the Schottky junction solar cells to overcome limitations of previous architectures, mainly low J_{sc}, V_{oc} and stability. As shown in Figure 1-15(b), the P-type layer and the N-type layer that constitute the homojunction are composed of the same type of CQDs; this junction is also called a quantum junction (QJ). Obtaining stable N-type and P-type doping within the same type of CQD film is due to the development of CQD surface engineering (e.g., solid-state ligand exchange and understanding of ligand effects). The main advantage of this architecture is the extensive controllability of the bandgap due to quantum-to-quantum matching, while forming optimal energy level alignment in a solely material system, which can overcome band offset challenges between CQDs and other materials. Notably, in this type of solar cell, photons can be absorbed on both sides of the QJ. Thus, carriers can be efficiently generated and separated to enhance the charge collection efficiency of the electron acceptor layers, thereby increasing J_{sc}. In addition, due to further reduction of interface recombination, V_{oc} will increase, resulting in improved efficiency of PbS CQD type solar cells. Due to these advantages, the efficiency of the PbS QJ solar cell reached 6.6% in 2012,[79] which exceeded that of the Schottky junction solar cells. In addition, QJ solar cell realization opens an avenue to prospective multijunction solar cells.

Initially, the development of the P-N heterojunction solar cells (planar) that were based on CQDs was apparently also aimed at overcoming inherent limitations of Schottky solar cells by allowing for a thicker CQD absorber layer (several hundred nanometers) to improve carrier generation efficiency and moving the depletion region close to the front electrode to enhance the charge collection efficiency. Significant growth in efficiency has been achieved in the short term since these solar cells were developed in 2009 (from 3% to 12%),[70, 80] which is considerably higher compared to other architectures of PbS CQD-based solar cells, and these cells soon became a leader in this field. The P-N heterojunction solar cells that appeared first were of planar structure, as shown in Figure 1-15 (c). The typical device consists of a P-N heterojunction that is sandwiched between a transparent conduction electrode (ITO or FTO) and a metal electrode (Au), where the heterojunction is composed of an N-type metal oxide semiconductor (ZnO, TiO_2 and SnO_2) layer and a P-type CQD semiconductor layer. In this device, the depletion region near the interface of the metal oxide and the CQD layer separate charge carriers, which are mainly photogenerated in the CQD layer. Then, electrons are driven toward the metal oxide layer and injected. Since the metal oxide layer can extract electrons, it is called an electron transport layer (ETL). At the same time, the holes are driven from CQDs to the metal electrode by a built-in field around the depleted heterojunction. Therefore, the P-N heterojunction solar cells are also named depleted heterojunction solar cells (DHSCs). They have two advantages compared with the Schottky structure: more efficient carrier separation and relatively high V_{oc}. To improve the efficiency of heterojunction solar cells, it is necessary to address the competing balance between light absorption (e.g., by

increasing the absorber layer thickness) and charge collection (by enhancing the carrier diffusion length). For the CQD film with optimal bandgap (Shockley−Queisser limit, ca. 1.3 eV), and considering the absorption coefficient (~10^4 cm^{-1}, near the band edge), to absorb 90% of incident photons, the thickness of the CQD film needs to reach ~1 μm.[81] However, the minority carrier diffusion length of the CQD film is limited (typically 10–100 nm.)[81] by their high trap state densities and low electron mobilities. Moreover, only photo-generated carriers within one diffusion length of the depletion region can be effectively collected. As a result, the optimum CQD thickness of DHSCs can only be slightly larger than the depletion region width of the CQD layer. For example, the optimal thickness of the PbS CQD layer is approximately 300 nm, which severely limits the light absorption of the film, thereby resulting in low J_{sc} and the poor performance of CQDSCs. To overcome the competition between light absorption and charge extraction, two improvements are necessary: increase the minority carrier diffusion length and depletion region width of CQD DHSCs. There are two routes to overcoming these challenges, namely, the use of bulk heterojunction architectures and interface engineering, which are discussed in the next sections.

Bulk depleted heterojunction architectures were developed with the aim of increasing the depletion region width of CQD DHSCs. As shown in Figure 1-15 (d), this structure applied the main concept of the interpenetrating network: CQDs are interpenetrated with random or ordered nanostructured metal oxide (e.g., pillars and nanowire arrays). In this structure, the interface area is maximized and the depletion region is allowed to extend in all three dimensions of the CQD layer. Therefore, the absorbing layer can be thickened to micrometers, thereby greatly enhancing light absorption while still enabling efficient charge carrier collection. Via this strategy, J_{sc} is remarkably enhanced to higher than 30 mA/cm^2.[82] However, the main disadvantage is that the large interface area that is introduced also leads to severe interface recombination, more interfaces and more interfacial recombination, thereby resulting in lower V_{oc} than that of planar CQD DHSCs. Therefore, although bulk CQD DHSCs are superior to planar CQD DHSCs in terms of light absorption and electron extraction, their inherent disadvantages, e.g., difficulties in preparation of high-quality nanostructured metal oxide, excessive consumption of CQD materials and more surface defects, do not allow them to replace planar solar cells. In addition to the device architecture design, the application of interface engineering in CQD DHSCs to improve device performance is a very important strategy. Currently, the main achievements of CQD-based solar cells are generally the result of the application of interface engineering.

Interface Engineering

Interfacial engineering in CQD DHSCs has been demonstrated to be a key factor in suppressing interfacial recombination and improving electron extraction. As shown in Figure 1-16, in typical planar CQD DHSCs, there are three main interfaces: (1) the QD surface and/or QD–QD interface; (2) the QD/gold electrode interface, which has a very important impact on device performance; and (3) the QD/ETL (ZnO, TiO_2, SnO_2)

interface, which also has a very crucial impact on the performance of the device.[83]

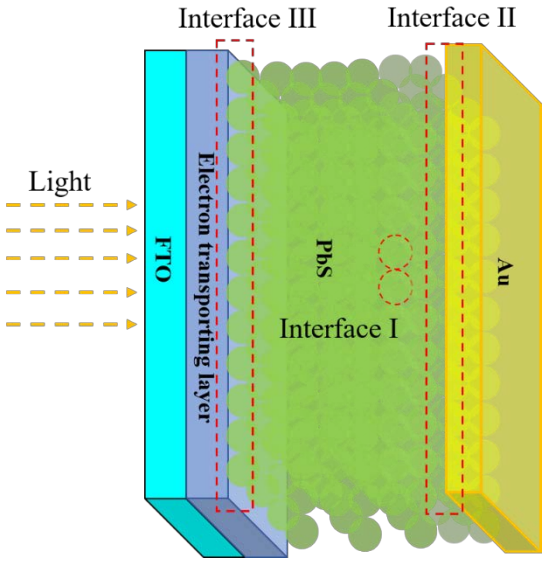

Figure 1-16. Schematic illustration of a CQD DHSCs structure.

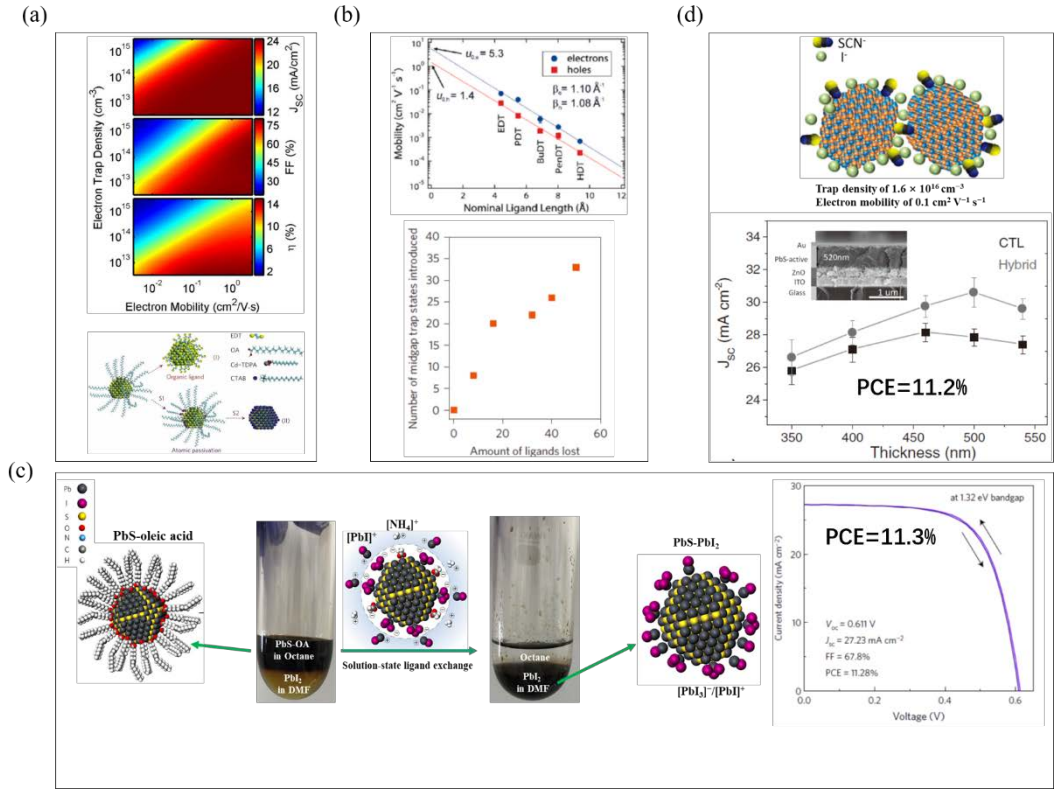

Figure 1-17. (a) Solar cell quality factor traps and simulated diagonal equivalence (upper);[84] Organic and atomic passivation strategies (bottom).[85] (b) Carrier mobility as a function of ligand length in ambipolar PbX QD field-effect transistors (upper);[86] The number of mid-gap trap states introduced by the ligands depicting the loss of the initial charge-balanced quantum dots (bottom).[87] (c) Solution-phase ligand exchange with metal halide precursors and ammonium acetate.[88] (d)

Schematic diagram of PbS CQD capped by I- and SCN- and separated by SCN-(upper); Measured J_{sc} with different active layer thicknesses.[89]

(1) ***Interface I***: Milestone breakthroughs in CQD solid-state solar cell development have benefited from CQD film quality improvement many times. The upper part of Figure 1-17(a) illustrates that the photovoltaic performance of DHSCSs strongly depends on the electron mobility and the trap density of the active layer. Changing the diffusion length can produce any change: the reduced electron trap density increases the carrier lifetime (τ), while the higher electron mobility (μ) increases the diffusion coefficient (D) through the Einstein relationship ($\mathrm{D} = \mu k_B T$, k_B is Boltzmann's constant). However, the charge transport in the CQD film occurs via band-like transport or hopping mechanisms. Thus, interdot coupling (e.g., the distance between adjacent quantum dots) is of crucial importance for solar cells. In addition, the innate large specific surface area of CQDs leads to many electronic trap states due to unsaturated dangling bonds on the CQD surface, which increase the carrier recombination, thereby reducing both the extractable current and the attainable voltage. For both issues, ligand strategies (bottom of Figure 1-17 (a)) are proven to be efficient paths to improving charge transport and decreasing surface trap states, e.g., organic-inorganic hybrid passivation and atomic passivation. The upper part of Figure 1-17 (b) shows the effects of ligand length on the mobility and coupling of CQDs: the mobilities of electrons and holes in PbX CQD increased exponentially with decreasing chain length of the ligand on the QD surface, with a decay length that is characteristic of a hopping mechanism.[90] For instance, the use of short thiol ligands (e.g., 1,2-Ethanedithiol(EDT), mercaptocarboxylic acids (MPA)) for PbS CQD DHSCs led to the highest PCE (5.1%) at the time due to increasing carrier mobility.[29] However, as shown in the bottom of Figure 1-17 (b), density functional theory calculations demonstrated that the number of trap states in the bandgap strongly depends on the number of ligands on the surfaces of QDs.[87] Therefore, it is essential that the cleanliness of the bandgap of the QD be ensured by surface passivation for the device performance. The application of inorganic metal ion (Cd^{2+}) and halide anion ((Cl^-, Br^- and I^-)) ligands for passivating QD is a milestone. This atomic inorganic ligand passivation strategy was first reported by Sargent's group[85] for obtaining dramatically increased carrier mobilities, decreased number of traps, and improved QD stability.[85, 91] Due to these advantages, a PCE of CQD DHSC of more than 6% was achieved. In general, the manufacture of CQD thin films is based on the LBL process by employing the above ligand exchange process, which leads to incomplete ligand exchange and low quantum dot utilization. To solve these problems, as shown in Figure 1-17 (c), a one-step spin coating process that employs the solution-state ligand exchange was developed. Using this technique, $[PbX_3]^-$/$[PbX]^+$-passivated PbS CQD films were prepared, which can significantly reduce the trap density, thereby leading to a certified PCE of 11.28% and good air stability.[88] The use of pseudohalogens in active layers of colloidal quantum dots (CQD) solar cells improves solar cell performance by reducing trap density and realizing thick CQD films. Very recently, as shown in Figure 1-17 (d),] a hybrid passivation approach (i.e., incorporation of I^- and SCN^- ions) was applied in PbS CQD

DHSCs by solution exchange, which can remarkably reduce the trap densities and implement thick CQD films (500 nm), thereby leading to an impressive PCE of 11.2% with a high J_{sc} of 31.50 mA/cm^2.[92]

(2) ***Interface II*:**

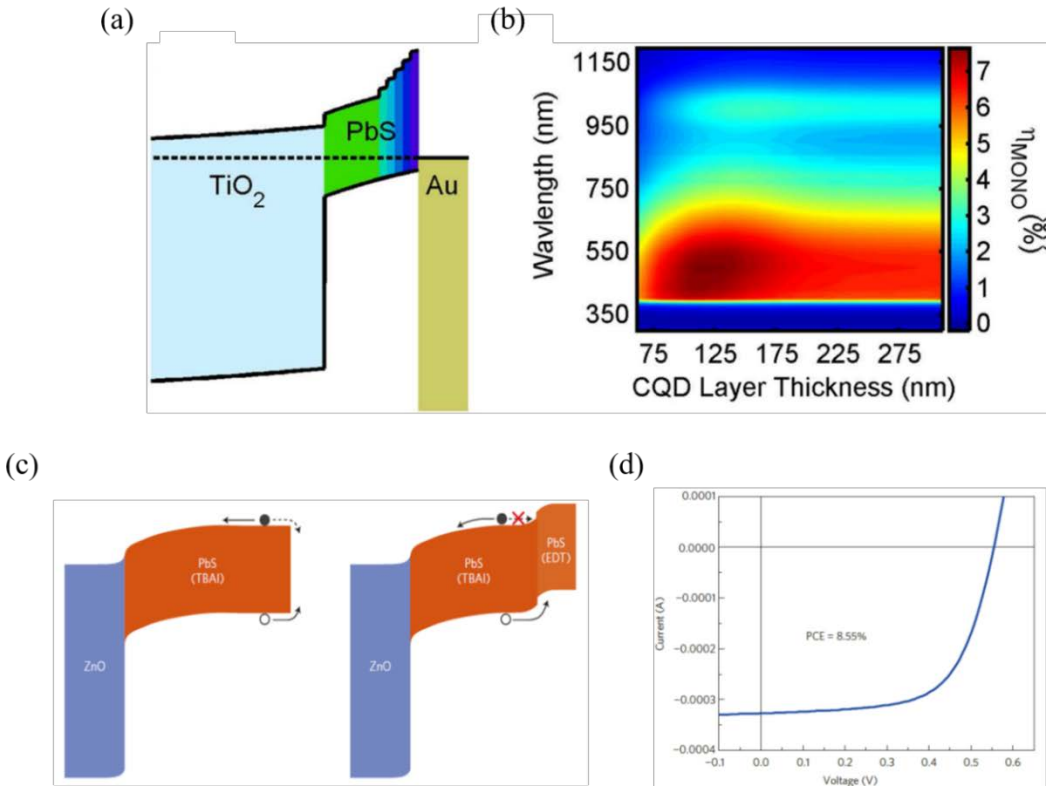

Figure 1-18. (a) Energy band diagram of a quantum funnel device and (b) Simulated monochromatic energy conversion efficiency of a device using an optimally placed quantum funnel.[93] (c) A schematic diagram of band bending in ZnO/PbS-TBAI (left) and ZnO/PbS-TBAI/PbS-EDT (right) devices under short-circuit conditions.[94] (d) Performance of PbS-TBAI/PbS-EDT devices after 37 days of air storage certified by a certified laboratory (Newport).[94]

The CQD/metal-electrode interface plays an important role in CQD DHSCs because this interface seriously affects the photogenerated electrons and holes' collection efficiency. To improve the performance of CQD solar cells, band alignment strategies are mainly applied in this interface. In CQDs system, it is easy to build a band alignment structure by taking advantage of quantum-size-effect tuning. As shown in Figure 1-18 (a), the band alignment structure acts as a quantum funnel between the absorbent layer and the electrode, to drive the performance-limiting minority electrons towards the desired electrode.[93] According to the simulated results from Figure 1-18 (b), the band alignment structure can substantially increase the diffusion length of electron carriers in thick devices, thereby increasing the carrier extraction efficiency.[93] In addition, Bawendi et al. introduced an EDT-passivated PbS CQD layer between a tetrabutylammonium iodide (TBAI)-treated (i.e., iodine-passivated) PbS CQD active

layer and the gold electrode, which acts as an electron blocking layer (EBL) or hole transporting layer (HTL), as shown in Figure 1-18 (c).[95] This band alignment engineering resulted in a certified PCE of 8.55% (Figure 1-18(d)), breaking through the efficiency bottleneck at the time.[95] Currently, high-efficiency PbS CQD DHSCs all employ Bawendi's structure.

(3) ***Interface III*:**

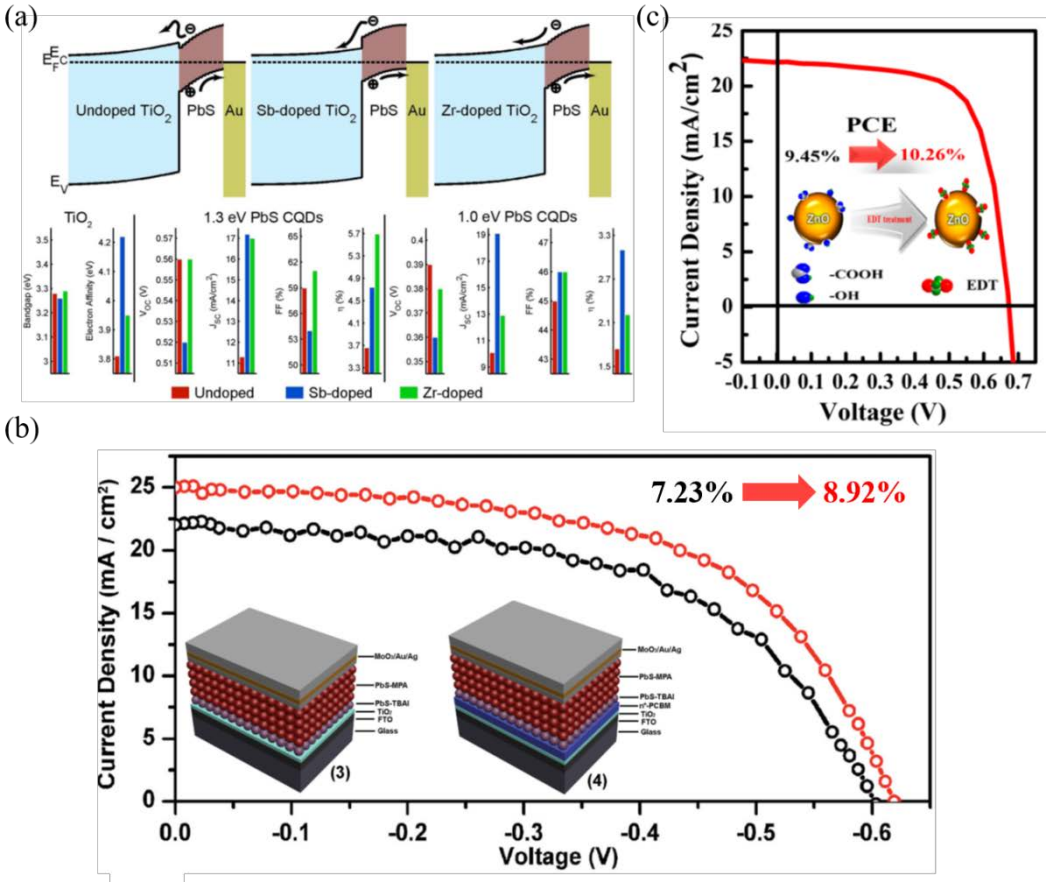

Figure 1-19. (a) Top row: Heterojunction band diagrams consumed with undoped TiO2, lanthanum-doped TiO_2 and zirconium-doped TiO_2. Bottom row, third to sixth columns: Performance metrics of 1.3 eV PbS CQD DH solar cells using the undoped, Sb-doped, and Zr-doped sol−gel TiO_2.[96] (b) Performance of PbS CQD DHSCs with/without N doping PCBM buffer layer.[97] (c) The J−V characteristics of the PbS CQD DHSCs fabricated with the chemically modified ZnO-np layers under AM 1.5G one-sun illumination. Insert: Chemically modified ZnO-np surface defect passivation schematic.[98]

In a CQDHSC, the p-type layer is a CQD film and the n-type layer is an ETL that accepts photogenerated electron carriers. Better engineering the heterointerface between CQDs and ETLs is a key strategy for the enhancement of device performance. To date, the energy-level alignment at the ETL/CQD interface by low-content doping of ETLs, and surface modification by introducing a buffer layer between ETLs and the CQD film and utilization of chemical modifier have been considered as interface

engineering approaches. For instance, as shown in Figure 1-19 (a), for interfaces of TiO_2/PbS CQDs, smaller or even negative conduction band offset (CBO) results in larger V_{oc}, whereas a negative CBO reduces J_{sc}. The favorable CBO further aids in maximizing the product of V_{oc}, J_{sc}, and FF.[99] The control of CBO via doping of TiO_2 film with various elements (i.e., zirconium (Zr) and antimony (Sb)) is also considered. As shown in Figure 1-19 (b), Sargent's group used an ultrathin n-doped [6, 6]-phenyl-61-butyric acid methyl ester (PCBM) as the buffer layer between TiO_2 ETL and the PbS CQDs layer.[99] It was demonstrated that the introduction of PCBM to act as the buffer layer not only reduces interface defects but also broadens the depletion region in the CQD layer, thereby leading to enhanced electron injection from PbS to TiO_2 ETL, and a high PCE of 8.9% was achieved. In addition, as shown in Figure 1-19 (c), Jang et al. used a chemical modifier (1,2-ethanedithiol) to effectively reduce the surface defect state of the ETL (ZnO nanoparticle), which significantly suppressed interfacial recombination of carriers in ZnO/PbS CQD DHSCs. As a result, high-efficiency (10.26%) CQD PVs were achieved by improving the interfacial charge extraction.[98]

In summary, in the last few years, PbS CQD DHSCs have developed rapidly thanks to great efforts in the interface engineering of three interfaces (Figure 1-16). Via various interface engineering strategies, the highest efficiency has reached 12% (certified); however, this is far below the theoretical value of 44%. The present study focuses on the preparation of QDs and devices and does not consider the internal mechanism of the CQD DHSCs. Therefore, further fundamental studies on how to improve the efficiency of CQD DHSCs through the internal mechanism are necessary and important. In these thesis, we focus on the injection and recombination of photogenerated carriers at the PbS CQD/metal electrode (Interface II) and the PbS ETL/CQD (Interface III) interfaces, through interface engineering.

1.4 Perovskite Photovoltaics

Solar cells that are based on perovskite materials are the most promising next-generation solar cells, which is mainly due to their excellent physical and chemical properties, cheap preparation processes, and certification efficiencies of more than 20%.[100] It is necessary to understand the origin of high performance in perovskite-based solar cells to realize the maximum theoretical PCE (31.4%).[101] In addition, the stability and hysteretic behavior issues are still an obstacle to the commercialization of PSCs and require further studies.

1.4.1 Crystal structure and Physicochemical characteristic

The perovskite material acts as an absorber of PSCs and directly determines the performance of the PSCs. Perovskite is derived from the mineral calciumtitanate ($CaTiO_3$) and is named after a Russian mineralogist (Lev Perovski).[102] As shown in Figure 1-20 (a), all perovskite compound materials have the same molecular structure of ABX_3, where A and B are cations, which are located in a cube-octahedral site and an

octahedral site, respectively. *X* is an anion species, such as oxygen, carbon, nitrogen or halogen; when *X* is the O^{2-} anion, *A* is divalent and *B* is tetravalent. In organic-inorganic hybrid metal halide perovskites, *A* is a monovalent organic cation (e.g., methylammonium, $CH_3NH_3^+$ (MA^+) or formamidinium, $CH(NH_2)_2^+$(FA^+) or an inorganic cation (e.g., K^-, Rb^-, Cs^-) and occupies the vertex of the face-centered cubic lattice; *B* is metal cation (e.g., Pb^{2+}, Sn^{2+}, Ge^{2+}) and occupies the core of the octahedra; and *X* is a halogen anion (e.g., Cl^-, Br^-, or I^-, or a coexistence of several halogens) and occupies the apex of the octahedra.

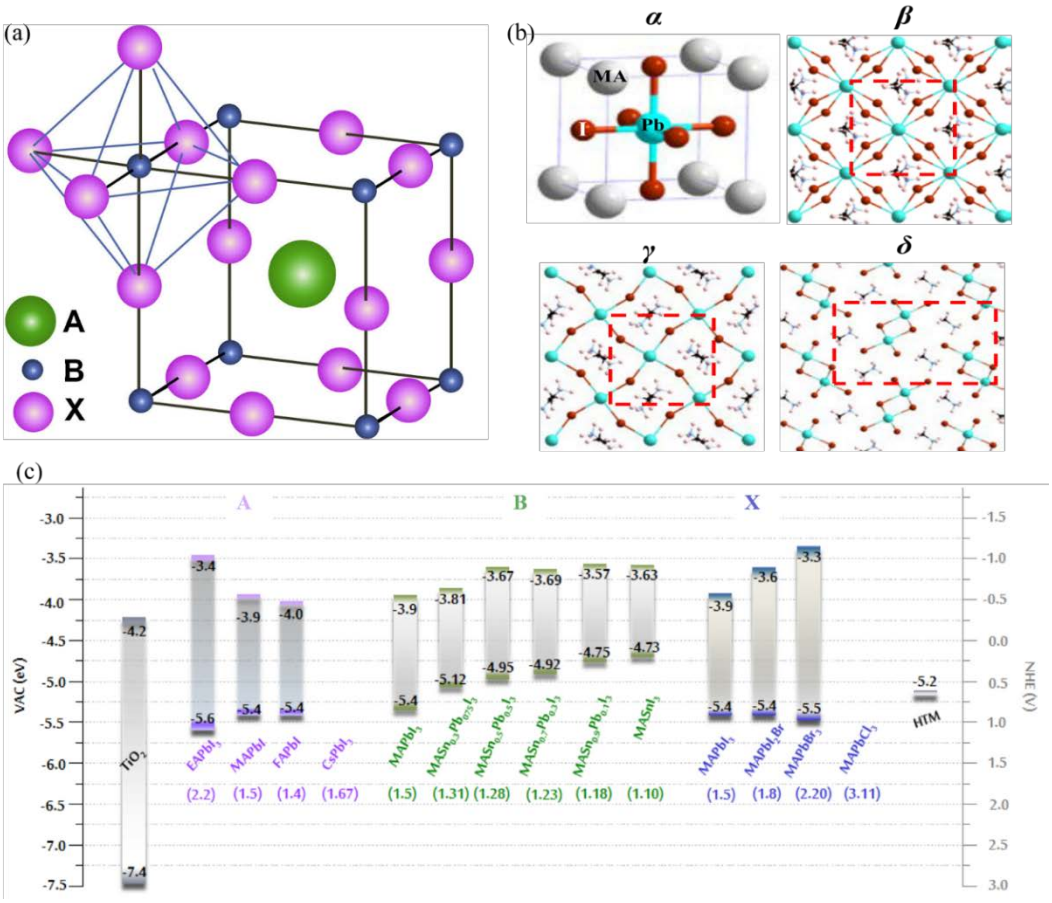

Figure 1-20. (a) ABX_3 perovskite structure shows BX_6 octahedrons and larger cations occupy cubic octahedral sites.[103] (b) The atomic structure of α phase, β phase, γ phase, and δ phase $CH_3NH_3PbI_3$ ($MAPbI_3$).[104] The unit cells of β and γ phases are ($\sqrt{2}\times\sqrt{2}\times2$), based on the α phase. (c) Energy levels vs. vacuum and NHE for various perovskite absorbers.[105]

As shown in Figure 1-20 (b), in the cubic phase of $CH_3NH_3PbI_3$ ($MAPbI_3$), the *A*-site cation is $CH_3NH_3^+$ and the *B*-site cation is Pb^{2+}. In this thesis, we also focus on $CH_3NH_3PbI_3$ perovskite material. Generally, organic-inorganic hybrid metal halide perovskites (ABX_3) have a variety of crystal structures. The crystal structure and crystal stability of perovskites are determined by octahedral factors (μ) and tolerance factors (t). These factors are respectively defined by the following equations:[106]

$$\mu = \frac{r_B}{r_X} \qquad (1\text{-}3)$$

$$t = \frac{r_A + r_X}{\sqrt{2}(r_B + r_X)} \qquad (1\text{-}4)$$

where r_A, r_B and r_X are the efficient ionic radii for the A, B and X groups, respectively. For a compound that is based on the ABX_3 structure, when the values of the octahedral factor (μ) and tolerance factor (t) satisfy $0.44<\mu<0.90$ and $0.81<t<1.11$, the compound can be identified as perovskite.[106] For perovskite, when the value of the tolerance factor lies between 0.89 and 1, the structure with the α phase (cubic) is formed predominantly; if the tolerance coefficient is smaller (i.e., $0.80<t<0.89$), the lower-symmetry β-phase (tetragonal) or γ-phase (orthorhombic) structures could form.[107] Interestingly, perovskites with FA cations and Cs cations, e.g., $FAPbI_3$, $CsPbI_3$ and $CsSnI_3$, have a larger tolerance factor (t >1) and exhibit a hexagonal yellow non-perovskite δ phase at room temperature.[108] Notably, phase transformation between those structures at finite temperature occurs in most perovskites. For $MAPbI_3$, the α-to-β-to-γ phase transitions occur at 330 K and 160 K, respectively.[108]

Changes in the A-site, B-site, and X-site atom or group in the cubic structure of an organic-inorganic hybrid metal halide perovskite will affect the band structure of the perovskite. As shown in the left part of Figure 1-20 (c), the bandgap (~1.5 eV) of $CH_3NH_3PbI_3$ is close to the optimum value. To tune the bandgap to the optimum value, the MA^+ could be replaced by FA^+ to form $FAPbI_3$ ($NH_2CH_2{=}NH_2PbI_3$) with a bandgap of 1.4 eV, which significantly broadens the range of absorption wavelengths, thereby effectively improving the short-circuit current density (J_{sc}) of the device.[109] When using larger-sized $CH_3CH_2NH_2$ (EA) as the A-site group, the bandgap of perovskite increases to 2.2 eV.[110] In addition, the use of inorganic atoms (Cs^+) instead of organic functional groups can produce fully inorganic perovskite; the bandgap of $CsPbI_3$ is 1.73 eV.[64] Based on the structural formation criteria, in the cubic ABX_3 structure, only the above molecules can be used to tune the bandgap by changing the groups of the A site. In $MAPbI_3$ perovskite material, congeners Sn, Ge, etc., are used to replace the toxic element Pb at the B site. By controlling the ratio of Sn (or Ge) and lead elements, one can regularly control the bandgap of the material (middle part of Figure 1-20 (c)). For example, in perovskite $MAPb_xSn_{1-x}I_3$, to control the ratio between Sn and Pb (i.e., x from 1 to 0), the bandgap can be tuned from 1.55 to 1.17 eV and, thus, the light absorption can be enlarged from the visible to the near-infrared region (1060 nm).[111] However, at present, the best PCE of lead-free organic-inorganic hybrid PSCs that has been achieved is approximately 7%; further study is required.[112] As shown in the right part of Figure 1-20 (c), in the X site of $MAPbX_3$, as the size of the halogen atoms decreases, i.e., I → Br →Cl, the bandgap gradually increases from 1.5 to 3.11.[113] Thus, a bandgap of ABX_3 that is smaller than 1.51 eV cannot be obtained solely via tuning the halogen; it is necessary to alter the elements of both the B and X sites simultaneously.[114]

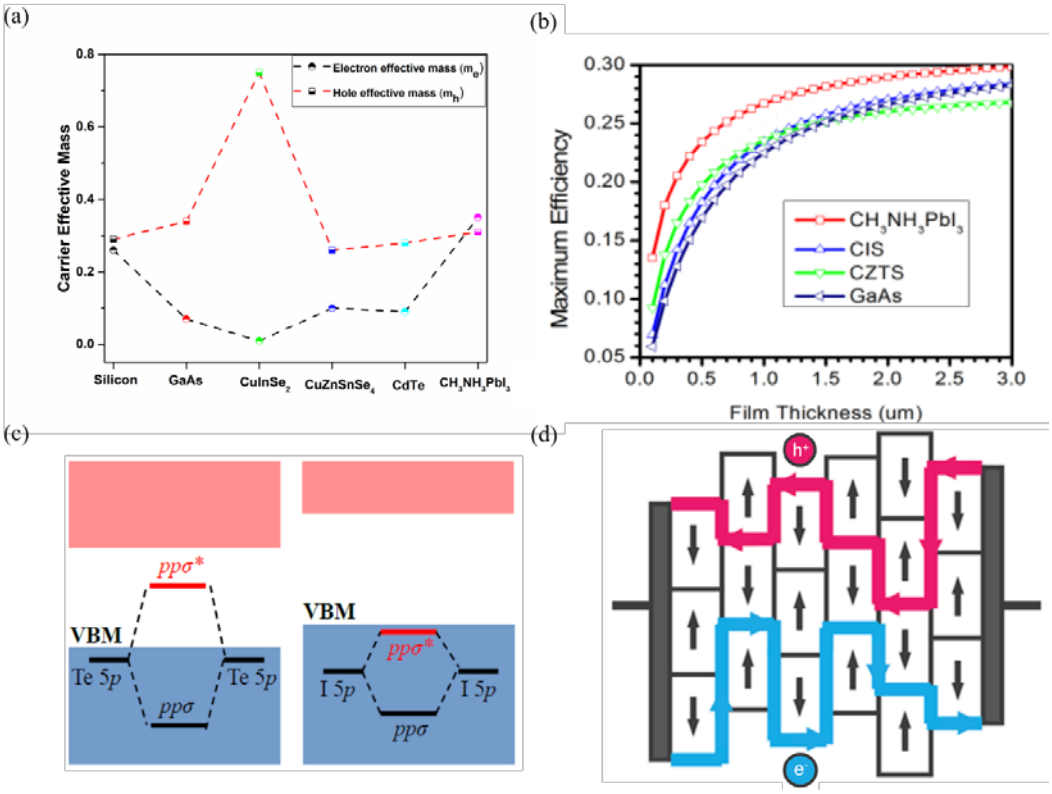

Figure 1-21. (a) DFT-PBE calculated effective masses for electrons and holes of different photovoltaic semiconductors.[104] (b) Calculated maximum efficiencies of $CH_3NH_3PbI_3$, $CuInSe_2$ (CIS), Cu_2ZnSnS_4 (CZTS), and GaAs as a function of film thickness.[115] (c) The schematic diagrams of defect state formation at CdTe and perovskite grain boundaries (GBs).[104] (d) The schematic diagrams of ferroelectric multidomain as hypothesized in halide perovskite solar cells. The diffusion highways for carriers are indicated by red and blue lines and arrows.[116]

In addition to having a broad and tunable optical bandgap, perovskite materials have other optoelectronic properties that are essential for building an efficient photovoltaic device. Carrier transport in a PV device is an essential parameter and must be highly efficient. Free carriers are usually associated with large diffusion lengths. In semiconductors, carrier transport is directly associated with the diffusion length and mobilities. According to Equation (1-5), the mobilities and diffusion coefficients both depend inversely on the effective mass.

$$\mu = \frac{e\tau}{m^*} \qquad (1\text{-}5)$$

where μ is the mobility, m^* is the effective mass, and τ is the temperature-dependent scattering lifetime.[117] As shown in Figure 1-21(a), carriers in perovskite (α-phase $MAPbI_3$) have a smaller effective mass than that of GaAs, which is close to that of silicon.[104] However, mobility that exceeds 200 $cm^2V^{-1}s^{-1}$ for PSCs has been reported, which is much lower than those for GaAs, which is mostly attributable to higher electron−phonon coupling in perovskites.[118] Despite this lower mobility, the PSCs still

show excellent charge extraction efficiency due to the long carrier lifetimes (100 ns ~ 15 μs, under one sun) of perovskite, which also result in extremely long diffusion length (more than 1 μm).[117] Notably, the effective mass of the electron and hole in $MAPbI_3$ is balanced, which may result in ambipolar conductivity in PSCs. The long-range ambipolar transport property of PSCs facilitates the preparation of the planar P-I-N-junction solar cell.

One of the superior features of PSC is that perovskite possess high optical absorption coefficients (up to 10^4 cm^{-1}). Thus, a 500 nm perovskite layer can absorb enough sunlight to achieve more than 20% PCE. The optical absorption of a semiconductor depends not only on the optical bandgap but also on the joint density of states (JDOS). As mentioned above, $MAPbI_3$ possesses an optimal light absorption bandgap (~1.5 eV) and higher JDOS than that of GaAs.[115] Therefore, $MAPbI_3$ has stronger light absorption than GaAs. As shown in Figure 1-21(b), the halide perovskites ($MAPbI_3$ and $CsPbI_3$) show much higher conversion efficiencies than CIS, CZTSe and GaAs for any thickness.[115]

Generally, metal halide perovskites are prepared by a low-temperature solution process, which inevitably results in the formation of many grain boundaries (GBs) in the perovskite polycrystals. In conventional polycrystalline light absorbers, the presence of GBs could significantly degrade the electronic and optical properties of the semiconductor and endanger the performance of the solar cell. For example, the GBs that are inherent in the absorbing layer of the CdTe solar cell generate deep-level defects in the bandgap, and these defects, as carrier recombination centers, severely harm carrier lifetime and the performance of the device.[119] However, in perovskites, GBs do not cause deep-level defects due to their large atomic sizes and loose crystal structures. The different effects of GBs on CdTe and perovskites can be explained by their electronic structures. As shown in Figure 1-21(c), the antibonding ppσ* states that are associated with GBs in CdTe are in its bandgap, while the antibonding ppσ* states in perovskite are below its valence band. In addition, the perovskites possess a large dielectric constant (25.7), which effectively reduces the effect of defects on carriers. Therefore, the bulk recombination and trap densities are low in PSCs.

In addition, the metal halide perovskites possess a dipole moment of the non-centrosymmetric organic cation, which makes the perovskite exhibit spontaneous polarity, i.e., the perovskite material has ferroelectricity.[116] As shown in Figure 1-21 (d), the presence of ferroelectric domains can create internal junctions that facilitate electron-hole pair separation and transport, thereby reducing recombination.[116]

Although not fully understood yet, these outstanding optoelectronic properties in perovskites cause them to surpass most traditional photovoltaic semiconductors, thereby underpinning their success in PV applications.

1.4.2 Device architectures and Fabrication method

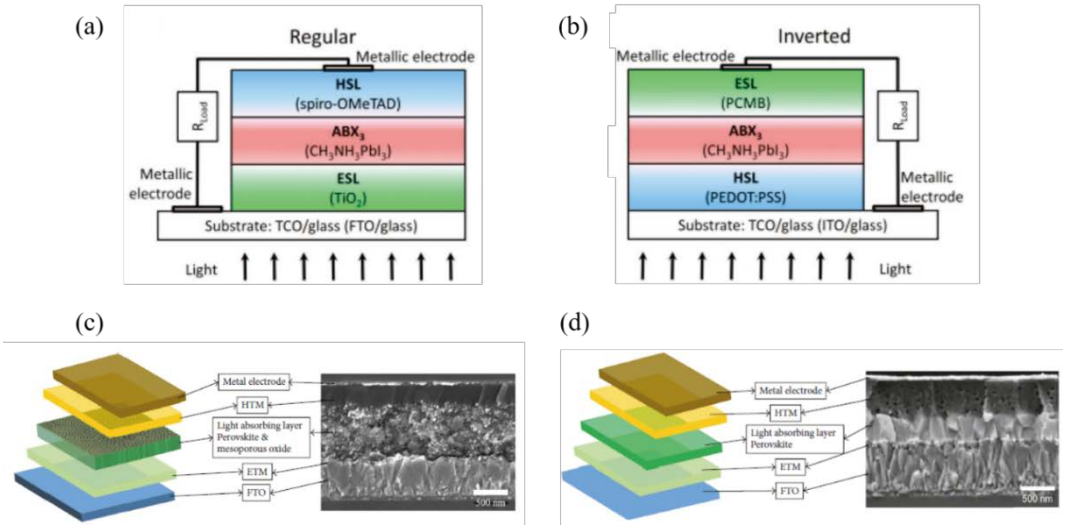

Figure 1-22. Basic structure of PSCs in (a) regular and (b) inverted configurations.[120] Schematic diagram and SEM section image of (c) mesoscopic architecture PSCs (regular) and (d) planar heterojunction structure PSCs (regular).[121]

The typical structure of a PSC consists of five parts: a metal as a back electrode, a metal oxide as a front electrode, and a perovskite as a light-absorbing layer, which is sandwiched between electron- and hole-selective layers. As shown in Figure 1-22(a), the most successful and extensively studied architecture was initially an electron-selective layer (ESL), e.g., TiO_2, ZnO and SnO_2, on a fluorine-doped tin oxide (FTO)/glass substrate, followed the perovskite layer and later the ESL, e.g., spiro-OMeTAD; the metal electrodes are often made of gold (Au) in order to achieve better ohmic contact.[122] This "regular" structure, namely, the N-I-P configuration, is commonly employed in PSCs with higher efficiency at present.[123] Figure 1-22 (b) shows another important structure compared with the conventional structure, the ESL and the HSL are replaced in this structure; thus, this structure is also called an inverted structure (i.e., P-I-N configuration). For inverted PSCs, the organic materials that are used for the selective layer are mainly fullerene derivatives and organic compounds, with [6,6]-phenyl-C-61-butyric acid methyl ester (PCBM) and poly(3,4-ethylenedioxythiophene) doped with poly(4-styrenesulfonate) (PEDOT: PSS) being the most common for ESL and HSL, respectively.[124]

The regular structures of PSCs further divided into the mesoporous structure and the planar heterostructure. The main difference between these structures is the material of the ETL. Figure 1-22 (c) shows a typical mesoporous PSC, in which TiO_2 mesoporous framework material acts as an ESL, which helps to form an interconnected absorbing layer that permeates perovskite into the pores of mesoporous TiO_2. The mesoscopic structure is demonstrated to improve charge extraction by decreasing the carrier diffusion length. In PSCs, in addition to TiO_2, mesoscopic metal oxides, such as ZnO,

Al_2O_3, and ZrO_2, are typically used. This structure has been adopted by the initial solid-state PSCs (9.7%)[125] and the highest certified PSCs (22.1%) at present.[126] Figure 1-22 (d) shows the typical planar heterojunction structure of PSCs. In this structure, the metallic oxide compact layer acts as an ESL, and two interfaces are formed between the perovskite layer and the ESL and HSL. The development of planar PSCs benefits from the discovery of ambipolar properties for perovskite materials. Compared with mesoporous PSCs, the planar PSCs simplify the fabrication process. The studies on planar PSCs contribute to the understanding of the mechanisms of electron-hole separation, carrier injection and recombination for the development of highly efficient PSCs. At present, the efficiency of PSCs that are based on planar structures has exceeded 20%.[127] In this thesis, our research focuses on planar regular PSCs.

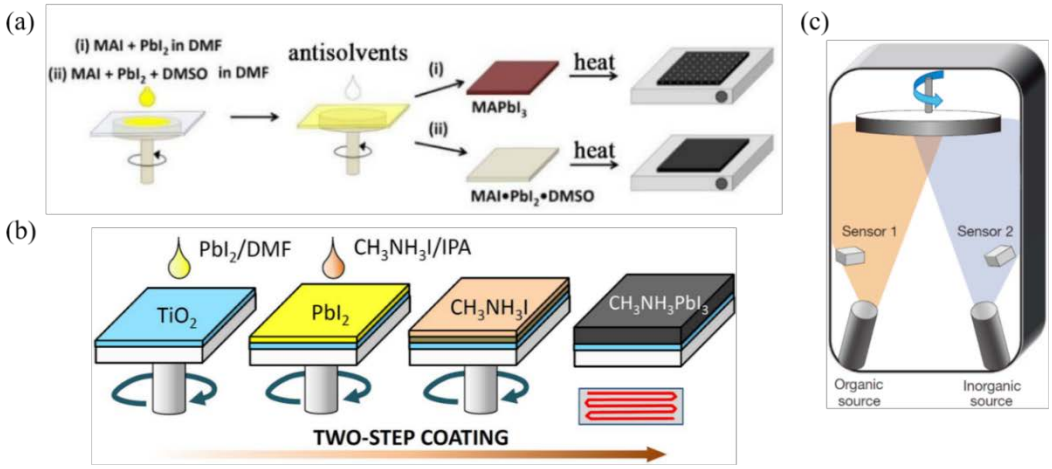

Figure 1-23. Illustration of typical deposition methods for perovskite layer formation: (a) solution-based anti-solvents method,[128] (b) solution-based two-step method,[129] (c) vapor deposition.[130]

In addition to the design of the device architecture, the development of high-efficiency PSCs requires the preparation of high-quality crystalline perovskite films, i.e., films that are uniform, smooth, and pin-hole-free. After several years of development, the fabrication methods of perovskite film can be roughly divided into three types: the solution-based anti-solvent method, the solution-based two-step method and vapor deposition. The anti-solvent method (solvent engineering), which was first reported by Jeon's group,[131] is a widely adopted method for preparing high-quality perovskite film.[132] As shown in Figure 1-23 (a), the anti-solvent method generally has two routes: (i) spin-coating a mixed solution of PbX_2 and MAI in DMF solvent, followed by spin-coating chlorobenzene as an anti-solvent to promote the formation of a perovskite film;[133] (ii) first forming an intermediate product (DMSO-$MAPbI_3$) with PbI_2, MAI and DMSO, and then melting it into DMF and forming a perovskite film with an anti-solvent.[134] Afterwards, a gas-assisted anti-solvent method was developed by Cheng's group,[135] which yields more-uniform perovskite films due to the production of densely packed single-crystalline grains. Although this method is simple, it is not easy to control the morphology and size of the perovskite crystals.

The solution-based two-step method was first reported by Burschka et al.[136] As shown in Figure 1-23 (b), in this method, the PbI_2 layer is formed and reacted with MAI solution. This method can control the $MAPbI_3$film morphology and optoelectronic properties by controlling the PbI_2 dipping time and the MAI solution concentration.[121] Compared to the anti-solvent method, this method has relatively flexible requirements on the preparation environment: as long as the ambient humidity is less than 60%, the performance of the prepared PSCs is unlikely to be affected by the humidity.[137] Moreover, the perovskite film that is prepared by this method has better thermal stability on the ESL layer that is prepared by a low-temperature method such as zinc oxide, and the required temperature is low (<150 ℃) for preparing high-quality perovskite films via this method.[138] Therefore, the preparation of perovskites using a two-step process has the potential to produce flexible devices. Bi et al. achieved a stable PSC through a two-step method and demonstrated a power conversion efficiency (PCE) of 21.6% and a certified PCE of 21.02%.[138] In this thesis, our perovskite films were prepared by the solution-based two-step method.

Although the solution-based method is simple and economical, more internal defects will be introduced in synthetic crystals, thereby reducing the device's fill factor and V_{oc}. To solve these problems, the vapor-deposition method was developed to produce perovskite film with high surface density and fewer defects. As shown in Figure 1-23 (c), by thermal evaporation from dual sources of PbX_2 and MAX, PbX_2 and MAX are deposited simultaneously or alternately on the pre-coated TiO_2 substrate to form $MAPbX_3$ film. This method was first reported by Snaith et al., who achieved PCE of planar PSC of over 15%.[130] However, this method is very demanding on the equipment and produces a toxic (PbI_2) atmosphere; thus, it requires further development.

The preparation method strongly influences the properties of perovskite films. Through the development of preparation methods, one can obtain compact perovskite films with high purity, few defects, and high coverage, and achieve a high PCE of PSCs.

1.4.3 Interface engineering in perovskite solar cells

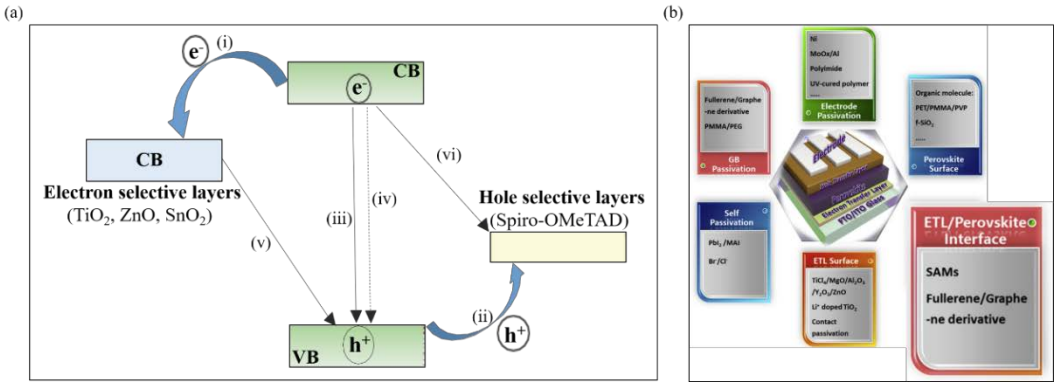

Figure 1-24. (a) Schematic diagram of energy levels and transport processes of electrons and

holes in a ESL/perovskite/HSL cell. (i) Electron injection; (ii) hole injection; (iii) radiative exciton recombination; (iv) non-radiative exciton recombination; (v) back electron transfer at the ESL/perovskite interface; (vi) back charge transfer at the perovskite/HSL interface. (b) Diagram summarizing the surface and interface engineering for perovskite solar cells.[139]

In PSCs, in addition to the overall properties of the perovskite as an absorbing material, the surface and interface between the absorber layer, the carrier selective layer and the electrode contact layer are very important for efficient carrier collection. As shown in Figure 1-24 (a), for the typical PSCs, in the perovskite absorbing layer, electron-hole pairs that are generated by photoexcitation are separated at the both heterojunction interfaces of ESL/perovskite and perovskite/HSL and the separated electrons and holes are injected into the ESL (process (i)) and the HSL (process (ii)), respectively, to realize carrier transport.[140] In the process, there are also carrier behaviors that are detrimental to solar cell performance, such as band-to-band recombination (process (iii)), non-radiative recombination (process (iv)), and back-transfer recombination of electrons and holes at the ESL/perovskite interface and the perovskite/HSL interface (processes (v) and (vi), respectively).[140]

To mitigate the abovementioned adverse factors, interface engineering is considered a very effective method. As shown in Figure 1-24 (b), massive efforts have been expended on the development of interface (grain boundaries (GBs), electron-extraction interfaces, and hole-extraction interfaces) engineering as a universal way to improve the photovoltaic performance of PSCs. Notably, both inherent disadvantages of PSCs, i.e., hysteresis and instability, can also be improved via this engineering. (1) Interface engineering for the GBs: Although in the above section it is mentioned that theoretically the grain boundary does not cause many deep-level defects in the perovskite material, it is difficult to achieve perfect grain boundaries in practical preparation. Therefore, to obtain a low-defect-concentration perovskite material, in addition to controlling the preparation method, passivation of GBs in a perovskite film is also widely used. In the perovskite $MAPbI_3$ film, self-passivation of GBs by PbI_2 and MAI would be effectively suppressed the carrier recombination,[141] enhance the fluorescence emission lifetime,[142] and increase polaron binding energy,[143] thereby increasing V_{oc} (to as high as 1.15 V)[144] and reducing the hysteresis of PSCs.[145] In addition to self-passivation, the organic molecules (e.g., PCBM.)[146] and halide ions (Br- and Cl-) have also been shown to effectively passivate GBs of perovskite film.[147] (2) Interface engineering at the ESL/perovskite interface: The interface between the ESL and perovskite is essential for efficient charge transportation, and it mainly affects three aspects of the PSCs: energy-level alignment, perovskite film morphology control, and device stability. Proper energy-level alignment has been demonstrated to be an advantageous method for achieving high charge collection efficiency and V_{oc} in PSCs simultaneously. Zhou et al. used yttrium-doped TiO_2 as an ESL in PSCs to suppress carrier recombination, match energy levels and improve the electron extraction at the electrode, which resulted in a device PCE of up to 19.3%.[148] In addition to band alignment, passivation of the surface of metal oxide (TiO_2, ZnO, SnO_2) as ESLs in PSCs could reduce charge recombination

and improve stability. Doping the ESL[149], introducing an organic monolayer between the ESL and perovskite,[150] and passivation of the surface of the ESL with halogen ions[151] have been demonstrated to reduce interfacial recombination and improve the device performance of PSCs. The perovskite film morphological characteristics, such as coverage, crystallinity and preferred orientation, which are affected by ETM/perovskite interface, are closely related to the device performance. Using hydrophilic-lipophilic balance theory to introduce an organic-molecule (e.g., 3-aminopropanoic acid SAMs) layer into the interface, which could improve the morphology of the perovskite film and increase the light absorption, the results in significant improvement of the device performance.[152] (3) Interface engineering at the perovskite/HSL interface: The perovskite/HSL interface is related to the hole extraction, which also impacts the device performance. At present, for regularly structured PSCs, lithium-doped spiro-MeOTAD is the most widely used HSL. However, the polar solvent (e.g., 4-Tert-butylpyridine or acetonitrile) in the precursor solution of spiro-MeOTAD is likely to cause damage to the perovskite film and this organic material is relatively expensive. However, no mature material can replace spiro-MeOTAD as an HSL in PSCs; this requires further study.

In summary, the conventional structure of the PSCs is transparent conductive oxide (TCO)/ ESL/perovskite absorber layer/HSL/metal back contact. Substantial effort has been focused on the improvement of the performance and stability of the perovskite materials, e.g., via the fabrication method, composition control, and encapsulation. However, the carrier dynamics at the interface have not been systematically studied, which would be beneficial to the understanding of the working mechanism and the device performance. In this thesis, for the study of PSCs, we mainly focused on understanding the interfacial charge transfer at the interface of the ESL/perovskite absorber layer.

1.5 Thesis Objectives and Outline

In a typical heterojunction solar cell, charge generation, separation, and transportation strongly depend on the several interfaces and interfacial regions. This thesis will systematically investigate the effects of the interface engineering on the performance of CQD DHSCs, especially for carrier transmission and recombination, and use energy level control to modify the interface of CQDSCs and PSCs to reduce the interfacial recombination in CQDSCs and PSCs. The purpose of these studies is to improve the understanding of charge carrier dynamics in CQDSCs and PSCs, so that more efficient designing and optimizing the interfaces, and ultimately the solar cell efficiency can be further improved.

C**hapter 2.** I explore the basic principles of solar cells, including the basic concepts of p-n junctions, solar spectrum solar cell operation and current-voltage characteristics.

C**hapter 3.** In this chapter, I focus on the application of energy level alignment (ELA) in the absorber/electrode interface of TiO_2/PbS QDs/Au quantum dot heterojunction

solar cells. I have designed an ELA architecture (i.e., the graded structure) through interface engineering by using different QD size layers in order to explore the effect of ELA on the photovoltaic performance of PbS QDHSCs. Compared to the ungraded device (without the ELA), the optimized graded architecture (containing the ELA) solar cells exhibited a great increase (21.4%) in short-circuit current density (J_{sc}). A J_{sc} value greater than 30 mA/cm^2 has been realized in planar PbS QDHSCs with a thickness of the active layer of only approximately 200 nm. As a result, a power conversion efficiency (PCE) as high as 7.25% (area: 0.16 cm^2) was achieved. In addition, I have investigated the origin of the improvement in J_{sc} and the change in the recombination mechanism of the graded structure PbS QDHSCs using ELA by using light intensity-dependent J_{sc} and V_{oc}, transient absorption spectroscopy measurements. The originalities of this work are: (1) provides a useful strategy to improve the effective diffusion lengths and photogenerated carriers of PbS QDHSCs via simple architecture design; (2) reveals the charge recombination mechanism would be able to guide further improvements of QDHSCs and/or different kinds of solar cells. Part of this chapter was published in ACS Applied Materials & Interfaces, 2017, 10.1021/acsami.7b06552.

C**hapter 4.** In this chapter, I focus on the control of the conduction band offset (CBO) between the ETL/absorber layer in the PbS QDHSCs. I used a thin (~30nm) magnesium-doped zinc oxide film ($Zn_{1-x}Mg_xO$, x=0, 0.05, 0.10, 0.15, 0.20) as ETLs. We have studied the effects of the properties (e.g., defect distribution and carrier concentration) of the $Zn_{1-x}Mg_xO$ layer and the CBO between the ETL/absorber layer in the PbS QDHSCs by transient photovoltage (TPV) decay and ultrafast transient absorption (TA) spectroscopy measurement. I found that in Mg-doped ZnO/PbS QDHSCs the ZnO layer does not need to have a lower conduction band energy to realize efficient charge transfer; that is, although a spike structure is formed between the QDs and the ‘‘electron acceptor’’, charge injection can still occur, and improved injection of photogenerated electrons can occur at a certain CBO. The originalities of this work are: (1) for the first time, I found Mg doping can greatly alter the photophysical properties of ZnO and especially, the formed spike structure between $Zn_{1-x}Mg_xO$/PbS QDs can inhibits charge recombination, meanwhile the formed shallow defect state can serve as additional pathway to transport the photoexcited electrons from QDs to electron collecting electrode; (2) high-efficiency PbS QDHSCs (10.6%) based on the optimized $Zn_{1-x}Mg_xO$ ETL was obtained. Part of this chapter was published in Nanoscale Horizons, 2018, 10.1039/C8NH00030A.

C**hapter 5.** In this chapter, I systematically investigated the effects of the CBO between the ESL and the perovskite layer in planar-heterojunction perovskite solar cells. I found that the charge recombination at the interface between the ESL and the perovskite is strongly dependent on the CBO values. A favorable CBO would be reducing charge recombination at the ESL/perovskite interface and hence improves device performance. The mechanism for this improved performance is discussed in detail through characterization of photoluminescence (PL) spectra, charge injection and charge recombination through fluorescence spectroscopy and ultrafast transient

absorption (TA) spectroscopy. The originalities of this work are: (1) For the first time, the CBO effect on the performance of PSCs was demonstrated experimentally; (2) The effects of CBO on carrier kinetics were characterized by various methods and the optimal CBO values were obtained. This has guiding significance for the further improvement of the efficiency of PSCs.

C**hapter 6.** Here, I summarize key results from the thesis and discuss the future development prospects of QDSCs and PSCs.

Chapter 2: Fundamental physics of solar cells

2.1 Fundamentals of p-n Junction

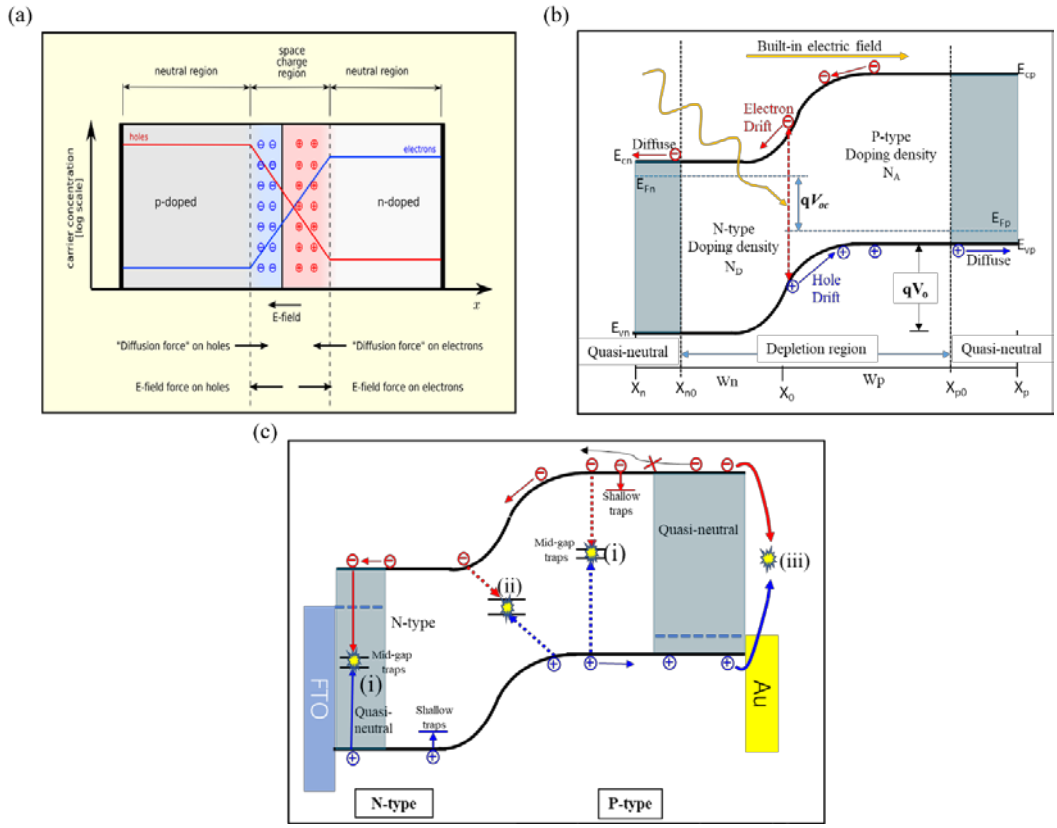

Figure 2-1. (a) When the p-type and n-type semiconductors are in physical contact, carriers diffuse due to the concentration gradient at the interface to form a depletion region. When equilibrium is established, a built-in electric field will be formed in the depleted region, eventually preventing minority carriers from diffusing.[153] (b) Schematic diagram of the p-n junction. qV_{oc} is the difference between the quasi-Fermi level F_n in the n-type material and the quasi-Fermi level F_p in the p-type material. (c) Several recombination ways of Carriers in Heterojunction Solar Cells. Intermediate gap states and shallow traps exist in p-type and n-type materials. Shallow traps capture and/or release free carriers to the valence band/guide band by thermal activation (kT).

Heterojunction solar cells are based on junctions formed at the interface between P-doped and N-doped semiconductors, called P-N junctions. Due to the different carrier concentrations in these two semiconductors, when they are in contact, the carriers will diffuse toward each other along the concentration gradient, i.e., electrons will diffuse to the P-type semiconductor from the N-type semiconductor, while holes will diffuse in the opposite direction. In this process, a region that is no longer electrically neutral (i.e., depletion region) will form near the interface between the two semiconductors. The

electric field that is generated in this region, in the opposite direction of the carrier diffusion, will prevent further carrier diffusion until the driving force of the electric field is balanced with the that of the concentration gradient. At this point, the P-N junction has a uniform Fermi level and reaches thermal equilibrium. As shown in Figure 2-1(a), this diffusion forms a quasi-neutral region in each semiconductor and creates a built-in electric field in the depletion region at the interface. The concentrations of doping density in these two semiconductors determine the widths ($W_{depletion}$) of their respective depletion regions, as defined by the following equation:

$$W_{depletion} = \sqrt{\frac{2\varepsilon kT}{q^2}\left(\ln\left(\frac{N_A N_D}{n_i^2}\right)\left(\frac{1}{N_A}+\frac{1}{N_D}\right)\right)} \qquad (2\text{-}1)$$

where ε is the permittivity, k is the Boltzmann constant, T is the temperature, q is the elementary charge, and N_A and N_D are the acceptor density and donor density, respectively. As shown in Figure 2-1(b), the depletion region is not evenly distributed in the two semiconductors. X_{n0} and X_{p0} denote the depletion regions in the P-side and N-side, respectively:

$$X_{n0} = \frac{W_{depletion}}{1+\frac{N_A}{N_D}} \qquad (2\text{-}2)$$

$$X_{p0} = \frac{W_{depletion}}{1+\frac{N_D}{N_A}} \qquad (2\text{-}3)$$

According to Equation 2-1, the depletion region thickness can be reduced by increasing the doping density. The total width of the depletion region is determined by the lightly doped semiconductors. The difference in the Fermi level before the N-type semiconductor is in contact with the P-type semiconductor is defined as the built-in potential (V_0) of the P-N junction:

$$V_0 = \frac{kT}{q} ln \frac{N_A N_D}{n_i^2} \qquad (2\text{-}4)$$

The value of V_0 in the P-N junction is determined by the doping concentration of the semiconductor and the maximum open-circuit voltage (V_{oc}) in the photovoltaic device is determined by V_0. The electric field strength (E) of the built-in electric field is also determined by V_0:

$$E = \frac{V_0}{W_{depletion}} \qquad (2\text{-}5)$$

Effective carrier transport for a photovoltaic device is necessary. The carrier transport mechanism in the depletion region is dominated by drift, while the carrier transport mechanism in the quasi-neutral region is dominated by diffusion. The drift length (l_{drift}) of carriers in the depletion region is determined by E, the carrier mobility μ and the average carrier lifetime τ:

$$l_{drift} = \mu E \tau \qquad (2\text{-}6)$$

When a P-N junction is under illumination, photogenerated electron hole pairs in the depletion region will be swept by the built-in field to the N-type and P-type materials. The value of l_{drift} is used to determine whether each carrier can be swept out of the depletion region by the electric field before carrier recombination. Because there is no electric field in the quasi-neutral region, the charge carriers that are generated in this region must diffuse to the edge of the depletion region (in the case of minority carriers) or to their collecting electrode (in the case of majority carriers) to be successfully extracted. The extraction efficiency of carriers in this region strongly depends on the diffusion length ($l_{diffusion}$) of the carriers. The value of $l_{diffusion}$ is determined by diffusion coefficient D and carrier lifetime τ as follows:

$$l_{diffusion} = \sqrt{D\tau} \qquad (2\text{-}7)$$

The carrier mobility μ and diffusion coefficient D are related by the Einstein relation:

$$D = \frac{kT\mu}{q} \qquad (2\text{-}8)$$

Photogenerated electron-hole pairs in the depletion and the quasi-neutral regions are finally separated by E in the space charge region. The electrons drift to the N-type semiconductor from the P-type semiconductor, whereas the holes drift to the P-type semiconductor. Then, a photocurrent (I_{ph}) from the N-side to the P-side is formed. The photocarriers drift and accumulate to form an electric field in the opposite direction of E and produce a current that opposes the photocurrent. When I_{ph} is equal to the forward junction current, a stable potential between both ends of the P-N junction is the photogenerated voltage. When the external circuit is short-circuited, the forward current of the PN junction is zero and the external circuit current is the short-circuit current (J_{sc}); when the external current across the junction is zero, the photogenerated voltage is the open-circuit voltage (V_{oc}). As shown in Figure 2-1(c), in the course of solar cell work, due to the presence of trap states in the P- and N-type semiconductors and at the interface, carrier transmission will be adversely affected, thereby reducing the performance of the device. The deep-level trap states (mid-gap states) in the bandgap generally serve as recombination centers for photogenerated carriers and significantly damage device performance. Shallow levels of defects will slow down the mobility of carriers to an extent but increase the carrier lifetime, and the overall effect does not degrade the performance of the solar cell.

2.2 The solar spectrum

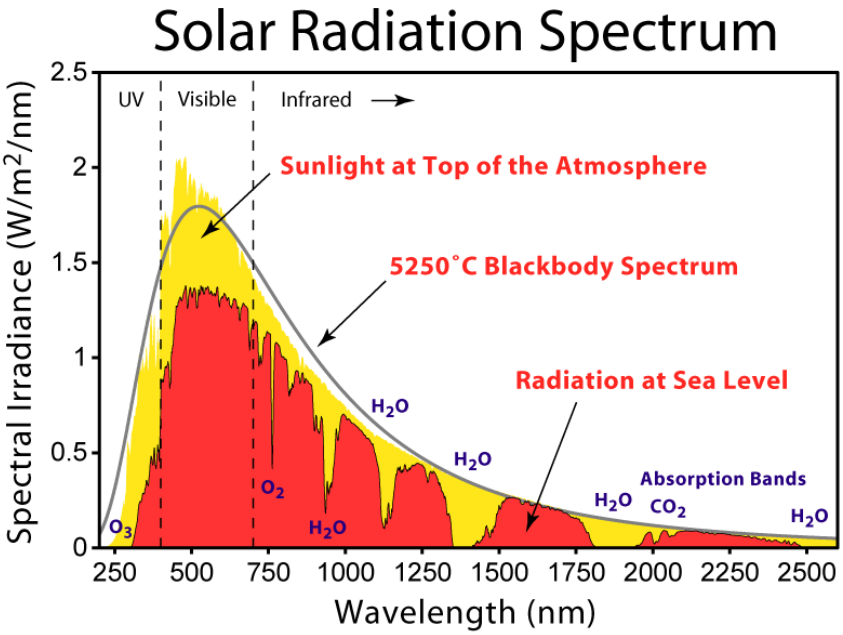

Figure 2-2. Extraterrestrial solar spectrum, the spectrum of a 5250℃ (5525 K) blackbody and terrestrial spectrum. (Spectra data are referenced from ASTMG 173-03)[154]

Solar cell performance is characterized by s one-sun simulated illumination, typically using the American Testing and Materials Association AM (Air Quality Factor) 1.5. As shown in Figure 2-2, the radiation from the extraterrestrial sun is very similar to that of a black body with a temperature of 5250℃ (5525 K). The radiation wavelength from the sun is very wide, with a range of 100 nm to approximately 1 mm, where most of the power is concentrated at visible wavelengths. The sunlight that reaches the top of the atmosphere contains only 40% of the visible spectrum, while the rest contains approximately 50% of the infrared and 10% of the ultraviolet portions of the electromagnetic spectrum.[155] The total power of these wavelengths is 1361 W/m^2 and is designated AM 0.[155] Some of this energy is absorbed by ozone (O_3), oxygen (O_2), water (H_2O) and carbon dioxide (CO_2) as the light passes through the atmosphere. Therefore, light that reaches the ground has suffered losses from various wavelength bands. Taking into account the zenith angle of sunlight in mid-latitude regions, the photovoltaic industry defines the light intensity (1000 W/m2) in the area with a solar zenith angle of 48.2 ˚as a standard solar constant: AM 1.5.[156]

2.3 Characterization of Solar Cells

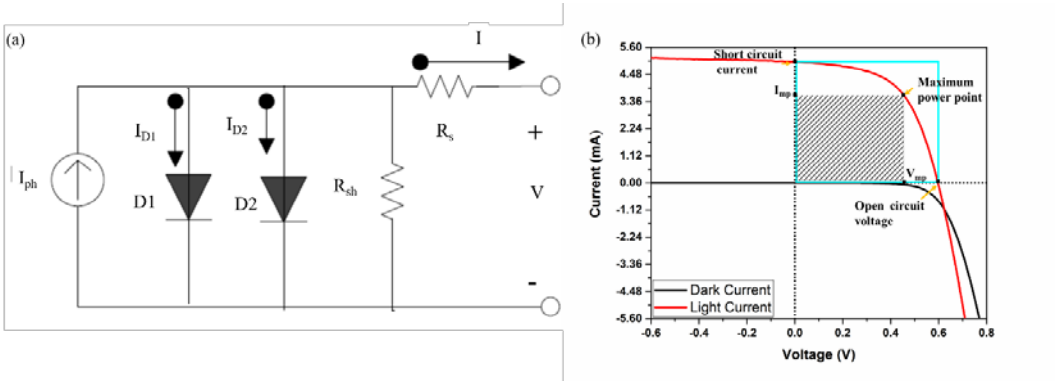

Figure 2-3. (a) Practical double diode model of solar cell. (b) Solar cell J-V characteristics in the dark and 1-sun illumination. The area of the pattern represents the maximum power output, which is the product of the optimal operating current and voltage.

The double diode model is generally used to relax the output characteristics of the PV model. As shown in Figure 2-3(a), this model consists of five parts: an ideal constant-current source I_{sc}; two diodes D1 (representing the diffusion process) and D2 (representing the recombination process) with ideality factors of n_1=1 and n_2=2, respectively; series resistance (R_s); and shunt resistance (R_{sh}). The output voltage and current relations can be expressed as follows:

$$I = I_{ph} - I_{01}\left(exp\frac{V+IR_s}{n_1V_T}\right) - I_{02}\left(exp\frac{V+IR_s}{n_2V_T}\right) - \frac{V+IR_s}{R_{sh}} \qquad (2\text{-}9)$$

where I_{01} and I_{02} are dark saturation currents that correspond to the neutral and depletion regions of the P-N junction, respectively, and V_T is the thermal voltage (25.69 mV at 25°C). Figure 2-3 (b) shows the typical solar cell current and voltage characteristics, i.e., the I-V curve, in the dark and under illumination, which are used to define parameters for characterizing the solar cell performance. The significance of the dark I-V curve lies in the characterization of the rectification effect of solar cells. For solar cells, the dark current includes the reverse saturation current (I_{01} and I_{02}) and the leakage current. A solar cell with better performance should have a higher rectification ratio, i.e., the forward dark current should be higher than the reverse dark current. Under illumination, when V=0, the current that is provided by I_{ph} is the short-circuit current (I_{sc}). I_{sc} is the maximum photogenerated current per unit area that can be extracted from a solar cell. I_{sc} is induced by the generation and collection of photogenerated carriers and mainly depends on the area of the solar cell, the power of the incident light source, the spectrum of the incident light (AM 1.5), the optical properties (reflection and absorption) and the collection probability (recombination and the minority carrier lifetime). In a solar cell with negligible interfacial recombination, the equation for I_{sc} of the unit area (J_{sc}) can be approximated as follows:

$$J_{sc} = qG(l_n + l_p) \quad (2\text{-}10)$$

where G is the generation rate and l_n and l_p are the electron and hole diffusion lengths, respectively.

When I=0, the output voltage of the battery is the open-circuit voltage and can be expressed as:

$$V_{oc} = \frac{kT}{q} ln \frac{I_{sc}+I_{01}}{I_{01}} \approx \frac{kT}{q} ln \frac{I_{sc}}{I_{01}} \quad (2\text{-}11)$$

This equation shows that for $V_{oc,}$ the key factor is the saturation current I_{01}: low I_{01} requires low recombination in the quasi-neutral region of the solar cell. The V_{oc} decay can be used to measure the recombination mechanism in the device.

In the ideal case, the solar cell output power can be expressed as:

$$\mathrm{P} = \mathrm{IV} = I_{sc}V - I_{01}V(\exp(V_T) - 1) \quad (2\text{-}12)$$

According to Equation 2-12, the maximum output voltage (V_{mp}) and the maximum output current (I_{mp}) can be obtained:

$$V_{mp} = V_{oc} - V_T ln \frac{V_{mp}}{V_T} \quad (2\text{-}13)$$

$$I_{mp} \cong I_{sc}(1 - \frac{V_T}{V_{mp}}) \quad (2\text{-}14)$$

According to Figure 2-3 (b), the shadow area is the maximum output power ($\mathrm{P_{mp}}$), which can be expressed as:

$$P_{mp} = V_{mp}I_{mp} \cong I_{sc}\left[V_{oc} - V_T \ln\left(1 + \frac{V_{mp}}{V_T}\right) - V_T\right] \quad (2\text{-}15)$$

The fill factor (FF) is defined as the ratio of the maximum power from the solar cell to the product of V_{oc} and I_{sc}, which can be expressed as:

$$\mathrm{FF} = \frac{V_{mp}I_{mp}}{V_{oc}I_{sc}} \quad (2\text{-}16)$$

Ideally, the value of FF is 1, which has a direct relationship with $V_{oc,}$ which can be determined via the following empirical expression:

$$\mathrm{FF} = \frac{V_{oc} - V_T ln\left(\frac{V_{oc}}{V_T} + 0.72\right)}{V_{oc} + V_T} \quad (2\text{-}17)$$

R_s and R_{sh} can be determined by the slopes of the I-V curve at V_{oc} and I_{sc}, respectively. R_s is related to carrier transport resistance and R_{sh} is related to carrier recombination loss. Smaller R_s and larger R_{sh} lead to $\mathrm{J_{mp}}$ and $\mathrm{V_{mp}}$ being closer to J_{sc} and V_{oc}, respectively, and increase the FF. In addition, as shown in Equation 2-9, R_{sh} mainly

affects I_{sc}, and R_{sh} mainly affects V_{oc}.

The overall power conversion efficiency of a solar cell (η) is the ratio of P_{mp} to P_{min} (maximum incident power; 100 mW/cm^2 for AM 1.5 illumination), which can be expressed as:

$$\eta = \frac{P_{mp}}{P_{min}} = \frac{I_{mp}V_{mp}}{P_{min}} = \frac{FFI_{sc}V_m}{P_{min}} \qquad (2\text{-}18)$$

In summary, V_{oc}, J_{sc}, FF and η are used to characterize solar cell performance.

Chapter 3: Recombination Suppression in PbS Quantum Dot Heterojunction Solar Cells by Energy-Level Alignment in the Quantum Dot Active Layers

3.1 Introduction

Quantum dot solar cells (QDSCs), as a very promising candidate for next-generation solar cells, have attracted much attention. This is mainly because of the many and varied advantages of QDs, such as their bandgap tunability due to the quantum size effect, facile solution processing, and multiple exciton generation (MEG) as well as their effect of slowing down the cooling of hot electrons.[30-31, 157] Due to the large (18 nm) Bohr radius of lead sulfide (PbS), PbS QDs have a broadly tunable bandgap in the size range of 3–5 nm, making them competitive for photovoltaic applications.[158] Since the first near-infrared-absorbing (λ > 800 nm) colloidal QDSCs were reported,[32] PbS quantum dot heterojunction solar cells (QDHSCs) have developed rapidly as a result of the efforts focused on advanced QD surface engineering and designing and improving device architectures.[95, 159-160] In QDHSCs, normally, ZnO or TiO_2 thin films deposited on transparent electrodes (such as FTO) are used as electron transport layers, PbS or PbSe QDs are employed as the optical absorption layer, and Au deposited on the surface of the QD layers is used as an electrode to collect holes. To date, PbS QDHSCs with efficiencies of more than 11%[161-162] have been based on engineering the band alignment of two QD layers as well as better passivation using molecular halides.[95] The success originally depended on the reasonable tuning of energy level alignments (ELAs) between different PbS QD layers treated with different ligands. Tuning the ELA serves as the main route to improve the efficiencies of QDHSCs, mainly through two approaches: size-tunable bandgaps[93, 163-167] and ligand chemistry.[95] In addition, using graded doping[168] and surface dipole moments[169] to tune the ELA to improve performance in QDHSCs was demonstrated.

ELA within the light-absorbing, charge-transport active layer has previously been used in epitaxial compound semiconductor thin films such as GaAs and $CuIn_xGa_{1-x}Se_2$ thin film solar cells.[170-172] In those studies, ELA could improve photovoltaic (PV) performance through a variety of mechanisms and materials. For example, it could facilitate carrier collection, strengthen the built-in electric field, and improve the fill factor (FF), short-circuit current (J_{sc}) and open-circuit voltage (V_{oc}). As a result, improved photovoltaic conversion efficiencies have been experimentally demonstrated. However, the procedure to process the ELA

structure in a thin film solar cell is complicated, and it is difficult to fabricate an efficient barrier layer between the window layer and the back-electrode layer to reduce electron and hole carrier recombination. Above all, in the thin film layer, the composition variation can easily generate many bulk traps. As a result, the range of bandgap grading is greatly limited. In addition, current matching is required to optimize the thin film solar cells, which requires theoretical calculations and a large number of experimental practices.[172]

Compared with the preparative techniques of the abovementioned compound semiconductor thin film solar cells, the use of size-tunable QDs to prepare ELA solar cells is a good alternative. Tuning the ELA by simply adjusting QD sizes is the greatest advantage of QD-based solar cells and is very easily achievable. Stacking multiple layers of QDs with different sizes will have the same material composition, and this renders the interfaces between the differently sized QDs symmetrical with bandgap changes. The bandgap-ordered QD layers can be created via a layer-by-layer spin coating process, and this method can be used to easily control the spatial bandgap variation according to a design. In QDHSCs, ELA has been used to improve carrier transport and collection, which can be ascribed to the quantum funnel effect, i.e., the ELA structure drives the performance-limiting electrons towards the electron-accepting electrode, resulting in the efficient collection of photogenerated carriers.[93] However, previous research results have been surprising,[93, 163, 167] showing the ELA structure to solely lead to an increase in device FF without an appreciable increase in J_{sc}. In addition, after inserting the ELA structure in standard QDHSCs, changes in the transport as well as the recombination mechanism of carriers are not clear.

In this work, we thus aim to design an engineered ELA architecture by using quantum size-effect tuning in order to explore the effect of ELA on the photovoltaic performance of PbS QDHSCs. Here, we utilized the advantages of ELA in the fabrication of solar cells and prepared three types of graded TiO_2/PbS QDHSCs, in which the PbS QDs and TiO_2 nanocrystals were both solution-processed under ambient conditions. Compared to an ungraded device (without the ELA), the optimized graded architecture (containing the ELA) solar cells exhibited a great increase (21.4%) in J_{sc}. A J_{sc} value greater than 30 mA/cm^2 has been realized in planar PbS QDHSCs, and a high efficiency of 7.25% has been reached. The photogenerated charge recombination mechanism in QDHSCs was explored via the light intensity dependence of J_{sc} and V_{oc} and transient voltage decay measurements. It was shown that the strategy of tuning the ELA of the PbS active layer significantly increased the diffusion length of minority carriers and reduced the trap-assisted recombination and interfacial recombination of the PbS/gold interface in the PbS QDHSCs. Furthermore, the performance of unencapsulated PbS QDHSCs remained stable for over 100 days of storage in ambient. Our results highlight the importance of ELA engineering in PbS

QDHSCs and demonstrate that this is an effective strategy to improve the photovoltaic properties of QDHSCs.

3.2 Experiments

Materials

Lead (II) oxide (Wako, 99.5%), oleic acid (OA, Wako, 60%), 1-octadecene (ODE, Aldrich, 90%), and bis (trimethylsilyl) sulfide (TMS_2 sulfide, Aldrich, 99.999%), Cadmium chloride ($CdCl_2$, Wako, 99.8%), Oleylamine (OLA, Aldrich, 70%), Tetradecylphosphonic acid (TDPA, Aldrich, 97%), Titanium diisopropoxide bis(acetylacetonate) (75 wt %, Aldrich), 1-butanol (Wako, 99%) were used as purchased without further purification.

PbS quantum dot synthesis

The synthesis of colloidal PbS QDs was according to a remodeled literature method,[173] various sizes of PbS QDs were prepared as described previously in literature.[174] In this work, PbS QDs were manipulated using the standard Schlenk line techniques.[95] The mixed solution of PbO (6 mmol), OA (15 mmol) and ODE (50 ml) in a three-neck flask (100 mL) was degassed under stirred at room-temperature and 80 °C for 20 min and 40 min, successively. The solution was then heated for 1 h up to 120 °C under a nitrogen atmosphere, then the solution was allowed to cool down to the required temperatures of 115, 105, 75, and 69 °C, followed by the injection of 3mmol TMS solution. Immediately after the injection, the heater was removed while keeping the solution stirring. When the solution was cooled to 75° C, a $CdCl_2$ -TDPA-OLA solution (1 mmol of $CdCl_2$, 0.1 mmol of TDPA and 3 mL of OLA) was injected into the PbS colloid. After cooling to room temperature, the PbS QDs were precipitated from the growth mixture and re-dispersed in toluene. The resulting precipitate was centrifuged and washed twice with acetone to remove unbound OA ligand from the PbS colloid and then dispersed in octane. Assuming that the reactant TMS is completely converted to PbS product, the concentration of PbS colloid is approximately 50 $mg \cdot ml^{-1}$.

TiO_2 compact layer synthesis

Thin TiO_2 compact layer was coated on FTO glass (25 mm × 25 mm). The TiO2 compact film was prepared according to a standard procedure which has been reported in the literature.[175] To prepare the precursor solution, 1.46 mL of Titanium diisopropoxide bis(acetylacetonate) and 10 mL of 1-butanol were stirred at room temperature for 30min. To form a sol, the solution should be filtered by 0.1 μm filter. A compact TiO_2 film was coated by spin-coating method with a low speed of 1000 rpm for 2s and at a high speed of 3000 rpm for 30s. The thickness of the TiO_2 compact film was controlled by the high speed of the spin coater. After spin coating, the film was thermally annealed at 500 °C for 30 min.

Device fabrication

The PbS heterojunction solar cell is prepared by depositing PbS colloidal quantum dots on a compactlayer of TiO_2 by a typical layer-by-layer method under ambient conditions using spin coating. To fabricate PbS heterojunction solar cells, PbS colloidal QDs were prepared on TiO_2 electrodes by a typical layer-by-layer method using a fully automatic spin-coater under ambient conditions. Each PbS colloidal layer was deposited at 2500 rpm and ligand exchange briefly with CTAB solution (30mM in methanol) was conducted by spin-cast at 2500 rpm. A ligand exchange step was performed twice to ensure complete exchange of the ligand with oleic acid on the surface of the PbS. The layers were then washed three times with methanol and spun at 2500 rpm to remove excess ligand. Then repeat the above steps until the desired thickness is reached. Finally, a 100-nm-thick gold electrode is deposited on the PbS layer by thermal evaporation. The contact sizes were 0.16 cm^2.

Characterization

Measure current density - voltage (J-V) using Keithley 2400 light source meter and solar simulator PEC-L10 AM 1.5. The IPCE spectrum was measured under illumination using a Nikon G250 monochromator equipped with a 300 W xenon arc lamp. The transient open circuit voltage decay was measured using a 630 nm diode laser with a repetition rate of 4 Hz and a pulse duration of 5 ns. Transient voltage attenuation measurements were performed without background light.

3.3 Results and discussion

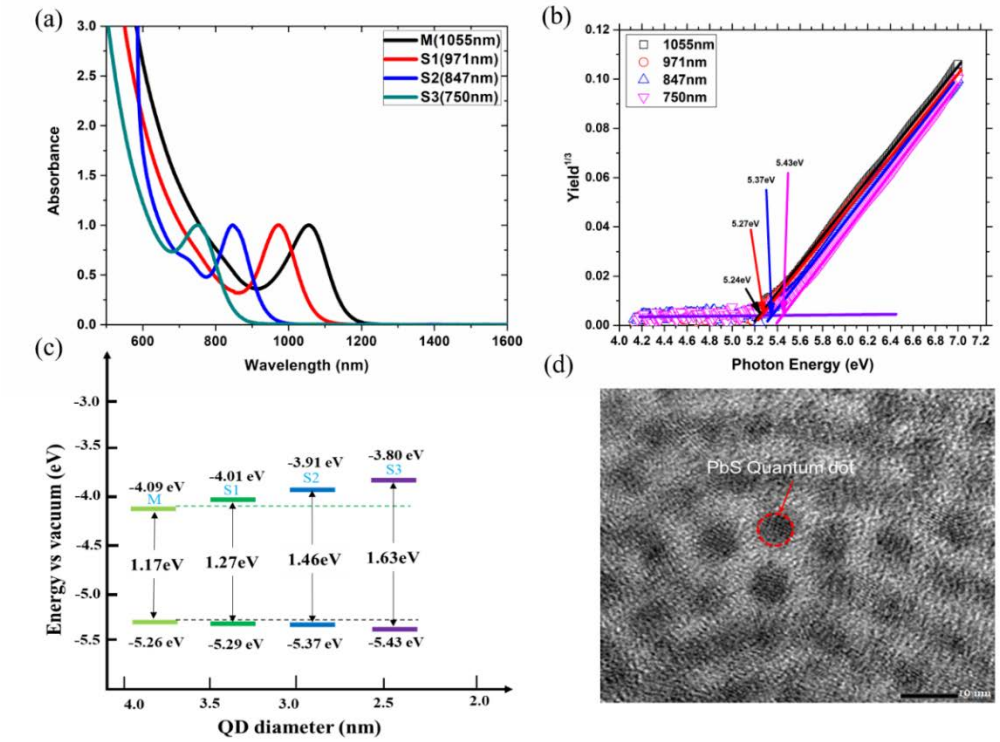

Figure 3-1. (a) The absorption spectra of the PbS QDs in octane. (b) Photoelectron yield (PY) spectra of the PbS QDs. (c) The energy-level diagram of the PbS QDs of different sizes. (d) A TEM image for PbS QDs with the first excitonic energy Eg of 1.17 eV.

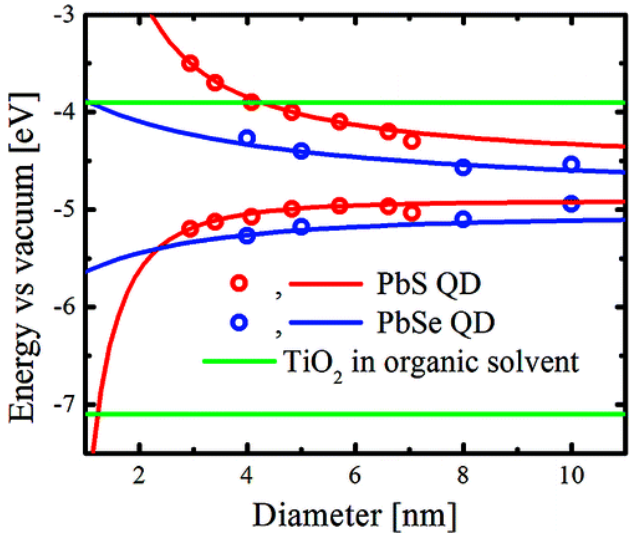

Figure 3-2. Size-dependent conduction band positions (upper three curves) and valence band positions (lower three curves) of bulk TiO_2 (green), PbS CQDs (red) and PbSe CQDs (blue). Reprinted with permission from reference [59].

In this work, different sizes of PbS QDs were synthesized using a remodeled hot-injection method,[173] and four sizes of PbS QDs were prepared by controlling the injection temperature. The absorbance spectra of the different sizes of PbS QDs as shows in Figure 3-1(a). The spectra demonstrate that the synthesis allows the preparation of QDs with a first excitonic absorption peak varying between 1055 and 750 nm (the first excitonic energy Eg: 1.17–1.63 eV). The diameter (d) of the PbS QDs is calculated using equation (1).[176] This equation allows us to determine d directly from E_g, avoiding a lengthy transmission electron microscopy (TEM) analysis for each sample synthesized. The calculated sizes of the QDs are 2.6–3.6 nm, and the four sizes of PbS were denoted M (3.6 nm), S1 (3.3 nm), S2 (2.9 nm), and S3 (2.6 nm).

$$E_g = 0.41 + \frac{1}{0.252d^2 + 0.283d} \qquad (1)$$

PbS QDs passivated by ligand molecules have asymmetric density of states and conductivity, as has been demonstrated.[177-178] When there is a bandgap variation, the change in the conduction band edge is much greater than that in the valence band edge, which is due to the hole mobility being greater than the electron mobility in PbS QD films.[179] Figure 3.2 shows the relationship between the band edges and diameters of PbS and PbSe QDs.[73] From this figure, we can see that within the 3–5 nm range, the changes in the conduction band are about a few hundred meV, while the valence band hardly varies. To further confirm these results, the valence band edge energy levels of the four sizes of PbS QDs were measured by using photoelectron yield (PY) spectroscopy, as shown in Figure 3-1(b). As the PY signal intensity has a good S/N ratio, the error bars are included within the points. The valence band edge is determined from the intersection of the baseline with the tangent to the spectra. Then, by combining the results of both of band gap and valence band edge levels, the conduction band edge levels were confirmed, as seen in Figure 3-1(c). Therefore, we believe that in the 2.6–3.6 nm range, the changes in the valence band edge are smaller than those in the conduction band edge as the size of the QDs varies. Thus, changes of size within a certain range can tune the conduction band minimum at the top of the absorber layer for the constructed ELA structure of the PbS quantum-junction solar cells. In addition, for the PbS QDHSCs, it was confirmed that the 3–5 nm range transmutes into the widespread optimal efficiency bandgap peak.[47] Thus, we can use these four sizes of PbS QDs to build an ELA structure. Figure 3-1(d) shows a typical TEM image of M-size PbS QDs, illustrating that the PbS QDs are spherical and that their diameter is very close to the calculated one.

In this work, we design and characterize an ungraded device as well as three other types of graded devices with different electron collection efficiencies. Figure 3-3 illustrates a spatial band diagram of a photoelectron cascade within a solar cell. In this work, we design and characterize an ungraded device and three types of graded devices with different electron collection efficiencies. In our

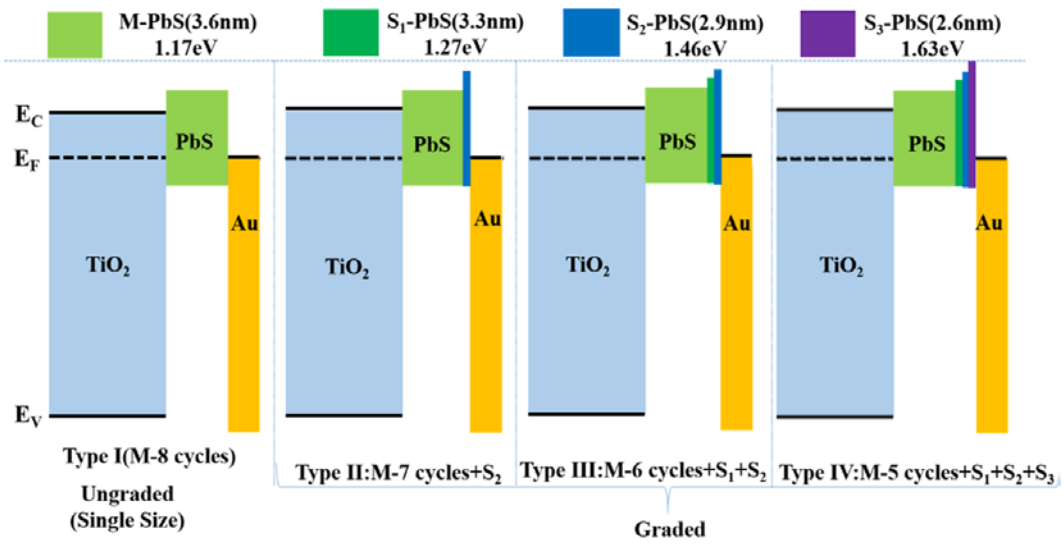

Figure 3-3. Spatial band diagrams of ungraded and graded QD solar cells. Color coding corresponds to larger bandgaps (more blue/violet). Type I: the active layer with M-PbS QDs (~300 nm thick), Type II: M-PbS (~260 nm) + S2-PbS (~40 nm), Type III: M-PbS (~220 nm) + S1-PbS (~40 nm) + S2-PbS (~40 nm). Type IV: M-PbS (~180 nm) + S1-PbS (~40 nm) + S2-PbS (~40 nm) + S3-PbS (~40 nm).

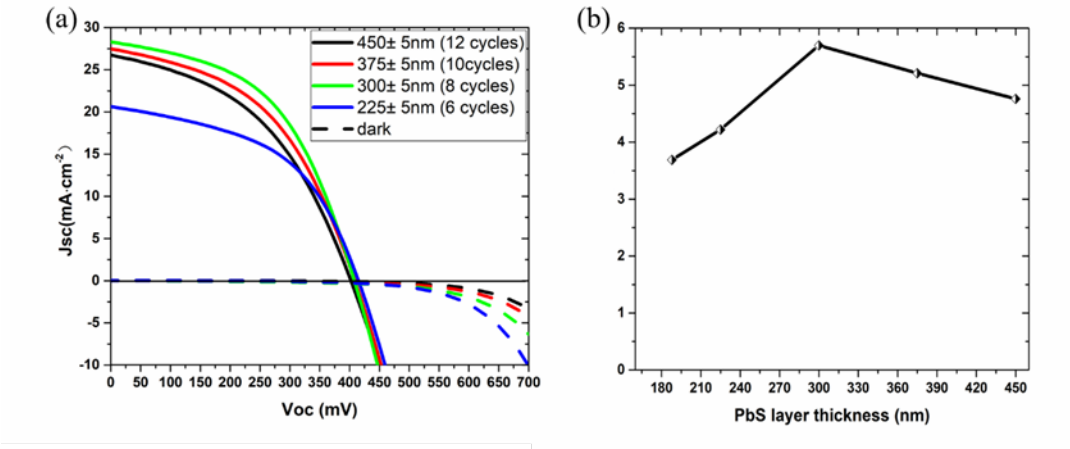

Figure 3-4. (a) J-V characteristics of Type I device under 1 sun illumination with four PbS layer thicknesses. The dash lines are for the dark J-V curves. The PbS QD bandgap is 1.17eV. (b) Power conversion efficiency (PCE) as a function of PbS QD layer thickness.

previous report,[82] solar cells employing PbS QDs with a first excitonic absorption peak at a wavelength λ = 1050 nm (first exciton energy Eg of 1.17 eV) showed high performance, and thus the PbS QDs with this absorption peak are employed to fabricate the ungraded device and the base layer of the graded devices, and other smaller-diameter QDs (Figure 3-1(a)) are employed to build the upper layers. The active layer of Type I (ungraded device) had a thickness of approximately 300 nm, an optimized thickness that achieved the best efficiency

(as shown in Figure 3-4), and the long ligands of the PbS QDs were exchanged with short ligands through a hexadecyltrimethylammonium bromide (CTAB) treatment.[82] All processes were performed under ambient conditions. For the devices using ELA engineering, the active layers of the three types of graded devices contained two, three and four compositions, respectively. Type II consisted of a 195-nm-thick film of M-PbS QDs (1.17 eV) deposited on the TiO_2 compact layer with a subsequent 28-nm-thick layer of S2-PbS QDs (1.46 eV); Type III consisted of a 165-nm-thick layer of M-PbS QDs with subsequent successive 28-nm-thick layers of S1-PbS (1.27 eV) and S2-PbS QDs; and Type IV consisted of a 140-nm-thick layer of M-PbS QDs with subsequent successive 28-nm-thick layers of S1, S2 and S3-PbS QDs (1.63 eV). Therefore, the thickness of the total active QD layers is ~220 nm for all the device types.

As an example, Figures 3-5 (a) and (b) show the schematic structure and a cross-sectional scanning electron microscopy (SEM) image, respectively, of a Type III graded solar cell with an Au electrode on the PbS QD layer. The approximately 30-nm-thick low-temperature-processed TiO_2 compact layer acts as an electron-accepting/hole-blocking layer. The bottom six cycles of the CTAB-passivated QD layer of this structure utilize the M-PbS QDs as the main charge generation layer, followed by single layers of CTAB-passivated S1 and then S2-PbS QDs as a spatial gradient ELA structure (Figure 3-5 (a)). The cross-sectional SEM image of a typical Type III device (Figure 3-5 (b)) shows an ~30-nm-thick TiO_2 layer and an ~ 220-nm-thick QD layer. In addition, the layer-by-layer process keeps each CQD layer fused together, rather than producing distinctly stratified interfaces.

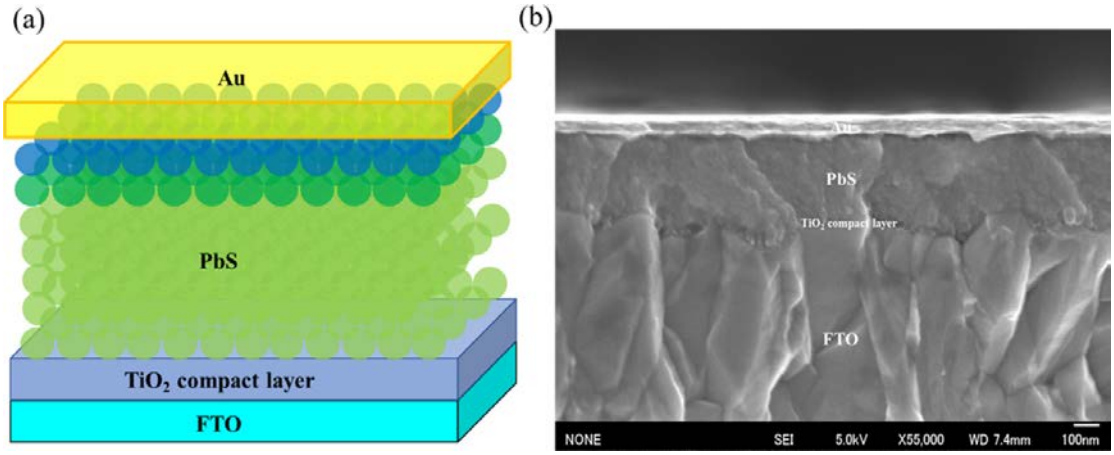

Figure 3-5. Schematic illustration of a graded device with Type III structure. (b) Cross-sectional SEM image of a typical device of Type III (~300 nm thick PbS QD active layer).

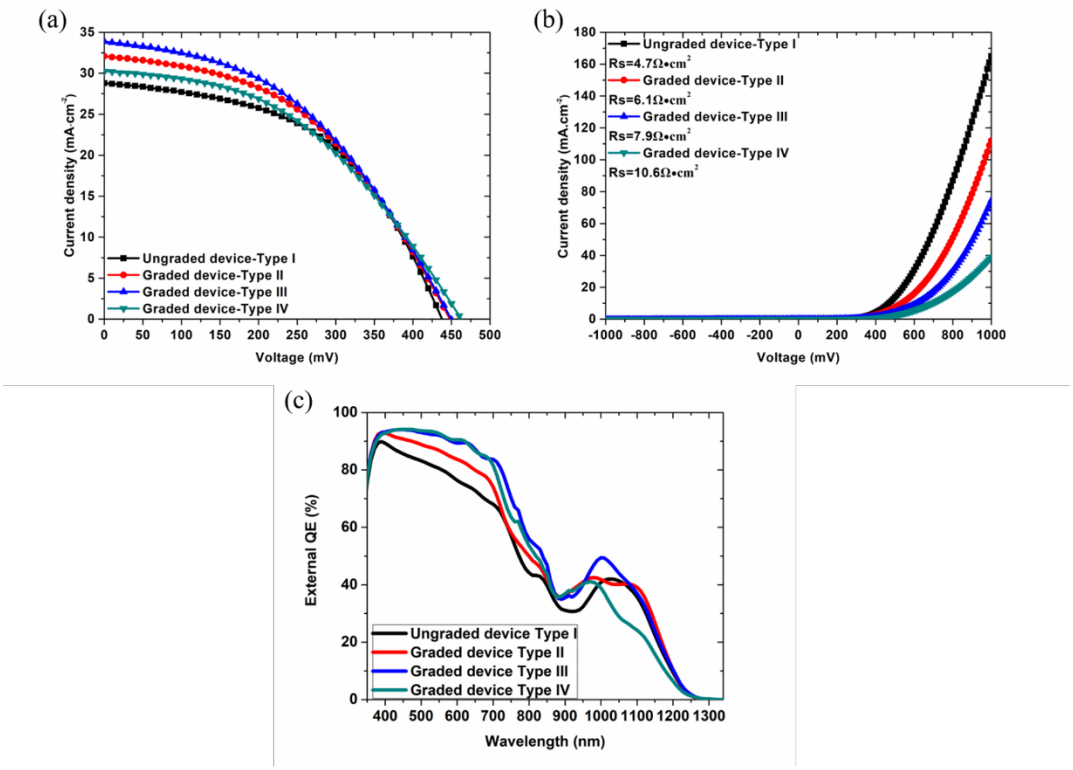

Figure 3-6. (a) J−V characteristics under simulated AM 1.5 G illumination for the ungraded and graded devices. (b) The dark-current characteristics of these devices. The series resistances (RS) were extracted by fitting these dark-current characteristics with a single diode model. (c) External quantum efficiency (EQE) spectra for the ungraded and graded devices

Table 3-1. Statistical Averages of the Photovoltaic Performance Parameters of 24 Devices for Each Type of the QDHSCs[a].

Sample	V_{oc} (mV)	J_{sc} (mA·cm^{-2})	FF (%)	PCE (%)	R_s (Ω·cm^2)	R_{sh} (Ω·cm^2)
Type I	427 ±9 (438)	25.82±1.39 (27.81)	48±1 (50)	6.12±0.13 (6.28)	4.56±1.14 (4.73)	111.4±11.7 (121.4)
Type II	438 ±8 (448)	30.92±1.12 (32.54)	46±2 (49)	6.82±0.12 (7.02)	5.88±1.76 (6.1)	124.2±17.6 (135.4)
Type III	441 ±8 (451)	32.65±1.03 (33.58)	46±2 (48)	7.12±0.11 (7.24)	7.28±2.16 (7.94)	677.9±19.2 (691.3)
Type IV	450±9 (462)	28.88±1.17 (30.29)	42±1 (44)	6.10±0.09 (6.22)	10.28±1.89 (10.57)	726.8±14.8 (736.1)

[a]The best results are shown in the parentheses.

In this work, the current density–voltage (photo J–V) characteristics of the four QDHSC types are shown in Figure 3-6 (a), with the extracted photovoltaic parameters listed in Table 3-1. Compared with the ungraded device (Type I), the graded devices (Types II, III) show desirably increased power conversion efficiencies (PCEs) that originate from the significant improvements in J_{sc} (~ 20% increase). From the J–V results, by employing different numbers of graded structure layers, we found that Types II and III of the ELA structure yielded an optimum result in this system and that an additional differently sized layer yielded no further benefits in photovoltaic properties. Remarkably, under 1-sun illumination, the best performance by a graded Type III QD device showed a J_{sc} of 33.6±1.2 mA/cm^2, V_{oc} of 451±2 mV, FF of 48±1% and PCE of 7.24 ± 0.29%.

The trend of improving performance with the ELA structure depended on two aspects: J_{sc} and V_{oc}. The most important improvement was that the average (as seen in Figure 3.7, 24 samples) J_{sc} was enhanced in the graded device compared to the ungraded one. The J_{sc} improved to 33.6 mA/cm^2 (Type III) compared to 28.8 mA/cm^2 (Type I), and the V_{oc} also slightly increased from 438 mV (Type I) to 462 mV (Type III) with the added layer of the ELA structure, while the FF decreased to 0.48 (Type III) from 0.50 (Type I). However, for the added three layers of differently size QDs (Type IV), we observed decreased efficiency due to the deteriorated J_{sc} and FF compared to the Type III solar cell.

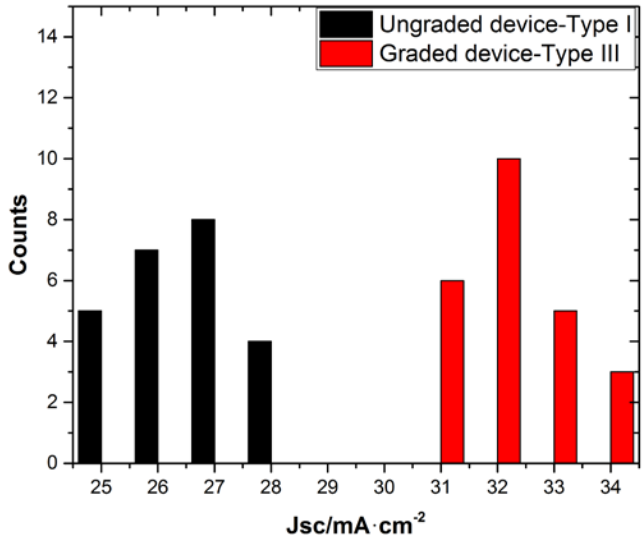

Figure 3-7. Histogram of the J_{sc} of the type I and type III QSHSCs for 24 devices.

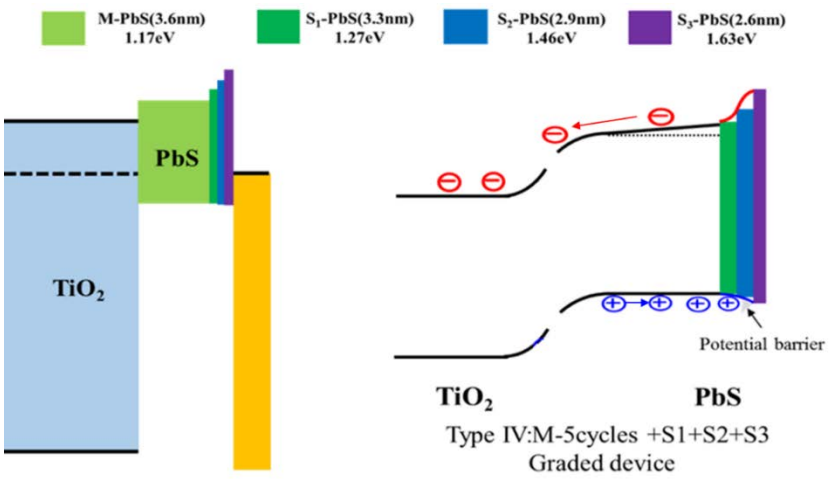

Figure 3-8. Band diagram of the valence band potential barrier in graded type IV PbS QDHSCs.

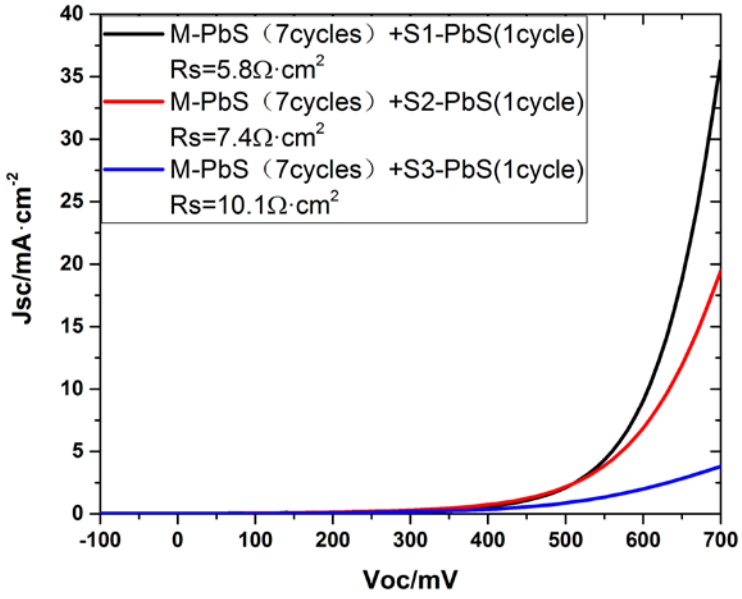

Figure 3-9. Dark J-V curves of 3 kinds of Type II model graded structure solar cells prepared using 3 kinds of differently-sized PbS quantum dot.

The dark current characteristics of the ungraded device and the three types of graded devices are shown in Figure 3-6(b) and suggest that the increasing number of ELA structure layers leads to an increase in series resistance (Table 3-1). Resistive losses are believed to be the main reason for the reduced FFs observed in QD devices.[180] The increased series resistance may arise from the valence band offset between the absorber layer (M) and the top layer (Sn, n=1, 2, 3), which causes a weak effect that blocks hole diffusion to the metal contact (Au), and a hole accumulation layer, which forms a weak barrier at the upper layer of the ELA structure. This barrier reduced hole collection in the graded devices

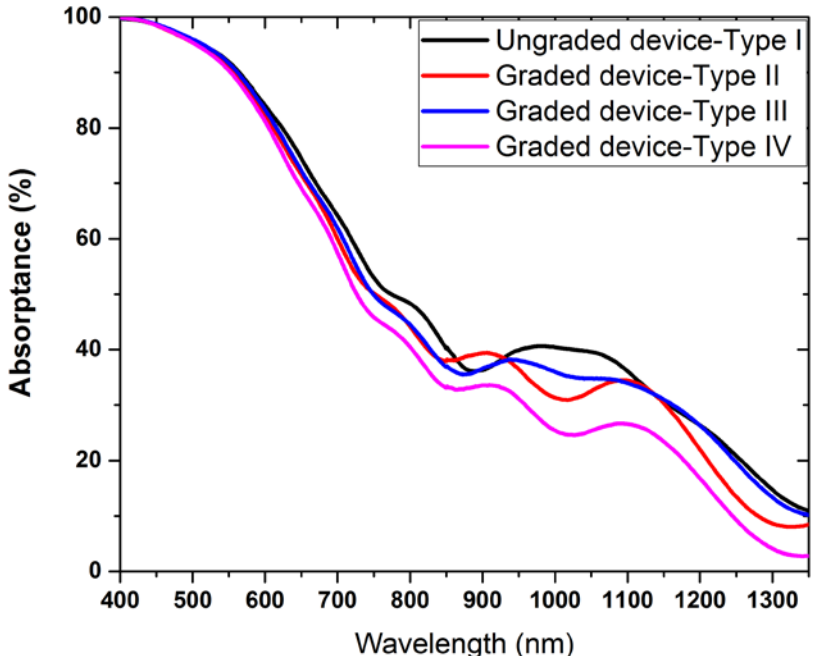

Figure 3-10. Typical absorption spectra of the optical absorption layers (i.e., the active layers) for the ungraded (Type I) and three types of graded (Type II, III and IV) QDHSCs used in this study.

compared with the ungraded device and caused interfacial effects at the metal contacts (Figure 3-8). Therefore, we used three differently sized PbS QDs to prepare three kinds of Type II model graded structure devices and measured their dark current characteristics. The results indicate that the series resistance increased with increasing valence band offset (Figure 3-9), revealing a reduction in hole transport to gold electrode due to increasing hole-blocking effect.

Our experimental results and the previously reported results clearly differ.[93, 163, 166-167] In our graded devices, J_{sc} can be increased to very high values, but FF deteriorates. The external quantum efficiency (EQE) results of the devices are shown in Figure 3-6(c). The EQE spectra show very different spectral signatures, suggesting that the performance differences between the ungraded device and the graded devices arise from the different light-harvesting abilities of the four kinds of QDHSCs. The optical absorption spectra (Figure 3-10) illustrate that the improvement of the J_{sc} of the graded energy level absorber is not attributable to an enhancement of the light absorption, which has also been confirmed by other groups.[165] Thus, the greater EQE of the graded devices is due to the quantum funnel effect [93] resulting from the ELA structure.

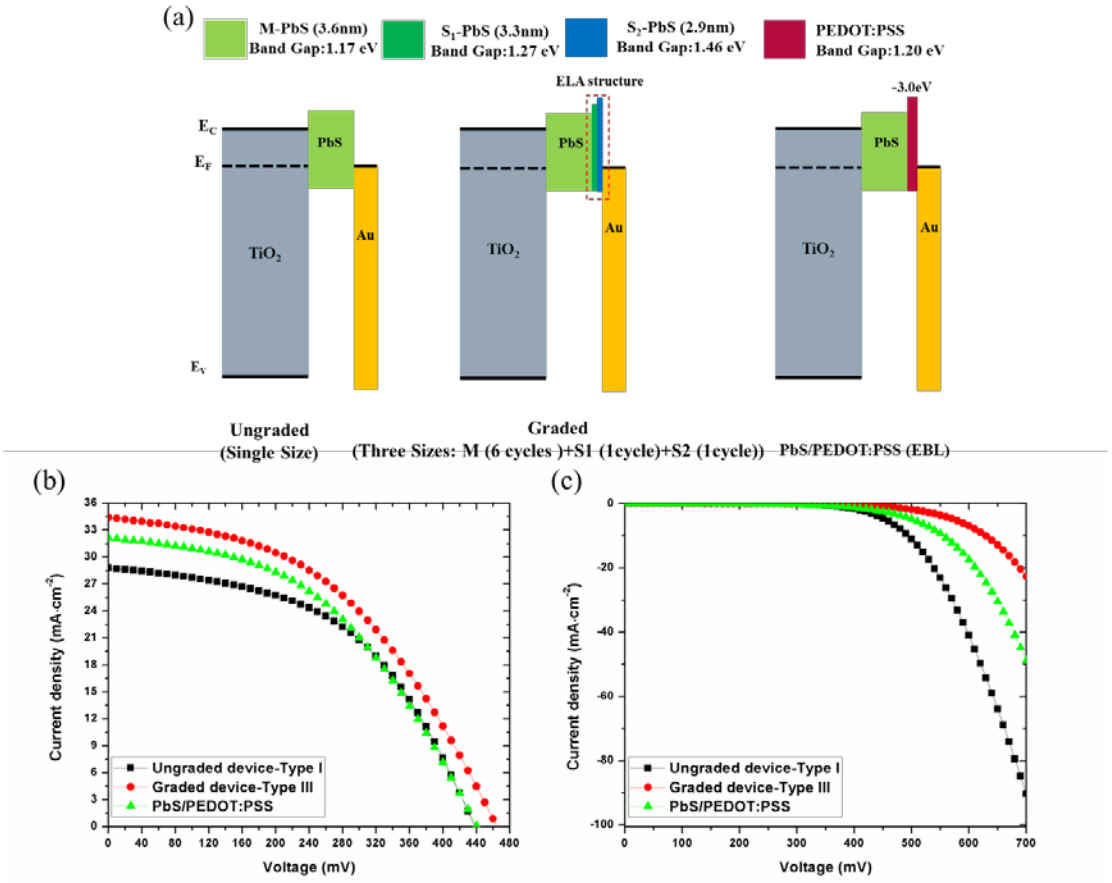

Figure 3-11. (a) Spatial band diagrams of ungraded device (Type I), the graded device (Type III) and a device which only contains an electron blocking layer (EBL) of PEDOT: PSS. (b) J-V characteristics under simulated AM 1.5 G illumination and (c) dark J-V characteristics of the three devices.

Table 3-2. Statistical average of the photovoltaic performance parameters of 24 devices for each of the type device. The champion results are shown in the parentheses.

Sample	J_{sc} (mA/cm^2)	V_{oc} (mV)	FF (%)	PCE (%)
Ungraded device-Type I	25.82±1.39 (27.81)	427 ±9 (438)	48±1 (50)	6.10±0.13 (6.28)
Graded device-Type III	32.65±1.03 (33.58)	441 ±8 (451)	46±2 (48)	7.12±0.11 (7.24)
PbS/PEDOT(EBL)	29.87±1.24 (31.11)	430±10 (440)	45±1 (46)	6.38±0.07 (6.53)

From the spatial band diagrams (Figure 3-3), the upper layer of both the Type II and Type III devices is the same, i.e., an S2-PbS QDs layer. Although the J_{sc} values of the two types of devices both increased, Type III has a higher J_{sc}. This result shows that for the Type II device, the role of the ELA structure is mostly to effectively block electrons, but the ELA structure of the Type III device, in addition to blocking electrons, also provides a multi-stage impetus to drive minority carriers generated at these depths towards the desired electrode. In order to further confirm this, we have compared the photovoltaic performances of the ungraded device (Type I), the graded device (Type III), and a new device which only contains an electron-blocking layer (EBL) of PEDOT: PSS. The QD active layers are the same for these three devices as shown in Figure 3-11. Here, we chose PEDOT: PSS as the electron-blocking layer material because it has a very good band-energy-level match for the PbS QDs used in the active layer (as shown in Figure 3-11 (a)). As shown in Figure 3-11 (b), (c) and Table 3-2, it is very clear that the photovoltaic performance has been enhanced significantly by the ELA structure (graded Type III device) compared to the device employing the EBL layer only. This result demonstrates that the graded energy-level structure does contribute to the improvement of the solar cell performance, but the improvement is not merely due to the formation of an electron-blocking layer.

Through integrating the EQE spectra with the AM1.5G solar spectrum for ungraded Type I and graded Type III devices, values of J_{sc} were calculated as 26.7 ± 0.92 and 30.7 ± 1.07 mA/cm^2, respectively, in good agreement with the measured J–V results (25.82 ± 1.39 and 32.65 ± 1.03 mA/cm^2). These results also suggest that the J_{sc} of these planar PbS QDHSCs with a PbS layer thickness of only approximately 300 nm can more closely approach the J_{sc} of depleted-bulk-heterojunction-structured PbS QDSCs, in which the active layer thickness is normally larger than 1000 nm (e.g., ZnO nanowires/PbS)[82, 181] The J_{sc} more than 30 mA/cm^2 in planar PbS QDHSCs were also reported by other two strategies.[92, 182] One strategy is that a cascaded-junction quantum dot solar cell was fabricated by using 3 kinds of sizes of highly monodispersed PbS QDs. [182] In the device, one layer of larger size PbS QDs with TBAI ligand was placed between ZnO and QD active layer to reduce the interfacial recombination at ZnO/QD interface and to decrease leakage current. [182] Then, one layer of smaller size PbS QDs with EDT ligand was placed between the QD active layer and the Au electrode as an electron-blocking/hole-extraction layer to decrease recombination at this interface. However, the organic ligand EDT passivated PbS quantum dot layer would have a negative influence on the illumination stability of device under air condition.[68, 183] Almost all of the PbS QDHSCs using EDT as passivation ligands were measured in N_2 atmosphere rather than in air.[88, 95, 161-162] In another strategy, a new-ligand (pseudohalogens) was employed for PbS QD surface passivation and a thick QD active layer (more than 500 nm) was used, which increased the J_{sc} largely.[92] In our devices, although the thickness of the active layer is only about 300 nm, J_{sc} values greater than 30 mA/cm^2 have been realized, which is originated from the ELA structure. The most important thing is that all of the PbS quantum dots at each layer are passivated with

inorganic ligands (Br-) in our devices, and all of processes including preparation, characterization and store are carried out under air condition in this work.

For our graded devices, the conduction band energy gradient produces an additional driving force for electrons, and the degree of band bending (the conduction bandgap variation with position) is in the order of Type IV > Type III > Type II. Figure 3-6 (c) shows that the EQE of the graded devices increased as the quantum funnel effect strengthened in the visible portion of the spectrum (400–750 nm) and long-wavelength range (850–1050 nm). This is because of the decreased recombination rate caused by the enhanced separation of the electrons and holes due to the driving force originating from the internal electric field and the ELA. In other words, the ELA structure causes an enhanced gradient in the carrier profile (i.e., an effective larger intrinsic electric field), and thus, the recombination rate decreases; this explains the further enhancement in EQE for the graded devices. In this work, the EQE spectrum shows that the improvement in J_{sc} in the graded device is mainly due to the visible light range of the photoelectric conversion, although the optical absorbance in the visible region is almost the same for the four devices. This result indicates that the charge collection efficiency decreases in the order of Type IV > Type III > Type II > Type I. The decrease in Type IV EQE in the 1000–1200 nm spectral range may be attributed to the decrease in the optical absorbance as shown in Figure 3-10.

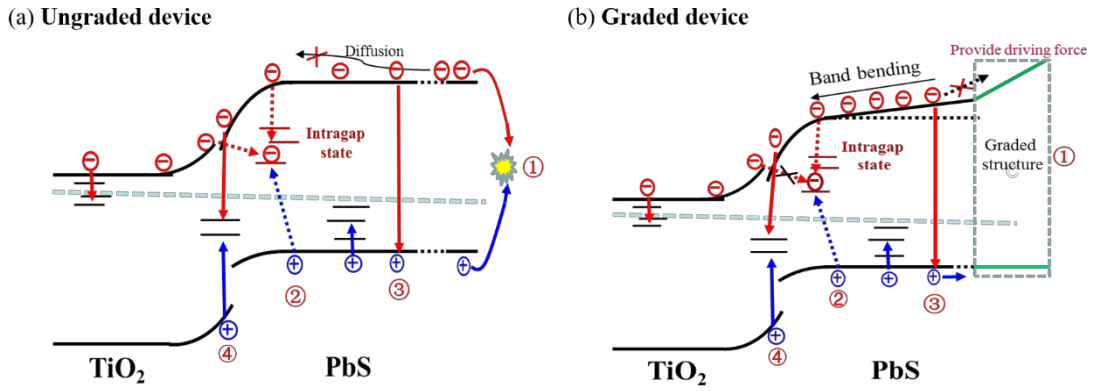

Figure 3-12. Possible recombination channels for photogenerated carriers in the PbS QDHSCs including (1) interfacial recombination at PbS/gold contact interface, (2) trap-assisted recombination, (3) band-to-band recombination, and (4) interfacial recombination at TiO_2 /PbS for (a) ungraded device and (b) graded devices

As shown in the above results, the J_{sc} and V_{oc} both increased by introducing the ELA structures, which indicates that the extracted current is increased and recombination within the quasineutral region is reduced, so the optimized ELA structure can increase the diffusion length such that it is longer than the quasineutral region. To investigate the mechanism of the performance enhancement in the graded structure solar cells, we need to understand the

recombination mechanism in the PbS QDHSCs. In the PbS QDHSCs, there are several possible recombination mechanisms. Figure 3-12 (a) shows the possible recombination processes, including interfacial recombination, trap-assisted recombination, and band-to-band recombination.[184] In this study, we focus on (1) interfacial recombination at the PbS/gold contact interface and (2) trap-assisted recombination in the PbS film through an intragap state. After employing the graded structure, the following three effects are anticipated, as shown in Figure 3-12 (b): i) The graded structure, as an electron-blocking layer, reduces the interfacial recombination at the PbS/gold interface; ii) The graded structure provides a multi-stage impetus to drive efficiency-limiting electrons towards the TiO_2 electron-transfer layer; and iii) the additional carriers can fill the trap states to reduce the trap-assisted recombination in the PbS QD active layers.

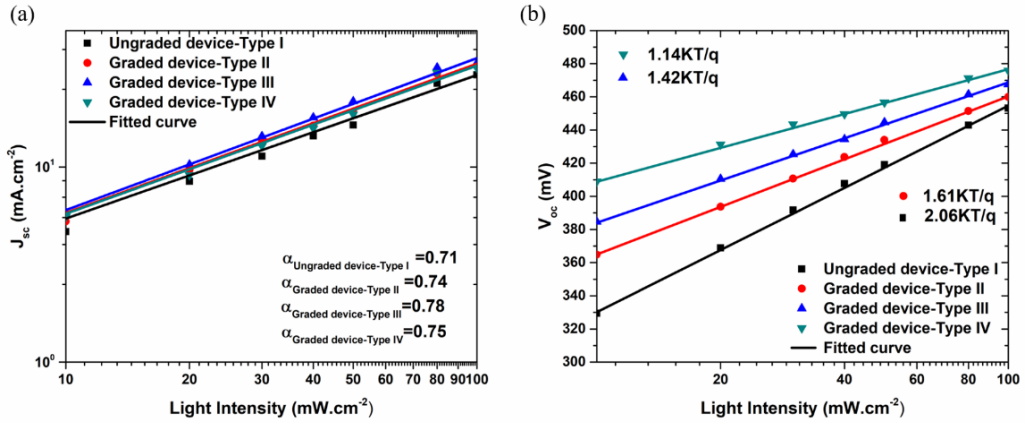

Figure 3-13. (a) Light-intensity dependence of J_{sc} and (b) light-intensity dependence of V_{oc} for the four types of QDHSCs. The solid lines are the fitting results.

To better understand the improvement in the short-circuit current and the change in the recombination mechanism of the graded structure PbS QDHSCs, we characterized the devices in several ways to investigate their working mechanisms. First, in order to gain a deep understanding of the mechanism driving to the improved photovoltaic performance in graded QD devices with different ELA structures, we investigated how J_{sc} and V_{oc} depend on the light intensity (P) in these devices (Figure 3-13(a), (b)). Figure 3-13 (a) displays the J_{sc} as a function of the light intensity P_{Light} in a double logarithmic scale. The J_{sc} values for all devices increased sub-linearly with the light intensity, and the experimental data are fitted with $J_{sc}(P)=P^{\alpha}_{Light}$,[185] to ascertain the contribution of the charge recombination in the loss mechanism for the photocurrent, where α is the exponential factor (called the recombination coefficient) and is obtained for the ungraded and graded devices from the fitting. If the α value is close to 1, that signifies that nongeminate recombination (such as trap-assisted recombination) at short-circuit conditions is negligible.[185-186] However, if the α value is smaller than 1, both trap-assisted recombination and interface state recombination are present in the solar cell.[187] In the current case, for the Type I ungraded device and the Type II, III, and IV graded

devices, a logarithmic dependence is observed at all ranges of light intensities with α being 0.71, 0.74, 0.78, and 0.75, respectively. The changes in the value of α correspond to the changes in J_{sc}. In the graded devices, a reduction in the nongeminate recombination is expected because of the decreased trap-assisted recombination in the PbS active layer (process 2 in Figure 3-12 (b)).

In these solar cells, by investigating the diode ideality factor n, the dominant recombination mechanism could also be determined. Two methods can be used to obtain the ideality factor: one is by fitting the dark J−V curves with the ideal diode equation; the other is by fitting the light intensity dependence of the V_{oc} curves. However, it is hard to ignore the influence of the series resistance in the former method. Using the latter method to determine the ideality factor n is usually considered to be a better estimate since it is not influenced by series resistance and is supposed to reflect the recombination mechanisms under open-circuit conditions.[187] Figure 3-13 (b) also shows the increase in V_{oc} for the four types of devices with increasing light intensity. For a standard junction solar cell, neglecting the series and shunt resistances, the light intensity (P_{Light}) dependence of the V_{oc} has the following relation:[188-189]

$$V_{oc}(P) = \frac{nkT}{q} ln\left(P_{Light}\right) + C \qquad (2)$$

where k is the Boltzmann constant, T is the temperature, q is the absolute value of electron charge, n is the ideality factor, C is a constant.

By fitting the V_{oc} *vs.* P_{Light} curves with equation (2), n is determined to be 2.06, 1.61, 1.42, and 1.14 for the ungraded device Type I and the graded devices Type II, III, IV, respectively (Figure 3-13 (b)). This phenomenon can be interpreted as being due to the carrier recombination characteristics, reflecting the different J–V characteristics of solar cells with different device structures. Ideally, for a standard p-n junction, when recombination in the neutral region dominates, the slope of V_{oc} versus the light intensity, i.e., when nkT/q has an ideality factor n, is close to 1. The diode current flows in forward-bias, and the recombination is dominated by band-to-band recombination where electrons in the conduction band recombine directly with holes in the valence band. On the other hand, when recombination within the space-charge region (or depletion region) dominates, the values of the ideality factor theoretically range from 1 to 2 ($1 < n \leq 2$), such as when trap-assisted recombination is dominant at the interfaces or the mid-gap states (n=2) in the PbS QD layer.[189] Our results (Figure 3-13 (b)) reveal the decrease in the ideality factor from 2.06 (ungraded) to 1.14 (graded) along with the increase in the number of layers of differently size QDs, reflecting that the relative contribution of trap-assisted recombination is reduced. This is because, in the graded structure as shown in Figure 3-12 (b), the intrinsic electric field induced by the graded structure increases in the order of Type IV > Type III > Type II. Thus, more charge carriers can be driven with the electric field increasing

and more trap states can be filled by charge carriers, which results in the strong suppression of the trap-assisted recombination. Thus, for the graded devices, the graded structure additionally acts like an increase in incident light intensity. Therefore, this validates the idea that trap-assisted recombination can be largely suppressed in the graded structure solar cells.

To directly investigate the possible charge-recombination processes, the transient photovoltage decays were measured. Upon illumination of the PbS QDHSCs by a 532 nm laser pulse under open-circuit conditions, open-circuit photovoltages of the solar cells are obtained. When the incident laser is switched off, all photogenerated carriers will ultimately recombine, leading to a decay in the photovoltage. The transient photovoltage decay depends on the recombination types and thus gives valuable information on carrier recombination. In addition, to obtain further detail about the effects of intragap states, we measured transient photovoltage decay without background illumination.

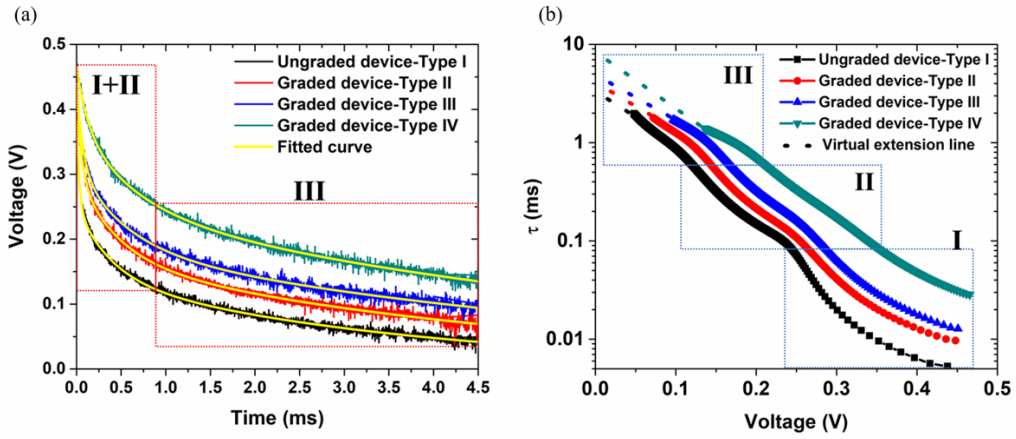

Figure 3-14. (a) Normalized open-circuit photovoltage decay curves for ungraded and graded PbS QDHSCs, showing three primary decay processes. (b) The effective carrier lifetimes calculated from the voltage decay curves.

Table 3-3. Fitted Proportionality Constants [a] and the time constant is obtained from the open-circuit photovoltage decay curve of PbS QDHSCs.

Cells	A_1 (A_1/ (A_1 + A_2 + A_3))	τ_1 (ms)	A_2 (A_2/ (A_1 + A_2 + A_3))	τ_2 (ms)	A_3 (A_3/ (A_1 + A_2 + A_3))	τ_3(ms)
Type I	0.131 (34.4%)	0.031±0.001	0.108 (28.3%)	0.384±0.001	0.143 (37.3%)	3.66±0.01
Type II	0.132 (30.5%)	0.056±0.001	0.128 (29.8%)	0.457±0.001	0.171 (39.7%)	4.98±0.01
Type III	0.126 (28.6%)	0.078±0.001	0.124 (28.3%)	0.547±0.001	0.190 (43.1%)	6.43±0.01
Type IV	0.087	0.127±0.001	0130	0.646±0.001	0.248	7.40±0.01

	(18.8%)		(27.9%)		(53.3%)	

[a] Includes the relative weights.

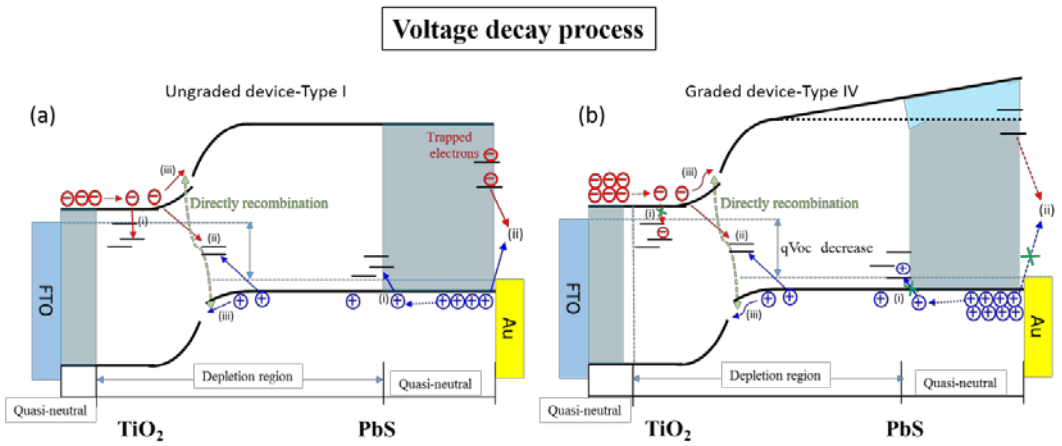

Figure 3-15. The V_{oc} decay process is mainly credited to three recombination channels: (i) natural trapping-assisted recombination in PbS and the TiO_2 film, (ii) charge recombination at the TiO_2/PbS interface defects and PbS/Au interface defects and (iii) direct recombination of photogenerated free electrons and holes in TiO_2 and PbS, respectively for (a) Ungraded device-Type I and (b) Graded device-Type IV.

Figure 3-14 (a) shows the transient photovoltage decay behaviors of the ungraded device and the three types of graded devices. The graded devices exhibited much slower decay processes than the ungraded device, which gave a direct proof of reduced recombination and increased carrier lifetime in the graded cells. In addition, for the graded cells, the decay processes slowed with the increase in the top layer number. The decay curves could be roughly divided into three processes, where section I and section II were both fast decay processes and section III was a slow decay process. These photovoltage decay processes correspond to different recombination processes occurring at different timescales. Therefore, the three decay processes suggest that there are at least three recombination mechanisms in this case. We can fit the decay curves very well by using a superposition of three exponential functions as shown in the following equation:

$$y(t) = A_1 e^{-t/\tau_1} + A_2 e^{-t/\tau_2} + A_3 e^{-t/\tau_3} \qquad (3)$$

where A_1, A_2, and A_3 are constants of proportionality and τ_1, τ_2 and τ_3 are constants of time. The fitted curves and the corresponding parameters are shown in Figure 3-13 (a) (yellow line) and Table 3-3, respectively. For equation (3), the fastest photovoltage decay process represents by the first exponential decay (section I), the second exponential decay to the sub-rapid voltage decay process (section II) and the third exponential decay to the slow photovoltage decay process (section III). Figure 3-15 shows that in the PbS QDHSCs, when the excitation light is switched off, the photogenerated free carriers could recombine through three channels: (i) natural trapping-assisted recombination in PbS and the TiO_2 films; (ii) interfacial recombination at the TiO_2/PbS interface defects and PbS/Au interface defects and (iii)

direct recombination of photogenerated free electrons in TiO_2 and holes in PbS layers. From our previous research results,[68, 82, 190] in the high V_{oc} regime (section I), the value of τ_{eff} was in the ultrafast timescale (~0.1 ms, constant τ_1), and thus, this regime could be related to trap-assisted recombination (process i in Figure 3-15). In the section II regime, the value of τ_{eff} was more than 0.2 ms (constant τ_2), and this regime could be related to interfacial recombination at the TiO_2/PbS and PbS/gold interfaces (process ii in Figure 3-15). In the low V_{oc} regime (section III), the value of τ_{eff} was more than 1 ms (constant τ_3); as this regime shows a long time-scale decay process, it could be related to direct recombination of free holes in the PbS layer and free electrons in the TiO_2 layer due to diffusion (process iii in Figure 3-15).

Table 3-3 shows the parameters obtained by fitting equation (3) to the V_{oc} decays in Figure 3-14 (a). In section I, the weight of A_1 decreases and the decay time constant τ_1 increases from the Type I device to the Type IV device. This shift reflects the reduction of trap-assisted recombination with the increasing extent of the band bending due to the trap states filling as mentioned above, which is consistent with the ideality n change for different devices. For section II, the weight of A_2 showed no obvious changes, but the decay time constant τ_2 increased continually from Type I to Type IV (process ii in Figure 3-15 (b)). This could be associated with the reduction in the recombination at the interfaces of PbS/Au in the four device structures. The section III decay process represents direct recombination between electrons and holes in the TiO_2 and PbS layers, respectively, where the V_{oc} will disappear completely after this process. As a result of other recombination proportion decreases in the graded cells, the weight of A_3 increased correspondingly. In addition, the decay time constant τ_3 significantly increased in the graded devices. We suspect that this is probably because more ELA structure layers can cause stronger band bending, which creates a quasi-electric field opposed to the electron diffusion direction in this situation, thus increasing the difficulty of direct recombination of electrons and holes.

The effective carrier lifetime (τ_{eff}) in the PbS QDHSCs from the photovoltage decay can be evaluated as defined by the following equations:[191-192]

$$\tau_{eff} = -\left(\frac{kT}{q}\right)/\frac{dV_{oc}}{dt} = \frac{1}{(\tau_n^{-1}+\tau_p^{-1})} \quad (4)$$

$$\tau_n^{-1} = \frac{(dn/dt)}{n} \quad (5)$$

$$\tau_p^{-1} = \frac{(\mathrm{d}p/dt)}{p} \quad (6)$$

where T is the temperature, k is the Boltzmann constant, q is the elementary charge, and n and p are the photoexcited electron and hole carrier densities in the PbS QDHSCs. τ_n and τ_p are the electron and hole lifetimes in the PbS QDHSCs. From the above equations, the open-circuit photovoltage decay is reliant on both the electron and hole

lifetimes in PbS QDHSCs.

The photovoltage-dependent carrier lifetime could also be arranged into three sections, replying to the three photovoltage decay processes, as shown in Figure 3-14 (b). Throughout the V_{oc} regime (sections I, II and III in Figure 3-14 (b)), the value of τ_{eff} increases below 0.2 ms, and the values of τeff in the graded devices were 2–6 times higher than in the ungraded device, in the order of Type IV > Type III > Type II > Type I, which can be understood through the above discussions. Based on these experimental results, the ELA structure was concluded to have three benefits in the V_{oc} decay processes: (i) reducing the interfacial recombination, e.g., at PbS/Au; (ii) reducing the trap-assisted recombination and (iii) slowing the direct recombination of free electrons and holes.

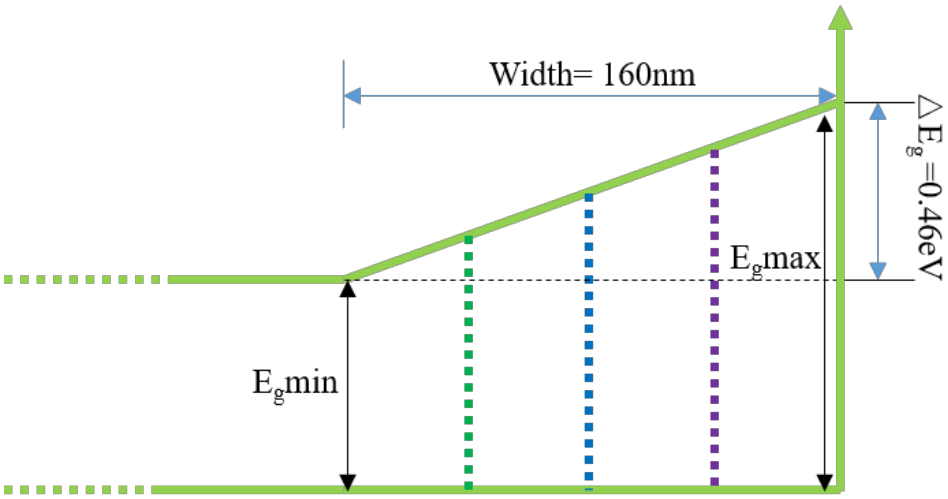

Figure 3-16. Band diagram for the PbS absorber layer of a graded Type IV device, with linear band-gap variation as a function of position (graded structure thickness).

According to the above analysis, in the graded structure, the carriers have a longer *"diffusion length"*, which will increase the probability of charge collection at the heterojunction, thus leading to an increased J_{sc}. Due to the band bending, the graded structure will provide a force similar to the drift force due to a quasi-electric field. In other words, in the graded device, electrons drift because of the electric field due to the potential variation and by the additional quasi-electric field associated with the conduction band variation with position.[193] Thus, in the case of a graded structure, a drift-diffusion length must be defined. If electron drift and diffusion are in the same direction, the drift-diffusion length will be[194]

$$L_n = \frac{l_n}{\sqrt{1+\left(\frac{\xi_e l_n}{2V_T}\right)^2 - \frac{\xi_e l_n}{2V_T}}} \qquad (7)$$

where l_n is the electron diffusion length, V_T is the thermal potential (kT/q) and ξ_e is the quasi-electric field in the ELA region. For the Type IV device (Figure 3.16), the

absorber layer thickness is approximately 300 nm, the diffusion length in the colloidal PbS QD film is (as per reports) l_n=80 ± 10 nm,[195] and the total band gap (conduction band) change is ΔE_g=0.46 eV. As mentioned above, the ELA structure can cause the band bending, and here we assume that the ELA structure of the adjacent layer of M-PbS also belong to this quasi-electric field. Thereby the space-charge width for this device could be on the order of 160 nm (M+S1+S2+S3-PbS, each layer). Therefore, the quasi-electric field caused by this band gap variation would be approximately ξ_e=2.88×10^4 V/cm directed towards the junction interface. The drift-diffusion length L_n will become approximately 720 nm, which is approximately 9 times the diffusion length (80 nm). Thus, the quasi-electric field attributed to an ELA structure built by differently sized PbS layers in a solar cell should result in a large increase in effective diffusion length.

Furthermore, we have evaluated two important properties, i.e., hysteresis and stability, for our solar cells. Figure 3.17(a) shows the hysteresis of our PbS QDHSCs, with no significant hysteretic effect (lower than 1%) identified. Then, the long-term stability was evaluated without any encapsulation in ambient atmosphere under dark conditions without any humidity control, as shown in Figure 3.17(b). Both the ungraded device (Type I) and the graded devices (e.g., Type III) were stable for over 150 days (>3600 h) without any significant degradation, exhibiting excellent long-term storage stability.

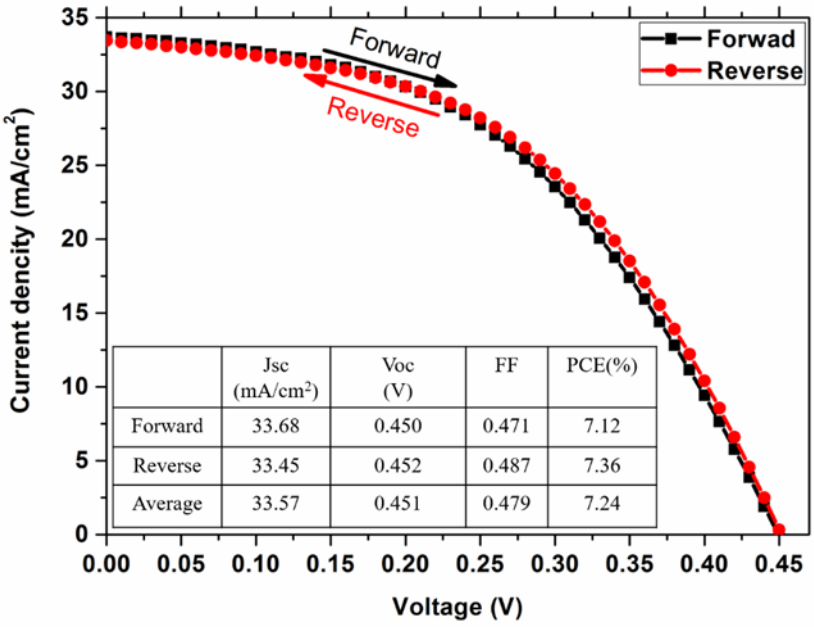

	Jsc (mA/cm²)	Voc (V)	FF	PCE(%)
Forward	33.68	0.450	0.471	7.12
Reverse	33.45	0.452	0.487	7.36
Average	33.57	0.451	0.479	7.24

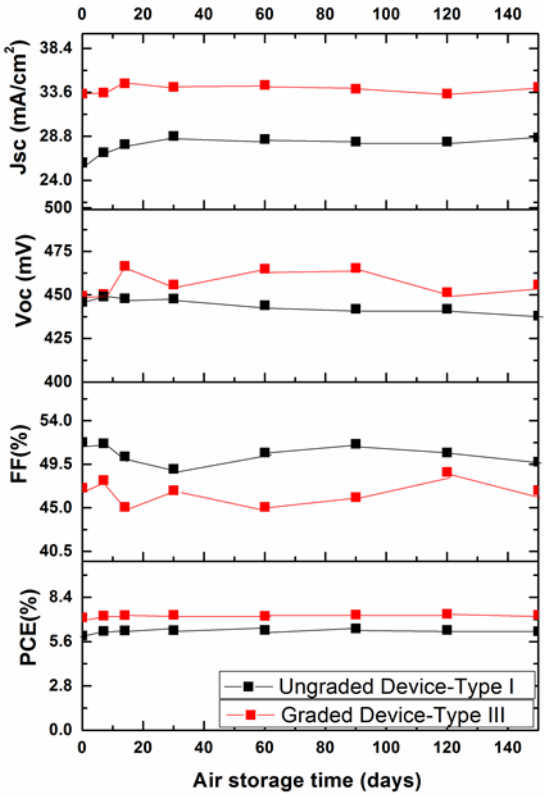

Figure 3-17. (a) J–V curves of graded device-Type III measured by forward and reverse scans under AM 1.5 G illumination. (b) Stability evaluation of the ungraded and graded Type III PbS QDHSCs. All devices were stored and tested in ambient conditions.

3.4 Conclusion

In summary, we have demonstrated that the ELA engineering in the active QD layers of QDHSCs can be used to improve the electron collection efficiency at the heterojunction and reduce trap-assisted and interfacial recombination. Through the ELA strategy, a great increase (from 28 to 33 mA/cm^2) in J_{sc} and a maximum efficiency of 7.24% (the active area is 16 mm^2) have been achieved by optimization of the structure. Grading the energy level does not cause much variation in the optical absorption, but it can improve the collection of photogenerated carriers. The ELA structure promotes separation of the electron−hole pairs, leading to a dramatic enhancement in the photoexcited carrier lifetime. This is directly associated with the enhanced effective diffusion length and increased J_{sc}. In our study, recombination mechanisms in PbS QDHSCs were investigated by examining the light intensity dependences of J_{sc} and V_{oc} and the transient photovoltage decay. Our results show that the ELA structure has two benefits for QDHSCs: (i) the ELA structure, as an electron-blocking layer, reduces the interfacial recombination at the PbS/Au interface; (ii) the ELA structure can drive more electron carriers toward the electron transfer layer, and the additional electron carriers can fill the trap states, reducing the trap-assisted

recombination in the PbS QDHSCs. With the increase in the number of graded structure layers, the electron driving force becomes stronger, leading to longer minority carrier lifetimes. However, although the graded Type IV device has the longest carrier lifetime, it does not have the best performance. This is because the presence of the graded structure causes gradual resistance increase by introducing undesirable band bending between the valence band of the M-size PbS layer and the gold contact. In the Type IV device, this barrier is hard to ignore, which seriously affected the transport of holes to the gold contact. Through the band energy engineering strategy and the optimization of the thickness of the graded structure, the Type III device achieved the best efficiency. The hysteresis and stability of the devices were also characterized. Negligible hysteretic effects were observed in our devices, and they exhibited wonderful storage stability in ambient conditions (without obvious performance decline after more than 150 days). In brief, this study emphasized band energy engineering in achieving high-efficiency planar heterojunction QD solar cells. The carrier recombination mechanisms explored in this work may be able to aid further improvements of QDHSCs and they can even benefit other types of solar cells. This study suggests a useful strategy for improving the effective diffusion lengths of photogenerated carriers in PbS QDHSCs via simple architecture design.

Chapter 4: Understanding Charge Transfer and Recombination by Interface Engineering for Improving the Efficiency of PbS Quantum Dot Heterojunction Solar Cells

4.1 Introduction

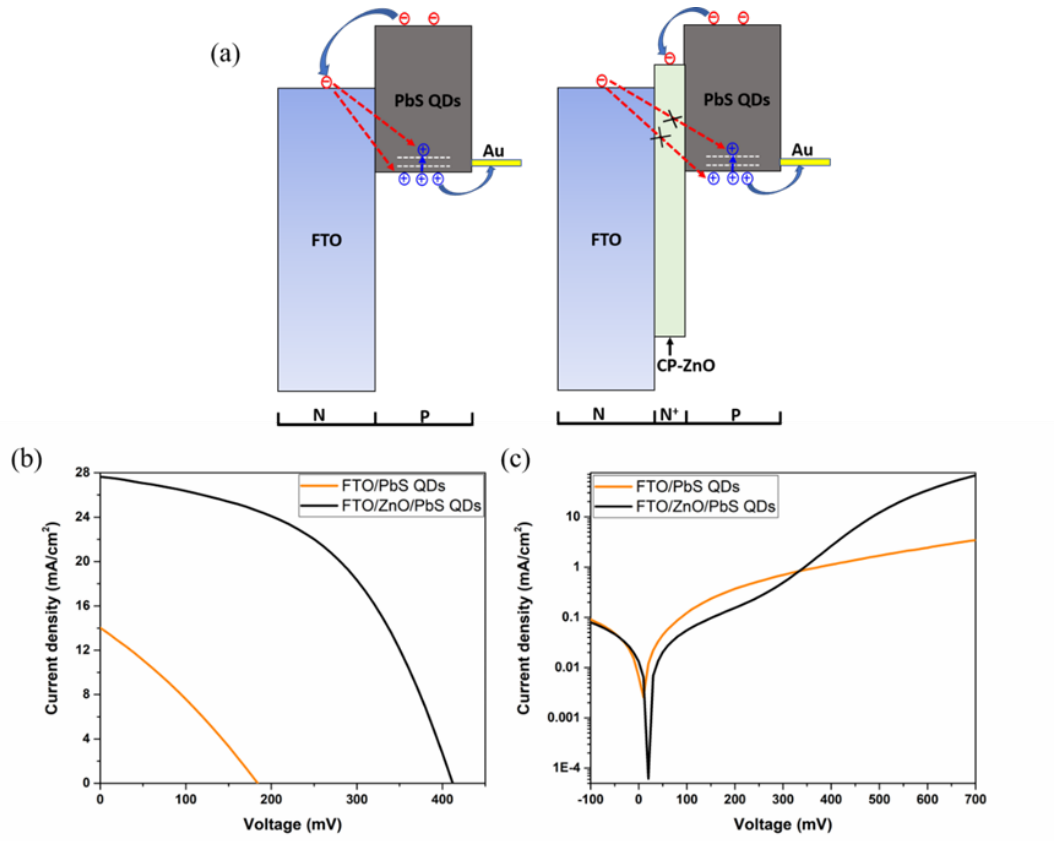

Figure 4-1. Schematic diagrams illustrate the band alignment and charge recombination in the cells without ZnO (Left) and with ZnO (Right). (b) Illumination J-V curves for the PbS QD solar cells with and without ZnO layer. (c) J-V curves measured under dark conditions.

Colloidal PbS QDs are often employed in depleted heterojunction solar cells, which contain five different parts: a transparent conducting oxide (TCO) layer (e.g., fluorine-doped tin oxide (FTO) and indium-doped tin oxide (ITO)), an electron transport layer (ETL) (or hole-blocking layer (HBL), e.g., ZnO, SnO_2, and TiO_2), PbS QDs, a hole-transport layer (HTL) (or electron-blocking layer

(EBL), e.g., MoOx and organic small molecules), and contact electrodes (e.g., Au and Ag).[67, 94, 196-198] Unlike perovskite solar cells, which can still function without the inclusion of a HTL or ETL, in PbS QD heterojunction solar cells (QDHSCs), both an ETL and a HTL are necessary for achieving high efficiency, because they enhance charge extraction and suppress charge recombination at the TCO/QD and QD/gold interfaces.[29, 199-200].[152] This may result because QDs have more surface defects than perovskites, which can cause severe back recombination of injected electron carriers at the FTO/QD interface (Figure 4-1).

In a QDHSC, the p-type layer is a QD film, and the n-type layer is an ETL that accepts photogenerated electron carriers. The built-in electric field is mainly distributed near the ETL/QD interface.[61, 198] Usually, when a favourable cliff-like conduction band structure forms at the ETL/QD interface (i.e., the conduction band of the QDs is higher than that of the ETL), electron injection will occur. When the conduction band of the QDs is lower than that of the ETL, forming a spike structure, electron injection will be retarded.[61, 199] Such observations have been demonstrated in QD-sensitized solar cells and $Cu(In,Ga)Se_2$ (CIGS) solar cells.[199, 201-203] However, in this work, we found that in magnesium (Mg)-doped ZnO/PbS QDHSCs, the ZnO layer does not need to have a lower conduction band energy to realize efficient charge transfer, that is, although a spike structure is formed between the QDs and the "*electron acceptor*", charge injection can still occur, and improved injection of photogenerated electrons can occur at a certain conduction band offset (CBO). Here, we used a thin Mg-doped ZnO film (~30 nm) ($Zn_{1-x}Mg_xO$, x=0, 0.05, 0.10, 0.15, 0.20) as an ETL with tuneable characteristics. In fact, $Zn_{1-x}Mg_xO$ films with high transparency and tuneable band gaps have been employed in PbX (X=S, Se) QDHSCs as a novel electron-transport material, and greatly improved solar cell efficiencies have been obtained with enhanced open-circuit voltage (V_{oc}).[197, 204-205] However, previous studies did not provide further insight into the role of Mg doping, for example, its impact on the carrier dynamics, including charge injection and recombination. Here, we explored the carrier injection and recombination mechanism in FTO/$Zn_{1-x}Mg_xO$/PbS QDHSCs by varying the Mg doping level in ZnO. The effect of Mg doping on the intrinsic properties (e.g., defect states and carrier concentration) of the $Zn_{1-x}Mg_xO$ layer and the ensuing device performance were systematically studied by several spectral measurements, such as transient photovoltage (TPV) decay measurement and ultrafast transient absorption (TA) spectroscopy. Interestingly, we found that Mg doping can greatly alter the photophysical properties of ZnO and, in particular, that the resulting spike band structure of $Zn_{1-x}Mg_xO$/PbS QDs can inhibit charge recombination, while the shallow defect states can serve as additional pathways to transport photoexcited electrons from the QDs to the electron-collecting electrode. More importantly, we also revealed the time constant of this transport process by TA measurement

4.2 Experiments

Materials. Lead (II) oxide (Wako, 99.5%), oleic acid (OA, Wako, 60%), 1-octadecene (ODE, Aldrich, 90%), and bis(trimethylsilyl) sulfide (TMS_2 sulfide, Aldrich, 99.999%), cadmium chloride ($CdCl_2$, Wako, 99.8%), oleylamine (OLA, Aldrich, 70%), tetradecylphosphonic acid (TDPA, Aldrich, 97%), zinc acetate dihydrate (Wako, 99.9%), magnesium acetate tetrahydrate (Wako, 99%), 2-aminoethanol (TCI, 99%), and 2-methoxyethanol (Wako, 99%) were used as purchased without further purification.

PbS quantum dot synthesis

The synthesis of colloidal PbS QDs was according to a remodeled literature method,[173] different-sized PbS QDs were prepared as described previously in literature.[174] In this work, PbS QDs were manipulated using the standard Schlenk line techniques.[6] The mixed solution of 6 mmol PbO, 15 mmol OA, and 50 ml of ODE in a 100 mL three-neck flask was stirred and degassed at room temperature and 90 °C for 20 min and 40 min, respectively. The solution was then heated for 1 h up to the required temperatures of 90, 130°C, followed by the injection of TMS solution. Immediately after the injection, the heater was removed while keeping the solution stirring. When the solution was cooled to 75° C, a $CdCl_2$ -TDPA-OLA solution (1 mmol of $CdCl_2$, 0.1 mmol of TDPA and 3 mL of OLA) was injected into the PbS colloid. After cooling to room temperature, the PbS QDs were precipitated from the growth mixture and re-dispersed in toluene. The resulting precipitate was centrifuged and washed twice with acetone to remove unbound OA ligand from the PbS colloid and then dispersed in octane. Assuming that the reactant TMS is completely converted to PbS product, the concentration of PbS colloid is approximately 50 $mg \cdot ml^{-1}$.

ZnO compact layer synthesis

Solution-processed ZnMgO thin films were fabricated on FTO glass by a modified sol-gel method according to previous reports.[62, 206] The FTO-glass substrate was ultrasonically washed sequentially in water, acetone and isopropanol for 30 minutes and then treated with ozone for 10 minutes. $Zn_{1-x}Mg_xO$ (x=0-0.20) precursor solutions were prepared using a fixed molar ratio of zinc acetate dihydrate and magnesium acetate tetrahydrate dissolved in a mixture of 2-methoxyethanol and 2-aminoethanol under stirring overnight, where the ratio of 2-aminoethanol to total metal acetate was 1.0 and the total concentration of metal acetate was 0.3 M. These transparent solutions were spin-coated on the top of the FTO-glasses, which were pretreated by oxygen plasma for 5 min. Then the films were pre-heated on a hot plate at 150 °C for 10 min, and further transferred into an oven for annealing at 290 °C for 30 min.

Device fabrication

To manufacture PbS QD heterojunction solar cells, PbS colloidal QDs were prepared

on ZnMgO compact layer by a typical layer-by-layer method under ambient conditions using spin coating. Each PbS colloidal layer was deposited at 2500 rpm and ligand exchange briefly with Hexadecyltrimethylammonium bromide (CTAB) solution (30 mM in methanol) was conducted also by spin-cast at 2500 rpm. The ligand exchange step was conducted twice to ensure complete ligand exchange with the oleic acid ligand on PbS surface. Each layer was then rinsed three times with methanol while spinning at 2500 rpm to remove excess unbound ligands. Then the PbS QD spin-coating procedure was repeated until desired thickness was reached. Contacts consisting of ~100 nm of gold were deposited on the PbS layer through a mask to create four identical cells on each substrate by thermal evaporation. The contact sizes were 0.16 cm^2.

Characterization

Current−voltage characterization was performed with a Keithley 2400 source measuring under AM 1.5 G with solar simulator PEC-L10. The IPCEs were measured by monochromatic illumination (300 W xenon arc lamp through Nikon G250 monochromator). X-ray photoelectron spectroscopy (XPS) data were measured by a photoelectron spectrometer, S4 JPS-90MX (JEOL, Ltd., Japan). Scanning electron microscope (SEM) was measured by a JEOL JSM-6340 F instrument (Japan). UV-vis absorption spectra were measured with a spectrophotometer (HITACHI, U-3900H, Japan). The transient photovoltage decay measurements were explored using a 630-nm diode laser (without a background light bias) with 5 ns pulse duration and 4 Hz pulse frequency. The voltage responses from the devices were recorded using an Iwatsu digital oscilloscope DS-5554. PL decay was measured by a NIR PL lifetime spectrometer (C12132, Hamamatsu Photonics). Transient absorption (TA) measurements were explored using a femtosecond TA setup. The laser source was a titanium/sapphire laser (CPA-2010, Clark-MXR Inc.) with a wavelength of 775 nm, a repetition rate of 1KHz, and a pulse width of 150 fs. In this study, pump excitation sample with a wavelength of 470 nanometers were used. The pump light intensity is 15 $\mu J/cm^2$. With a time, resolution of 100 fs, a 1500 nm time-resolved TA spectrum was obtained. The photoelectron yield spectrum (PYS) was measured using a BIP-KV205 ionization energy measurement system (Model BIP-KV205, Bunkoukeiki Co, Ltd)

4.3 Results and Discussion

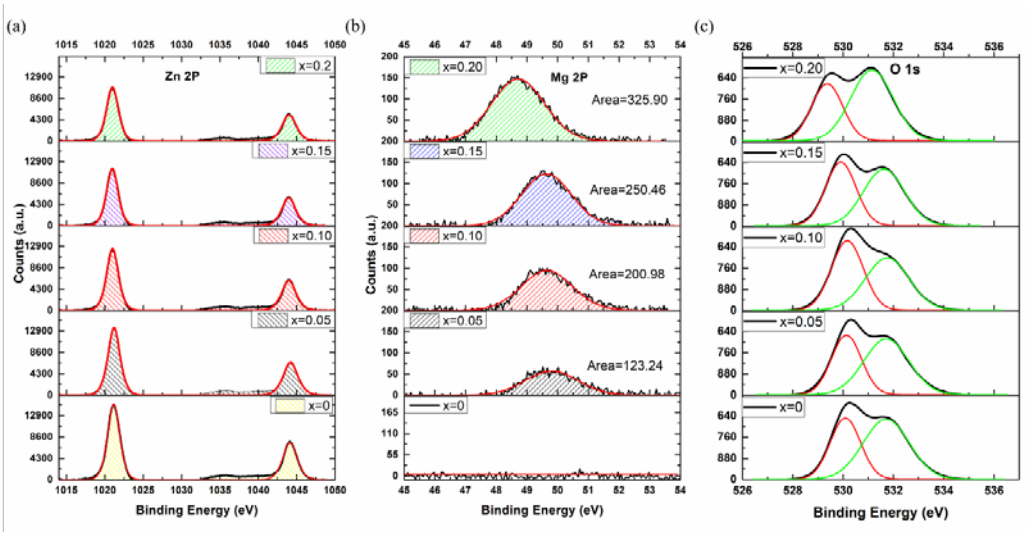

Figure 4-2. XPS spectra of the $Zn_{1-x}Mg_xO$ films (x=0, 0.05, 0.10, 0.15, 0.20): (a) Zn 2p, (b) Mg 2p, and (c) O 1s with two resolved O bonding (red and black lines) components.

The $Zn_{1-x}Mg_xO$ ETL was prepared using a sol-gel method as described previously.[62, 206] Briefly, the Zn-Mg mixed sol-gel solution was prepared by mixing zinc salt (Zn^{2+}) and magnesium salt (Mg^{2+}) (0%, 5%, 10%, 15% and 20% molar percentage based on metal ions), and then, the mixed sol-gel solution was spin-coated onto pre-cleaned FTO substrates and sintered at 290°C. A ZnO film without Mg doping was prepared as a reference.[62] X-ray photoelectron spectroscopy was carried out to verify the Mg doping. The binding energy (BE) scale was calibrated with the C 1s peak of carbon at 284.28 eV. Figure 4-2 shows the XPS spectra of the $Zn_{1-x}Mg_xO$ (x=0, 0.05, 0.10, 0.15, 0.20) films with different Mg doping levels. Typical BE peaks at 1021.3 and 1044.5 eV, assigned to Zn^{2+} $2P_{3/2}$ and $2P_{1/2}$, are observed in all $Zn_{1-x}Mg_xO$ spectra, as shown in Figure 4-2 (a), confirming the presence of divalent Zn ions in all samples.[207] As shown in Figure 4-2 (b), the BE peak assigned to Mg 2p is observed at 49.7 eV in the $Zn_{1-x}Mg_xO$ (x=0.5, 0.10, 0.15) spectra, while that of the x=0.2 film is observed at 48.7 eV with enhanced intensity and area, which suggests that increased Mg doping in $Zn_{1-x}Mg_xO$ can lead to the formation of MgO for $x \geq 0.2$. Figure 4-2 (c) shows BE components at 532.4 eV and 533.9 eV in the $Zn_{1-x}Mg_xO$ spectra, attributable to the O^{2-} ions in Zn-O or Mg-O and the oxygen-deficient components of the films, respectively.[208-210] The XPS results confirm the successful doping of Mg in the ZnO films.[211-212]

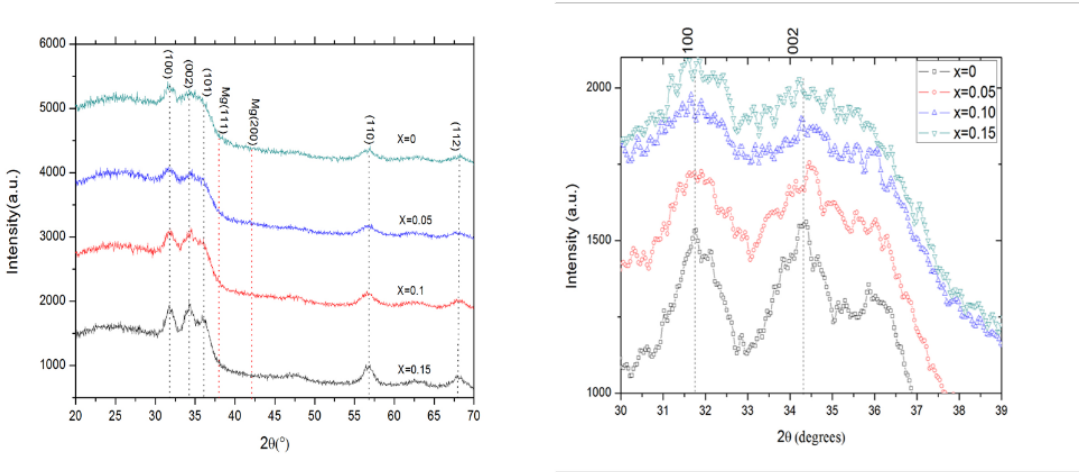

Figure 4-3. (a) XRD pattern of Mg content (x) of $Zn_{1-x}Mg_xO$ films on glass substrate. (b) Partial enlarged detail of (002) peak position of $Zn_{1-x}Mg_xO$ films.

Then we applied X-ray diffraction (XRD) measurements to investigate as obtained ZnMgO films on glass substrate as shown in Figure 4-3 (a). The films have been confirmed are polycrystalline samples possess hexagonal wurtzite structure due to five diffraction peaks corresponding to (100), (002), (101), (110) and (112) are observed. In spite of the both diffraction peaks of (002) and (101) became broadened and incorporated together with the Mg doping content increased, there is without new phase and no peak for MgO. This phenomenon indicating incorporation of Mg^{2+} into the Zn ions site of ZnO to substitute Zn^{2+} due to both have slightly difference of ionic radius (0.57 and 0.60 Å),[206] and there is no obvious change in the structure of the ZnO nanoparticles. However, the ion radius of Mg^{2+} is less than that of Zn^{2+}, which would decrease the spacing of ZnO crystal. According to the Bragg's law the decrease of crystal spacing distance would lead to the increase of crystal dihedral. Therefore, the shift of the (002) peak toward higher angle (Figure 4-3 (b)) is mainly due to the incorporation of smaller Mg ions.

The optical absorption spectra of the $Zn_{1-x}Mg_xO$-coated FTO samples, shown in Figure 4-4 (a), indicate a continuous blueshift of the absorption edges with increasing Mg content (x=0-0.2). The optical band gaps, *E*g, obtained by linearly extrapolating the Tauc plot $[(\alpha h\nu)^2$ vs. photon energy$]$[213], are presented in the inset of Figure 4-4 (a), and the corresponding band gap of the $Zn_{1-x}Mg_xO$ films continuously increases from 3.26 to 3.56 eV with Mg doping, which is in agreement with previous reports.[197, 212] According to other reports of $Zn_{1-x}Mg_xO$,[211, 214] the suitable doping of Mg^{2+} at Zn^{2+} sites in ZnO induces an obvious change in the conduction band minimum (CBM) of the ternary oxide, but the influence on the valence band maximum (VBM) of $Zn_{1-x}Mg_xO$ is negligible. To verify these results, the VBM energy levels of the five $Zn_{1-x}Mg_xO$ samples were measured by photoelectron yield spectroscopy (PYS), as shown in Figure 4-4 (b). The VBM energy levels were obtained from the intersection of the baseline and the tangent to the spectra, and we also found a negligible effect of

Mg doping on the VBM energy levels of the $Zn_{1-x}Mg_xO$ films. The energy band diagram of the $Zn_{1-x}Mg_xO$ films is schematically depicted in Figure 4-4 (c) by combining the above results of both the band gap and the VBM energy levels. From this energy band diagram, a continuous shift in the CBM towards higher energy with increasing Mg doping is observed. The general trend of these values is good agreement with previous reports.[197, 215]

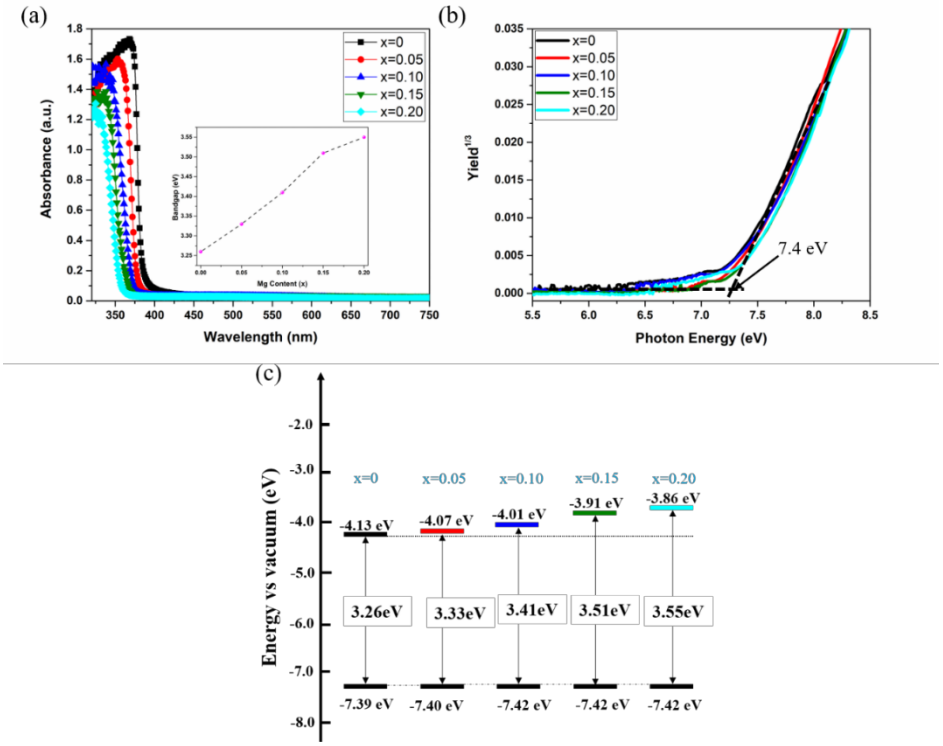

Figure 4-4 (a) Optical absorption spectra (the inset shows an increase in the bandgap of $Zn_{1-x}Mg_xO$ films with Mg doping) and (b) Photoelectron yield spectroscopy (PYS) of the $Zn_{1-x}Mg_xO$ films. (c) Experimentally determined diagram of energy levels (relative to the vacuum level) of the $Zn_{1-x}Mg_xO$ films (x=0-0.20), the valence band maximum (VBM) and the conduction band minimum (CBM) are represented in eV.

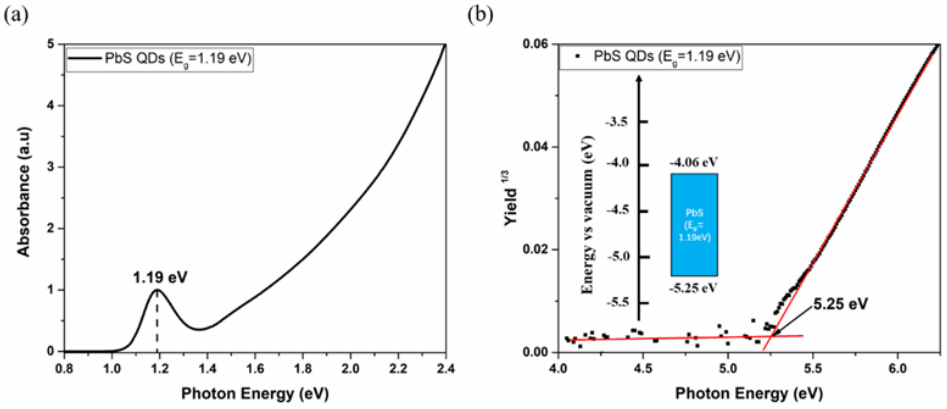

Figure 4-5. (a) Absorption spectra of the PbS QDs (Eg=1.19 eV) in octane. (b) PYS spectra of the PbS QD thin films. The inset shows the vacuum energy level diagram of the PbS QDs.

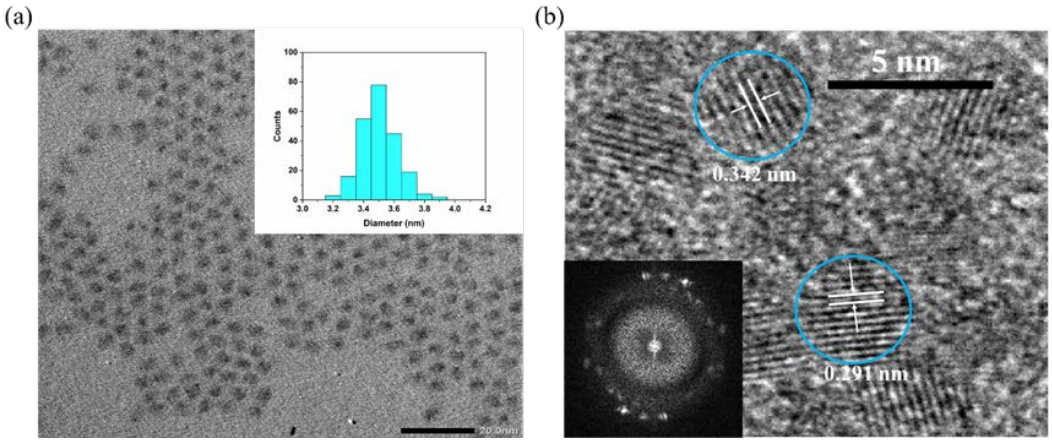

Figure 4-6. (a) TEM micrograph of PbS QDs. Inset displays size histogram. (b) High-resolution TEM image of PbS QDs; Inset displays SAED patterns of the corresponding PbS QDs.

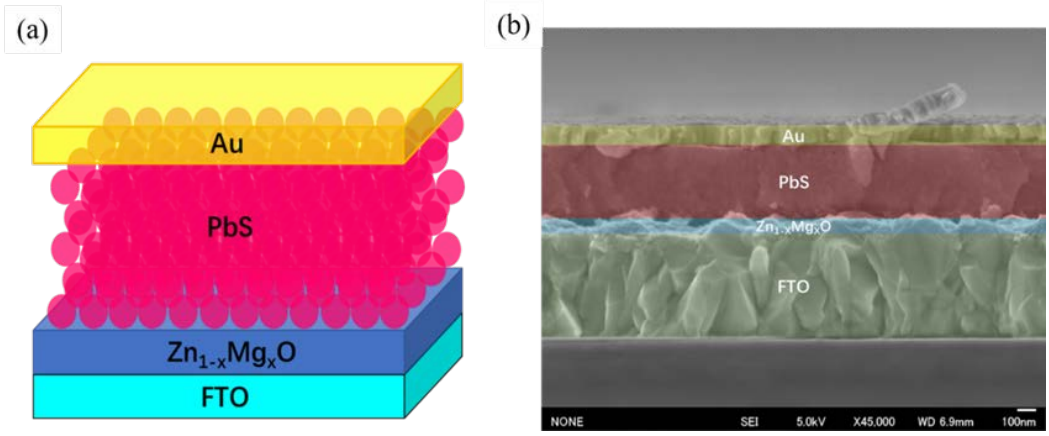

Figure 4-7 (a) Schematic illustration of $Zn_{1-x}Mg_xO$ /PbS solar cell structure. (b) Cross-sectional SEM image of a typical $Zn_{1-x}Mg_xO$/PbS solar cell (~300 nm thick PbS QD active layer).

Our above characterization suggests that ZnO films can be doped with Mg by a facile sol-gel method, and the band gaps can be also easily tuned by adjusting doping degree of Mg. Next, we used $Zn_{1-x}Mg_xO$ (x=0, 0.05, 0.10, 0.15, 0.20) thin film (~30 nm) to prepare PbS QDHSCs. PbS QDs were synthesized using an adjusted hot-injection method,[173] and QDs with different sizes were prepared by controlling the injection temperature. The excitonic peak of PbS QDs was located at 1.19 eV as shown in Figure 4-5 (a), and the valence band edge energy levels (-5.24 eV) of the PbS QDs were confirmed by photoelectron yield spectroscopy (PYS) as shown in Figure 4-5 (b). By combining the results of both band gap and valence band edge levels, the conduction band edge levels (-4.05 eV) were determined, as seen in the inset of Figure 4-5 (b). The corresponding transmission electron microscope (TEM) image reveals that the average size of the PbS QDs is approximately 3.5 nm (Figure 4-6 (a)), and the high-resolution transmission electron microscopy (HR-TEM) image shows that the PbS QDs exhibit a high-crystalline structure with interplanar distances of 0.342 and 0.291 nm, corresponding to the (111) and (200) planes of rock-salt PbS, respectively (Figure 4-6 (b)). The crystallinity of PbS QD is further supported by

the selected area electron diffraction (SAED) pattern (see insets in Figure 4-6 (b)). Figures 4-7 (a) and (b) show the typical schematic structure and a cross-sectional scanning electron microscopy (SEM) image, respectively, of a $Zn_{1-x}Mg_xO$/PbS solar cell, wherein the PbS QD layer (~300 nm) serves as the light absorbing layer.

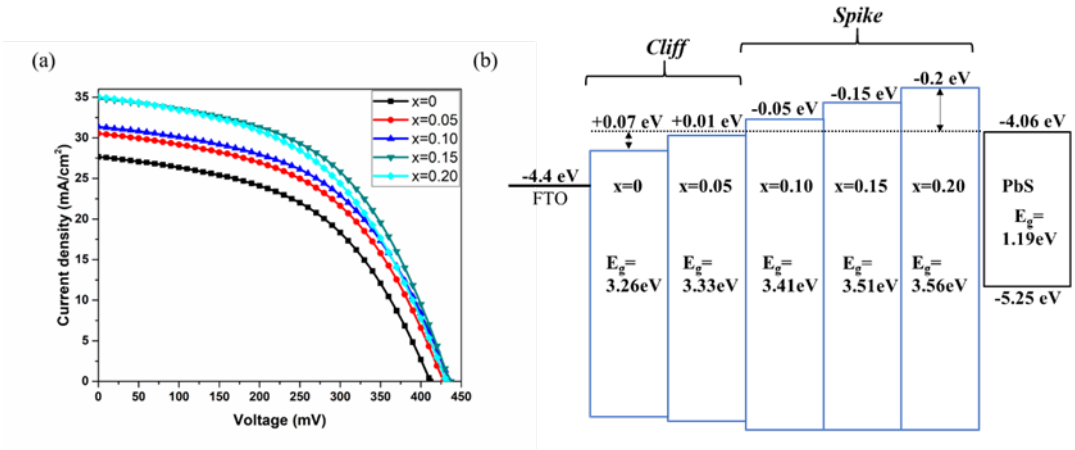

Figure 4-8. (a) J-V characteristics of PbS QDHSCs with $Zn_{1-x}Mg_xO$ (x=0~0.20) under simulated AM 1.5G illumination. (b) Band alignment of PbS QDs and $Zn_{1-x}Mg_xO$ with different Mg contents (x=0~0.2).

Table 4-1 Statistical averages of the photovoltaic performance parameters of 24 devices for each type of the QDHSCs [a].

Sample	J_{sc} (mA/cm^2)	V_{oc} (mV)	*FF* (%)	R_s (Ω.cm^2)	R_{sh} (Ω.cm^2)	*PCE* (%)
x=0	26.34±0.75 (27.64)	419.06±5.8 (412)	49.94±0.85 (49.3)	64.33±3.02 (67.35)	99.86±2.97 (102.83)	5.51±0.11 (5.62)
x=0.05	29.33±0.88 (30.53)	434.18±6.35 (428)	50.53±1.52 (49.9)	55.66±4.78 (60.44)	204.93±4.23 (209.16)	6.43±0.08 (6.51)
x=0.10	30.91±1.27 (31.36)	437.53 ±4.19 (436)	51.05±1.21 (50.3)	52.33±3.71 (48.92)	220.27±3.14 (223.41)	6.79±0.09 (6.88)
x=0.15	33.59±1.32 (34.86)	437.62±6.95 (437)	51.82±1.55 (51.1)	43.52±2.96 (40.56)	174.03±3.99 (178.02)	7.55±0.21 (7.76)
x=0.20	34.23±0.93 (35.05)	434.12±6.05 (434)	47.18±1.55 (48.3)	59.33±4.11 (57.75)	74.17±3.67 (78.44)	7.01±0.34 (7.35)

[a] Results for the device with highest PCE are shown in parentheses.

Figure 4-8 (a) shows the typical photocurrent density−voltage ($J-V$) characteristics of the five types of QDHSCs upon standard 100 mW cm^{-2} AM1.5G illumination. We measured 24 devices for each type of QDHSC. The average values of photovoltaic parameters such as open-circuit voltage (V_{oc}), short-circuit current (J_{sc}), fill factor (*FF*), series resistance (R_s), shunt resistance

(R_{sh}), and PCE are summarized in Table 4-1. Compared with the undoped device (ZnO), the $Zn_{1-x}Mg_xO$ films significantly improved the device performance. As expected, the V_{oc} was continuously enhanced with increasing Mg doping level due to the reduced loss of electrons, as observed in other reports.[197, 204] We consider the enhanced V_{oc} to result from the higher CBM of $Zn_{1-x}Mg_xO$, which is shown in Figure 4-8 (b). However, when the Mg doping level exceeds 10%, the V_{oc} becomes saturated due to dominant charge recombination at the $Zn_{1-x}Mg_xO$/QD interface caused by the high level of Mg doping, as demonstrated previously.[215-217] Surprisingly, the J_{sc} of the device continued to increase at high Mg doping level. For example, the J_{sc} of the device with a 15% Mg doping level was greatly improved by 30%. The control photovoltaic device based on pure ZnO showed a PCE of 5.51 ± 0.11%, with a smaller V_{oc} of 419.06 ± 5.8 mV and a lower *FF* of 49.94 ± 0.85%. The solar cell based on the optimized Mg doping level achieved the highest efficiency of 7.55 ± 0.21%, with a V_{oc} of 437.62 ± 6.95 mV, J_{sc} of 33.59 ± 1.32 mA/cm^2 and *FF* of 51.82± 1.55%, as shown in Table 1, providing an improvement in efficiency of over 36% compared to the ZnO control devices.

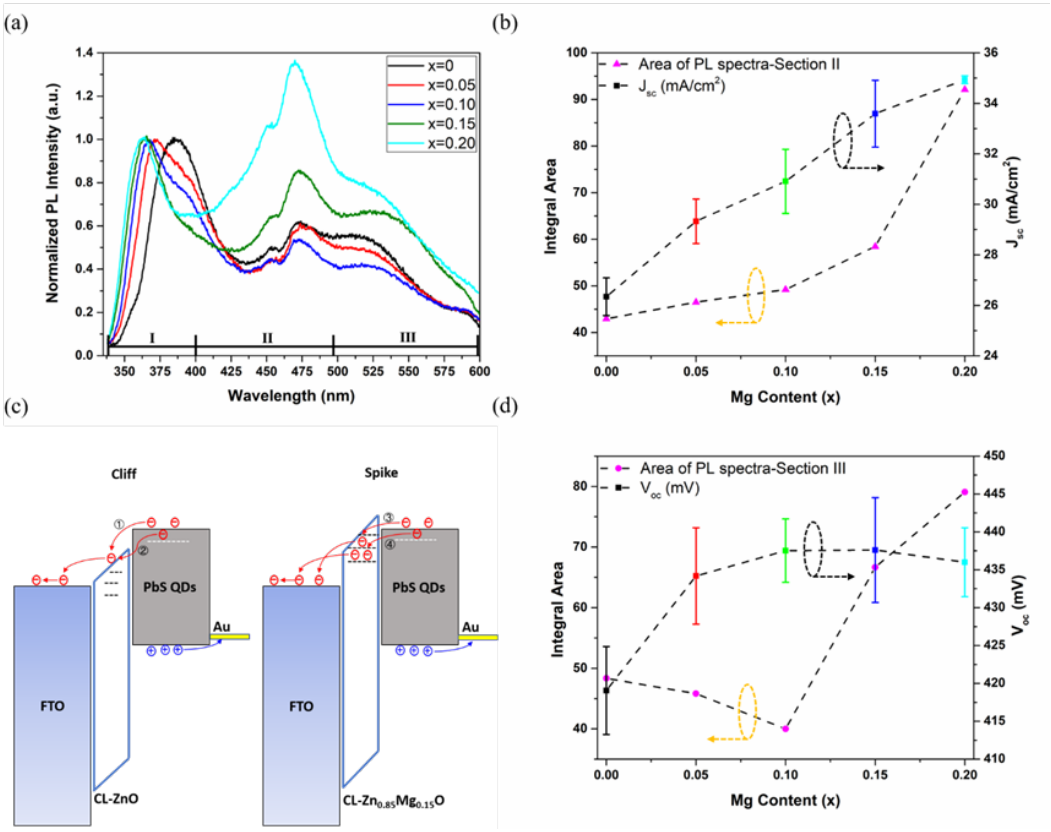

Figure 4-9. (a) Room temperature PL spectra of $Zn_{1-x}Mg_xO$ films (x=0, 0.05, 0.10, 0.15 and 0.20). (b)The integral area of section II range of PL spectra of $Zn_{1-x}Mg_xO$ films and J_{sc} of $Zn_{1-x}Mg_xO$/PbS QDHSCs. (c) Carrier-injection processes for photogenerated electrons (red arrows) and holes (blue arrow) in $Zn_{1-x}Mg_xO$/PbS QDHSCs (cliff and spike structure) under short circuit condition. ① Photogenerated electrons can be injected from the QDs CB to the $Zn_{1-x}Mg_xO$ CB; ②Captured

photo-generated carriers can be injected from QDs intragap state to the $Zn_{1-x}Mg_xO$ CB; ③ Photogenerated electrons can be injected from the QDs CB to the $Zn_{1-x}Mg_xO$ shallow defects; ④ Captured photo-generated carriers can be injected from QD intragap state to the $Zn_{1-x}Mg_xO$ shallow defects. (d) The integral area of section III range of PL spectra of $Zn_{1-x}Mg_xO$ films and V_{oc} of $Zn_{1-x}Mg_xO$/PbS QDHSCs.

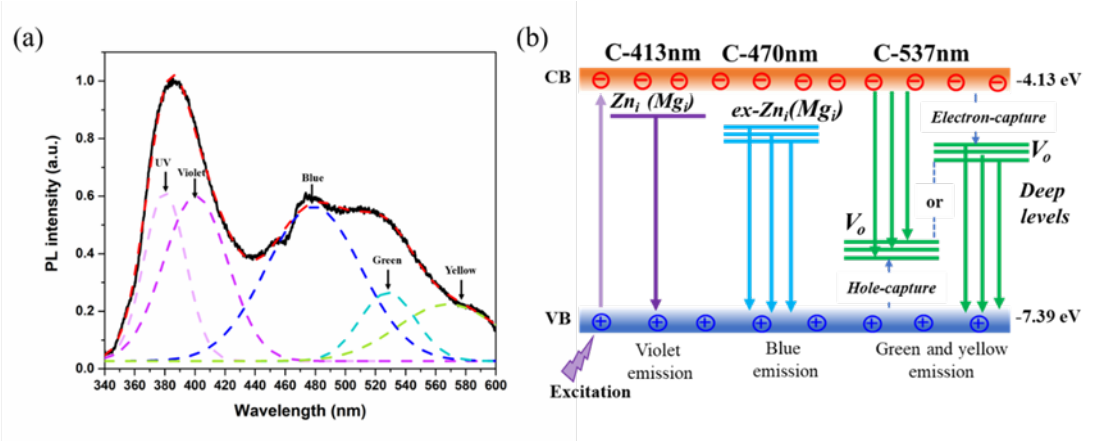

Figure 4-10. (a) Gaussian fitting curves of ultraviolet (UV), violet, blue, green and yellow emissions, exhibiting several sub-bands with similar peak positions to those observed in excitation-dependent PL spectra at room temperature. (b) Schematic illustration of PL emission process in ZnO. The Kröger Vink notation uses: CB = conduction band, VB = valance band, C = center, i = interstitial site, Zn = zinc, O = oxygen, and V = vacancy.

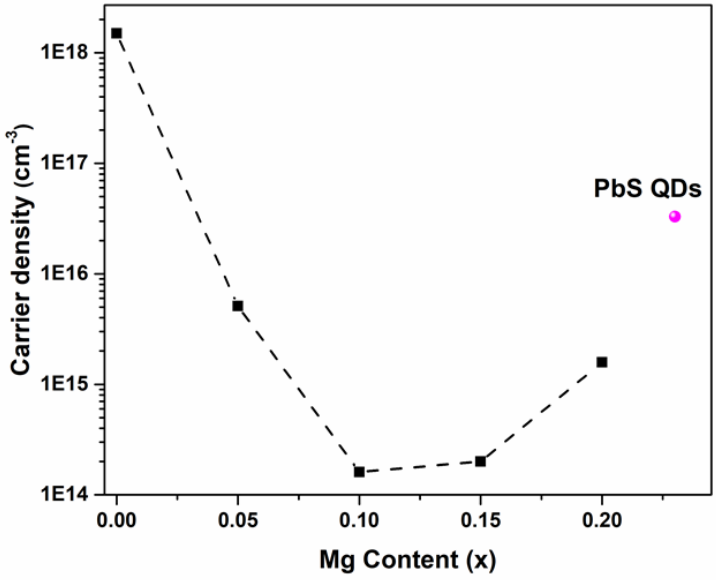

Figure 4-11. Carrier density of $Zn_{1-x}Mg_xO$ and PbS quantum dot at room temperature derived from Hall-effect measurement.

To elucidate the difference in the photovoltaic performance when changing the Mg doping level in ZnO, we first investigated the band alignment between the PbS and $Zn_{1-x}Mg_xO$ layers. As shown in Figure 4-9 (b), the CBO values between the PbS QDs (Eg=1.19 eV) and $Zn_{1-x}Mg_xO$ were controlled from +0.07 eV to -0.2 eV by changing the Mg doping level in ZnO. When the Mg doping level was below 10%, the CB of $Zn_{1-x}Mg_xO$ was lower than that of the PbS QDs, i.e., the CBO was positive, thus forming a cliff structure; when the Mg doping amount was above 10%, the conduction band of $Zn_{1-x}Mg_xO$ was higher than that of the PbS QDs, i.e., the CBO was negative, thus forming a spike structure. Generally, the larger the conduction band offset of the cliff structure (CBO_{cliff}), the better the injection of the photogenerated electrons will be. However, when the ETL/QD interface forms a spike structure (CBO_{spike}), the injection of photogenerated electrons is retarded.[61, 199, 204] However, in our case, a large CBO_{spike} in a certain range instead led to better electron injection and an enhanced J_{sc}, which may be related to the presence of shallow defect states in the $Zn_{1-x}Mg_xO$ films and the decreased carrier concentration due to Mg doping, which will be discussed further below.

To investigate the effect of Mg doping on the performance of the solar cell, room-temperature photoluminescence (PL) were first carried out. Figure 4-9 (a) shows the PL spectra of the $Zn_{1-x}Mg_xO$ samples under room temperature. The PL spectrum of the ZnO film was fitted by Gaussian function as shown in Figure 4-10 (a), which gives five peaks with different centers at 380, 400, 478, 529, and 572 nm. The narrow ultraviolet emission at 380 nm is related to the near band edge transitions in ZnO. Furthermore, the edges of this near band edge-related emission also show a continuous shift toward short wavelength with increasing x value, which also reflects the bandgap broadening due to Mg doping, consistent with the results of the optical absorption spectra in Figure 4-4 (a). Emission regions of 400~600 nm are attributed to the shallow and deep level defects (as shown in Figure 4-10 (b)) within the ZnO crystal, such as interstitials and vacancies of zinc and oxygen.[218] Generally, the violet (400 nm) and blue (470 nm) emission in PL spectra of ZnO are related to shallow defects, the green (529 nm) and yellow (572nm) are related to deep defects.[219] Therefore, the PL spectra can be divided into three sections I, II, and III, which is band, shallow and deep defects-dominated emission, respectively. Figure 4-9 (b) shows the integral area of shallow defect-related emission ranges in PL spectra (i.e., section II). It is well known that the integrated area of the PL emission from defect states is proportional to the defect state density of the corresponding energy level. Interestingly, we found that the change of integral area for section II (shallow defect state emission) with Mg doping content was in good accordance with the change of J_{sc}, suggesting that the electron transfer process may have some relations with shallow defect states. This can be understood by the fact that in the absence of external excitation, it is difficult for the charge carriers to transfer from low energy levels to high energy levels. Besides, although the thickness of

$Zn_{1-x}Mg_xO$ is thin (~30 nm), it is still not enough for the electrons to transport directly from QDs to FTO either by tunneling. So, we thought that when forming a spike structure, the shallow defect states in $Zn_{1-x}Mg_xO$ layer may act as additional pathway for the charge carriers to transfer from the QDs to the FTO electrode. As shown in Figure 4-9 (c), we depicted that in our PbS QDHSCs, when $Zn_{1-x}Mg_xO$ and PbS QDs form a *cliff* structure, the photogenerated electrons can be transferred from the QDs conduction band by pathway ① and intragap-states (pathway ②) to $Zn_{1-x}Mg_xO$ conduction band; When $Zn_{1-x}Mg_xO$ and PbS QDs form a *spike* structure, the photogenerated carriers are difficult to transfer into $Zn_{1-x}Mg_xO$ through pathway ① and ② due to the energy barrier. But due to the favorable energy level alignment between the shallow defects level of $Zn_{1-x}Mg_xO$ and the conduction band or intragap states of PbS QDs, photogenerated electrons can be injected into the $Zn_{1-x}Mg_xO$ by pathway ③ and ④, and then collected by the FTO electrode. In addition, the charge injection rate from absorber to ETL depend on the density of accepting states (i.e., sub-band-gap surface states) of ETL.[184, 220-222] Thereby, Mg doped ZnO act as ESL provides a greater density of accepting states for electron injection due to lower carrier concentration in $Zn_{1-x}Mg_xO$ (~10^{14} cm^{-3}), as show in Figure 4-11. The broadened optical-band gap of Mg doped ZnO enhances the light absorption of PbS QD layer which also beneficial for improvement of J_{sc}.

Notably, the properties of the ETL also have a significant effect on charge recombination in the device. Figure 4-9 (d) shows that as the Mg doping level increased, the integral area of section III (deep defect state emission) first decreased from x=0 to 0.10 and then increased from x=0.10 to 0.20, suggesting that with an increase in the Mg doping level, the deep defects caused by oxygen vacancies in $Zn_{1-x}Mg_xO$ gradually decrease, but when the Mg doping level exceeds 10%, the excessive Mg doping may introduce new deep defects in ZnO, e.g., $Mg_{Interstitial}$ (as seen in Figure 4-10 (b)), which can easily become carrier recombination centres,[219] leading to greater charge recombination at the $Zn_{1-x}Mg_xO$/PbS QD interface. This also explains the saturated V_{oc} observed under excessive Mg doping conditions, as shown in Figure 4-9 (d). However, our *J-V* results show that when the Mg doping level exceeds 10%, the V_{oc} tends to decrease to a saturated value rather than continuously decrease, possibly because the formed *spike* band structure alleviates interfacial recombination to a certain extent, as demonstrated in other types of heterojunction solar cells.[203, 215, 217] Therefore, the change in V_{oc} with increased Mg doping level in our QDHSCs is considered to be a combined effect of defect states in $Zn_{1-x}Mg_xO$ and the formed CBO.

To gain further insight into the effect of Mg doping in $Zn_{1-x}Mg_xO$ on the charge recombination in the solar cells, the diode performance of solar cells was studied by the dark *J-V* characteristic. As can be seen in the Figure 4-12 (a), PbS QDHSCs showed a decrease in overall dark current with increasing Mg doping content. We speculated that

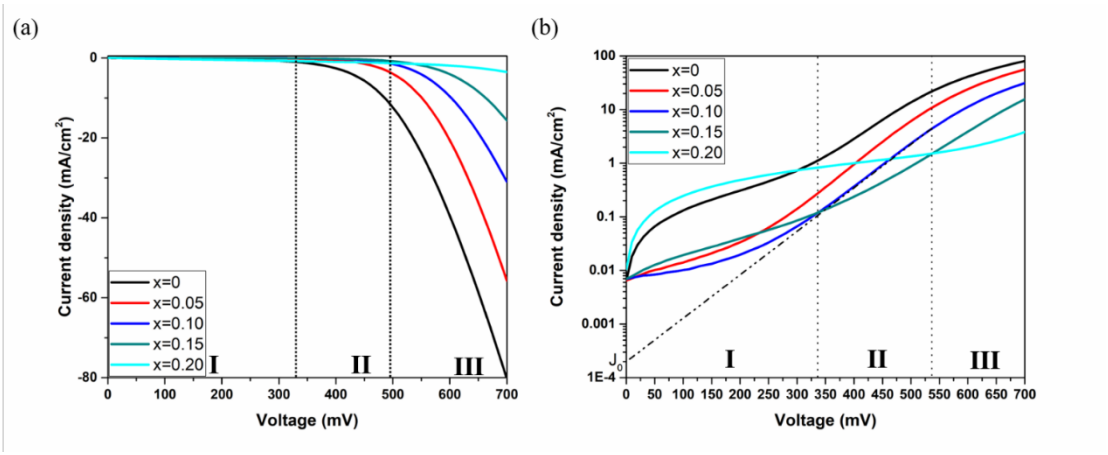

Figure 4-12. (a) Typical *J-V* characteristics of PbS QDHSCs with $Zn_{1-x}Mg_xO$ (x=0~0.20) ETLs measured under dark. (b) Semilog plot of *J-V* curves measured under dark and using the absolute values of current density. The three regions indicate three different effects in the solar cell: Region I account for leakage (shunt) currents, Region II accounts for recombination currents, and Region III accounts for series resistance.

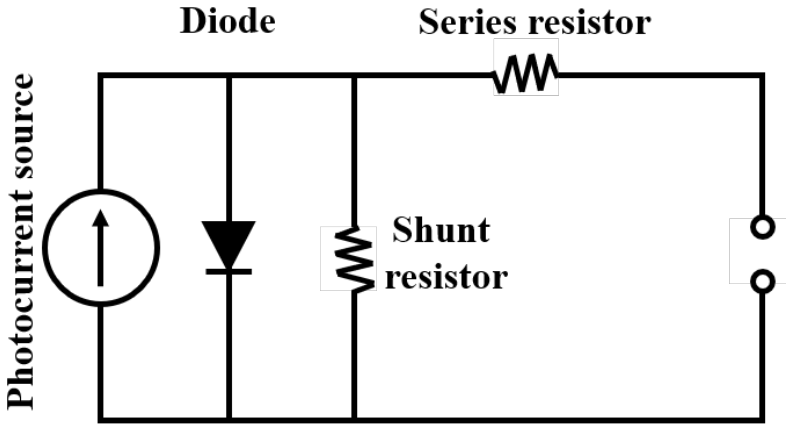

Figure 4-13. Traditional solar cell equivalent circuit model. The photocurrent source is only the result of the solar cell converting the absorbed photons into free charge. The diode represents the electron-hole recombination at the PN junction, the series resistance represents the resistance through the cell's internal resistance, and the shunt resistance represents the model's leakage current through the cell. (For example, through a pinhole).

the decrease in dark current of the devices may be related to the fact that the $Zn_{1-x}Mg_xO$ layer has in fact placed into the built-in potential region, which may be due to improvement of the Femi level of ZnO by Mg doping.[184] In order to obtain further clues about the effect of Mg-doped ZnO on device performance, we analyzed diode behavior in the dark for our devices through introduction of the traditional equivalent circuit model (Figure 4.14)[223]. In this model, the solar cell *J-V* behavior includes four constituent parts: a photocurrent source, diode, series resistor, and shunt resistor. Mathematically this model can be represented by the following equation:[224]

$$J = J_0 \left[exp\left(\frac{q(V-JR_S)}{nk_BT}\right) - 1 \right] + \frac{V-JR_S}{R_{sh}} - J_{ph} \quad (4\text{-}1)$$

where q is the elementary charge, J_0 is the reverse bias saturation current density, n is the diode ideality factor, k_B is Boltzmann's constant, T is temperature, R_s is the series resistance, and R_{sh} is the shunt resistance.

Table 4-2. Diode ideality factor (n) and reverse saturation current density (J_0) of the PbS QDHSCs with $Zn_{1-x}Mg_xO$ (x=0~0.20).

Sample	*n*	J_0
x=0	1.73	7.374E-3
x=0.05	1.39	3.867E-4
x=0.10	1.35	1.974E-4
x=0.15	1.82	1.865E-3
x=0.20	2.54	3.727E-2

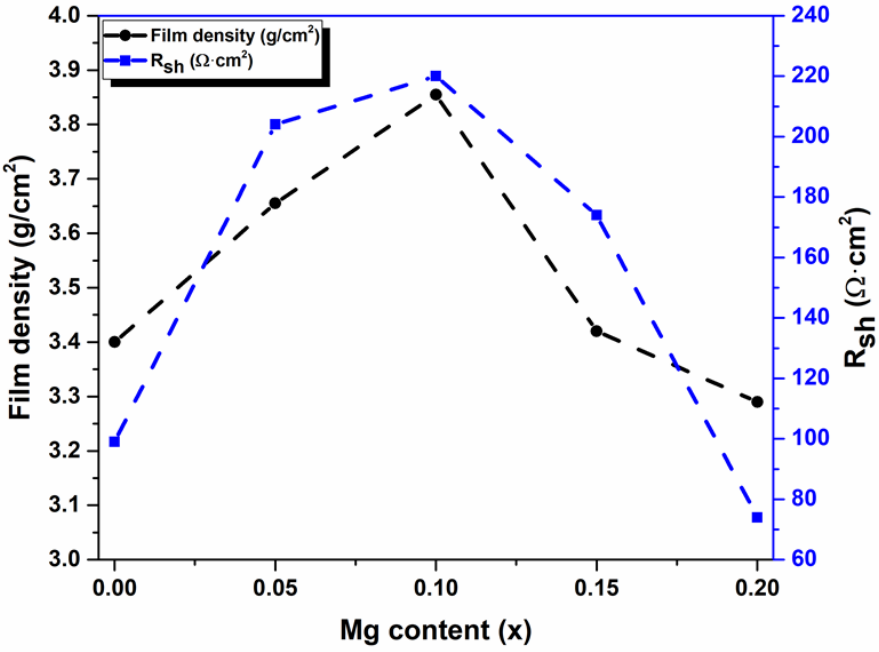

Figure 4-14. Film density of ZnMgO, FF and Rsh of S-PbS QDHSCs with increasing Mg doping content.

Figure 4-12 (b) shows the dark curves derived from Figure 4-12 (a) using the semi-log scale, which can be divided into regions I, II, and III, corresponding to the three parts of eq. (4-1), which describe how the different components of the solar cell equivalent circuit (Figure 4-13) affect the *J-V* response of the cell at different voltages. At low voltages (region I), the *J-V* curve is mainly related to R_{sh} (shunt current); at intermediate voltages (region II: the 1st term in eq. (4-1)), the *J-V* curve is related to diode parameters J_0 and n (recombination current); while at high voltages (region III: the 2^{ed} term in eq. (4-1)), the *J-V* curve is determined by R_s.[224] These regions provide important information when evaluating the *J-V* response curve. For instance, a steep slope in region III generally indicates a low R_s.[224] Thus, according to the observation of the dark current density in regions I, II and III in Figure 4-12 (b), we found that the changes in R_{sh} and R_s of the devices with increasing Mg doping level are in agreement with the R_{sh} and R_s measured from *J-V* characterization under illumination (Table 4-1). When the Mg doping level was increased from 0 to 10%, the current leakage (region I) of the device continuously decreased, but when the Mg doping level was above 20%, significant current leakage was observed. This could be attributed to the fact that the appropriate Mg doping level (x=0.1) leads to better crystallization of the ZnO film and further decreases the defects and current leakage of the thin films.[225]

According to the least-square fitting of the dark *J-V* curves in section II to eq. (4-1), the value of n and J_0 of the PbS QDHSCs with $Zn_{1-x}Mg_xO$ are determined, as summarized in Table 4-2.[226] The n value is related to recombination mechanism in solar cells, when n is close to 1, the direct recombination (band-to-band) dominates, otherwise indirect recombination mechanisms such as interfacial recombination and trap-assisted recombination (n = 2) dominate.[67] Our results show the changes in the n value of the five types of devices correspond to the changes in density of deep defects of $Zn_{1-x}Mg_xO$ with increasing Mg doping content. The decrease in the ideality factor n from 1.73 (x=0) to 1.35 (x=0.10) along with the increase in the Mg doping content in ZnO indicates that the relative contribution of indirect recombination (the back-transfer recombination of the injected electrons trapped by the deep defects of $Zn_{1-x}Mg_xO$) is reduced under the open-circuit conditions due to the removal of the $Zn_{1-x}Mg_xO$ deep trap sites. When the content of Mg is more than 10%, with the increase of deep level defects in $Zn_{1-x}Mg_xO$, the ideal diode factors increases rapidly and are larger than that of undoped devices. Although $Zn_{1-x}Mg_xO$ and PbS QDs have formed spike structure at this time, this does not have a beneficial effect on the indirect recombination of charges. In addition, Neil C. Greenham group has previously reported that reducing the ZnO carrier concentration by nitrogen doping can prevent interfacial recombination in CQDSCs,[184] however, our results show that the interfacial recombination is not suppressed despite the much lower carrier concentration of Mg-doped device than that of undoped devices. These results indicate that in un-illuminated conditions, indirect recombination of charges in the PbS QDHSCs strongly depends on the deep level defect concentration of $Zn_{1-x}Mg_xO$. In additional, the J_0 values displayed a similar tendency

with the 10% Mg doping device, showing the smallest J_0 value and the lowest charge recombination.

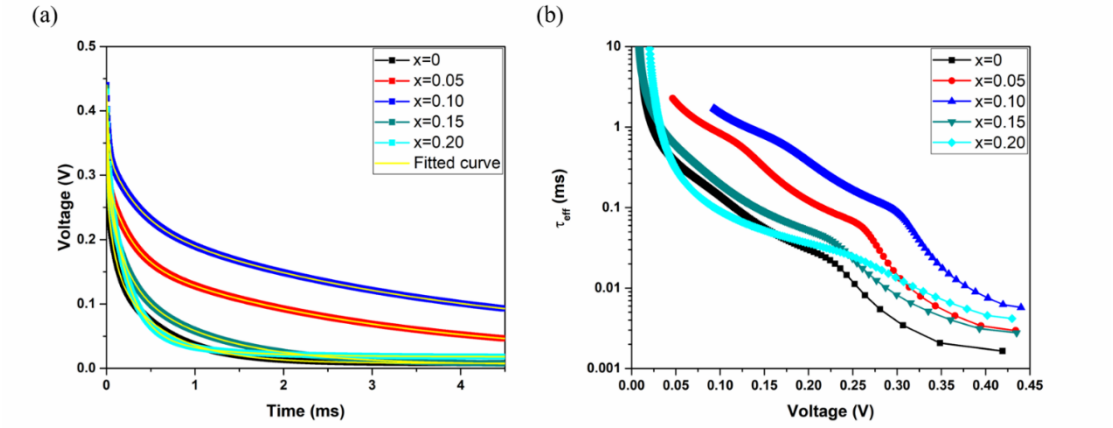

Figure 4-15. (a) Open-circuit photovoltage decay curves for $Zn_{1-x}Mg_xO$/PbS QDHSCs, showing three decay processes. (b) The effective carrier lifetimes calculated from the voltage decay curves for $Zn_{1-x}Mg_xO$/PbS QDHSCs.

Table 4-3. Time constants and weight obtained by fitting the open-circuit photovoltage decay curves of the PbS QDHSCs with a three-exponential function as shown in the table.

Sample	$V_{oc} = A_1e^{-t/\tau_1} + A_2e^{-t/\tau_2} + A_3e^{-t/\tau_3}$					
	A_1 ($A_1/(A_1+A_2+A_3)$)	τ_1 (ms)	A_2 ($A_2/(A_1+A_2+A_3)$)	τ_2 (ms)	A_3 ($A_3/(A_1+A_2+A_3)$)	τ_3 (ms)
x=0	0.440 (47.5%)	0.023±0.0006	0.426 (46.0%)	0.285±0.004	0.060 (6.5%)	2.275±0.004
x=0.05	0.323 (32.4%)	0.015±0.001	0.294 (29.5%)	0.408±0.001	0.381 (38.1%)	3.46±0.01
x=0.10	0.243 (24.3%)	0.025±0.0005	0.259 (26.0%)	0.411±0.003	0.495 (49.7%)	5.17±0.03
x=0.15	0.381 (38.4%)	0.019±0.0005	0.366 (36.9%)	0.273±0.005	0.245 (24.7%)	1.438±0.006
x=0.20	0.269 (27.1%)	0.023±0.001	0.658 (66.2%)	0.256±0.001	0.067 (6.7%)	8.166 ±0.005

In order to analyze in detail, the changes in the recombination mechanism in $Zn_{1-x}Mg_xO$/PbS QDHSCs with increasing Mg content, transient photovoltage (TPV) decay analysis is performed. When a PbS QDHSC is illuminated by a laser pulse at the open-circuit condition, open-circuit photovoltage is generated across the full device. When the incident laser is switched off, all photogenerated carriers will recombine and thus leading to the decay of photovoltage.[67-68, 82, 227] Figure 4-15 (a) shows the TPV decay curves of the solar cells with increasing Mg doping content in ZnO. All decay curves could be fitted by a three-exponential-function equation and the corresponding

parameters are summarized in Table 4-3. The three-component fitting means there are at least three recombination processes in this case,[67] similar to our previously reported results.[67-68, 82, 227] First, the ultrafast process (< 0.1 ms, constant τ_1 in Table 4.3, in the high V_{oc} regime) can be related to the inherent trapping-assisted recombination in PbS and the $Zn_{1-x}Mg_xO$ films. In Table 4-3, the weight of A_1 decreases and the decay time constant τ_1 increases from the x=0 device to the x=0.1 device. This shift reflects the reduction of the $Zn_{1-x}Mg_xO$ film trap sites density and thus reduced radiation recombination caused by deep level defects of $Zn_{1-x}Mg_xO$. For the second process (in the low V_{oc} regime), its related constant τ_2 value is more than 0.2 ms and this process could be related to interfacial recombination at the $Zn_{1-x}Mg_xO$ /PbS interfaces. Table 4-3 shows that the trends of the value of A_2 and decay time constant τ_2 are in good agreement with the trend of the intensity of deep level defect (Figure 4-9 (b)) in $Zn_{1-x}Mg_xO$ with increasing Mg doping. This indicates that reduction in the $Zn_{1-x}Mg_xO$ deep level defect density can reduce the chance of interfacial recombination between the trapped electrons in the $Zn_{1-x}Mg_xO$ layers and the holes in the valence band (or intragap states near the VB) of PbS QDs. Through the third decay process V_{oc} disappears completely, this process represents direct recombination between electrons in the conduction band of $Zn_{1-x}Mg_xO$ and holes in the valance band of PbS layers. The weight of A_3 and the decay time constant τ_3 significantly increased in the case of $Zn_{0.9}Mg_{0.1}O$. We find that solar cells based on the $Zn_{0.8}Mg_{0.2}O$ have the longest recombination lifetime (τ_3) in process 3, probably because of the larger conduction band offset (0.2 eV) between the $Zn_{0.8}Mg_{0.2}O$ and PbS QDs which forms an energy barrier that slows the direct recombination of free electrons and holes. The effective carrier lifetimes (τ_{eff}) were determined from the TPV decay curves with defined equations (see details in the Chapter 3). As shown in Figure 4-15 (b), the dependence of effective carrier lifetime on photovoltage could also be divided into three sections, corresponding to the three photovoltage decay processes. Throughout the V_{oc} regime, the values of τ_{eff} in the $Zn_{0.9}Mg_{0.1}O$-based device were 2~3 times higher than those in the other devices, in the order of 10% > 5% > 0% > 15% > 20% in terms of Mg doping content, which can be understood through the above discussions. Although $Zn_{0.9}Mg_{0.1}O$-based cells show the longest recombination lifetime, we find that $Zn_{0.85}Mg_{0.15}O$-based solar cell has the largest V_{oc} boost with its V_{oc} decay is the fastest. This indicates that the recombination of photogenerated carriers in the device is related to both factors, i.e., deep level defects in $Zn_{1-x}Mg_xO$ and the formed CBO.

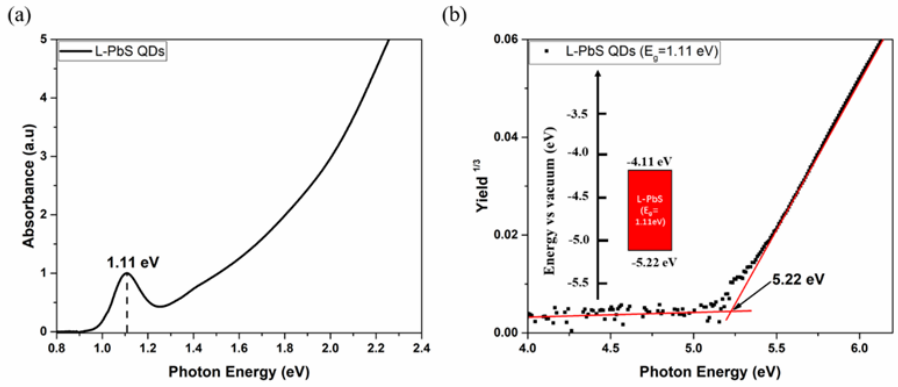

Figure 4-16. (a) Absorption spectra of the L-PbS QDs (E_g=1.11 eV) in octane. (b) PYS spectra of the L-PbS QD thin films. The inset shows the vacuum energy level diagram of the L-PbS QDs.

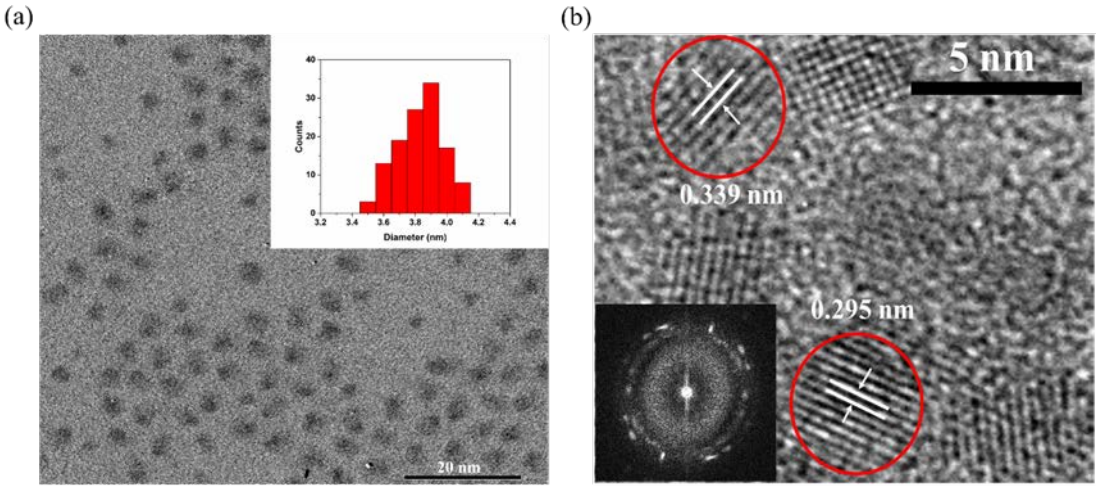

Figure 4-17. (a)TEM micrograph of L-PbS QDs. Inset displays size histogram. (b) High-resolution TEM image of L-PbS QDs; Inset displays SAED patterns of the corresponding L-PbS QDs.

For the above-studied PbS QDs (denoted as "M-PbS", *E*g=1.19eV), the effect of conduction band offset on suppressing interfacial recombination of charge carriers is not obvious, which we attribute to the relatively small value of the conduction band offset between $Zn_{1-x}Mg_xO$ and the QDs. So, large-sized PbS QDs (denoted as "L-PbS") were prepared to increase the value of conduction band offset between the $Zn_{1-x}Mg_xO$ and PbS QDs. Figure 4-16 (a) shows the first exciton absorption peak of L-PbS QDs was located at 1.11 eV. The valence band edge energy levels of the L-PbS QDs were confirmed to be -5.22 eV by PYS measurement as shown in Figure 4-16 (b). By combining the results of both bandgap and valence band edge levels, the conduction band edge levels were determined to be -4.11 eV (the inset of Figure 4-16 (b)). The TEM and HRTEM images shows that the average size of the L-PbS QDs is approximately 3.9 nm and the high crystallization of QDs (Figure 4-17). Photovoltaic parameters of the QDHSCs based on L-PbS are summarized in Figure 4-18. Figure 4-19 (a) shows

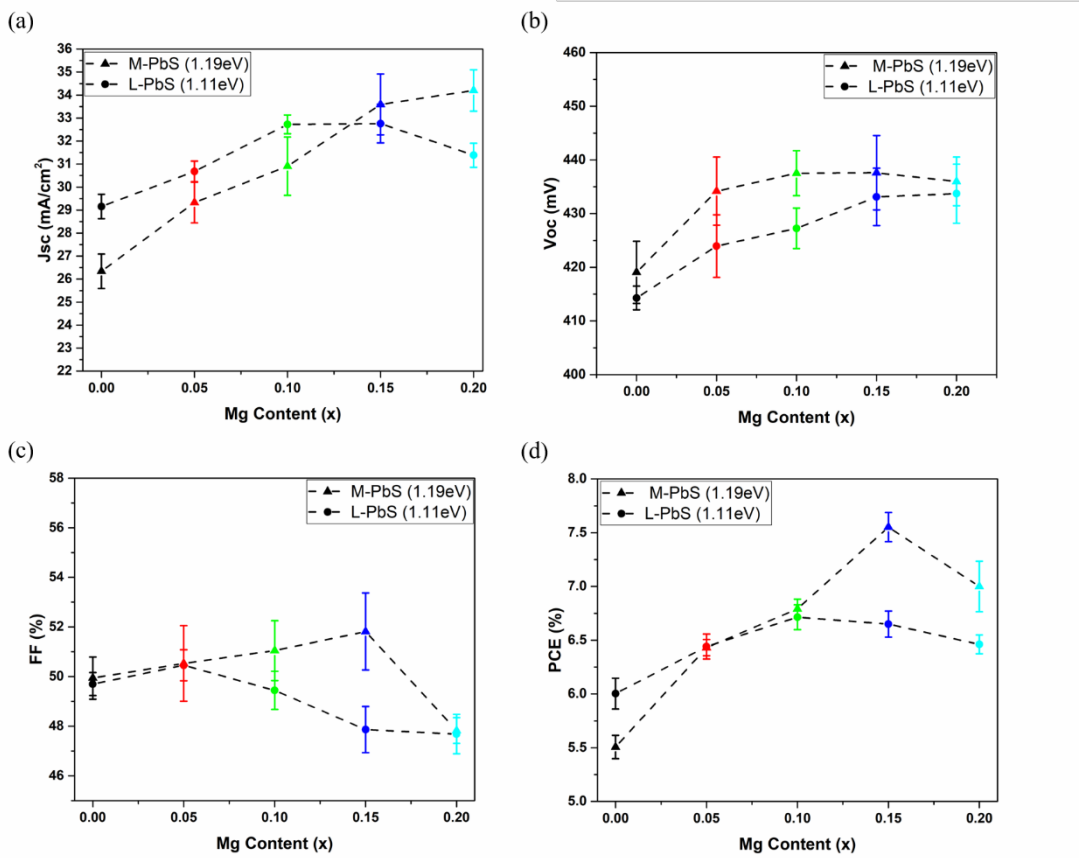

Figure 4-18 Statistics of the device performance using two sizes of PbS QDs and $Zn_{1-x}Mg_xO$ electron transporting layer (x=0, 0.05, 0.10, 0.15, 0.20): (a) J_{sc}, b) V_{oc}, (c) FF, and (d) PCE. The solid data points represent the average values, and the error bars stand for the standard deviations.

both *"cliff"* and *"spike"* structures of conduction band offset (CBO) in PbS QDHSCs. The CBO values between the L-PbS QDs and the $Zn_{1-x}Mg_xO$ were controlled from +0.10 eV to -0.25 eV by changing the Mg doping content in ZnO. In QDHSCs, V_{oc} loss strongly depend on charge recombination, which are mainly dominated by junction characteristics.[228] V_{oc} loss of all devices is shown in Figure 4-19 (b). The V_{oc} loss was defined as $E_g/q - V_{oc}$, where q is the elementary charge. Compared with the effect of $Zn_{1-x}Mg_xO$, the influence of the size changing of QDs on the V_{oc} loss is more obvious. With the increase in QD size, we can see PL lifetime of the QDs has increased from 276 ns to 985 ns, as shown in Figure 4-20. The increase in PL lifetime is believed to be mainly due to the reduction of surface defects in PbS QDs. In addition, compared with the smaller PbS QDs, defect states are mainly distributed near the CBM in large-sized QDs.[229] So, devices based on larger QDs showed smaller values of V_{oc} loss. We found that the V_{oc} loss of L-PbS QDs-based devices decreases with increasing of deep defects in $Zn_{1-x}Mg_xO$ when Mg doping content is more than 10%. We consider that this can be due to the fact that the positive effect of larger value of CBO_{spike} on carrier recombination is greater than the negative effect of the deep defects of

$Zn_{1-x}Mg_xO$. We have also measured the effective carrier lifetimes (τ_{eff}) of L-PbS-based devices by the TPV decay as shown in Figure 4-19 (c). As expected, for L-PbS QD-based devices, their variations in carrier lifetime in the high-voltage region are in line with the change of deep defect density in $Zn_{1-x}Mg_xO$ (x = 0~0.2) film. Note that for the L-PbS QDHSCs, the τ_{eff} of both devices based on x=0.15 and 0.20 are longer than that of the undoped device in low voltage regime, which is different from that observed in M-PbS QDHSCs. According to previous analysis, the medium voltage regime is related to interfacial recombination, but the defect density of $Zn_{1-x}Mg_xO$ (x=0.15 and 0.20) is higher than that of ZnO (see Figure 4-15 (a)). Therefore, we confirm that the reduction of charge recombination is related to the increase of CBO_{spike} value. In the medium-voltage regime, the value of τ_{eff} increases with increasing value of CBO_{spike}. But from the photovoltaic performance of those QDHSCs based on L-PbS QDs (Figure 4-18), we found that the electron injection is impeded when the CBO_{spike} value exceeds 0.2 eV, which also results in reduced J_{sc} and *FF*.

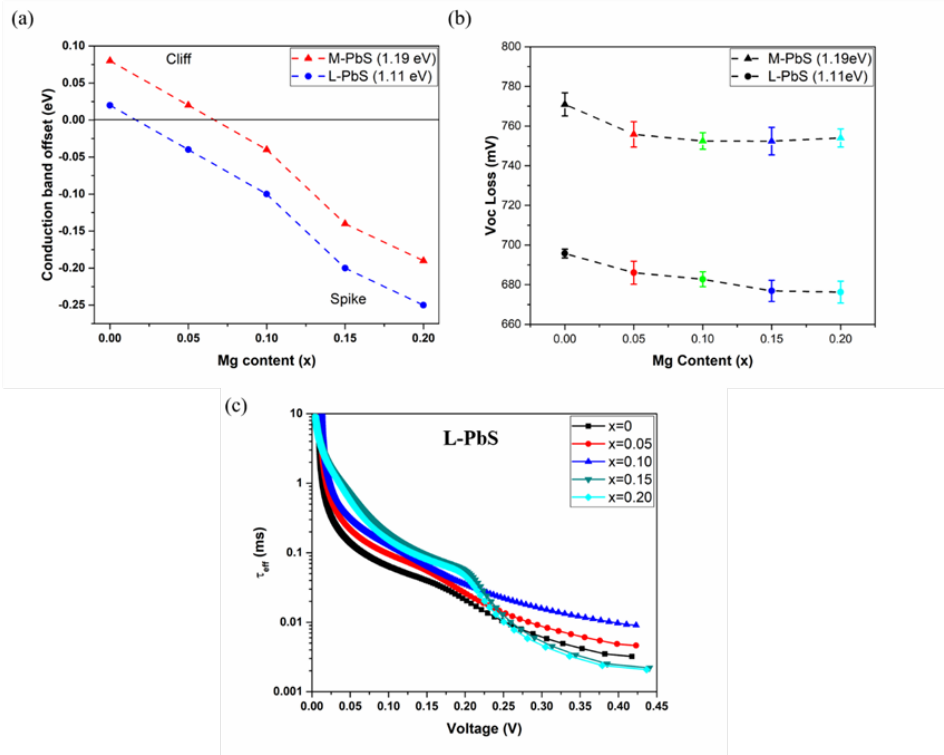

Figure 4-19. (a) The conduction band offset values for both PbS QDs (i.e., M-PbS:1.19 eV and L-PbS:1.11 eV) with $Zn_{1-x}Mg_xO$, respectively. (b)The V_{oc} loss of both M-PbS QDHSCs and L-QDHSCs, respectively. (c) The effective carrier lifetimes calculated from the voltage decay curves for $Zn_{1-x}Mg_xO$/L-PbS QDHSCs.

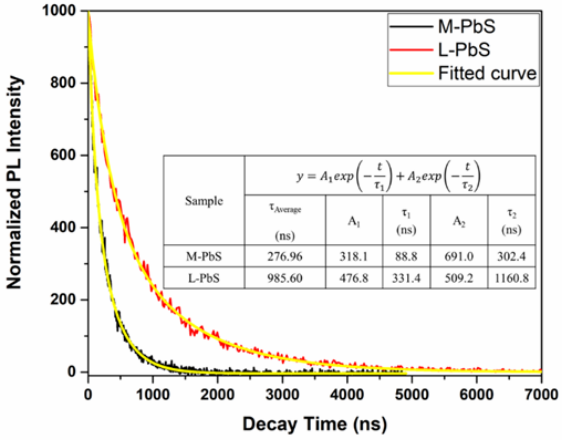

Sample	$y = A_1 exp\left(-\frac{t}{\tau_1}\right) + A_2 exp\left(-\frac{t}{\tau_2}\right)$				
	$\tau_{Average}$ (ns)	A_1	τ_1 (ns)	A_2	τ_2 (ns)
M-PbS	276.96	318.1	88.8	691.0	302.4
L-PbS	985.60	476.8	331.4	509.2	1160.8

Figure 4-20. PL decay curves of PbS QDs (oleic acid passivated) of both sizes at room temperature.

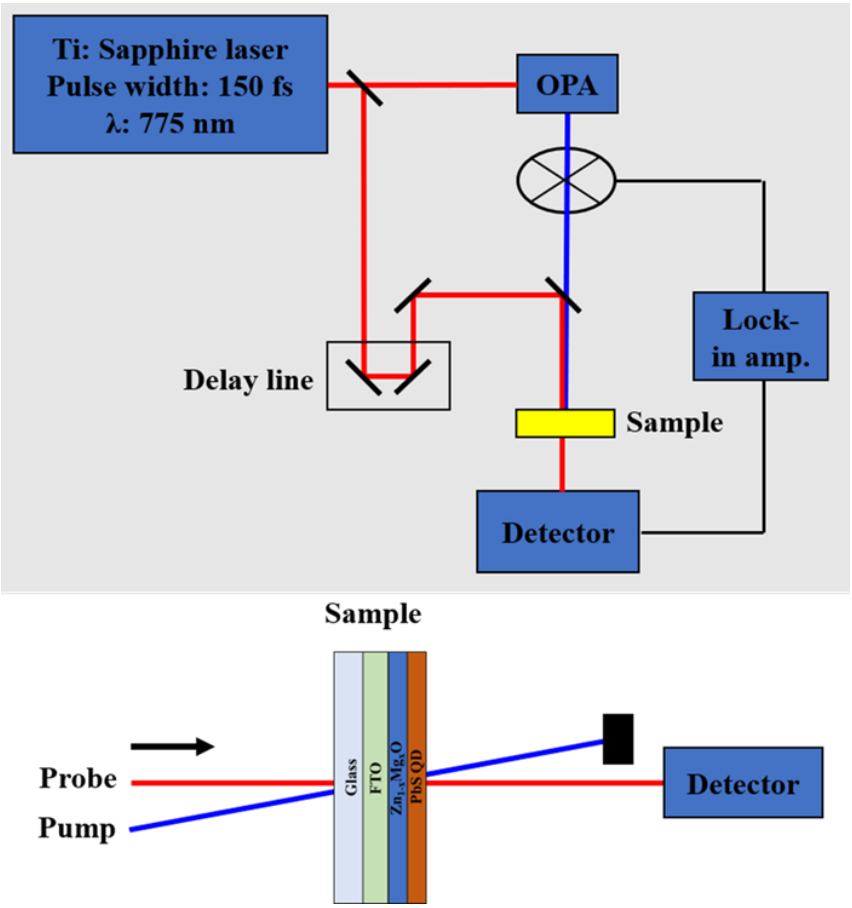

Figure 4-21. A schematic diagram of the TA setup, showing the concept of the pump-probe experiments. The pump and probe pulse overlap in the heterojunctions, and the absorbance change in the probe pulse is detected at different time delays.

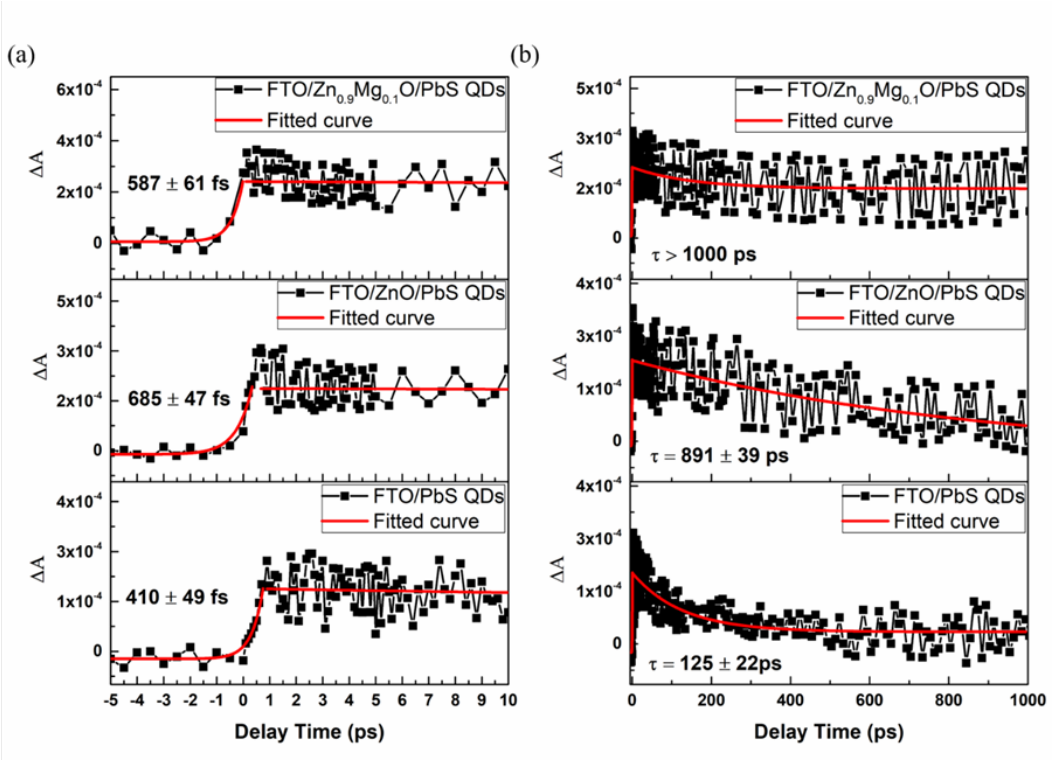

Figure 4-22. TA responses of the different samples of FTO/M-PbS QDs, FTO/ZnO/M-PbS QDs, and $Zn_{1-x}Mg_xO$/FTO/M-PbS QDs, measured with a pump light wavelength of 470 nm and probe wavelength of 1500 nm with a pump light intensity of 15 μJ/cm^2. (a) Injection process of the photogenerated electrons from PbS QDs into the FTO electrode (red lines are fitted lines); (b) Decay process of the injected electrons in FTO electrode (red lines are fitted lines).

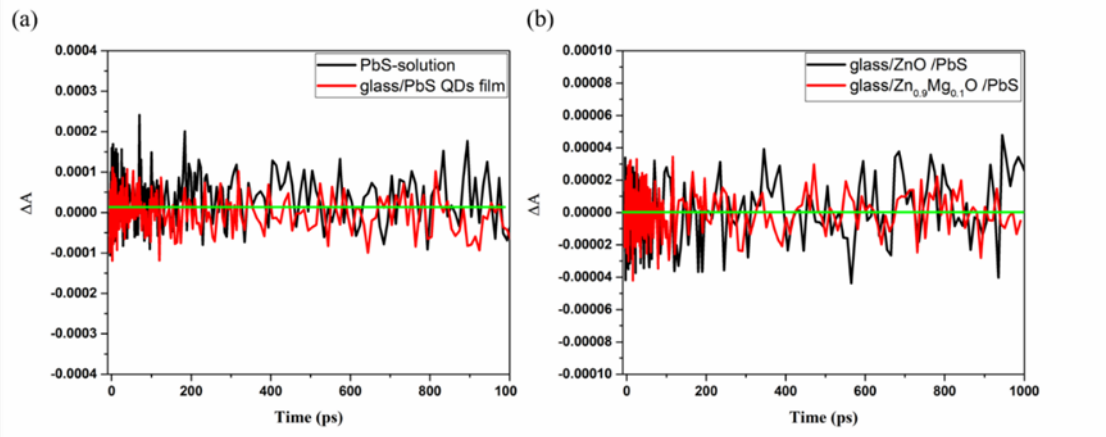

Figure 4-23. TA responses of the (a) free PbS QDs and PbS QDs layer on glass substrate, and (b) Glass/ZnO/ PbS QDs and Glass/$Zn_{1-x}Mg_xO$/ PbS QDs measured with a pump light wavelength of 470 nm and probe light wavelengths of 1500 nm and pump light intensity:15 μJ/cm^2.

To investigate the role of Mg doping on the electron injection from M-PbS QDs to $Zn_{1-x}Mg_xO$ and FTO electrode at the heterojunction, we performed femtosecond (fs)-TA spectroscopy with broadband capability (470~1600 nm)

and 150 fs temporal resolution, as schematically shown in Figure 4-21. Because the free carrier absorption in transparent conductive glass, e.g., FTO, ZnO, ITO, is mainly located in infrared range of 1400~4100 nm, we therefore focus on this range to investigate the dynamics of the injected electrons.[230] The dotted black line in Figure 4-22 shows TA kinetics of the PbS QDs layer on the FTO, ZnO/FTO and $Zn_{1-x}Mg_xO$/FTO (from bottom to up). The FTO/$Zn_{1-x}Mg_xO$/PbS QDs sample was excited with light wavelengths of 470 nm and probed with light wavelength range from 1400 to1600 nm, same as used in the case of PbS QD solution and PbS QD films deposited on glass and $Zn_{1-x}Mg_xO$ (without FTO). No TA signal could be observed in this wavelength range (1400-1600 nm) for both PbS QD solution and the PbS QD films on glass (as shown in Figure 4-23 (a)). In addition, no TA signal was observed in the $Zn_{1-x}Mg_xO$/PbS sample on the glass substrate (as shown in Figure 4-23 (b)). Therefore, we confirm that the TA response shown in Figure 4-22 is assigned to the absorption signal of electrons transferred into FTO electrode from the PbS QDs. The TA response of the FTO/$Zn_{1-x}Mg_xO$/PbS QD composite can be well fitted using the following single exponential $y(t) = A_0 e^{\frac{t}{\tau}} + y_0$ (for injection process) for the time scale up to 1 ps and $y(t) = A_0 e^{\frac{-t}{\tau}} + y_0$ (for recombination process) for the time scale longer than 1 ps, respectively.

Bottom part of Figure 4-22 (a) shows the injection dynamics for photogenerated electrons from PbS QDs to FTO, the time constant (410 ± 49 fs) is much faster than that from photoexcited PbS QDs into TiO_2 (<1 ns).[231] When introducing ZnO thin film (~30 nm) between the FTO and PbS QD layer, the electron transfer rate becomes slower. We found the electron injection from PbS QDs to FTO electrodes through the ZnO compact layer occurs on a time scale of a few hundred femtoseconds (here is 685 ± 47 fs), which is in good agreement with previous reports.[232] In addition, the electron transfer from the photoexcited PbS QDs to FTO through $Zn_{0.9}Mg_{0.1}O$ compact layer is faster (587 ± 61 fs) than that from photoexcited PbS QDs into FTO through ZnO compact layer. This result thus suggests that the transportion of the photogenerated electrons to the FTO electrode is through the shallow defect states in $Zn_{1-x}Mg_xO$ when the conduction band between $Zn_{1-x}Mg_xO$ and the QD forms a spike structure. As can be seen in Figure 4-22 (b), the FTO/PbS QD sample shows an ultrafast recombination time of 125 ± 22 ps, but when the ZnO film is introduced between the FTO and PbS QDs the recombination time is significantly increased (895 ± 31 ps). Therefore, we conclude that the ZnO layer serves as a hole-blocking layer to prevent recombination of the injected electrons in FTO with photogenerated holes in PbS QDs, as shown in Figure 4-1. But on the other hand, deep defects in ZnO can act as recombination centers for the photogenerated electrons and holes. When $Zn_{0.9}Mg_{0.1}O$ with fewer deep defects was introduced as a hole-blocking layer, no obvious recombination of carriers can be found up

to 1 ns, which means the recombination occurs much longer than the observable time scale in our experiments here.

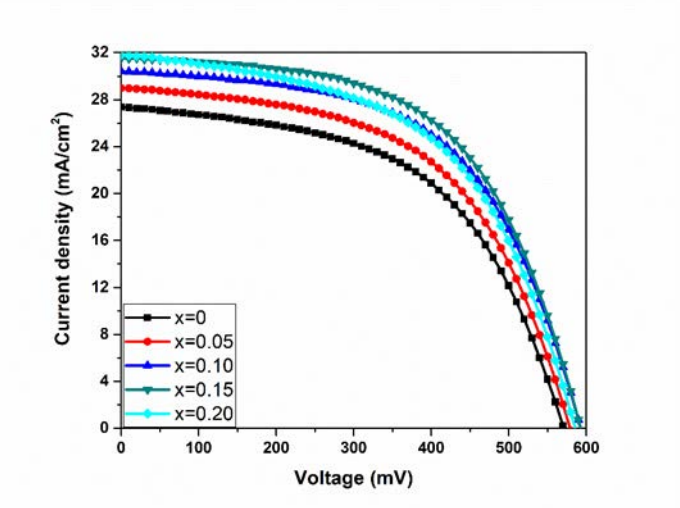

Figure 4-24. J-V curves of the best performing photovoltaic devices under AM 1.5G illumination. The structure of the solar cell device is FTO/$Zn_{1-x}Mg_xO$/M-PbS/EDT-PbS /Au (x=0,0.05,0.10,0.15,0.20).

Table 4-4. Statistical Averages of the Photovoltaic Performance Parameters of 12 Devices for Each Type of the QDHSCs[a].

Sample	J_{sc} (mA/cm^2)	V_{oc} (mV)	FF	PCE (%)
x=0	26.58±0.89 (27.37)	578.2±4.4 (571)	0.529±0.012 (0.534)	8.11±0.27 (8.35)
x=0.05	28.86±1.41 (28.98)	584.4±7.9 (580)	0.535±0.009 (0.541)	8.89±0.17 (9.08)
x=0.10	30.35±1.48 (30.41)	591.6±10.8 (590)	0.549±0.013 (0.563)	9.96±0.11 (10.10)
x=0.15	31.84±0.36 (31.52)	590.8±5.2 (590)	0.560±0.009 (0.570)	10.49±0.10 (10.60)
x=0.20	32.04±0.76 (31.81)	585.5±3.7 (585)	0.535±0.012 (0.532)	9.77±0.14 (9.92)

[a] Results for the device with highest PCE are shown in parentheses.

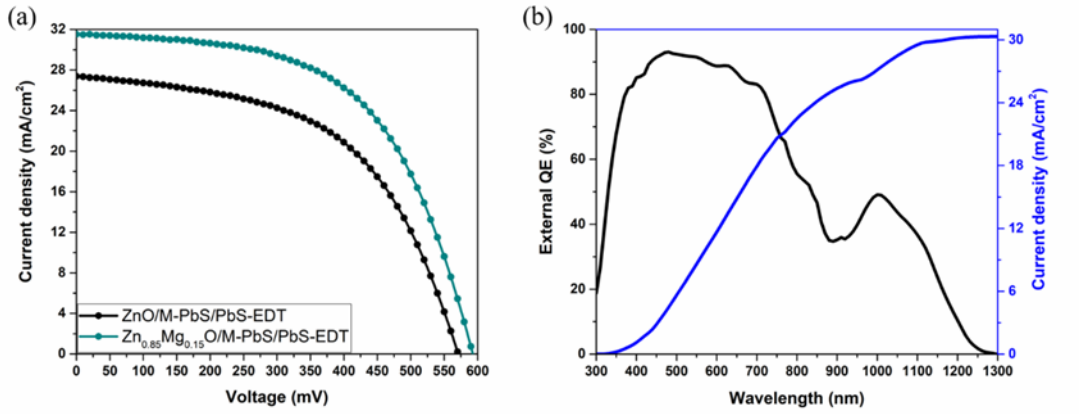

Figure 4-25. (a) *J-V* curves and (b) the external quantum efficiency of the best performing photovoltaic devices under AM 1.5G illumination. The structure of the solar cell device is FTO/$Zn_{0.85}Mg_{0.15}O$ (~30 nm)/M-PbS/EDT-PbS /Au.

As shown in Figure 4-8 (a), the solar cells based on $Zn_{0.85}Mg_{0.15}O$ has the best power conversion efficiency. According to our previous report,[67] interfacial recombination at the PbS/Au interface is also very important for the performance of QDHSCs. At present, high-efficiency PbS QDHSCs typically employ Bawendi's structure, i.e., an EDT passivated QD layer is used as efficient electron blocking layer (or hole transporting layer). Here we then followed Bawendi's recipe to introduce the EDT-treated PbS QD layer to act as HTL to prevent interfacial recombination at the PbS/Au interface. We prepared five batch devices with structure of FTO/$Zn_{1-x}Mg_xO$/M-PbS (~260 nm)/PbS-EDT (~40 nm)/Au, the J-V characteristics are shown in Figure 4.24 and Table 4-4. We found that solar cells based on $Zn_{0.85}Mg_{0.15}O$ also show the best power conversion efficiency at the presence of HTL. By combining all these advantages, the $Zn_{0.85}Mg_{0.15}O$/M-PbS QD-based solar cells achieved a high PCE of 10.6 % with J_{sc} of 31.5 mA/cm^{-2} and V_{oc} of 590 mV, as shown in Figure 4-25 (a) and parentheses of Table 4-4, which is significantly improved than the undoped device (8.3%). The External QE spectra were integrated with the AM1.5 G solar spectrum for the best QDHSCs values of J_{sc} was calculated as 30.3 mA/cm^2, respectively, and are in good accordance with the measured J−V result (31.52 mA/cm^2).

4.4 Conclusions

In summary, for the first time, we systematically demonstrated that in QDHSCs, the formed spike structure between the ETL and QDs can inhibit charge recombination and shallow defect states in the ETL can transport photoexcited electrons from the QDs to the electron-collecting electrode. More importantly, we also revealed that this transport process occurs on the ultrafast time scale of a few hundred fs. Considering the above results, the optimized

$Zn_{0.85}Mg_{0.15}O$/M-PbS QD-based device exhibited a maximum PCE of 10.6% (J_{sc} increased from 27.3 to 31.5 mA/cm^2 and V_{oc} increased from 533 to 555 mV). Our study demonstrates the importance of optimizing the energy level alignment and physical properties of the ETL layer towards the overall performance.

Chapter 5: Effect of the Conduction Band Offset on Interfacial Recombination Behavior of the Planar Perovskite Solar Cells

5.1 Introduction

Over the past decade, solar cells based on the organic-inorganic perovskite materials have been studied as a promising technique to create new breakthroughs in the energy field.[123, 233-234] Noteworthy, perovskite materials are attracting massive attention due to their extraordinary photonic and electronic properties, e.g., direct band gaps, high absorption coefficient, long photoexcited carrier lifetimes and diffusion lengths, and low Urbach energy.[235-239] For the perovskite solar cells (PSCs), state-of-the-art power conversion efficiencies (PCEs) have been raised to 22.7% due to a revolutionary breakthrough in the materials and architecture engineering.[240] These breakthroughs are based on low-cost technology, thus promoting a bright future for PSCs technology to be a viable alternative for the traditional photovoltaic materials.

The conventional structure of the PSCs is transparent conductive oxide (TCO)/electron selective layer (ESL)/perovskite absorber layer/hole transport layer (HTL)/metal back contact. Of course, much efforts have been focused on the improvement of performance and stability of the perovskite materials, e.g., fabrication method, composition control, and encapsulation, etc.[126, 241-244] Both perovskite compositional and film fabrication control have contributed a lot to the development of the PSCs. As well, optimizing the interfaces in the PSCs is also essential for improving the photovoltaic performance. As for the planar PSCs, the interface of the ESL/perovskite absorber layer is extremely vital to the overall performance of the devices, since the carrier injection and recombination are directly related to the ESL.[148, 245-248] Accordingly, interface engineering and control at the ESL/perovskite interface is necessary for achieving high-efficiency planar PSCs.[249-250] The effect of the ESL/perovskite interface on the device is mainly described in the following three aspects: energy level alignment, perovskite film morphology, and device stability. The property of the ESL plays key role in optimizing the performance of the interface. So far, surface modification and low-content doping of metal oxides have been considered as a way of improving the properties of ESLs. For instance, metal ions (e.g., Mg, Li, Y, Nb, etc.)-doped ZnO and TiO_2 have been utilized as efficient ESLs to enhance the efficiency to over 19%, owing to the improved performance of carrier extraction and/or injection.[148, 251-254] Taking advantage of highly conductive polymer materials (e.g., self-assembled monolayer, PCBM)[150, 255-256] and carbon materials (e.g., carbon dots, graphene, and carbon nanotubes)[257-259] to modify ESL has also been proved to be an

efficient method for enhancing both charge extraction and electron mobility, and therefore device performance. Besides the conductivity and surface trap states of ESL, the energy level alignment at the ESL/perovskite interface also greatly affect the interfacial recombination and carrier injection.

In fact, the energy level alignment at the interface can be quantitatively described by the conduction band offset (CBO), i.e., the difference between the conduction band minimum (CBM) energy levels of the ESL (or electron transporting layer) and the absorber layer. Up to now, the effects of the CBO on carrier recombination at the interface have been widely studied in other types of planar heterojunction solar cells, such as Cu(In,Ga)Se_2, silicon solar cells and PbS quantum dot solar cell.[203, 215-216, 260-263] Also, the effect of the CBO on carrier recombination has been theoretically studied in perovskite solar cells.[264] However, to our best knowledge, it is scarce to experimentally investigate the influence of CBO between the ESL and the absorber layers on device performance of the PSCs. In this study, to understand the operation mechanism and optimum design of the device, we explored the effect of the CBO at the ESL/perovskite interface on the solar cell performance of the PSCs. Magnesium doped zinc oxide ($Zn_{1-x}Mg_xO$ (ZMO)) films with tunable bandgaps acting as the ESL were prepared by a low-temperature sol-gel method. The solution-processed ZMO films have good electron-transporting properties and tunable bandgaps, whose energy level is highly dependent on the content of Mg doping, thereby enabling us to tune the CBO value at the ESL/perovskite interface as well as the properties of the ZMO (e.g., defect density and carrier concentration). We find that an appropriate amount of Mg doping could lead to a favorable CBO, which reduces charge recombination at the ESL /perovskite interface and hence improves the device performance. Compared to the PSCs fabricated with the pure ZnO ESL (11.2%), $Zn_{0.90}Mg_{0.10}O$-based PSCs exhibited a great increase of over 35% in PCE with a champion efficiency of 15.6%. The mechanism for this improved performance including the charge injection and charge recombination dynamics, has been investigated using fluorescence spectroscopy, Hall-effect measurement and ultrafast transient absorption (TA) spectroscopy.

5.2 Experiments

Materials.

Lead (II) iodide (Kanto,98%), 40%Methylamine Methanol Solution (Wako), Hydriodic Acid (57%, TCI), Spiro-OMeTAD [2,2',7,7'-tetrakis-(N,N-di-4-methoxyphenylamino)-9,9'-spirobifluorene,>99.0%] (Xi'an Polymer Light Technology), lithium salts (Aldrich, >99.0%), N,N-dimethylformamide (DMF, Aldrich, >99.9%) 1-octadecene (ODE, Aldrich, 90%), and isopropanol (Wako, >99.9%) zinc acetate dihydrate (Wako, 99.9%), magnesium acetate tetrahydrate (Wako, 99%), 2-aminoethanol (TCI, 99%), and 2-methoxyethanol (Wako, 99%) were used as purchased without further purification.

ZnO compact layer synthesis

Solution-processed ZnMgO thin films were fabricated on FTO glass by a modified sol-gel method according to previous reports.[62, 206] The FTO-glass substrate was ultrasonically washed sequentially in water, acetone and isopropanol for 30 minutes and then treated with ozone for 10 minutes. Using a fixed molar ratio of zinc acetate dihydrate and magnesium acetate tetrahydrate dissolved in a mixture of 2-methoxyethanol and 2-aminoethanol, $Zn_{1-x}Mg_xO$ was prepared under stirring overnight (x=0-0.20) The precursor solution, wherein the total amount of 2-aminoethanol to metal acetate is 1.0, the total metal acetate concentration is 0.3M. These transparent solutions were spin-coated on the top of the FTO-glasses, which were pretreated by oxygen plasma for 5 min. Then the films were pre-heated on a hot plate at 150 °C for 10 min, and further transferred into an oven for annealing at 290 °C for 30 min.

Synthesis of CH_3NH_3I.

Methylammonium iodide MAI ($MA=CH_3NH_3$) was prepared to according to reported.[265-266] 30ml of hydroiodic acid (57 wt% in water) was reacted with 27.8ml of methylamine (40 wt% in methanol) at 0℃ for 2 h. From the solution, a dark brown precipitate was recovered using a rotary evaporator at 60℃ for 2 h. The resulting precipitate was washed with diethyl ether several times until the colour of the precipitate changed to white, and then recrystallized from ethanol. The white precipitate was collected by filtration and dried under vacuum for 24 h before storage in a glove box filled with Ar.

Device fabrication

To fabricate ZMO/$MAPbI_3$ heterojunction solar cells, a 550 mg/mL precursor solution of PbI_2 in DMF (with 110 μL TBP in 1 mL PbI2 precursor solution) was then spin-coated on the top of ZnMgO compact layer at 4000 rpm for 30 s in the glove-box and dried at 70℃ for 10 min. After cooling to room temperature, the CH_3NH_3I 2-propanol solution (10 mg/mL) was dropped on the PbI_2 film and left for 60 seconds, then spin at 4000 rpm for 30 s followed by annealing at 70℃ for 20 min to give a desired crystallite formation. As hole-transporting material (HTM), a Spiro- OMeTAD solution [75 mg of Spiro-OMeTAD, 28.8 mL of TBP, and 17.5 mL of a lithium-bis-(trifluoromethanesulfonyl) imide (Li-TFSI) solution (520 mg Li-TFSI/1 mL acetonitrile) in 1 mL chlorobenzene] was spin-coated at 4000 rpm for 30 s on the $CH_3NH_3PbI_3$. Contacts consisting of ~100 nm of gold was deposited on the HTM layer through a mask to create four identical cells on each substrate by thermal evaporation. The contact sizes were 0.16 cm^2.

Characterization

Current−voltage characterization was measured with a Keithley 2400 source measuring under AM 1.5 G with solar simulator PEC-L10. The IPCEs were measured by monochromatic illumination (300 W xenon arc lamp through Nikon G250 monochromator). X-ray photoelectron spectroscopy (XPS) data were measured by a photoelectron spectrometer, S4 JPS-90MX (JEOL, Ltd., Japan). Scanning Electron

Microscope (SEM) was measured by a JEOL JSM-6340 F instrument (Japan). UV-vis absorption spectra were measured with a spectrophotometer (HITACHI, U-3900H, Japan). The photoelectron yield spectrum (PYS) was measured using a BIP-KV205 ionization energy measurement system (Model BIP-KV205, Bunkoukeiki Co, Ltd). Two kinds of TA setup were used to characterize the charge injection (a femtosecond TA technique: fs-TA)[267-268] and the charge recombination dynamics (a nanosecond TA technique: ns-TA)[269-270] in the samples. In the fs-TA setup, the laser source is a titanium/sapphire laser (CPA-2010, Clark-MXR Inc.) with a wavelength of 775 nm, a repetition rate of 1 kHz, and a pulse width of 150 fs. In this study, a perovskite material was excited using a pump with a wavelength of 470 nm. The pump light intensity is 15 $\mu J/cm^2$. With a time resolution of 100 fs, a 750 nm time-resolved TA spectrum was obtained. In the ns-TA setup, the pump light source was an OPO (Surelite II-10FP) output excited by a Nd:YAG nanosecond pulsed laser (Panther, Continuum, Electro-Optics Inc.). The pulse width is 5ns and the repetition rate is 0.5Hz. We use pulsed light with a wavelength of 470 nm as the pump light to excite the sample. The probe light comes from a fiber-coupled CW semiconductor laser. A probe wavelength of 1400 nm was used to study free carriers in the transparent conductive film (TCO). For all measurements, pump light and probe light were irradiated from the glass side, and TA measurements were performed in an N_2 atmosphere.

5.3 Results and Discussion

At forward bias state, i.e., at open circuit, the interfacial recombination mainly occurs through the pathway of back-transfer recombination in which the electrons that have been injected into the FTO electrode and the free holes in the $MAPbI_3$ film recombine through the deep level defect at the interface of ESL/$MAPbI_3$. In order to obtain better electron injection in PSCs, the conduction band minimum (CBM) of "electron acceptor" (i.e., ESL) is usually lower than that of perovskite, i.e., formed a "*cliff*" structure, the CBO value is negative (-). However, at the open-circuit, in the PSCs with the cliff structure, after the separation, electrons and holes accumulate near the interface which results in larger charge recombination through the interface defects, as shown in Figure 5-1 (a). If the energy level control is used, the CBM of the ESL is higher than that of perovskite, i.e., forms a "*spike*" structure, the CBO value is positive (+) (as shown in Figure 5-1 (b)), the presence of a notch at the interface leads to stronger band bending in the conduction and valence bands of the absorber and ESL which can prevent electrons and holes from approaching the interface, and then reduce the charge recombination at the interface. Without considering the effect on electron injection, theoretically, the larger the value of CBO_{spike}, the stronger the suppression of charge recombination and the smaller the open-circuit voltage (V_{oc}) deficit. In order to illuminate this effect, we constructed a $Zn_{1-x}Mg_xO$ (x=0, 0.05, 0.10, 0.15) /perovskites system with CBO value tunable by using the tunable bandgaps of Mg-doped ZnO act as ESLs in PSCs. Below we will discuss in detail the characteristics of the $Zn_{1-x}Mg_xO$ films and the PSCs with different x values.

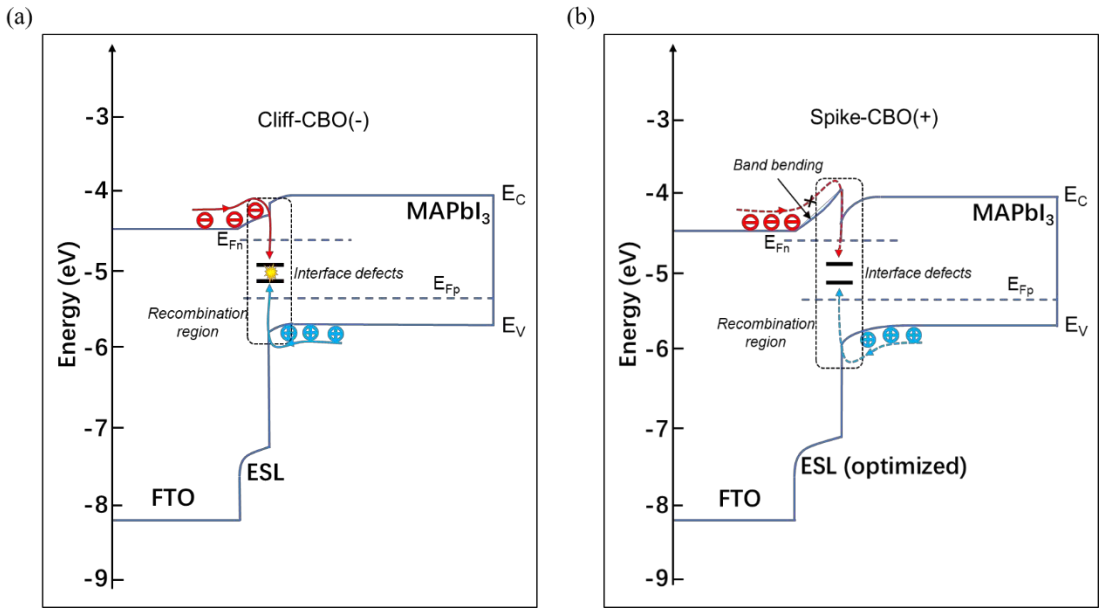

Figure 5-1. Schematic illustration of charge recombination at interface of ZMO/$MAPbI_3$ layers under open circuit, when the conduction band minimums (CBM) of the ZMO ESL layer are (a) below (i.e., the CBO value is minus and it is a "*Cliff*" structure) and (b) above (i.e., the CBO value is plus and it is a "*Spike*" structure) that of the $MAPbI_3$ absorber layer.

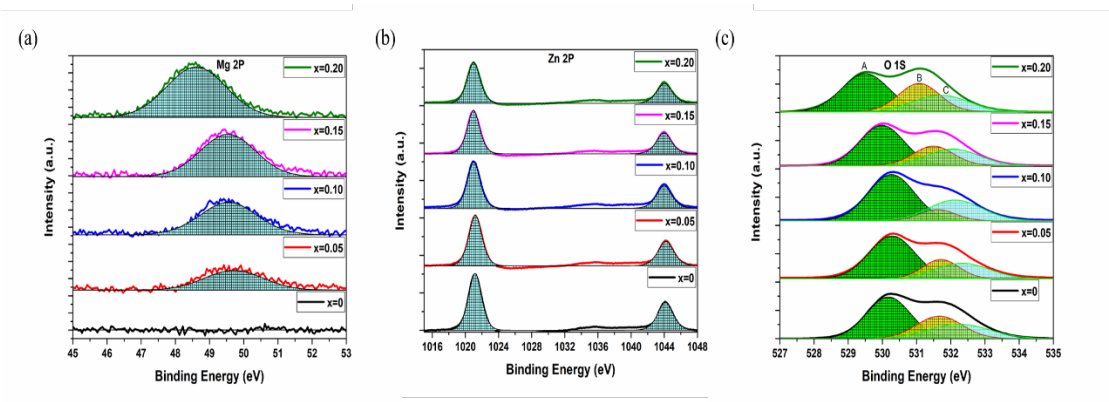

Figure 5-2. (a) High-resolution XPS spectra of $Zn_{1-x}Mg_xO$ (x=0, 0.05, 0.10, 0.15, 0.20) ESL derived from controlled precursor sol concentrations for a) Zn 2p, b) Mg 2p, and c) O 1s core levels, respectively.

Table 5-1. The XPS oxygen peaks were deconvoluted to three different near-Gaussian subpeaks with the peaks range is A, B, and C.

Sample	**A(A/(A+B+C))**	**B(B/(A+B+C))**	**C(C/(A+B+C))**
x=0	4797.8 (48.5%)	2539.8 (25.7%)	2551.9 (25.8%)
x=0.05	5123.6 (55.5%)	1893.2 (20.5%)	2214.0 (24%)
x=0.10	5664.2 (58.9%)	1640.7 (17.1%)	2306.6 (24%)
x=0.15	4763.9 (51.5%)	2299.1 (24.6%)	2274.0 (23.9%)
x=0.20	4846.4 (45.9%)	3033.3 (28.7%)	2687.7 (25.4%)

In the **Chapter 4** we have demonstrated that the successful incorporation of different compositions of Mg into ZnO films by the sol-gel method as shown by the XPS spectra of Figure 5-2.[263] Here, to investigate the incorporation of Mg atom into the ZnO host lattice structure, we have explored the deconvoluted Gaussian subpeaks of O1s XPS spectra for ZnO and Mg-doped ESL films (Figure 5-2 (c)). Both the pristine ZnO and the Mg-doped ZnO films show a main peak (O 1S-A) and shoulder peaks (O 1S-B and-C) in the O 1S XPS spectra. The O 1S-A is attributed to O^{2-} ions in the stoichiometric wurtzite ZMO structure compound system (Zn-O or Mg-O). The O 1S-B is related with O^{x-} ions in the oxygen-deficient regions within the ZnO matrix and is connected to oxygen vacancies. This peak can be also related to the surface adsorbed group on the ZnO surface. O 1S-C is usually attributed to chemically adsorbed oxygen on the surface, dissociated oxygen or OH-groups.[271-273] The weight of the relevant subpeak area B/(A+B+C) (Table 5-1) represents the relative quantity of oxygen vacancies in ZMO thin films. We found that the weight of O 1S-B decreases first (x from 0 to 0.10) and then increases (x from 0.10 to 0.20) with increasing doping of Mg. This result indicates that appropriate amount of Mg doping in ZnO could reduce the oxygen vacancy concentration, which may reduce the carrier concentration of ZMO.[274] Therefore, the Mg dopant can serve to suppress the formation of oxygen vacancy. On the other hand, the weight of the C/(A+B+C) peak area (Table 5-1) of Mg-doped ZnO is a little smaller for x increasing up to 0.15 than the that of the ZnO, which may be associated with a reduction of hydroxyl groups in the ZMO ESLs due to Mg doping. Thereby, ZMO acting as ESL in PSCs can improve the thermal stability of devices, as has been demonstrated by other reports.[251]

We also characterized ZMO film morphology by AFM. Figure 5-3 (a) shows the AFM image of the ZMO surface on FTO substrate, which was compared to that of the ZMO surface on a glass substrate (Figure 5-3 (b)). On the glass substrate, all films

showed the smooth surface with average surface roughness estimated being ~2 nm. The estimated rough surface measurement of the FTO surface is about 44.8 nm. After the ZMO film deposition, the roughness remains at about 25 nm, but without cracks and voids, which we believe could help to decrease the photocurrent leakage at the ZMO/perovskite interface. The rough morphology also increases the contact area between the perovskite film and the ZMO, which is beneficial for light absorption and carrier extraction.

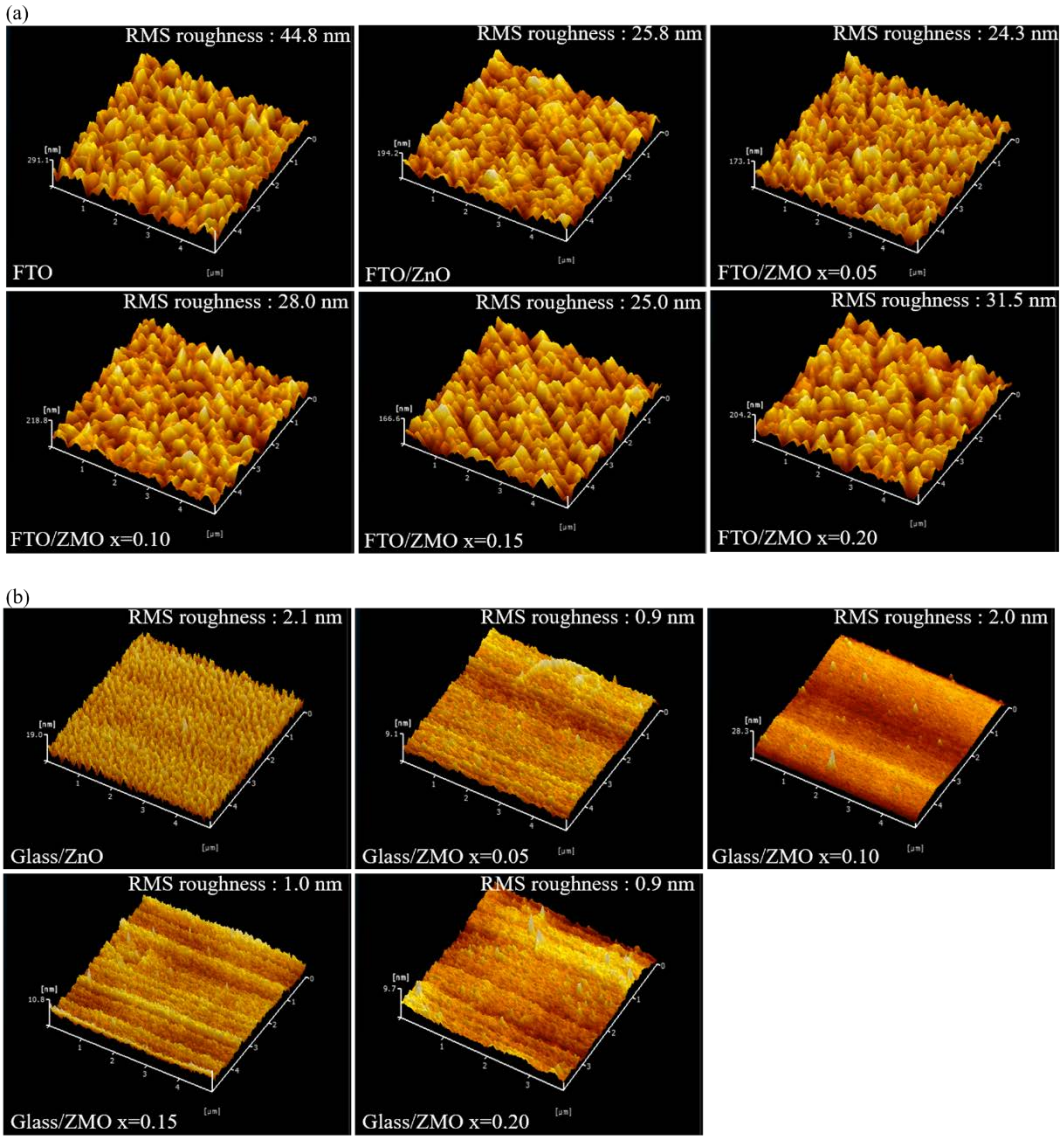

Figure 5-3. Top-view AFM image of FTO and $Zn_{1-x}Mg_xO$ (x=0, 0.05, 0.10, 0.15, 0.20) film on (a) FTO substrate and (b) Glass substrate.

The optical bandgaps (E_g) of the ZMO and $CH_3NH_3PbI_3$ ($MAPbI_3$) films were confirmed by the optical absorption spectra (Figure 5-4 (a)) and photoacoustic spectrum (Figure 5-4 (c)), respectively. The corresponding bandgap of the ZMO films continuously increases from 3.26 to 3.56 eV as x increases from 0 to 0.2 and the band gap of $MAPbI_3$ film is 1.55 eV, which are in good agreement with other reports.[197, 212,

[275] The photoelectron yield (PY) spectroscopy measurements were performed to investigate the relative position of the valence band maximum (VBM) of ZMO and $MAPbI_3$ films, as shown in Figure 5-4 (b) and (d), respectively. We found that the influence of Mg doping on the energy levels of VBM of the ZMO is little , i.e., the VBM of the ZMO remains almost the same value as that of the ZnO, which has also been found by other groups.[214] Based on the above results, the energy band diagram of the ZMO and the $MAPbI_3$ films were determined, as shown in Figure 5-5 (a). As expected, a continues upshift of the conduction band minimum (CBM) energy position of the ZMO films with increasing Mg doping content was observed. Importantly, we found that when the Mg doping exceeds 5%, the CBM of the ZMO becomes higher than that of the $MAPbI_3$, that is, the transition from the cliff structure to the spike structure. We have fabricated perovskite solar cells with the planar structure. The two-step deposition method was employed to prepare $MAPbI_3$ active layers on the ZMO-ESLs, and the entire device manufacturing process is performed at a low temperature (< 300°C). A cross-sectional scanning electron microscopy (SEM) image of the solar cell is shown in Figure 5-5 (b).

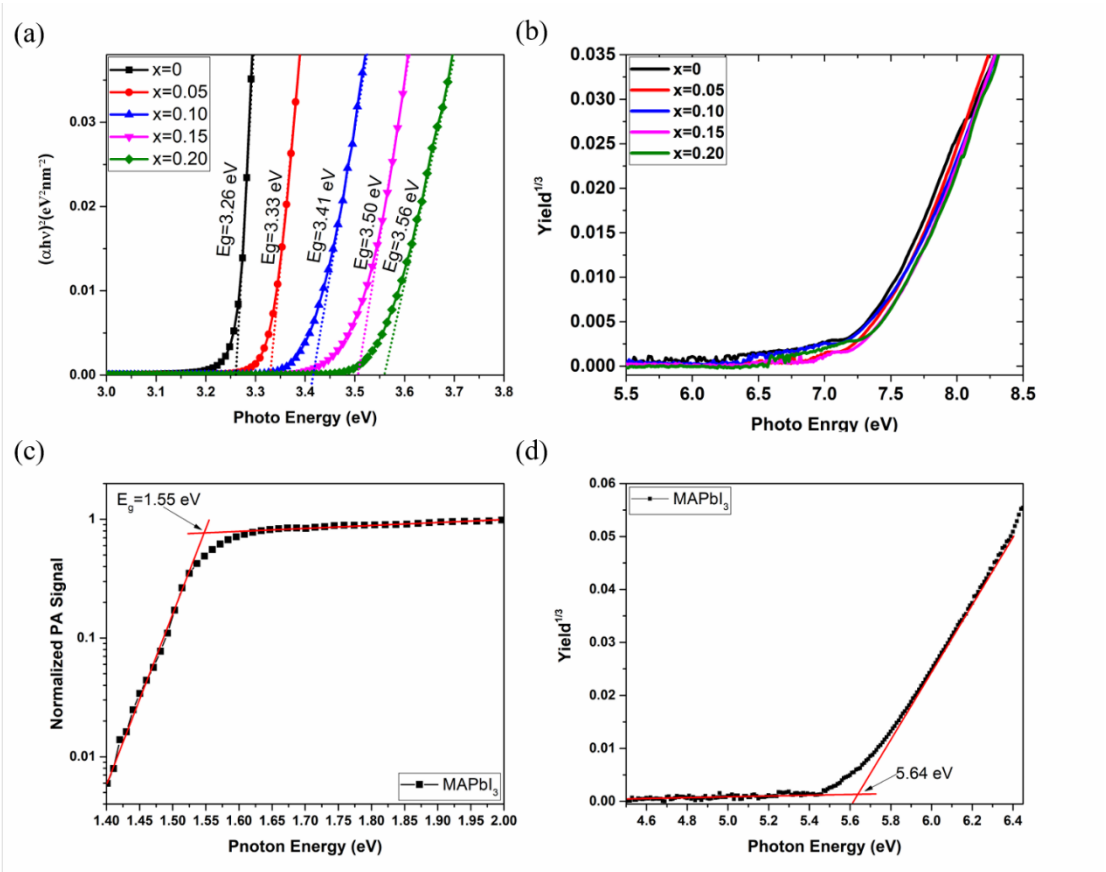

Figure 5-4. (a) An increase in the bandgap from the optical absorption and (b) photoelectron yield (PY) spectroscopy of $Zn_{1-x}Mg_xO$ films. (c) Photoacoustic (PA) spectra and (d) photoelectron yield (PY) spectroscopy of $MAPbI_3$ film.

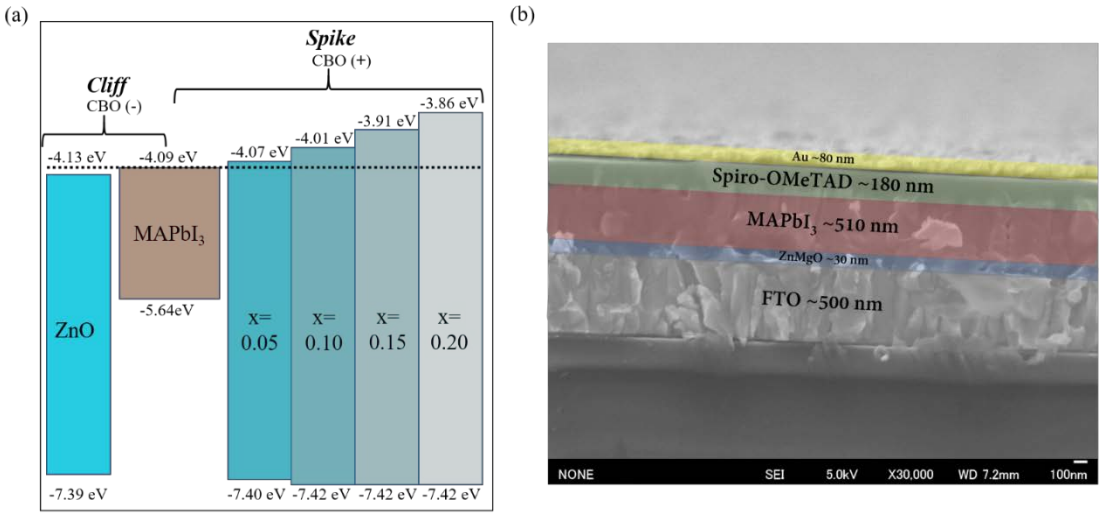

Figure 5-5. (a) Experimentally determined diagram of energy levels (relative to the vacuum level) of $Zn_{1-x}Mg_xO$ films (x=0-0.20) (the valence band maximum (VBM) and the conduction band minimum (CBM) are represented in eV). (b) Cross-sectional SEM image of a typical device of perovskite device structure.

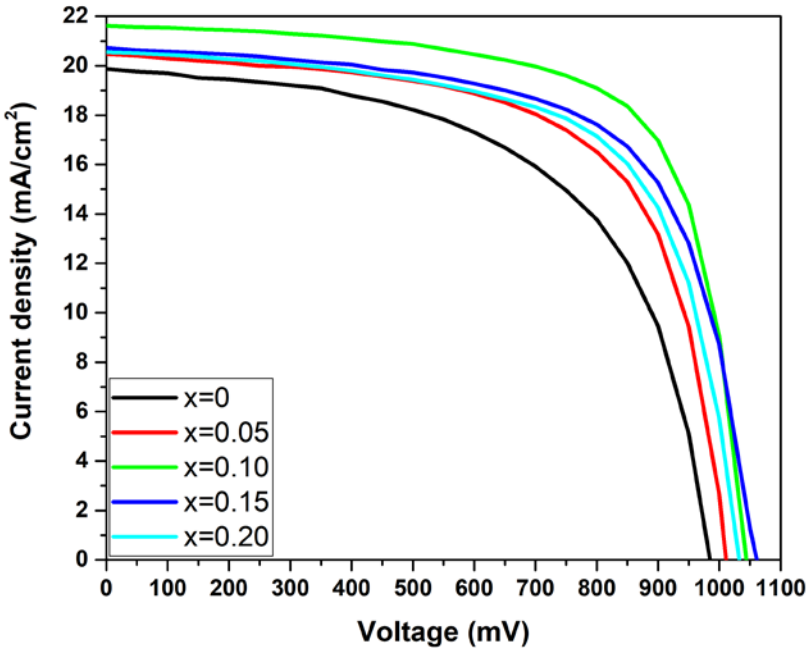

Figure 5-6. J-V characteristics of $MAPbI_3$ PSCs with $Zn_{1-x}Mg_xO$ (x=0~0.20) under simulated AM 1.5G illumination.

Table 5-2. Statistical averages of the photovoltaic performance parameters of 24 devices for each type of the PSCs [a].

Sample	J_{sc} (mA/cm^2)	V_{oc} (mV)	*FF* (%)	*PCE* (%)
x=0	18.41±0.66 (19.87)	945.36±18.94 (985)	61.81±2.57 (57.28)	10.75±0.40 (11.21)
x=0.05	19.76±0.85 (20.48)	974.67±17.72 (1011)	64.31±3.75 (63.83)	12.58±0.31 (13.21)
x=0.10	20.67±0.57 (21.62)	1034.52 ±22.54 (1044)	67.87±2.03 (69.14)	14.20±0.36 (15.60)
x=0.15	20.42±0.90 (20.73)	1044.8±7.35 (1061)	62.52±2.59 (64.7)	13.30±0.22 (14.23)
x=0.20	20.07±0.89 (20.55)	1027.84±18.43 (1050)	61.22±2.05 (63.6)	12.99±0.35 (13.72)

[a] Results for the device with highest PCE are shown in parentheses.

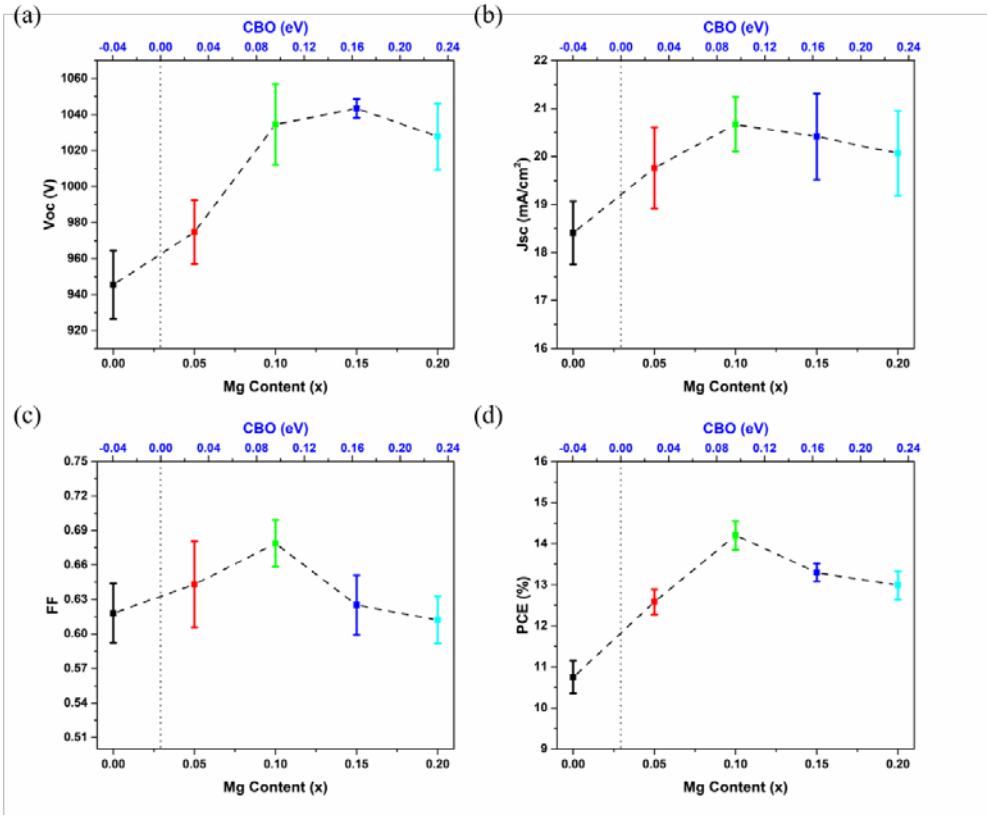

Figure 5-7. Statistics of photovoltaic performances of planar structure PSC devices (FTO/$Zn_{1-x}Mg_xO$/$MAPbI_3$/Au) as a function of x (x = 0, 0.05, 0.10, 0.15, 0.20) in the $Zn_{1-x}Mg_xO$ ESL and the CBO value between the ESL and $MAPbI_3$: (a)V_{oc}, b) J_{sc}, (c) *FF*, and (d) *PCE*. The solid data points represent the average values, and the error bars stand for the standard deviations.

We prepared five batch PSC devices using $Zn_{1-x}Mg_xO$ as the ESLs with x = 0, 0.05, 0.1, 0.15, 0.20 and 24 devices were constructed for each batch. The typical photocurrent density−voltage (*J*−*V*) characteristics of the five types of PSCs upon standard 100 mW/cm^2 AM1.5G illumination are shown in Figure 5-6. Figure 5-7 shows the device performance statistics with the average value and standard deviation for the PSCs as a function of CBO and the Mg doping content of ZMO/$MAPbI_3$ layers. The corresponding photovoltaic parameters and average values are summarized in Table 5-2. The CBOs were controlled in a range from –0.04 to 0.23 eV. As expected, a considerable enhancement in open-circuit voltage (V_{oc}) was observed for all Mg-doped samples when spike structure was formed between the ZMO and the $MAPbI_3$ (i.e., the positive CBO). However, when the positive CBO is more than 0.2 eV, the V_{oc} decreased. The short-circuit current density (J_{sc}) of the solar cells first increases with increasing of the CBO (from -0.04 to 0.1 eV) and then decreases when CBO is more than 0.1 eV. Photovoltaic devices employing $Zn_{0.9}Mg_{0.1}O$ ESL show the best performance with power conversion efficiency (*PCE*) of 15.6% with V_{oc} of 1044 mV, J_{sc} of 21.6 mA/cm^2 and *FF* of 69.1%, higher than that of the device based on the pristine ZnO which shows a *J*sc of 19.9 mA/cm^2, V_{oc} of 985 mV, *FF* of 57.3%, and *PCE* of 11.21%, respectively. From the *J*-*V* results we have found that the photovoltaic (PV) performance of the PSCs strongly depends on the doping content of Mg in the ZMO-ESLs.

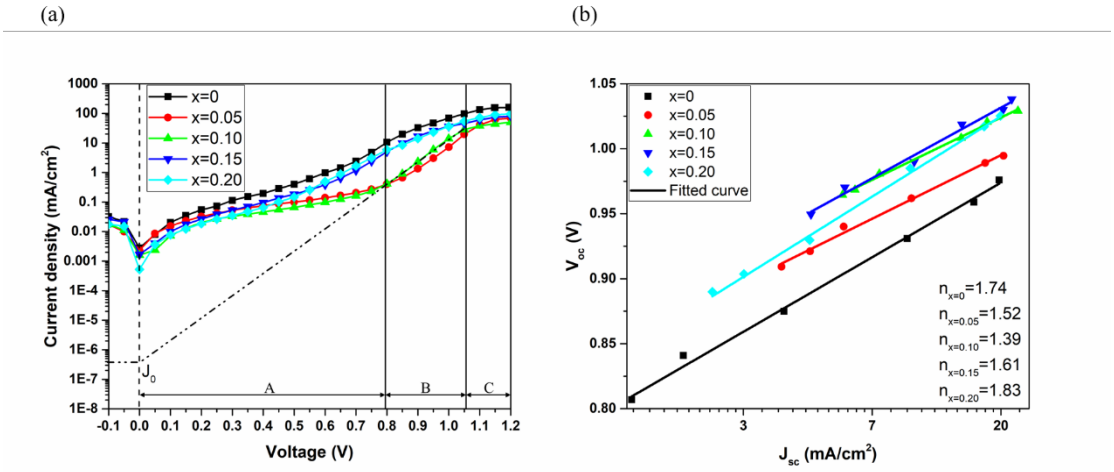

Figure 5-8. Device characteristics of the planar structure PSC devices (FTO/ZMO/$MAPbI_3$/Au). (a) *J*−*V* characteristics of devices in the dark. (b)V_{oc} plotted against the logarithm of J_{sc} in the devices.

To understand the difference in the photovoltaic performance when changing the Mg doping level in ZnO, we first investigated the carrier recombination mechanism in PSCs. The diode parameters in the solar cells, e.g., ideality factor *n* and reverse saturation current J_0, are important indicators of the dominant recombination mechanism. Figure 5-8 (a) shows the dark *J*-*V* curves of the PSC (FTO/ZMO/$MAPbI_3$/Au) devices, by fitting the dark *J*−*V* curves with the ideal diode equation (5-1):[263, 276]

$$J_{dark}(\mathrm{V}) = J_0\left[\exp\left(\frac{eV}{nkT}\right) - 1\right] \qquad (5\text{-}1)$$

where *k* is the Boltzmann constant, *T* is the temperature. *n* and J_0 with various Mg contents x were determined by fitting eq. (5-1) to the dark *J-V* curves in the region B of Figure 5-8 (a) and the results are summarized in Table 5-3. In addition, the dark J-V response in region A and C is affected by the shunt behavior, and the series resistance, respectively.[226] The *n* first decreased from 2.12 to 1.62 as the Mg content increased from 0 to 10% and then increased up to 2.43 with a further rise in the Mg content, and the J_0 shows the same trend of changes as the Mg content increased. When band-to-band recombination dominates, the *n* should be close to unity. If the Shockley-Read-Hall (SRH) recombination within the space-charge region (e.g., interfacial recombination or trap-assisted recombination) is active, the *n* should be more than 1.[228] The 10% Mg-doped device shows the smallest *n* value, indicating the best SRH recombination suppression, which could be attributed to suitable CBO and/or suitable physics properties (e.g., the lower defect density) of the ZMO ESL. Also, the J_0 values displayed a similar tendency with the 10% Mg-doped device showing the smallest J_0 value.

Table 5-3 Diode ideality factor (n) and reverse saturation current density (J_0) of the PSCs with $Zn_{1-x}Mg_xO$(x=0~0.20).

Sample	*n*	J_0
x=0	2.12	2.557E-4
x=0.05	1.71	1.256E-6
x=0.10	1.62	3.672E-7
x=0.15	1.84	3.891E-5
x=0.20	2.43	1.962E-4

Alternatively, *n* can be also obtained from the light intensity dependence of the J_{sc} and V_{oc} according to the equation (5-2):[228]

$$V_{oc} = \frac{nkT}{q} ln\left(\frac{J_{sc}}{J_0}\right) \qquad (5\text{-}2)$$

As shown in the Figure 5-8 (b), the variation tendency of ideality factor *n* determined from the light intensity dependence of the J_{sc} and V_{oc} according to the Eq. (5-2) agrees

with that of dark *J*−*V* characteristics. In solar cells, different ideality factors mean different recombination mechanisms at open circuit, our results suggest that the charge recombination in the PSCs under the dark or illumination strongly depends on the Mg-doping level in ZMO.

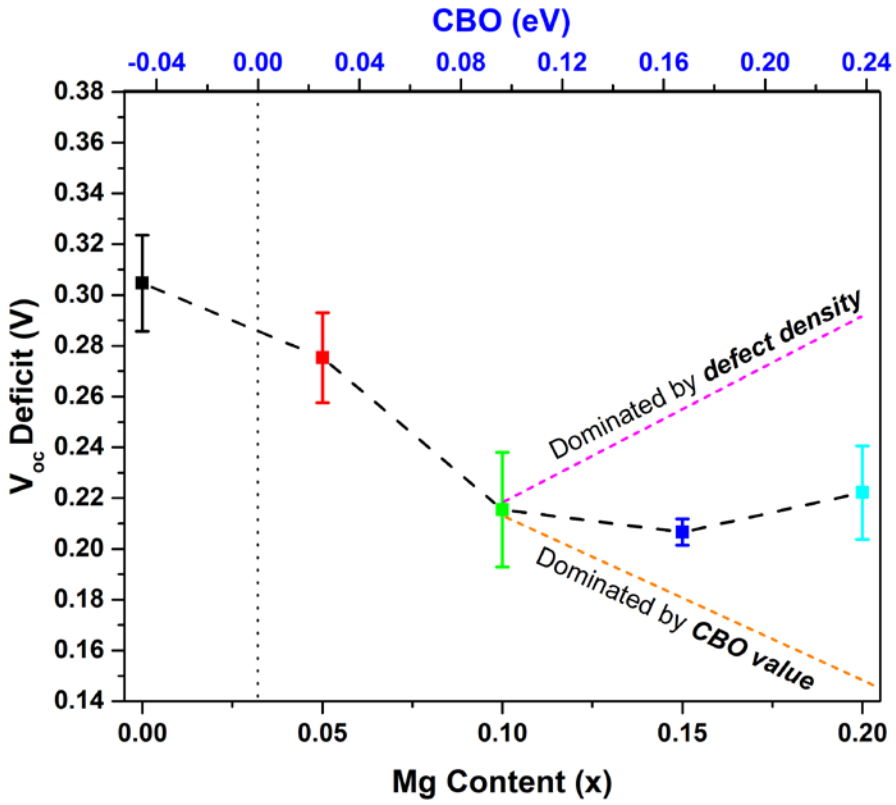

Figure 5-9. Experimental results and theoretical prediction of the V_{oc} deficit of ZMO-based PSCs. The V_{oc} deficit was defined as $E_g/q - V_{oc}$, where q is the elementary charge. Considering a thermodynamic limitation resulting in loss of ca. 0.3 V between E_g and V_{oc},[277] thus the 0.3 V thermodynamic loss has been subtracted from this, that is, V_{oc} deficit = $(E_g/q - 0.3\ V) - V_{oc}$.

However, above results show that when Mg doping-content exceeds 10%, the interfacial recombination does not continue to decrease as the CBO_{spike} value increases. In addition, when the Mg doping levels are high, it also shows that the V_{oc} deficit gradually becomes saturated rather than expected (as shown in Figure 5-9), that is, the greater the CBO_{spike} value, the lower the voltage loss. From previous studies,[263] we know that the doping of Mg can not only tune the CBM but also have a significant influence on the properties of the ZMO, e.g., defect distribution and carrier density, especially the deep level defect density may also be factors that affect the charge recombination of the PSCs. Therefore, we speculate that the influence of the interfacial recombination and V_{oc} deficit are dominated by two factors simultaneously: (1) Interface level structure, when the spike structure is formed at the interface which can further create a slight barrier to prevents injected electrons in the FTO electrode and holes in the $MAPbI_3$ layer returning back to the ZMO/$MAPbI_3$ interface for

recombination; (2) the concentration of the deep level defects from ZMO ESL which act as recombination center in the interface of ZMO/$MAPbI_3$. Below we will discuss in detail the impact of these both factors, i.e., CBO structure and ZMO properties, on the performance of the planar PSCs.

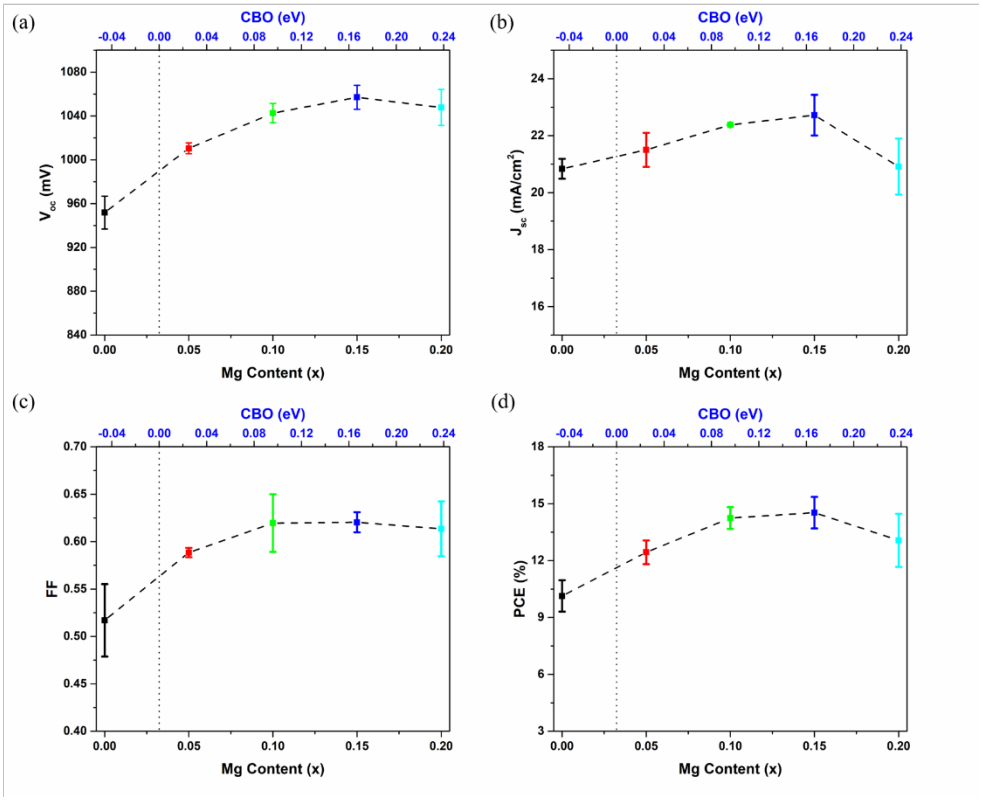

Figure 5-10. Statistics of device performance of PSCs based on 350 ℃-$Zn_{1-x}Mg_xO$ electron transporting layer (x=0, 0.05, 0.10, 0.15, 0.20): (a) V_{oc}, b) J_{sc}, (c) FF, and (d) PCE. The solid data points represent the average values, and the error bars stand for the standard deviations.

In the planar ZMO-based PSCs, the "recombination center" at the interface mainly results from the deep level defects in the ZMO-ESL. However, as known in our previous study,[263] varying the Mg doping concentration in the ZnO, not only the CBM was changed, but also the defect distribution and carrier concentration in the ZnO were affected. For better understanding how these two factors effect on interfacial recombination, we prepared the ZMO films with relatively low defect concentration by improving annealing temperature (350℃) [218, 278-279], and the PSCs based on these films. The photovoltaic performance statistics with the average value and standard deviation of the 350℃-ZMO based PSCs are summarized in Figure 5-10. Figure 5-11 (a) shows the PL spectra of the ZMO films with different annealing temperatures (e.g., bottom-290℃ and up-350℃) under room temperature. The bottom of Figure 5-11 (a) has been reported in our previous work.[263] The narrow ultraviolet emission at 380 nm is related to the near band edge transitions in ZnO. Emission regions of 400~600 nm is attributed to the shallow and deep level defects within the ZnO crystal, such as interstitials and vacancies of zinc and oxygen. The violet (400 nm) and blue (470 nm) emission in PL

spectra of ZnO are related to shallow defects, the green (529 nm) and yellow (572nm) are associated to deep defects.[218-219, 263] Figure 5-11 (b) shows the integral area of the deep defect related emission range (within the red border) in the PL spectra of both 290°C-ZMO and 350°C-ZMO films. Due to the integrated area of the PL emission from defect states is proportional to the defect state density of the corresponding energy level, we found that compared with the effect of doping content of Mg, the influence of the annealing temperature on the deep defect density of ZMO is more obvious. As shown in our previous reports, the deep defects were caused mainly by the oxygen vacancy or metal cation (Zn^{2+} and Mg^{2+}) interstitial in ZMO film. Thus, our results shows that the appropriate amount of Mg doping ($x \leq 0.15$) or increasing the annealing temperature of the film in air can reduce the density of deep defects in the ZMO.[263]

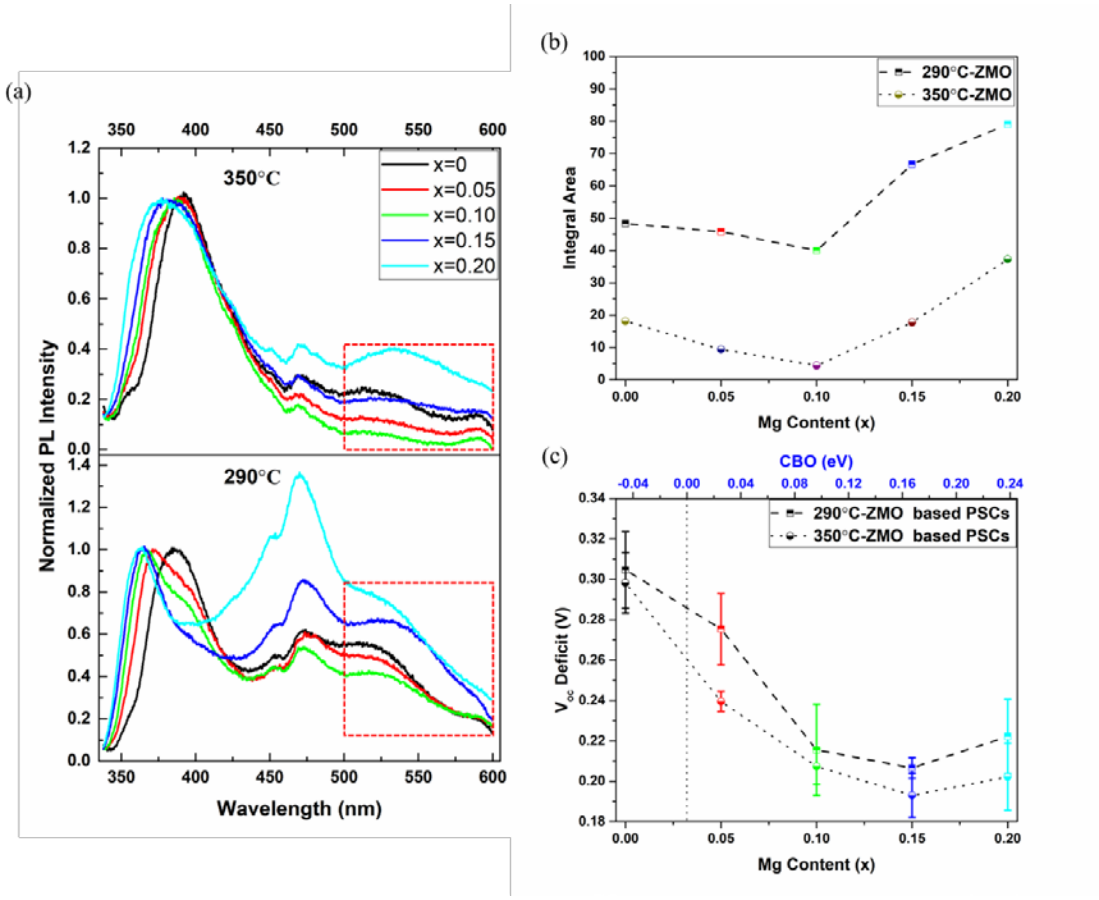

Figure 5-11. (a) Room temperature PL spectra of the $Zn_{1-x}Mg_xO$ films (x=0, 0.05, 0.10, 0.15 and 0.20) with different annealed temperature (bottom: 290°C[263] and up: 350°C). (b) The integral area of the green-yellow (500-600 nm) range of both PL spectra of 290°C-ZMO and 350°C-ZMO films. (c) The V_{oc} deficit of both 290°C-ZMO based PSCs and 350°C-ZMO based PSCs.

For heterojunction solar cell, V_{oc} deficit can well reflect the charge recombination at interface. As shown in Figure 5-11 (c), the PSCs based on 350°C-ZMO shows slightly lower V_{oc} deficit than the PSCs based on 290°C-ZMO could be due to their difference of deep defect densities. Notably, the variation trend of V_{oc} deficit with Mg doping level in both kinds of PSCs (based on 290°C-ZMO and 350°C-ZMO) are very similar, which

indicate that Mg-doping has the same effect on these two types of PSCs. Interestingly, the deep defect density (relative values due to normalized) in both 290℃-ZMO and 350℃-ZMO films did not show significant changes with the increase of Mg-doping level when Mg doping content is below 15% (as shown in Figure 5-11 (b)), however, V_{oc} deficit of the PSCs based on both kinds of ZMO all shows the significant changes with increasing Mg doping level (as shown in Figure 5-11 (c)). So, we can conclude that the interfacial recombination in PSCs is mainly dominated by the CBO at the interface of ZMO/$MAPbI_3$. But we also found that when the doping amount of Mg exceeds 15%, the *Voc* deficit tends to be a saturated value rather than decreases continuously. We think that the change of the V_{oc} deficit with the increase of Mg doping content in our PSCs is a combined effect of the formed CBO between the ZMO/$MAPbI_3$ and deep defect states in ZMO. When the doping content of Mg in ZnO exceeds 15%, the positive effect of the CBO_{spike} on the reduction of interfacial recombination is cancelled by the negative impact of the deep defects of ZMO.

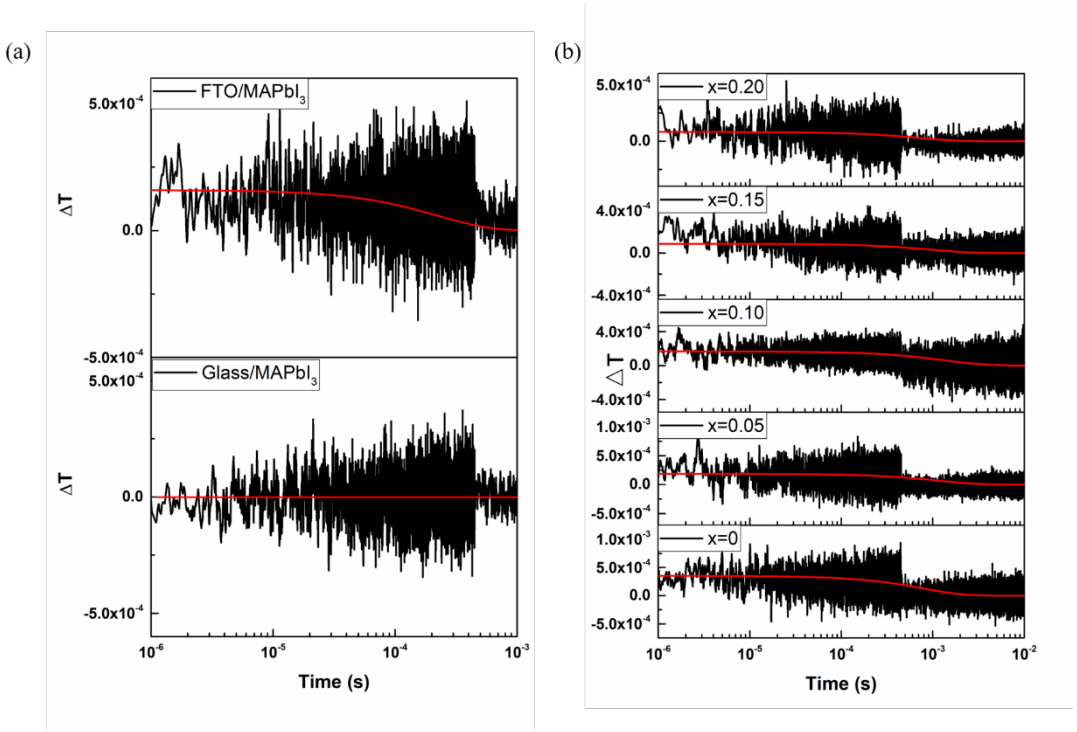

Figure 5-12. Nanosecond TA responses of (a) Glass/ $MAPbI_3$ and FTO/$MAPbI_3$, and (b) FTO/ $Zn_{1-x}Mg_xO$/$MAPbI_3$ (x=0, 0.05, 0.10, 0.15, 0.20) (red lines are fitted lines).

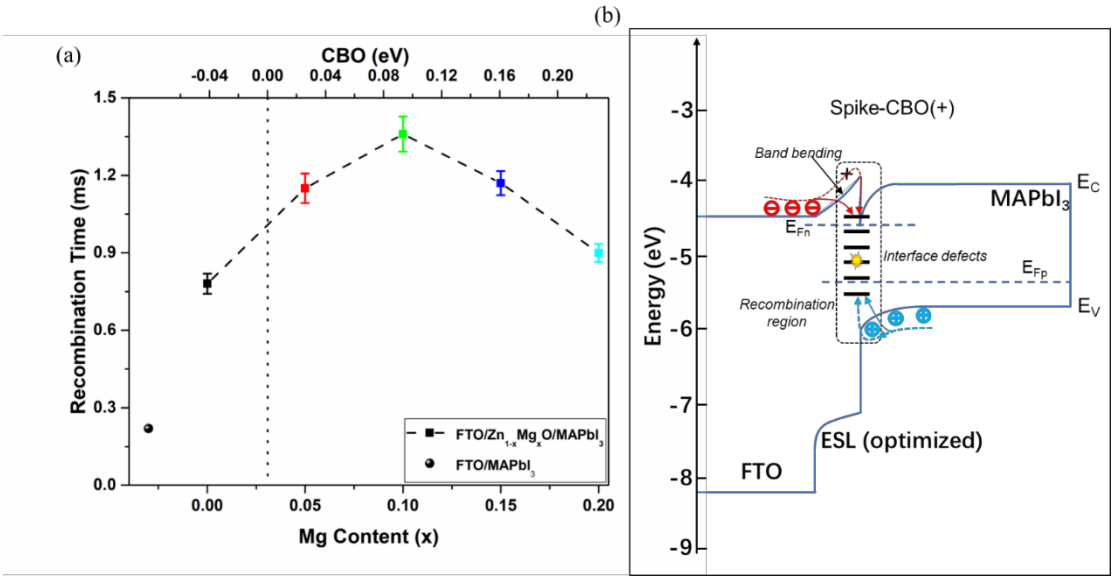

Figure 5-13. (a) Nanosecond (ns) TA-response (recombination process) of ZMO/$MAPbI_3$ with increasing of Mg content (x=0~0.2). (b)Schematic illustrations of charge recombination at interface of ZMO/$MAPbI_3$ layers at open circuit, when the Mg-doping content more than 10%.

To more intuitively explore the mechanism of electron recombination at the ZMO/ $MAPbI_3$ heterojunction, we performed the nanosecond (ns)-TA measurements. TA measurements were conducted on $MAPbI_3$ deposited on FTO/ZMO films. Generally, in PSCs, the charge recombination at the interface occurs in a timescale of over 1 ns, and thus we measured the relaxation dynamics (charge recombination) of the injected electrons in FTO using the ns-TA setup.[280] Figure 5-12 (a) and (b) shows the TA responses of $MAPbI_3$ deposited on glass, FTO and FTO/ZMO, which were measured with the pump wavelength was 470 nm and the probe wavelength was 1400 nm. Because the free carrier absorption in FTO is mainly located in an infrared range of 1400~4100 nm, we, therefore, focus on this range to investigate the dynamics of the injected electrons.[230] As shown in the bottom of Figure 5-12 (a), no TA responses could be observed at this wavelength (1400 nm) for $MAPbI_3$ films on glass. Therefore, we confirm that the TA response of FTO/$MAPbI_3$ (upper part of Figure 5-12 (a)) and FTO/ZMO/$MAPbI_3$ (Figure 5.12 (b)) is assigned to the absorption signal of electrons transferred into FTO electrode from the $MAPbI_3$. Figure 5-13 (a) shows the recombination time from all samples by fitting results of ns-TA response with an exponential function ($y(t) = A_0 e^{-\frac{t}{\tau}} + y_0$). We found that for the PSCs without ESL, the recombination is fastest with a time constant of 0.22 ± 0.01 ms. Then the recombination is suppressed after ESL was introduced and became slowest for x= 0.1 where CBO_{spike} is 0.08 eV (1.36 ± 0.068 ms). Therefore, the presence of an optimized ESL (form a spike structure) can effectively suppress back recombination of injected electron carriers at the FTO/$MAPbI_3$ interface and significantly improve device performance, as shown in Figure 5-14. When x> 0.1 where CBO_{spike} is larger than 0.1 eV, the recombination became faster again. This result could be due to the large increase

in deep defect density, and the negative effect of deep defects on interfacial recombination exceed the positive effect of the spike structure, as shown in Figure 5-11 (b).

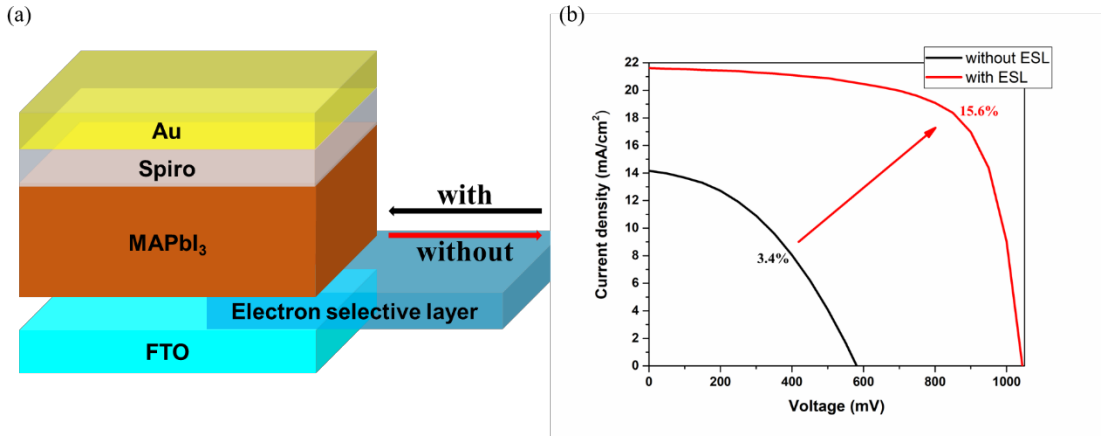

Figure 5-14. (a) Schematic illustration structure and (b) J-V characteristics under simulated AM 1.5G illumination of a planar perovskite solar cell.

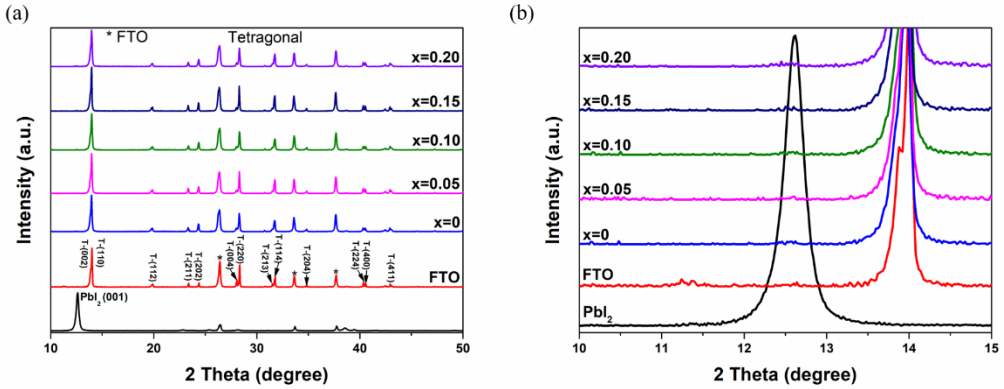

Figure 5-15. XRD patterns of $MAPbI_3$ perovskite films fabricated on top of FTO and FTO/$Zn_{1-x}Mg_xO$ ESL films (a) full figure and (b) partial enlarged detail (the * signs denote the peaks for FTO/glass substrate).

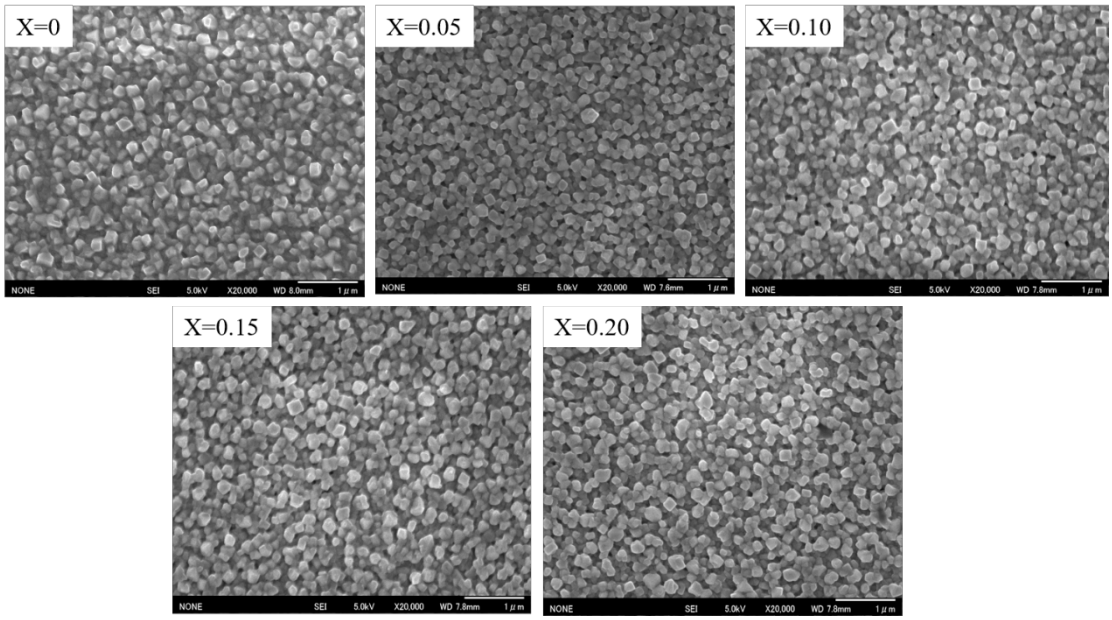

Figure 5-16. The top view SEM images of $MAPbI_3$ perovskite films fabricated on top of $Zn_{1-x}Mg_xO$ (x=0,0.05,0.10,0.15,0.20) ESL films.

Besides, the perovskite film morphology and crystallization which are also affected by ESL/perovskite interface are highly related to the device performance.[148, 281] Figure 5-15 depicts the XRD patterns of the $MAPbI_3$ films on five ETL films. For all the perovskite films, we can observe the diffraction peaks are in good accordance with previously reported XRD patterns of $MAPbI_3$. The diffraction peaks in all the perovskite film patterns agree well with previously reported XRD patterns for $MAPbI_3$. The patterns of all the films showed the same characteristic peak without PbI_2 residue, therefore the $MAPbI_3$ films were considered to be not affected by the $Zn_{1-x}Mg_xO$ substrates. The surface of scanning electron microscopy (SEM) of $MAPbI_3$ on the ZMO also shows the same surface morphologies, as shown in Figure 5-16. This result confirms the photovoltaic performances of the ZMO-based PSCs here were controlled by other reasons such as the interfacial recombination rather than the morphology and crystallization of the $MAPbI_3$ film.

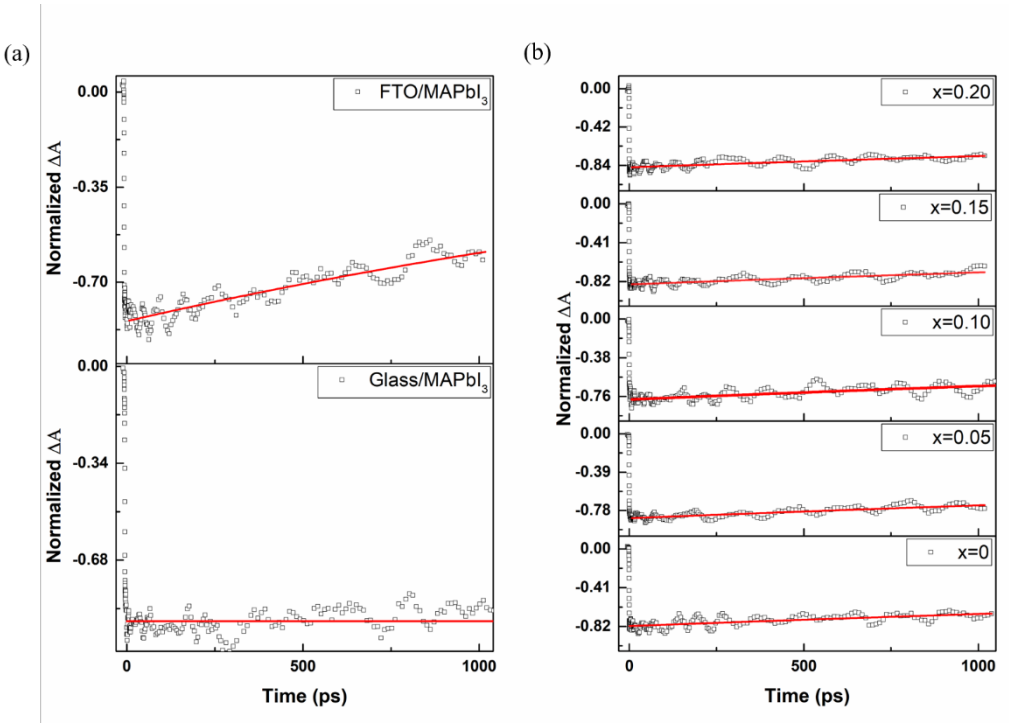

Figure 5-17. (a) Femtosecond TA responses of (a) Glass/ $MAPbI_3$ and FTO/$MAPbI_3$, and (b)FTO/ $Zn_{1-x}Mg_xO$/$MAPbI_3$ (x=0, 0.05, 0.10, 0.15, 0.20) (red lines are fitted lines).

There is a problem that cannot be ignored when constructing the spike structure at the interface, that is, the effect of spike structure on electron injection. The observation that the positive CBO does not benefit J_{sc} was reported in the other types of solar cells.[264] To further investigate the photoexcited electron injection dynamics at the ZMO/$MAPbI_3$ heterojunction, we performed the femtosecond (fs)-TA measurements with a pump light wavelength of 470 nm and a probe light wavelength of 750 nm. The photon energy of the probe wavelength corresponds to the band gap of the $MAPbI_3$., thus we can observe bleach signals at this probe wavelength as shown in Figure 5.17.[280] The bottom and upper parts of Figure 5-17 (a) show the normalized fs-TA responses of the Glass/$MAPbI_3$ and FTO/$MAPbI_3$, respectively. As shown in the bottom of Figure 5-17 (a), no decay of the TA response was observed for $MAPbI_3$ on glass, but for FTO/$MAPbI_3$ (the upper part of Figure 5-17 (a)) and FTO/ZMO/$MAPbI_3$ (Figure 5-17 (b)), there are an obvious decay of the TA response. According to our previous work,[280] thus, we confirm this decay originates from electron injection from the perovskite to the ZMO/FTO. Figure 5-18 (a) shows the injection time from all samples by fitting the fs-TA response with an exponential function ($y(t) = A_0 e^{\frac{-t}{\tau}} + y_0$). In the case of FTO/$MAPbI_3$ without ESL, it shows the fastest injection (2.8 ± 0.1 ns), when the ZMO thin film is introduced between the FTO and the $MAPbI_3$, the electron transfer rate becomes slower. Despite the formation of the spike structure, the sample with x=0.1 shows a little faster injection rate with a time constant of 5.5 ± 0.4 ns compared to the other FTO/ZMO/$MAPbI_3$ samples. This result indicates that when a large CBO_{spike} in a

certain range occur, the charge injection is not affected by the energy barrier. This could be due to some shallow defect states in the ZMO layer can act as additional pathways for charge carriers to transfer from the $MAPbI_3$ to the FTO electrode.[263] But when CBO_{spike} continues to increase beyond 0.1 eV, the electron, in this case, was impeded by the spike, therefore, the injection rate becomes smaller with the increase of CBO_{spike}.

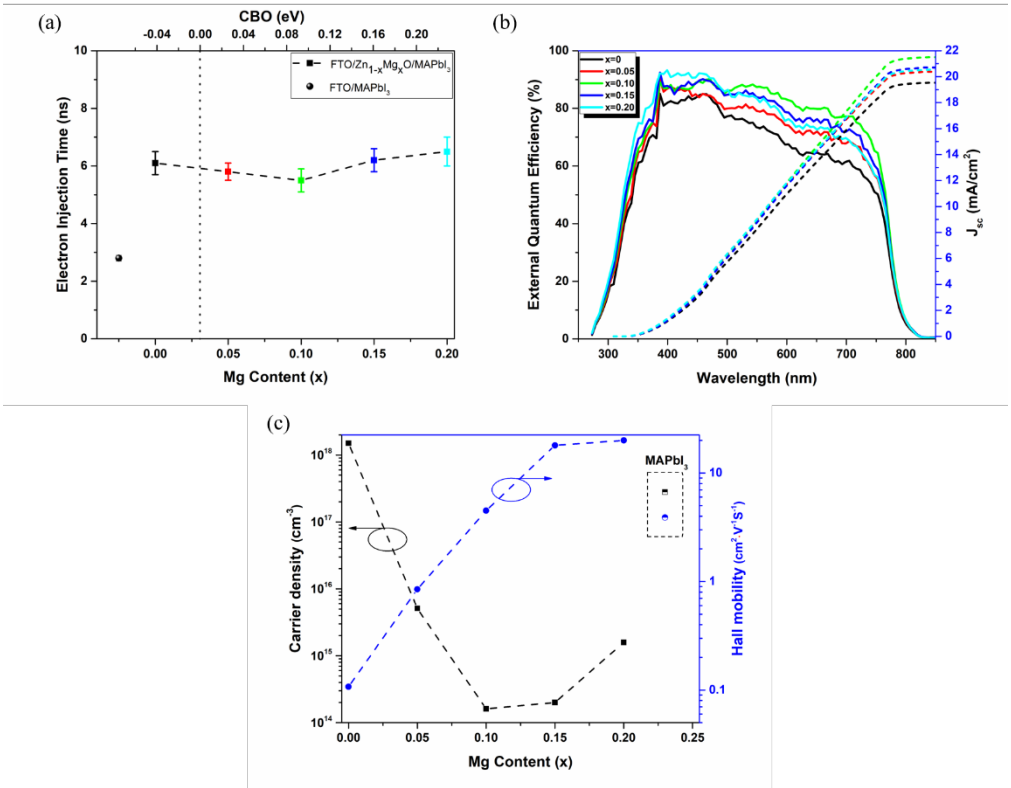

Figure 5-18. (a) Femtosecond (fs) TA-response (injection process) of $ZMO/MAPbI_3$ with increasing of Mg content (x=0~0.2). (b) External quantum efficiency (EQE) spectra and their integrated photocurrents for the $ZMO/MAPbI_3$ PSCs. (c) Carrier density, electron mobility of ZMO and $MAPbI_3$ film at room temperature from Hall effect measurement.

Figure 5-18 (b) depicts external quantum efficiency (EQE) of the typical $ZMO/MAPbI_3$ PSCs with the best PCE at each Mg content (x = 0, 0.05, 0.10, 0.15, and 0.20), the corresponding *J-V* characteristics are shown in Figure 5-6, and their cell parameters are listed in detail in Table 5-2. Integrating the EQE data with the AM 1.5G solar spectrum gave calculated J_{sc} values of approximately 19.52, 20.16, 21.32, 20.41, and 20.24 mA/cm^2 for the PSCs with the ZnO and doped ZMO ESLs, respectively, which are in good agreement with the J_{sc} values obtained from the *J-V* curves. We found that benefiting from the broadened optical band gap of ZMO, the EQE increased gradually in the region of 340–400 nm, which is due to the increased light absorption by the following $MAPbI_3$ absorbing layer.[197] Considering the integrated increased EQE within the 340–400 nm spectral range just contributes to a maximum J_{sc} gain no more than 0.3 mA/cm^2, the additional J_{sc} increase for the PSCs with Mg doing could result from other factors.

Figure 5-18 (c) shows the Hall effect measurement results of ZMO films. We found that the carrier concentration of Mg-doped ZnO films ($<10^{16}$ cm^{-3}) was significantly lower than that of the pure ZnO (~10^{18} cm^{-3}). A more significant difference in carrier concentration would expand the built-in electric field at the interface of ZMO and $MAPbI_3$,[184] shifting the built-in electric field toward the ZMO film and thus contributing to improve the charge collection efficiency of the FTO electrode. Moreover, the charge transfer rate is expected to depend on the density of accepting states;[221, 282] thus, lowering the carrier concentration in ZMO would produce more electron accepting states for electron transfer. The increased Hall carrier mobility resulting from increasing the Mg-doping content also ensures that electrons can quickly transport to the FTO electrode. All the aforementioned factors contribute to the increase in J_{sc}; however, the J_{sc} begins to decrease when the Mg doping exceeds 10% due to the excessive increase of the CBO_{spike} (more than 0.1 eV), which causes an extraction barrier of photogenerated electrons.

5.4 Conclusions

The effect of the CBO in planar PSCs was systematically investigated by introducing ZMO-ESLs into the devices. The tunability of the electronic energy levels in the ZMO-ESL, which was achieved by controlling the doping amount of Mg, enabled the optimization of the conduction band energy level alignment. We found that in ZMO/perovskite system although interfacial recombination is affected by two factors, i.e., the CBO structure and ZMO properties, when the doping content of Mg in ZnO is less than 15%, CBO structure is dominated, and a higher conduction band energy of the ESL with a CBO value up to 0.16 eV at the interface of ZMO/$MAPbI_3$ is beneficial to the overall performance. However, an optimized composition exists for both the suppression of recombination and enhancement of electron injection, which is $Zn_{0.9}Mg_{0.1}O$ in this case. Using TA measurements, we revealed that the electron injection from photoexcited $MAPbI_3$ to an FTO through a ZMO compact layer occurs on the timescale of a few nanoseconds in planar PSCs. Benefiting from the reduced interfacial charge recombination and enhanced charge injection, the PSC with the ZMO shows a PCE as high as 15.6%, which is much higher than the 11.2% efficiency for solar cells with ZnO. These results demonstrate a potential guideline for designing and fabricating high-efficiency PSCs using band-alignment engineering.

Chapter 6 Summary and Prospective

We have demonstrated that the energy level alignment (ELA) engineering at the interface between the active QD layers and the metal electrode of QDHSCs can be used to improve the electron collection efficiency at the heterojunction and reduce trap-assisted and interfacial recombination. Through the ELA strategy, a great increase (from 28 to 33 mA/cm^2) in J_{sc} and a maximum efficiency of 7.24% (the active area is 16 mm^2) have been achieved by optimization of the structure. By the explored of carrier dynamics we found that the ELA structure not only as an electron-blocking layer, reduces the interfacial recombination at the PbS/Au interface, but also the ELA structure can drive more electron carriers toward the electron transfer layer, and the additional electron carriers can fill the trap states, reducing the trap-assisted recombination in the PbS QDHSCs. In brief, this study emphasized band energy engineering in achieving high-efficiency planar heterojunction QD solar cells. The carrier transportion and recombination mechanisms explored in this work may be able to aid further improvements of QDHSCs and they can even benefit other types of solar cells. This study suggests a useful strategy for improving the effective diffusion lengths of photogenerated carriers in PbS QDHSCs via simple architecture design.

For the first time, we have demonstrated that in quantum dot heterojunction solar cells (QDHSCs) a spike structure at the interface, i.e., the energy level of the conduction band of the electron transporting layer (ETL) is higher than that of the QD absorber, can suppress the charge recombination at the interface. We find that efficient charge injection can still occur even when the spike structure is formed between the QD absorber and the ETL. We think that this is because that the shallow defect states in the ETL can serve as additional pathways to transport the photoexcited electrons from the QDs to the electron collecting electrode (FTO). By taking advantage of these characteristics, we greatly improve the efficiency (10.6%) of the QDHSCs just by slightly tuning the conduction band energy offset between the ETL and the QDs. In addition, by probing free electron absorption in FTO using broadband transient absorption spectroscopy, we find that ultra-fast electron transfer occurs in a time scale of a few hundred femtoseconds from PbS QDs to FTO through the $Zn_{1-x}Mg_xO$ compact layer. We believe that our findings would provide guidance for enhancing the photovoltaic performance of QD-based solar cells further.

The effect of the conduction band offset in planar PSCs was systematically investigated by introducing ZMO-ESL into the device. The tunability of the electronic energy levels in the ZMO-ESL by controlling the doping amount of Mg allows for an optimization of the conduction band energy level alignment. We found that a higher conduction band energy of the electron selective layer by no more than 0.2 eV is beneficial for the overall performance, which leads to a suppressed interfacial recombination and thus an increased V_{oc}. By TA measurement we also revealed the time constant of electron injection from photoexcited $MAPbI_3$ to FTO through ZMO compact layer. Benefiting from the reduced interfacial charge recombination and

enhanced charge injection, the PSC with ZMO exhibited a considerable increase (~35%) in PCE compared with the solar cell with ZnO. These results demonstrated a potential guideline for the designing and fabricating high-efficiency PSCs through band alignment engineering.

For CQDSCs, the highest certified efficiency just is 12% (PbS CQDSCs) and 13.4% ($CsPbI_3$), respectively, thus the priority is to further increase efficiency in order to compete with other existing solar energy technologies. Current limitations for device efficiency are mainly due to low V_{oc} and FF, so further research needs to exploit more passivation approaches, and careful engineering electrode materials and tuning the CQD properties, which enables reduced recombination loss, increased carrier diffusion length and higher electron collection efficiency. For PSCs, although their efficiencies have reached levels comparable to those of conventional commercial solar cells, their stability test results under light illumination and at maximum power output point are still insufficient. Therefore, further improvement of the stability output of the PSCs in a real working condition is the primary task for future research. Moreover, deep understanding charge dynamics and interface properties of CQDSCs and PSCs are required to advance device towards the production further.

Bibliography

1. COUNCIL, W. E. *World Energy Issues Monitor 2017*; **April 2017**.

2. economics, B. e. *BP Energy Outlook-2018 edition*; **2018**.

3. Administration, U. S. E. I. *International Energy Outlook 2017*; DOE/EIA-0484(2017); **September 14, 2017**.

4. Agency, I. E. *Market Report Series: Renewables 2017*; **4 October 2017**; p 189.

5. Becquerel, A. E., Mémoire sur les Effets Électriques Produits sous L'influence des Rayons Solaires. *Comptes Rendus Séances Hebd* **1839,** *9*, 561-567.

6. Fritts, C. E., On a new form of selenium cell, and some electrical discoveries made by its use. *Am. J. Sci.* **1883,** *Series 3 Vol. 26* (156), 465-472.

7. Einstein, A., Über einen die Erzeugung und Verwandlung des Lichtes betreffenden heuristischen Gesichtspunkt. *Annalen der Physik* **1905,** *322* (6), 132-148.

8. E. A. Davis, I. F., *J.J. Thompson And The Discovery Of The Electron*. CRC Press: **June 2, 1997**; Vol. 72, p 266.

9. Chapin, D. M.; Fuller, C. S.; Pearson, G. L., A New Silicon p-n Junction Photocell for Converting Solar Radiation into Electrical Power. *J. Appl. Phys.* **1954,** *25* (5), 676-677.

10. Brendan M. Kayes, H. N., Rose Twist, Sylvia G. Spruytte, Frank Reinhardt, Isik C. Kizilyalli, and Gregg S. Higashi 27.6% CONVERSION EFFICIENCY, A NEW RECORD FOR SINGLE-JUNCTION SOLAR CELLS UNDER 1 SUN ILLUMINATION. In *37th IEEE Photovoltaic Specialists Conference*, **2011**; pp 000004-000008.

11. (ITRPV), I. T. R. f. P. *ITRPV Eighth Edition 2017 including maturity report*; **2017**.

12. Lauermann, T.; Fröhlich, B.; Hahn, G.; Terheiden, B., Diffusion-based model of local Al back surface field formation for industrial passivated emitter and rear cell solar cells. *Progress in Photovoltaics: Research and Applications* **2015,** *23* (1), 10-18.

13. Conibeer, G.; Green, M.; Corkish, R.; Cho, Y.; Cho, E.-C.; Jiang, C.-W.; Fangsuwannarak, T.; Pink, E.; Huang, Y.; Puzzer, T.; Trupke, T.; Richards, B.; Shalav, A.; Lin, K.-l., Silicon nanostructures for third generation photovoltaic solar cells. *Thin Solid Films* **2006,** *511-512*, 654-662.

14. Green, M. A.; Hishikawa, Y.; Dunlop, E. D.; Levi, D. H.; Hohl-Ebinger, J.; Ho-Baillie, A. W. Y., Solar cell efficiency tables (version 51). *Progress in Photovoltaics: Research and Applications* **2018,** *26* (1), 3-12.

15. Shumkov, I. First Solar hits efficiency of 22.1% with CdTe research cell. https://renewablesnow.com/news/first-solar-hits-efficiency-of-22-1-with-cdte-research-cell-514244/.

16. James S. Ward, B. E., Rommel Noufi, Miguel Contreras, Kannan Ramanathan, Carl Osterwald and; Emery, K. *Cu(In,Ga)Se2 solar cells measured under low flux optical concentration*;

14683843; 16 October 2014, **2014**; pp 2934-2937.

17. Green, M. A.; Hishikawa, Y.; Warta, W.; Dunlop, E. D.; Levi, D. H.; Hohl-Ebinger, J.; Ho-Baillie, A. W. H., Solar cell efficiency tables (version 50). *Progress in Photovoltaics: Research and Applications* **2017,** *25* (7), 668-676.

18. Photovoltaics, N. N. C. f. Best Research-Cell Efficiencies. https://www.nrel.gov/pv/assets/images/efficiency-chart.png.

19. O'Regan, B.; Grätzel, M., A low-cost, high-efficiency solar cell based on dye-sensitized colloidal TiO2 films. *Nature* **1991,** *353*, 737.

20. Yan, J.; Saunders, B. R., Third-generation solar cells: a review and comparison of polymer:fullerene, hybrid polymer and perovskite solar cells. *RSC Advances* **2014,** *4* (82), 43286-43314.

21. Mathew, S.; Yella, A.; Gao, P.; Humphry-Baker, R.; Curchod, B. F. E.; Ashari-Astani, N.; Tavernelli, I.; Rothlisberger, U.; Nazeeruddin, M. K.; Grätzel, M., Dye-sensitized solar cells with 13% efficiency achieved through the molecular engineering of porphyrin sensitizers. *Nature Chemistry* **2014,** *6*, 242.

22. Wu, J.; Lan, Z.; Lin, J.; Huang, M.; Huang, Y.; Fan, L.; Luo, G.; Lin, Y.; Xie, Y.; Wei, Y., Counter electrodes in dye-sensitized solar cells. *Chem. Soc. Rev.* **2017,** *46* (19), 5975-6023.

23. Ye, M.; Wen, X.; Wang, M.; Iocozzia, J.; Zhang, N.; Lin, C.; Lin, Z., Recent advances in dye-sensitized solar cells: from photoanodes, sensitizers and electrolytes to counter electrodes. *Mater. Today* **2015,** *18* (3), 155-162.

24. Yan, C.; Barlow, S.; Wang, Z.; Yan, H.; Jen, A. K. Y.; Marder, S. R.; Zhan, X., Non-fullerene acceptors for organic solar cells. *Nature Reviews Materials* **2018,** *3*, 18003.

25. Hou, J.; Inganäs, O.; Friend, R. H.; Gao, F., Organic solar cells based on non-fullerene acceptors. *Nature Materials* **2018,** *17*, 119.

26. Lu, L.; Zheng, T.; Wu, Q.; Schneider, A. M.; Zhao, D.; Yu, L., Recent Advances in Bulk Heterojunction Polymer Solar Cells. *Chem. Rev.* **2015,** *115* (23), 12666-12731.

27. Friedlmeier, T. M. W., N.; Walter, T.; Dittrich, H.; Schock, H.-W. In *Heterojunctions based on Cu2ZnSnS4 and Cu2ZnSnSe4 thin films*, 14th European Photovoltaic Solar Energy Conference Spain, Spain, **1997**.

28. Wang, W.; Winkler, M. T.; Gunawan, O.; Gokmen, T.; Todorov, T. K.; Zhu, Y.; Mitzi, D. B., Device Characteristics of CZTSSe Thin-Film Solar Cells with 12.6% Efficiency. *Adv. Energy Mater.* **2014,** *4* (7), 1301465.

29. Pattantyus-Abraham, A. G.; Kramer, I. J.; Barkhouse, A. R.; Wang, X.; Konstantatos, G.; Debnath, R.; Levina, L.; Raabe, I.; Nazeeruddin, M. K.; Grätzel, M.; Sargent, E. H., Depleted-Heterojunction Colloidal Quantum Dot Solar Cells. *ACS Nano* **2010,** *4* (6), 3374-3380.

30. Peng, Z. A.; Peng, X., Formation of High-Quality CdTe, CdSe, and CdS Nanocrystals Using

CdO as Precursor. *J. Am. Chem. Soc*. **2001,** *123* (1), 183-184.

31. McGuire, J. A.; Joo, J.; Pietryga, J. M.; Schaller, R. D.; Klimov, V. I., New Aspects of Carrier Multiplication in Semiconductor Nanocrystals. *Acc. Chem. Res.* **2008,** *41* (12), 1810-1819.

32. Zaban, A.; Mićić, O. I.; Gregg, B. A.; Nozik, A. J., Photosensitization of Nanoporous TiO2 Electrodes with InP Quantum Dots. *Langmuir* **1998,** *14* (12), 3153-3156.

33. Sanehira, E. M.; Marshall, A. R.; Christians, J. A.; Harvey, S. P.; Ciesielski, P. N.; Wheeler, L. M.; Schulz, P.; Lin, L. Y.; Beard, M. C.; Luther, J. M., Enhanced mobility CsPbI₃ quantum dot arrays for record-efficiency, high-voltage photovoltaic cells. *Science Advances* **2017,** *3* (10).

34. Kojima, A.; Teshima, K.; Shirai, Y.; Miyasaka, T., Organometal Halide Perovskites as Visible-Light Sensitizers for Photovoltaic Cells. *J. Am. Chem. Soc.* **2009,** *131* (17), 6050-6051.

35. Babayigit, A.; Boyen, H.-G.; Conings, B., Environment versus sustainable energy: The case of lead halide perovskite-based solar cells. *MRS Energy & Sustainability* **2018,** *5*, E1.

36. I. Ekimov, A.; Onushchehko, A., *Quantum Size Effect in Three-Dimensional Microscopic Semiconductor Crystals*. **1981**; Vol. 34, p 363.

37. Byers, R. J.; Hitchman, E. R., Quantum Dots Brighten Biological Imaging. *Prog. Histochem. Cytochem.* **2011,** *45* (4), 201-237.

38. Kim, M. R.; Ma, D., Quantum-Dot-Based Solar Cells: Recent Advances, Strategies, and Challenges. *J. Phys. Chem. Lett.* **2015,** *6* (1), 85-99.

39. Colvin, V. L.; Schlamp, M. C.; Alivisatos, A. P., Light-emitting diodes made from cadmium selenide nanocrystals and a semiconducting polymer. *Nature* **1994,** *370*, 354.

40. Clifford, J. P.; Konstantatos, G.; Johnston, K. W.; Hoogland, S.; Levina, L.; Sargent, E. H., Fast, sensitive and spectrally tuneable colloidal-quantum-dot photodetectors. *Nature Nanotechnology* **2008,** *4*, 40.

41. Jasim, K. E., Quantum Dots Solar Cells, Solar Cells In *Solar Cells-New Approaches and Reviews*, Kosyachenko, L. A., Ed. IntechOpen, **October 22nd 2015**.

42. Bimberg, D.; Pohl, U. W., Quantum dots: promises and accomplishments. *Mater. Today* **2011,** *14* (9), 388-397.

43. Brus, L., Electronic wave functions in semiconductor clusters: experiment and theory. *The Journal of Physical Chemistry* **1986,** *90* (12), 2555-2560.

44. Jasim, K. E., Dye Sensitized Solar Cells - Working Principles, Challenges and Opportunities. In *Solar Cells Leonid*

Kosyachenko, A., Ed. IntechOpen: **November 9th 2011**

45. Polman, A.; Knight, M.; Garnett, E. C.; Ehrler, B.; Sinke, W. C., Photovoltaic materials: Present efficiencies and future challenges. *Science* **2016,** *352* (6283).

46. Shockley–Queisser limit. https://en.wikipedia.org/wiki/Shockley%E2%80%93Queisser_limit.

47. Shockley, W.; Queisser, H. J., Detailed Balance Limit of Efficiency of p-n Junction Solar Cells. *J. Appl. Phys.* **1961,** *32* (3), 510-519.

48. Beard, M.; Johnson, J.; Luther, J.; Nozik, A., *Multiple exciton generation in quantum dots versus singlet fssion in molecular chromophores for solar photon conversion*. **2015**; Vol. 373.

49. Jianjun, T.; Garcia, B., *Semiconductor quantum dot-sensitized solar cells*. **2013**; Vol. 4.

50. Beard, M. C., Multiple Exciton Generation in Semiconductor Quantum Dots. *J. Phys. Chem. Lett.* **2011,** *2* (11), 1282-1288.

51. Smith, C.; Binks, D., Multiple Exciton Generation in Colloidal Nanocrystals. *Nanomaterials* **2014,** *4* (1), 19-45.

52. Ellingson, R. J.; Beard, M. C.; Johnson, J. C.; Yu, P.; Micic, O. I.; Nozik, A. J.; Shabaev, A.; Efros, A. L., Highly Efficient Multiple Exciton Generation in Colloidal PbSe and PbS Quantum Dots. *Nano Lett.* **2005,** *5* (5), 865-871.

53. Lin, X.; Ji, G.; Liu, Y.; Huang, Q.; Yang, Z.; Du, Y., Formation mechanism and magnetic properties of hollow Fe3O4 nanospheres synthesized without any surfactant. *CrystEngComm* **2012,** *14* (24), 8658-8663.

54. Wei, W.; Quanguo, H.; Rong, H.; Jingke, H.; Hong, C., *Preparation and characterization of magnetite Fe3O4 nanopowders*. **2007**; Vol. 36, p 238-243.

55. Yang, H.; Luan, W.; Tu, S.-t.; Wang, Z. M., Synthesis of nanocrystalsvia microreaction with temperature gradient: towards separation of nucleation and growth. *Lab on a Chip* **2008,** *8* (3), 451-455.

56. Williams, J. V.; Kotov, N. A.; Savage, P. E., A Rapid Hot-Injection Method for the Improved Hydrothermal Synthesis of CdSe Nanoparticles. *Ind. Eng. Chem. Res.* **2009,** *48* (9), 4316-4321.

57. Polte, J., Fundamental growth principles of colloidal metal nanoparticles - a new perspective. *CrystEngComm* **2015,** *17* (36), 6809-6830.

58. Dalmaschio, C. J.; Ribeiro, C.; Leite, E. R., Impact of the colloidal state on the oriented attachment growth mechanism. *Nanoscale* **2010,** *2* (11), 2336-2345.

59. Sargent, E. H., Colloidal quantum dot solar cells. *Nature Photonics* **2012,** *6*, 133.

60. Wang, R.; Shang, Y.; Kanjanaboos, P.; Zhou, W.; Ning, Z.; Sargent, E. H., Colloidal quantum dot ligand engineering for high performance solar cells. *Energy & Environmental Science* **2016,** *9* (4), 1130-1143.

61. Tang, J.; Liu, H.; Zhitomirsky, D.; Hoogland, S.; Wang, X.; Furukawa, M.; Levina, L.; Sargent, E. H., Quantum Junction Solar Cells. *Nano Lett.* **2012,** *12* (9), 4889-4894.

62. Yin, Z.; Zheng, Q.; Chen, S.-C.; Cai, D., Interface Control of Semiconducting Metal Oxide

Layers for Efficient and Stable Inverted Polymer Solar Cells with Open-Circuit Voltages over 1.0 Volt. *ACS Appl. Mater. Inter.* **2013,** *5* (18), 9015-9025.

63. Kramer, I. J.; Sargent, E. H., The Architecture of Colloidal Quantum Dot Solar Cells: Materials to Devices. *Chem. Rev.* **2014,** *114* (1), 863-882.

64. Liu, F.; Zhang, Y.; Ding, C.; Kobayashi, S.; Izuishi, T.; Nakazawa, N.; Toyoda, T.; Ohta, T.; Hayase, S.; Minemoto, T.; Yoshino, K.; Dai, S.; Shen, Q., Highly Luminescent Phase-Stable CsPbI3 Perovskite Quantum Dots Achieving Near 100% Absolute Photoluminescence Quantum Yield. *ACS Nano* **2017,** *11* (10), 10373-10383.

65. Shieh, F.; Saunders, A. E.; Korgel, B. A., General Shape Control of Colloidal CdS, CdSe, CdTe Quantum Rods and Quantum Rod Heterostructures. *The Journal of Physical Chemistry B* **2005,** *109* (18), 8538-8542.

66. Rakhlin, M. V.; Belyaev, K. G.; Klimko, G. V.; Mukhin, I. S.; Kirilenko, D. A.; Shubina, T. V.; Ivanov, S. V.; Toropov, A. A., InAs/AlGaAs quantum dots for single-photon emission in a red spectral range. *Sci. Rep.* **2018,** *8* (1), 5299.

67. Ding, C.; Zhang, Y.; Liu, F.; Nakazawa, N.; Huang, Q.; Hayase, S.; Ogomi, Y.; Toyoda, T.; Wang, R.; Shen, Q., Recombination Suppression in PbS Quantum Dot Heterojunction Solar Cells by Energy-Level Alignment in the Quantum Dot Active Layers. *ACS Appl. Mater. Inter.* **2017**.

68. Zhang, Y.; Ding, C.; Wu, G.; Nakazawa, N.; Chang, J.; Ogomi, Y.; Toyoda, T.; Hayase, S.; Katayama, K.; Shen, Q., Air Stable PbSe Colloidal Quantum Dot Heterojunction Solar Cells: Ligand-Dependent Exciton Dissociation, Recombination, Photovoltaic Property, and Stability. *J. Phys. Chem. C* **2016,** *120* (50), 28509-28518.

69. Sargent, E. H., Infrared photovoltaics made by solution processing. *Nature Photonics* **2009,** *3*, 325.

70. Xu, J.; Voznyy, O.; Liu, M.; Kirmani, A. R.; Walters, G.; Munir, R.; Abdelsamie, M.; Proppe, A. H.; Sarkar, A.; García de Arquer, F. P.; Wei, M.; Sun, B.; Liu, M.; Ouellette, O.; Quintero-Bermudez, R.; Li, J.; Fan, J.; Quan, L.; Todorovic, P.; Tan, H.; Hoogland, S.; Kelley, S. O.; Stefik, M.; Amassian, A.; Sargent, E. H., 2D matrix engineering for homogeneous quantum dot coupling in photovoltaic solids. *Nature Nanotechnology* **2018**.

71. Rajathi, S.; Kirubavathi, K.; Selvaraju, K., Structural, morphological, optical, and photoluminescence properties of nanocrystalline PbS thin films grown by chemical bath deposition. *Arabian Journal of Chemistry* **2017,** *10* (8), 1167-1174.

72. Machol, J. L.; Wise, F. W.; Patel, R. C.; Tanner, D. B., Vibronic quantum beats in PbS microcrystallites. *Physical Review B* **1993,** *48* (4), 2819-2822.

73. Hyun, B.-R.; Zhong, Y.-W.; Bartnik, A. C.; Sun, L.; Abruña, H. D.; Wise, F. W.; Goodreau, J. D.; Matthews, J. R.; Leslie, T. M.; Borrelli, N. F., Electron Injection from Colloidal PbS Quantum Dots into Titanium Dioxide Nanoparticles. *ACS Nano* **2008,** *2* (11), 2206-2212.

74. Zherebetskyy, D.; Scheele, M.; Zhang, Y.; Bronstein, N.; Thompson, C.; Britt, D.; Salmeron,

M.; Alivisatos, P.; Wang, L.-W., Hydroxylation of the surface of PbS nanocrystals passivated with oleic acid. *Science* **2014,** *344* (6190), 1380-1384.

75. Brown, P. R.; Kim, D.; Lunt, R. R.; Zhao, N.; Bawendi, M. G.; Grossman, J. C.; Bulović, V., Energy Level Modification in Lead Sulfide Quantum Dot Thin Films through Ligand Exchange. *ACS Nano* **2014,** *8* (6), 5863-5872.

76. Luther, J. M.; Law, M.; Beard, M. C.; Song, Q.; Reese, M. O.; Ellingson, R. J.; Nozik, A. J., Schottky Solar Cells Based on Colloidal Nanocrystal Films. *Nano Lett.* **2008,** *8* (10), 3488-3492.

77. Ma, W.; Swisher, S. L.; Ewers, T.; Engel, J.; Ferry, V. E.; Atwater, H. A.; Alivisatos, A. P., Photovoltaic Performance of Ultrasmall PbSe Quantum Dots. *ACS Nano* **2011,** *5* (10), 8140-8147.

78. Clifford, J. P.; Johnston, K. W.; Levina, L.; Sargent, E. H., Schottky barriers to colloidal quantum dot films. *Appl. Phys. Lett.* **2007,** *91* (25), 253117.

79. Zhijun, N.; Yuan, R.; Sjoerd, H.; Oleksandr, V.; Larissa, L.; Philipp, S.; Xinzheng, L.; David, Z.; H., S. E., All-Inorganic Colloidal Quantum Dot Photovoltaics Employing Solution-Phase Halide Passivation. *Adv. Mater.* **2012,** *24* (47), 6295-6299.

80. Leschkies, K. S.; Beatty, T. J.; Kang, M. S.; Norris, D. J.; Aydil, E. S., Solar Cells Based on Junctions between Colloidal PbSe Nanocrystals and Thin ZnO Films. *ACS Nano* **2009,** *3* (11), 3638-3648.

81. H., C. G.; Larissa, L.; Riccardo, C.; Oleksandr, V.; H., S. E., Record Charge Carrier Diffusion Length in Colloidal Quantum Dot Solids via Mutual Dot-To-Dot Surface Passivation. *Adv. Mater.* **2015,** *27* (21), 3325-3330.

82. Chang, J.; Kuga, Y.; Mora-Sero, I.; Toyoda, T.; Ogomi, Y.; Hayase, S.; Bisquert, J.; Shen, Q., High reduction of interfacial charge recombination in colloidal quantum dot solar cells by metal oxide surface passivation. *Nanoscale* **2015,** *7* (12), 5446-5456.

83. Sogabe, T.; Shen, Q.; Yamaguchi, K. In *Recent progress on quantum dot solar cells: a review*, SPIE: **2016**; p 27.

84. Kramer, I. J.; Sargent, E. H., Colloidal Quantum Dot Photovoltaics: A Path Forward. *ACS Nano* **2011,** *5* (11), 8506-8514.

85. Tang, J.; Kemp, K. W.; Hoogland, S.; Jeong, K. S.; Liu, H.; Levina, L.; Furukawa, M.; Wang, X.; Debnath, R.; Cha, D.; Chou, K. W.; Fischer, A.; Amassian, A.; Asbury, J. B.; Sargent, E. H., Colloidal-quantum-dot photovoltaics using atomic-ligand passivation. *Nature Materials* **2011,** *10*, 765.

86. Liu, Y.; Gibbs, M.; Puthussery, J.; Gaik, S.; Ihly, R.; Hillhouse, H. W.; Law, M., Dependence of Carrier Mobility on Nanocrystal Size and Ligand Length in PbSe Nanocrystal Solids. *Nano Lett.* **2010,** *10* (5), 1960-1969.

87. Ip, A. H.; Thon, S. M.; Hoogland, S.; Voznyy, O.; Zhitomirsky, D.; Debnath, R.; Levina, L.; Rollny, L. R.; Carey, G. H.; Fischer, A.; Kemp, K. W.; Kramer, I. J.; Ning, Z.; Labelle, A. J.; Chou, K. W.; Amassian, A.; Sargent, E. H., Hybrid passivated colloidal quantum dot solids. *Nature Nanotechnology* **2012,** *7*, 577.

88. Liu, M.; Voznyy, O.; Sabatini, R.; García de Arquer, F. P.; Munir, R.; Balawi, Ahmed H.; Lan, X.; Fan, F.; Walters, G.; Kirmani, Ahmad R.; Hoogland, S.; Laquai, F.; Amassian, A.; Sargent, Edward H., Hybrid organic–inorganic inks flatten the energy landscape in colloidal quantum dot solids. *Nature Materials* **2016,** *16*, 258.

89. Bin, S.; Oleksandr, V.; Hairen, T.; Philipp, S.; Mengxia, L.; Grant, W.; H., P. A.; Min, L.; James, F.; Taotao, Z.; Jie, L.; Mingyang, W.; Jixian, X.; Younghoon, K.; Sjoerd, H.; H., S. E., Pseudohalide-Exchanged Quantum Dot Solids Achieve Record Quantum Efficiency in Infrared Photovoltaics. *Adv. Mater.* **2017,** *29* (27), 1700749.

90. Song, J. H.; Jeong, S., Colloidal quantum dot based solar cells: from materials to devices. *Nano Convergence* **2017,** *4* (1), 21.

91. Kovalenko, M. V.; Scheele, M.; Talapin, D. V., Colloidal Nanocrystals with Molecular Metal Chalcogenide Surface Ligands. *Science* **2009,** *324* (5933), 1417-1420.

92. Sun, B.; Voznyy, O.; Tan, H.; Stadler, P.; Liu, M.; Walters, G.; Proppe, A. H.; Liu, M.; Fan, J.; Zhuang, T.; Li, J.; Wei, M.; Xu, J.; Kim, Y.; Hoogland, S.; Sargent, E. H., Pseudohalide-Exchanged Quantum Dot Solids Achieve Record Quantum Efficiency in Infrared Photovoltaics. *Adv. Mater.* **2017,** *29* (27), 1700749.

93. Kramer, I. J.; Levina, L.; Debnath, R.; Zhitomirsky, D.; Sargent, E. H., Solar Cells Using Quantum Funnels. *Nano Lett.* **2011,** *11* (9), 3701-3706.

94. Chuang, C.-H. M.; Brown, P. R.; Bulović, V.; Bawendi, M. G., Improved performance and stability in quantum dot solar cells through band alignment engineering. *Nature Materials* **2014,** *13*, 796.

95. Chuang, C.-H. M.; Brown, P. R.; Bulović, V.; Bawendi, M. G., Improved performance and stability in quantum dot solar cells through band alignment engineering. *Nature Materials* **2014,** *13* (8), 796-801.

96. Huan, L.; Jiang, T.; J., K. I.; Ratan, D.; I., K. G.; Xihua, W.; Armin, F.; Rui, L.; Lukasz, B.; Larissa, L.; H., S. E., Electron Acceptor Materials Engineering in Colloidal Quantum Dot Solar Cells. *Adv. Mater.* **2011,** *23* (33), 3832-3837.

97. Ruili, W.; Xun, W.; Kaimin, X.; Wenjia, Z.; Yuequn, S.; Haoying, T.; Hao, C.; Zhijun, N., Highly Efficient Inverted Structural Quantum Dot Solar Cells. *Adv. Mater.* **2018,** *30* (7), 1704882.

98. Azmi, R.; Oh, S.-H.; Jang, S.-Y., High-Efficiency Colloidal Quantum Dot Photovoltaic Devices Using Chemically Modified Heterojunctions. *ACS Energy Letters* **2016,** *1* (1), 100-106.

99. Yuan, M.; Voznyy, O.; Zhitomirsky, D.; Kanjanaboos, P.; Sargent, E. H., Synergistic Doping of Fullerene Electron Transport Layer and Colloidal Quantum Dot Solids Enhances Solar Cell Performance. *Adv. Mater.* **2015,** *27* (5), 917-921.

100. Assadi, M. K.; Bakhoda, S.; Saidur, R.; Hanaei, H., Recent progress in perovskite solar cells. *Renewable and Sustainable Energy Reviews* **2018,** *81*, 2812-2822.

101. Sha, W. E. I.; Ren, X.; Chen, L.; Choy, W. C. H., The efficiency limit of CH3NH3PbI3

perovskite solar cells. *Appl. Phys. Lett.* **2015,** *106* (22), 221104.

102. Ibn-Mohammed, T.; Koh, S. C. L.; Reaney, I. M.; Acquaye, A.; Schileo, G.; Mustapha, K. B.; Greenough, R., Perovskite solar cells: An integrated hybrid lifecycle assessment and review in comparison with other photovoltaic technologies. *Renewable and Sustainable Energy Reviews* **2017,** *80*, 1321-1344.

103. Giorgi, G.; Fujisawa, J.-I.; Segawa, H.; Yamashita, K., Small Photocarrier Effective Masses Featuring Ambipolar Transport in Methylammonium Lead Iodide Perovskite: A Density Functional Analysis. *J. Phys. Chem. Lett.* **2013,** *4* (24), 4213-4216.

104. Yin, W.-J.; Yang, J.-H.; Kang, J.; Yan, Y.; Wei, S.-H., Halide perovskite materials for solar cells: a theoretical review. *Journal of Materials Chemistry A* **2015,** *3* (17), 8926-8942.

105. Wang, B.; Xiao, X.; Chen, T., Perovskite photovoltaics: a high-efficiency newcomer to the solar cell family. *Nanoscale* **2014,** *6* (21), 12287-12297.

106. Travis, W.; Glover, E. N. K.; Bronstein, H.; Scanlon, D. O.; Palgrave, R. G., On the application of the tolerance factor to inorganic and hybrid halide perovskites: a revised system. *Chemical Science* **2016,** *7* (7), 4548-4556.

107. Park, N.-G., Perovskite solar cells: an emerging photovoltaic technology. *Mater. Today* **2015,** *18* (2), 65-72.

108. D'Innocenzo, V.; Grancini, G.; Alcocer, M. J. P.; Kandada, A. R. S.; Stranks, S. D.; Lee, M. M.; Lanzani, G.; Snaith, H. J.; Petrozza, A., Excitons versus free charges in organo-lead tri-halide perovskites. *Nat. Commun.* **2014,** *5*, 3586.

109. Pang, S.; Hu, H.; Zhang, J.; Lv, S.; Yu, Y.; Wei, F.; Qin, T.; Xu, H.; Liu, Z.; Cui, G., NH2CH═NH2PbI3: An Alternative Organolead Iodide Perovskite Sensitizer for Mesoscopic Solar Cells. *Chem. Mater.* **2014,** *26* (3), 1485-1491.

110. Im, J.-H.; Chung, J.; Kim, S.-J.; Park, N.-G., Synthesis, structure, and photovoltaic property of a nanocrystalline 2H perovskite-type novel sensitizer (CH3CH2NH3)PbI3. *Nanoscale Research Letters* **2012,** *7* (1), 353.

111. Ogomi, Y.; Morita, A.; Tsukamoto, S.; Saitho, T.; Fujikawa, N.; Shen, Q.; Toyoda, T.; Yoshino, K.; Pandey, S. S.; Ma, T.; Hayase, S., CH3NH3SnxPb(1–x)I3 Perovskite Solar Cells Covering up to 1060 nm. *J. Phys. Chem. Lett.* **2014,** *5* (6), 1004-1011.

112. Zhu, Z.; Chueh, C. C.; Li, N.; Mao, C.; Jen, A. K. Y., Realizing Efficient Lead-Free Formamidinium Tin Triiodide Perovskite Solar Cells via a Sequential Deposition Route. *Adv. Mater.* **2018,** *30* (6), 1703800.

113. Noh, J. H.; Im, S. H.; Heo, J. H.; Mandal, T. N.; Seok, S. I., Chemical Management for Colorful, Efficient, and Stable Inorganic–Organic Hybrid Nanostructured Solar Cells. *Nano Lett.* **2013,** *13* (4), 1764-1769.

114. Hao, F.; Stoumpos, C. C.; Cao, D. H.; Chang, R. P. H.; Kanatzidis, M. G., Lead-free solid-state organic–inorganic halide perovskite solar cells. *Nature Photonics* **2014,** *8*, 489.

115. Yin, W. J.; Shi, T.; Yan, Y., Unique Properties of Halide Perovskites as Possible Origins of the Superior Solar Cell Performance. *Adv. Mater.* **2014,** *26* (27), 4653-4658.

116. Frost, J. M.; Butler, K. T.; Brivio, F.; Hendon, C. H.; van Schilfgaarde, M.; Walsh, A., Atomistic Origins of High-Performance in Hybrid Halide Perovskite Solar Cells. *Nano Lett.* **2014,** *14* (5), 2584-2590.

117. Ahmadi, M.; Wu, T.; Hu, B., A Review on Organic–Inorganic Halide Perovskite Photodetectors: Device Engineering and Fundamental Physics. *Adv. Mater.* **2017,** *29* (41), 1605242.

118. Herz, L. M., Charge-Carrier Mobilities in Metal Halide Perovskites: Fundamental Mechanisms and Limits. *ACS Energy Letters* **2017,** *2* (7), 1539-1548.

119. Li, C.; Wu, Y.; Poplawsky, J.; Pennycook, T. J.; Paudel, N.; Yin, W.; Haigh, S. J.; Oxley, M. P.; Lupini, A. R.; Al-Jassim, M.; Pennycook, S. J.; Yan, Y., Grain-Boundary-Enhanced Carrier Collection in CdTe Solar Cells. *Phys. Rev. Lett.* **2014,** *112* (15), 156103.

120. Almora, O.; Vaillant-Roca, L.; Garcia-Belmonte, G., Perovskite Solar Cells: A brief Introduction and some Remarks. *2017* **2017,** *34* (1), 11.

121. Zhou, D.; Zhou, T.; Tian, Y.; Zhu, X.; Tu, Y., Perovskite-Based Solar Cells: Materials, Methods, and Future Perspectives. *Journal of Nanomaterials* **2018,** *2018*, 15.

122. Ausfelder, F.; Beilmann, C.; Bertau, M.; Bräuninger, S.; Heinzel, A.; Hoer, R.; Koch, W.; Mahlendorf, F.; Metzelthin, A.; Peuckert, M.; Plass, L.; Räuchle, K.; Reuter, M.; Schaub, G.; Schiebahn, S.; Schwab, E.; Schüth, F.; Stolten, D.; Teßmer, G.; Wagemann, K.; Ziegahn, K. F., Energy Storage as Part of a Secure Energy Supply. *ChemBioEng Reviews* **2017,** *4* (3), 144-210.

123. Correa-Baena, J.-P.; Saliba, M.; Buonassisi, T.; Grätzel, M.; Abate, A.; Tress, W.; Hagfeldt, A., Promises and challenges of perovskite solar cells. *Science* **2017,** *358* (6364), 739-744.

124. Meng, L.; You, J.; Guo, T.-F.; Yang, Y., Recent Advances in the Inverted Planar Structure of Perovskite Solar Cells. *Acc. Chem. Res.* **2016,** *49* (1), 155-165.

125. Kim, H.-S.; Lee, C.-R.; Im, J.-H.; Lee, K.-B.; Moehl, T.; Marchioro, A.; Moon, S.-J.; Humphry-Baker, R.; Yum, J.-H.; Moser, J. E.; Grätzel, M.; Park, N.-G., Lead iodide perovskite sensitized all-solid-state submicron thin film mesoscopic solar cell with efficiency exceeding 9%. *Sci. Rep.*

126. Yang, W. S.; Park, B.-W.; Jung, E. H.; Jeon, N. J.; Kim, Y. C.; Lee, D. U.; Shin, S. S.; Seo, J.; Kim, E. K.; Noh, J. H.; Seok, S. I., Iodide management in formamidinium-lead-halide–based perovskite layers for efficient solar cells. *Science* **2017,** *356* (6345), 1376-1379.

127. Zhao, X.; Tao, L.; Li, H.; Huang, W.; Sun, P.; Liu, J.; Liu, S.; Sun, Q.; Cui, Z.; Sun, L.; Shen, Y.; Yang, Y.; Wang, M., Efficient Planar Perovskite Solar Cells with Improved Fill Factor via Interface Engineering with Graphene. *Nano Lett.* **2018,** *18* (4), 2442-2449.

128. Ahn, N.; Son, D.-Y.; Jang, I.-H.; Kang, S. M.; Choi, M.; Park, N.-G., Highly Reproducible Perovskite Solar Cells with Average Efficiency of 18.3% and Best Efficiency of 19.7% Fabricated via Lewis Base Adduct of Lead(II) Iodide. *J. Am. Chem. Soc.* **2015,** *137* (27), 8696-8699.

129. Song, T.-B.; Chen, Q.; Zhou, H.; Jiang, C.; Wang, H.-H.; Yang, Y.; Liu, Y.; You, J.; Yang, Y., Perovskite solar cells: film formation and properties. *Journal of Materials Chemistry A* **2015,** *3* (17), 9032-9050.

130. Liu, M.; Johnston, M. B.; Snaith, H. J., Efficient planar heterojunction perovskite solar cells by vapour deposition. *Nature* **2013,** *501*, 395.

131. Jeon, N. J.; Noh, J. H.; Kim, Y. C.; Yang, W. S.; Ryu, S.; Seok, S. I., Solvent engineering for high-performance inorganic–organic hybrid perovskite solar cells. *Nature Materials* **2014,** *13*, 897.

132. Yang, S.; Fu, W.; Zhang, Z.; Chen, H.; Li, C.-Z., Recent advances in perovskite solar cells: efficiency, stability and lead-free perovskite. *Journal of Materials Chemistry A* **2017,** *5* (23), 11462-11482.

133. Shen, D.; Yu, X.; Cai, X.; Peng, M.; Ma, Y.; Su, X.; Xiao, L.; Zou, D., Understanding the solvent-assisted crystallization mechanism inherent in efficient organic-inorganic halide perovskite solar cells. *Journal of Materials Chemistry A* **2014,** *2* (48), 20454-20461.

134. Wu, W.-Q.; Chen, D.; McMaster, W. A.; Cheng, Y.-B.; Caruso, R. A., Solvent-Mediated Intragranular-Coarsening of CH3NH3PbI3 Thin Films toward High-Performance Perovskite Photovoltaics. *ACS Appl. Mater. Inter.* **2017,** *9* (37), 31959-31967.

135. Huang, F.; Dkhissi, Y.; Huang, W.; Xiao, M.; Benesperi, I.; Rubanov, S.; Zhu, Y.; Lin, X.; Jiang, L.; Zhou, Y.; Gray-Weale, A.; Etheridge, J.; McNeill, C. R.; Caruso, R. A.; Bach, U.; Spiccia, L.; Cheng, Y.-B., Gas-assisted preparation of lead iodide perovskite films consisting of a monolayer of single crystalline grains for high efficiency planar solar cells. *Nano Energy* **2014,** *10*, 10-18.

136. Burschka, J.; Pellet, N.; Moon, S.-J.; Humphry-Baker, R.; Gao, P.; Nazeeruddin, M. K.; Grätzel, M., Sequential deposition as a route to high-performance perovskite-sensitized solar cells. *Nature* **2013,** *499*, 316.

137. Xu, Y.; Zhu, L.; Shi, J.; Xu, X.; Xiao, J.; Dong, J.; Wu, H.; Luo, Y.; Li, D.; Meng, Q., The Effect of Humidity upon the Crystallization Process of Two-Step Spin-Coated Organic–Inorganic Perovskites. *Chemphyschem* **2016,** *17* (1), 112-118.

138. Bi, D.; Yi, C.; Luo, J.; Décoppet, J.-D.; Zhang, F.; Zakeeruddin, Shaik M.; Li, X.; Hagfeldt, A.; Grätzel, M., Polymer-templated nucleation and crystal growth of perovskite films for solar cells with efficiency greater than 21%. *Nature Energy* **2016,** *1*, 16142.

139. Zhao, P.; Kim, B. J.; Jung, H. S., Passivation in perovskite solar cells: A review. *Materials Today Energy* **2018,** *7*, 267-286.

140. Marchioro, A.; Teuscher, J.; Friedrich, D.; Kunst, M.; van de Krol, R.; Moehl, T.; Grätzel, M.; Moser, J.-E., Unravelling the mechanism of photoinduced charge transfer processes in lead iodide perovskite solar cells. *Nature Photonics* **2014,** *8*, 250.

141. Wang, C.; Zhao, D.; Yu, Y.; Shrestha, N.; Grice, C. R.; Liao, W.; Cimaroli, A. J.; Chen, J.; Ellingson, R. J.; Zhao, X.; Yan, Y., Compositional and morphological engineering of mixed cation perovskite films for highly efficient planar and flexible solar cells with reduced hysteresis. *Nano*

Energy **2017,** *35*, 223-232.

142. Wang, S.; Dong, W.; Fang, X.; Zhang, Q.; Zhou, S.; Deng, Z.; Tao, R.; Shao, J.; Xia, R.; Song, C.; Hu, L.; Zhu, J., Credible evidence for the passivation effect of remnant PbI2 in CH3NH3PbI3 films in improving the performance of perovskite solar cells. *Nanoscale* **2016,** *8* (12), 6600-6608.

143. Wang, H. Y.; Hao, M. Y.; Han, J.; Yu, M.; Qin, Y.; Zhang, P.; Guo, Z. X.; Ai, X. C.; Zhang, J. P., Adverse Effects of Excess Residual PbI2 on Photovoltaic Performance, Charge Separation, and Trap-State Properties in Mesoporous Structured Perovskite Solar Cells. *Chemistry – A European Journal* **2017,** *23* (16), 3986-3992.

144. Jiang, F.; Rong, Y.; Liu, H.; Liu, T.; Mao, L.; Meng, W.; Qin, F.; Jiang, Y.; Luo, B.; Xiong, S.; Tong, J.; Liu, Y.; Li, Z.; Han, H.; Zhou, Y., Synergistic Effect of PbI2 Passivation and Chlorine Inclusion Yielding High Open-Circuit Voltage Exceeding 1.15 V in Both Mesoscopic and Inverted Planar CH3NH3PbI3(Cl)-Based Perovskite Solar Cells. *Adv. Funct. Mater.* **2016,** *26* (44), 8119-8127.

145. Kim, Y. C.; Jeon, N. J.; Noh, J. H.; Yang, W. S.; Seo, J.; Yun, J. S.; Ho-Baillie, A.; Huang, S.; Green, M. A.; Seidel, J.; Ahn, T. K.; Seok, S. I., Beneficial Effects of PbI2 Incorporated in Organo-Lead Halide Perovskite Solar Cells. *Adv. Energy Mater.* **2016,** *6* (4), 1502104.

146. Xu, J.; Buin, A.; Ip, A. H.; Li, W.; Voznyy, O.; Comin, R.; Yuan, M.; Jeon, S.; Ning, Z.; McDowell, J. J.; Kanjanaboos, P.; Sun, J.-P.; Lan, X.; Quan, L. N.; Kim, D. H.; Hill, I. G.; Maksymovych, P.; Sargent, E. H., Perovskite–fullerene hybrid materials suppress hysteresis in planar diodes. *Nat. Commun.* **2015,** *6*, 7081.

147. Hwang, B.; Gu, C.; Lee, D.; Lee, J.-S., Effect of halide-mixing on the switching behaviors of organic-inorganic hybrid perovskite memory. *Sci. Rep.* **2017,** *7*, 43794.

148. Zhou, H.; Chen, Q.; Li, G.; Luo, S.; Song, T.-b.; Duan, H.-S.; Hong, Z.; You, J.; Liu, Y.; Yang, Y., Interface engineering of highly efficient perovskite solar cells. *Science* **2014,** *345* (6196), 542-546.

149. Nagaoka, H.; Ma, F.; deQuilettes, D. W.; Vorpahl, S. M.; Glaz, M. S.; Colbert, A. E.; Ziffer, M. E.; Ginger, D. S., Zr Incorporation into TiO2 Electrodes Reduces Hysteresis and Improves Performance in Hybrid Perovskite Solar Cells while Increasing Carrier Lifetimes. *J. Phys. Chem. Lett.* **2015,** *6* (4), 669-675.

150. Wojciechowski, K.; Stranks, S. D.; Abate, A.; Sadoughi, G.; Sadhanala, A.; Kopidakis, N.; Rumbles, G.; Li, C.-Z.; Friend, R. H.; Jen, A. K. Y.; Snaith, H. J., Heterojunction Modification for Highly Efficient Organic–Inorganic Perovskite Solar Cells. *ACS Nano* **2014,** *8* (12), 12701-12709.

151. Tan, H.; Jain, A.; Voznyy, O.; Lan, X.; García de Arquer, F. P.; Fan, J. Z.; Quintero-Bermudez, R.; Yuan, M.; Zhang, B.; Zhao, Y.; Fan, F.; Li, P.; Quan, L. N.; Zhao, Y.; Lu, Z.-H.; Yang, Z.; Hoogland, S.; Sargent, E. H., Efficient and stable solution-processed planar perovskite solar cells via contact passivation. *Science* **2017**.

152. Ke, W.; Fang, G.; Wan, J.; Tao, H.; Liu, Q.; Xiong, L.; Qin, P.; Wang, J.; Lei, H.; Yang, G.; Qin, M.; Zhao, X.; Yan, Y., Efficient hole-blocking layer-free planar halide perovskite thin-film solar cells. *Nat. Commun.* **2015,** *6*, 6700.

153. PowerGuru “P- N junction”. http://www.powerguru.org/p-n-junction/.

154. Commons, W., Solar Spectrum.

155. Collins, D. G.; Blättner, W. G.; Wells, M. B.; Horak, H. G., Backward Monte Carlo Calculations of the Polarization Characteristics of the Radiation Emerging from Spherical-Shell Atmospheres. *Appl. Opt.* **1972,** *11* (11), 2684-2696.

156. Gueymard, C. A.; Myers, D.; Emery, K., Proposed reference irradiance spectra for solar energy systems testing. *Solar Energy* **2002,** *73* (6), 443-467.

157. Pattantyus-Abraham, A. G.; Kramer, I. J.; Barkhouse, A. R.; Wang, X. H.; Konstantatos, G.; Debnath, R.; Levina, L.; Raabe, I.; Nazeeruddin, M. K.; Gratzel, M.; Sargent, E. H., Depleted-Heterojunction Colloidal Quantum Dot Solar Cells. *Acs Nano* **2010,** *4* (6), 3374-3380.

158. Wise, F. W., Lead Salt Quantum Dots: the Limit of Strong Quantum Confinement. *Acc. Chem. Res.* **2000,** *33* (11), 773-780.

159. Lan, X.; Voznyy, O.; Kiani, A.; García de Arquer, F. P.; Abbas, A. S.; Kim, G.-H.; Liu, M.; Yang, Z.; Walters, G.; Xu, J.; Yuan, M.; Ning, Z.; Fan, F.; Kanjanaboos, P.; Kramer, I.; Zhitomirsky, D.; Lee, P.; Perelgut, A.; Hoogland, S.; Sargent, E. H., Passivation Using Molecular Halides Increases Quantum Dot Solar Cell Performance. *Adv. Mater.* **2016,** *28* (2), 299-304.

160. Kim, G.-H.; García de Arquer, F. P.; Yoon, Y. J.; Lan, X.; Liu, M.; Voznyy, O.; Yang, Z.; Fan, F.; Ip, A. H.; Kanjanaboos, P.; Hoogland, S.; Kim, J. Y.; Sargent, E. H., High-Efficiency Colloidal Quantum Dot Photovoltaics via Robust Self-Assembled Monolayers. *Nano Lett.* **2015,** *15* (11), 7691-7696.

161. Lan, X.; Voznyy, O.; García de Arquer, F. P.; Liu, M.; Xu, J.; Proppe, A. H.; Walters, G.; Fan, F.; Tan, H.; Liu, M.; Yang, Z.; Hoogland, S.; Sargent, E. H., 10.6% Certified Colloidal Quantum Dot Solar Cells via Solvent-Polarity-Engineered Halide Passivation. *Nano Lett.* **2016,** *16* (7), 4630-4634.

162. Kim, Y.; Bicanic, K.; Tan, H.; Ouellette, O.; Sutherland, B. R.; García de Arquer, F. P.; Jo, J. W.; Liu, M.; Sun, B.; Liu, M.; Hoogland, S.; Sargent, E. H., Nanoimprint-Transfer-Patterned Solids Enhance Light Absorption in Colloidal Quantum Dot Solar Cells. *Nano Lett.* **2017**.

163. Adinolfi, V.; Ning, Z.; Xu, J.; Masala, S.; Zhitomirsky, D.; Thon, S. M.; Sargent, E. H., Electric field engineering using quantum-size-effect-tuned heterojunctions. *Appl. Phys. Lett.* **2013,** *103* (1), 011106.

164. Ning, Z.; Ren, Y.; Hoogland, S.; Voznyy, O.; Levina, L.; Stadler, P.; Lan, X.; Zhitomirsky, D.; Sargent, E. H., All-Inorganic Colloidal Quantum Dot Photovoltaics Employing Solution-Phase Halide Passivation. *Adv. Mater.* **2012,** *24* (47), 6295-6299.

165. Jang, J.; Song, J. H.; Choi, H.; Baik, S. J.; Jeong, S., Photovoltaic light absorber with spatial energy band gradient using PbS quantum dot layers. *Sol. Energy Mater. Sol. Cells* **2015,** *141*, 270-274.

166. Zhang, X.; Zhang, Y.; Yan, L.; Wu, H.; Gao, W.; Zhao, J.; Yu, W. W., PbSe nanocrystal solar cells using bandgap engineering. *RSC Advances* **2015,** *5* (80), 65569-65574.

167. Kim, J. Y.; Adinolfi, V.; Sutherland, B. R.; Voznyy, O.; Kwon, S. J.; Kim, T. W.; Kim, J.; Ihee, H.; Kemp, K.; Adachi, M.; Yuan, M.; Kramer, I.; Zhitomirsky, D.; Hoogland, S.; Sargent, E. H., Single-step fabrication of quantum funnels via centrifugal colloidal casting of nanoparticle films. *Nat. Commun.* **2015,** *6*, 7772.

168. Ning, Z.; Zhitomirsky, D.; Adinolfi, V.; Sutherland, B.; Xu, J.; Voznyy, O.; Maraghechi, P.; Lan, X.; Hoogland, S.; Ren, Y.; Sargent, E. H., Graded Doping for Enhanced Colloidal Quantum Dot Photovoltaics. *Adv. Mater.* **2013,** *25* (12), 1719-1723.

169. Santra, P. K.; Palmstrom, A. F.; Tanskanen, J. T.; Yang, N.; Bent, S. F., Improving Performance in Colloidal Quantum Dot Solar Cells by Tuning Band Alignment through Surface Dipole Moments. *J. Phys. Chem. C* **2015,** *119* (6), 2996-3005.

170. Malik, R. J.; Capasso, F.; Stall, R. A.; Kiehl, R. A.; Ryan, R. W.; Wunder, R.; Bethea, C. G., High-gain, high-frequency AlGaAs/GaAs graded band-gap base bipolar transistors with a Be diffusion setback layer in the base. *Appl. Phys. Lett.* **1985,** *46* (6), 600-602.

171. Konagai, M.; Takahashi, K., Graded-band-gap pGa1−xAlxAs-nGaAs heterojunction solar cells. *J. Appl. Phys.* **1975,** *46* (8), 3542-3546.

172. Dullweber, T.; anna, G. H.; Rau, U.; Schock, H. W., A new approach to high-efficiency solar cells by band gap grading in Cu(In,Ga)Se2 chalcopyrite semiconductors. *Sol. Energy Mater. Sol. Cells* **2001,** *67* (1–4), 145-150.

173. Tang, J.; Kemp, K. W.; Hoogland, S.; Jeong, K. S.; Liu, H.; Levina, L.; Furukawa, M.; Wang, X.; Debnath, R.; Cha, D.; Chou, K. W.; Fischer, A.; Amassian, A.; Asbury, J. B.; Sargent, E. H., Colloidal-quantum-dot photovoltaics using atomic-ligand passivation. *Nat Mater* **2011,** *10* (10), 765-771.

174. Choi, H.; Ko, J.-H.; Kim, Y.-H.; Jeong, S., Steric-Hindrance-Driven Shape Transition in PbS Quantum Dots: Understanding Size-Dependent Stability. *J. Am. Chem. Soc.* **2013,** *135* (14), 5278-5281.

175. Jena, A. K.; Chen, H.-W.; Kogo, A.; Sanehira, Y.; Ikegami, M.; Miyasaka, T., The Interface between FTO and the TiO2 Compact Layer Can Be One of the Origins to Hysteresis in Planar Heterojunction Perovskite Solar Cells. *ACS Appl. Mater. Inter.* **2015,** *7* (18), 9817-9823.

176. Moreels, I.; Lambert, K.; Smeets, D.; De Muynck, D.; Nollet, T.; Martins, J. C.; Vanhaecke, F.; Vantomme, A.; Delerue, C.; Allan, G.; Hens, Z., Size-Dependent Optical Properties of Colloidal PbS Quantum Dots. *ACS Nano* **2009,** *3* (10), 3023-3030.

177. Koleilat, G. I.; Levina, L.; Shukla, H.; Myrskog, S. H.; Hinds, S.; Pattantyus-Abraham, A. G.; Sargent, E. H., Efficient, Stable Infrared Photovoltaics Based on Solution-Cast Colloidal Quantum Dots. *ACS Nano* **2008,** *2* (5), 833-840.

178. Tang, J.; Sargent, E. H., Infrared Colloidal Quantum Dots for Photovoltaics: Fundamentals and Recent Progress. *Adv. Mater.* **2011,** *23* (1), 12-29.

179. Kang, I.; Wise, F. W., Electronic structure and optical properties of PbS and PbSe quantum dots. *Journal of the Optical Society of America B* **1997,** *14* (7), 1632-1646.

180. Servaites, J. D.; Yeganeh, S.; Marks, T. J.; Ratner, M. A., Efficiency Enhancement in Organic Photovoltaic Cells: Consequences of Optimizing Series Resistance. *Adv. Funct. Mater.* **2010,** *20* (1), 97-104.

181. Kawawaki, T.; Wang, H.; Kubo, T.; Saito, K.; Nakazaki, J.; Segawa, H.; Tatsuma, T., Efficiency Enhancement of PbS Quantum Dot/ZnO Nanowire Bulk-Heterojunction Solar Cells by Plasmonic Silver Nanocubes. *ACS Nano* **2015,** *9* (4), 4165-4172.

182. Hou, B.; Cho, Y.; Kim, B. S.; Hong, J.; Park, J. B.; Ahn, S. J.; Sohn, J. I.; Cha, S.; Kim, J. M., Highly Monodispersed PbS Quantum Dots for Outstanding Cascaded-Junction Solar Cells. *ACS Energy Letters* **2016,** *1* (4), 834-839.

183. Ihly, R.; Tolentino, J.; Liu, Y.; Gibbs, M.; Law, M., The Photothermal Stability of PbS Quantum Dot Solids. *ACS Nano* **2011,** *5* (10), 8175-8186.

184. Ehrler, B.; Musselman, K. P.; Böhm, M. L.; Morgenstern, F. S. F.; Vaynzof, Y.; Walker, B. J.; MacManus-Driscoll, J. L.; Greenham, N. C., Preventing Interfacial Recombination in Colloidal Quantum Dot Solar Cells by Doping the Metal Oxide. *ACS Nano* **2013,** *7* (5), 4210-4220.

185. Gao, F.; Li, Z.; Wang, J.; Rao, A.; Howard, I. A.; Abrusci, A.; Massip, S.; McNeill, C. R.; Greenham, N. C., Trap-Induced Losses in Hybrid Photovoltaics. *ACS Nano* **2014,** *8* (4), 3213-3221.

186. Riedel, I.; Parisi, J.; Dyakonov, V.; Lutsen, L.; Vanderzande, D.; Hummelen, J. C., Effect of Temperature and Illumination on the Electrical Characteristics of Polymer–Fullerene Bulk-Heterojunction Solar Cells. *Adv. Funct. Mater.* **2004,** *14* (1), 38-44.

187. Sun, Z.; Sitbon, G.; Pons, T.; Bakulin, A. A.; Chen, Z., Reduced Carrier Recombination in PbS - CuInS2 Quantum Dot Solar Cells. *Sci. Rep.* **2015,** *5*, 10626.

188. Cowan, S. R.; Roy, A.; Heeger, A. J., Recombination in polymer-fullerene bulk heterojunction solar cells. *Physical Review B* **2010,** *82* (24), 245207.

189. Kemp, K. W.; Labelle, A. J.; Thon, S. M.; Ip, A. H.; Kramer, I. J.; Hoogland, S.; Sargent, E. H., Interface Recombination in Depleted Heterojunction Photovoltaics based on Colloidal Quantum Dots. *Adv. Energy Mater.* **2013,** *3* (7), 917-922.

190. Zhang, Y.; Wu, G.; Mora-Seró, I.; Ding, C.; Liu, F.; Huang, Q.; Ogomi, Y.; Hayase, S.; Toyoda, T.; Wang, R.; Otsuki, J.; Shen, Q., Improvement of Photovoltaic Performance of Colloidal Quantum Dot Solar Cells Using Organic Small Molecule as Hole-Selective Layer. *J. Phys. Chem. Lett.* **2017**, 2163-2169.

191. Berry, W. B.; Longrigg, P., Open-circuit voltage decay — measures of amorphous silicon material stability and module degradation. *Solar Cells* **1988,** *24* (3), 321-328.

192. Zaban, A.; Greenshtein, M.; Bisquert, J., Determination of the Electron Lifetime in Nanocrystalline Dye Solar Cells by Open-Circuit Voltage Decay Measurements. *Chemphyschem* **2003,** *4* (8), 859-864.

193. Benmir, A.; Aida, M. S., Analytical Modeling and Simulation of CIGS Solar Cells. *Energy Procedia* **2013,** *36*, 618-627.

194. Morales-Acevedo, A., Variable band-gap semiconductors as the basis of new solar cells. *Solar Energy* **2009,** *83* (9), 1466-1471.

195. Zhitomirsky, D.; Voznyy, O.; Hoogland, S.; Sargent, E. H., Measuring Charge Carrier Diffusion in Coupled Colloidal Quantum Dot Solids. *ACS Nano* **2013,** *7* (6), 5282-5290.

196. Khan, J.; Yang, X.; Qiao, K.; Deng, H.; Zhang, J.; Liu, Z.; Ahmad, W.; Zhang, J.; Li, D.; Liu, H.; Song, H.; Cheng, C.; Tang, J., Low-temperature-processed SnO2-Cl for efficient PbS quantum-dot solar cells via defect passivation. *Journal of Materials Chemistry A* **2017,** *5* (33), 17240-17247.

197. Hu, L.; Li, D.-B.; Gao, L.; Tan, H.; Chen, C.; Li, K.; Li, M.; Han, J.-B.; Song, H.; Liu, H.; Tang, J., Graphene Doping Improved Device Performance of ZnMgO/PbS Colloidal Quantum Dot Photovoltaics. *Adv. Funct. Mater.* **2016,** *26* (12), 1899-1907.

198. Lan, X.; Masala, S.; Sargent, E. H., Charge-extraction strategies for colloidal quantum dot photovoltaics. *Nature Materials* **2014,** *13*, 233.

199. Liu, H.; Tang, J.; Kramer, I. J.; Debnath, R.; Koleilat, G. I.; Wang, X.; Fisher, A.; Li, R.; Brzozowski, L.; Levina, L.; Sargent, E. H., Electron Acceptor Materials Engineering in Colloidal Quantum Dot Solar Cells. *Adv. Mater.* **2011,** *23* (33), 3832-3837.

200. Willis, S. M.; Cheng, C.; Assender, H. E.; Watt, A. A. R., The Transitional Heterojunction Behavior of PbS/ZnO Colloidal Quantum Dot Solar Cells. *Nano Lett.* **2012,** *12* (3), 1522-1526.

201. Mora-Seró, I.; Bisquert, J., Breakthroughs in the Development of Semiconductor-Sensitized Solar Cells. *J. Phys. Chem. Lett.* **2010,** *1* (20), 3046-3052.

202. Braga, A.; Giménez, S.; Concina, I.; Vomiero, A.; Mora-Seró, I., Panchromatic Sensitized Solar Cells Based on Metal Sulfide Quantum Dots Grown Directly on Nanostructured TiO2 Electrodes. *J. Phys. Chem. Lett.* **2011,** *2* (5), 454-460.

203. Minemoto, T.; Hashimoto, Y.; Shams-Kolahi, W.; Satoh, T.; Negami, T.; Takakura, H.; Hamakawa, Y., Control of conduction band offset in wide-gap Cu(In,Ga)Se2 solar cells. *Sol. Energy Mater. Sol. Cells* **2003,** *75* (1), 121-126.

204. Hoye, R. L. Z.; Ehrler, B.; Böhm, M. L.; Muñoz-Rojas, D.; Altamimi, R. M.; Alyamani, A. Y.; Vaynzof, Y.; Sadhanala, A.; Ercolano, G.; Greenham, N. C.; Friend, R. H.; MacManus-Driscoll, J. L.; Musselman, K. P., Improved Open- Circuit Voltage in ZnO–PbSe Quantum Dot Solar Cells by Understanding and Reducing Losses Arising from the ZnO Conduction Band Tail. *Adv. Energy Mater.* **2014,** *4* (8), 1301544-n/a.

205. Zhang, X.; Johansson, E. M. J., Reduction of charge recombination in PbS colloidal quantum dot solar cells at the quantum dot/ZnO interface by inserting a MgZnO buffer layer. *Journal of Materials Chemistry A* **2017,** *5* (1), 303-310.

206. Olson, D. C.; Shaheen, S. E.; White, M. S.; Mitchell, W. J.; van Hest, M. F. A. M.; Collins, R. T.; Ginley, D. S., Band-Offset Engineering for Enhanced Open-Circuit Voltage in Polymer–Oxide Hybrid Solar Cells. *Adv. Funct. Mater.* **2007,** *17* (2), 264-269.

207. Raj, C. J.; Prabakar, K.; Karthick, S. N.; Hemalatha, K. V.; Son, M.-K.; Kim, H.-J., Banyan

Root Structured Mg-Doped ZnO Photoanode Dye-Sensitized Solar Cells. *J. Phys. Chem. C* **2013,** *117* (6), 2600-2607.

208. Bang, S.; Lee, S.; Ko, Y.; Park, J.; Shin, S.; Seo, H.; Jeon, H., Photocurrent detection of chemically tuned hierarchical ZnO nanostructures grown on seed layers formed by atomic layer deposition. *Nanoscale Research Letters* **2012,** *7* (1), 290.

209. Liao, S.-H.; Jhuo, H.-J.; Cheng, Y.-S.; Chen, S.-A., Fullerene Derivative-Doped Zinc Oxide Nanofilm as the Cathode of Inverted Polymer Solar Cells with Low-Bandgap Polymer (PTB7-Th) for High Performance. *Adv. Mater.* **2013,** *25* (34), 4766-4771.

210. Yang, T.; Cai, W.; Qin, D.; Wang, E.; Lan, L.; Gong, X.; Peng, J.; Cao, Y., Solution-Processed Zinc Oxide Thin Film as a Buffer Layer for Polymer Solar Cells with an Inverted Device Structure. *J. Phys. Chem. C* **2010,** *114* (14), 6849-6853.

211. Yin, Z.; Zheng, Q.; Chen, S.-C.; Cai, D.; Zhou, L.; Zhang, J., Bandgap Tunable Zn1-xMgxO Thin Films as Highly Transparent Cathode Buffer Layers for High-Performance Inverted Polymer Solar Cells. *Adv. Energy Mater.* **2014,** *4* (7), 1301404-n/a.

212. Wei, M.; Boutwell, R. C.; Mares, J. W.; Scheurer, A.; Schoenfeld, W. V., Bandgap engineering of sol-gel synthesized amorphous Zn1−xMgxO films. *Appl. Phys. Lett.* **2011,** *98* (26), 261913.

213. Tauc, J.; Grigorovici, R.; Vancu, A., Optical Properties and Electronic Structure of Amorphous Germanium. *physica status solidi (b)* **1966,** *15* (2), 627-637.

214. Zhang, H. H.; Pan, X. H.; Lu, B.; Huang, J. Y.; Ding, P.; Chen, W.; He, H. P.; Lu, J. G.; Chen, S. S.; Ye, Z. Z., Mg composition dependent band offsets of Zn1-xMgxO/ZnO heterojunctions. *Phys. Chem. Chem. Phys.* **2013,** *15* (27), 11231-11235.

215. Minemoto, T.; Hashimoto, Y.; Satoh, T.; Negami, T.; Takakura, H.; Hamakawa, Y., Cu(In,Ga)Se2 solar cells with controlled conduction band offset of window/Cu(In,Ga)Se2 layers. *J. Appl. Phys.* **2001,** *89* (12), 8327-8330.

216. Törndahl, T.; Platzer-Björkman, C.; Kessler, J.; Edoff, M., Atomic layer deposition of Zn1−xMgxO buffer layers for Cu(In,Ga)Se2 solar cells. *Progress in Photovoltaics: Research and Applications* **2007,** *15* (3), 225-235.

217. Minemoto, T.; Murata, M., Theoretical analysis on effect of band offsets in perovskite solar cells. *Sol. Energy Mater. Sol. Cells* **2015,** *133* (Supplement C), 8-14.

218. Cross, R. B. M.; Souza, M. M. D.; Narayanan, E. M. S., A low temperature combination method for the production of ZnO nanowires. *Nanotechnology* **2005,** *16* (10), 2188.

219. Vempati, S.; Mitra, J.; Dawson, P., One-step synthesis of ZnO nanosheets: a blue-white fluorophore. *Nanoscale Research Letters* **2012,** *7* (1), 470.

220. Tvrdy, K.; Frantsuzov, P. A.; Kamat, P. V., Photoinduced electron transfer from semiconductor quantum dots to metal oxide nanoparticles. *Proc. Natl. Acad. Sci. U. S. A.* **2011,** *108* (1), 29-34.

221. Hyun, B.-R.; Bartnik, A. C.; Sun, L.; Hanrath, T.; Wise, F. W., Control of Electron Transfer from Lead-Salt Nanocrystals to TiO2. *Nano Lett.* **2011,** *11* (5), 2126-2132.

222. Tiwana, P.; Docampo, P.; Johnston, M. B.; Herz, L. M.; Snaith, H. J., The origin of an efficiency improving "light soaking" effect in SnO2 based solid-state dye-sensitized solar cells. *Energy & Environmental Science* **2012,** *5* (11), 9566-9573.

223. Simon M. Sze, K. K. N., *Physics of Semiconductor Devices*. 3rd Edition ed.; Wiley-Interscience: New York, USA, **2006**.

224. Servaites, J. D.; Ratner, M. A.; Marks, T. J., Organic solar cells: A new look at traditional models. *Energy & Environmental Science* **2011,** *4* (11), 4410-4422.

225. Saitoh, H.; Takano, A.; Kawaguchi, S.; Washio, T.; Ohshio, S.; Akasaka, H., Discharge property between magnesium oxide films with various true densities. *J. Ceram. Soc. Jpn.* **2009,** *117* (1366), 780-782.

226. Zhang, X.; Yang, D.; Yang, Z.; Guo, X.; Liu, B.; Ren, X.; Liu, S., Improved PEDOT:PSS/c-Si hybrid solar cell using inverted structure and effective passivation. *Sci. Rep.* **2016,** *6*, 35091.

227. Zhang, Y.; Wu, G.; Mora-Seró, I.; Ding, C.; Liu, F.; Huang, Q.; Ogomi, Y.; Hayase, S.; Toyoda, T.; Wang, R.; Otsuki, J.; Shen, Q., Improvement of Photovoltaic Performance of Colloidal Quantum Dot Solar Cells Using Organic Small Molecule as Hole-Selective Layer. *J. Phys. Chem. Lett.* **2017,** *8* (10), 2163-2169.

228. Chuang, C.-H. M.; Maurano, A.; Brandt, R. E.; Hwang, G. W.; Jean, J.; Buonassisi, T.; Bulović, V.; Bawendi, M. G., Open-Circuit Voltage Deficit, Radiative Sub-Bandgap States, and Prospects in Quantum Dot Solar Cells. *Nano Lett.* **2015,** *15* (5), 3286-3294.

229. Bozyigit, D.; Volk, S.; Yarema, O.; Wood, V., Quantification of Deep Traps in Nanocrystal Solids, Their Electronic Properties, and Their Influence on Device Behavior. *Nano Lett.* **2013,** *13* (11), 5284-5288.

230. Minami, T., Chapter Five - Transparent Conductive Oxides for Transparent Electrode Applications. In *Semiconductors and Semimetals*, Svensson, B. G.; Pearton, S. J.; Jagadish, C., Eds. Elsevier: **2013**, pp 159-200.

231. Leventis, H. C.; O'Mahony, F.; Akhtar, J.; Afzaal, M.; O'Brien, P.; Haque, S. A., Transient Optical Studies of Interfacial Charge Transfer at Nanostructured Metal Oxide/PbS Quantum Dot/Organic Hole Conductor Heterojunctions. *J. Am. Chem. Soc.* **2010,** *132* (8), 2743-2750.

232. Eita, M.; Usman, A.; El-Ballouli, A. a. O.; Alarousu, E.; Bakr, O. M.; Mohammed, O. F., A Layer-by-Layer ZnO Nanoparticle–PbS Quantum Dot Self-Assembly Platform for Ultrafast Interfacial Electron Injection. *Small* **2015,** *11* (1), 112-118.

233. Deschler, F.; Price, M.; Pathak, S.; Klintberg, L. E.; Jarausch, D.-D.; Higler, R.; Hüttner, S.; Leijtens, T.; Stranks, S. D.; Snaith, H. J.; Atatüre, M.; Phillips, R. T.; Friend, R. H., High Photoluminescence Efficiency and Optically Pumped Lasing in Solution-Processed Mixed Halide Perovskite Semiconductors. *J. Phys. Chem. Lett.* **2014,** *5* (8), 1421-1426.

234. Stranks, S. D.; Snaith, H. J., Metal-halide perovskites for photovoltaic and light-emitting devices. *Nature Nanotechnology* **2015,** *10*, 391.

235. Hodes, G., Perovskite-Based Solar Cells. *Science* **2013,** *342* (6156), 317-318.

236. Stranks, S. D.; Eperon, G. E.; Grancini, G.; Menelaou, C.; Alcocer, M. J. P.; Leijtens, T.; Herz, L. M.; Petrozza, A.; Snaith, H. J., Electron-Hole Diffusion Lengths Exceeding 1 Micrometer in an Organometal Trihalide Perovskite Absorber. *Science* **2013,** *342* (6156), 341-344.

237. De Wolf, S.; Holovsky, J.; Moon, S.-J.; Löper, P.; Niesen, B.; Ledinsky, M.; Haug, F.-J.; Yum, J.-H.; Ballif, C., Organometallic Halide Perovskites: Sharp Optical Absorption Edge and Its Relation to Photovoltaic Performance. *J. Phys. Chem. Lett.* **2014,** *5* (6), 1035-1039.

238. Joshi, P. H.; Zhang, L.; Hossain, I. M.; Abbas, H. A.; Kottokkaran, R.; Nehra, S. P.; Dhaka, M.; Noack, M.; Dalal, V. L., The physics of photon induced degradation of perovskite solar cells. *AIP Advances* **2016,** *6* (11), 115114.

239. Liu, F.; Ding, C.; Zhang, Y.; Ripolles, T. S.; Kamisaka, T.; Toyoda, T.; Hayase, S.; Minemoto, T.; Yoshino, K.; Dai, S.; Yanagida, M.; Noguchi, H.; Shen, Q., Colloidal Synthesis of Air-Stable Alloyed CsSn1–xPbxI3 Perovskite Nanocrystals for Use in Solar Cells. *J. Am. Chem. Soc.* **2017,** *139* (46), 16708-16719.

240. https://www.nrel.gov/pv/assets/images/efficiency-chart.png.

241. Yang, W. S.; Noh, J. H.; Jeon, N. J.; Kim, Y. C.; Ryu, S.; Seo, J.; Seok, S. I., High-performance photovoltaic perovskite layers fabricated through intramolecular exchange. *Science* **2015,** *348* (6240), 1234-1237.

242. Correa-Baena, J.-P.; Anaya, M.; Lozano, G.; Tress, W.; Domanski, K.; Saliba, M.; Matsui, T.; Jacobsson, T. J.; Calvo, M. E.; Abate, A.; Grätzel, M.; Míguez, H.; Hagfeldt, A., Unbroken Perovskite: Interplay of Morphology, Electro-optical Properties, and Ionic Movement. *Adv. Mater.* **2016,** *28* (25), 5031-5037.

243. Saliba, M.; Matsui, T.; Domanski, K.; Seo, J.-Y.; Ummadisingu, A.; Zakeeruddin, S. M.; Correa-Baena, J.-P.; Tress, W. R.; Abate, A.; Hagfeldt, A.; Grätzel, M., Incorporation of rubidium cations into perovskite solar cells improves photovoltaic performance. *Science* **2016,** *354* (6309), 206-209.

244. Li, X.; Bi, D.; Yi, C.; Décoppet, J.-D.; Luo, J.; Zakeeruddin, S. M.; Hagfeldt, A.; Grätzel, M., A vacuum flash–assisted solution process for high-efficiency large-area perovskite solar cells. *Science* **2016,** *353* (6294), 58-62.

245. Li, C.-Z.; Chang, C.-Y.; Zang, Y.; Ju, H.-X.; Chueh, C.-C.; Liang, P.-W.; Cho, N.; Ginger, D. S.; Jen, A. K. Y., Suppressed Charge Recombination in Inverted Organic Photovoltaics via Enhanced Charge Extraction by Using a Conductive Fullerene Electron Transport Layer. *Adv. Mater.* **2014,** *26* (36), 6262-6267.

246. Kim, J. H.; Chueh, C.-C.; Williams, S. T.; Jen, A. K. Y., Room-temperature, solution-processable organic electron extraction layer for high-performance planar heterojunction perovskite

solar cells. *Nanoscale* **2015,** *7* (41), 17343-17349.

247. Tan, H.; Jain, A.; Voznyy, O.; Lan, X.; García de Arquer, F. P.; Fan, J. Z.; Quintero-Bermudez, R.; Yuan, M.; Zhang, B.; Zhao, Y.; Fan, F.; Li, P.; Quan, L. N.; Zhao, Y.; Lu, Z.-H.; Yang, Z.; Hoogland, S.; Sargent, E. H., Efficient and stable solution-processed planar perovskite solar cells via contact passivation. *Science* **2017,** *355* (6326), 722-726.

248. Liu, F.; Zhu, J.; Wei, J.; Li, Y.; Lv, M.; Yang, S.; Zhang, B.; Yao, J.; Dai, S., Numerical simulation: Toward the design of high-efficiency planar perovskite solar cells. *Appl. Phys. Lett.* **2014,** *104* (25), 253508.

249. Schulz, P.; Edri, E.; Kirmayer, S.; Hodes, G.; Cahen, D.; Kahn, A., Interface energetics in organo-metal halide perovskite-based photovoltaic cells. *Energy & Environmental Science* **2014,** *7* (4), 1377-1381.

250. Yang, G.; Tao, H.; Qin, P.; Ke, W.; Fang, G., Recent progress in electron transport layers for efficient perovskite solar cells. *Journal of Materials Chemistry A* **2016,** *4* (11), 3970-3990.

251. Song, J.; Zheng, E.; Liu, L.; Wang, X.-F.; Chen, G.; Tian, W.; Miyasaka, T., Magnesium-doped Zinc Oxide as Electron Selective Contact Layers for Efficient Perovskite Solar Cells. *ChemSusChem* **2016,** *9* (18), 2640-2647.

252. Mahmud, M. A.; Elumalai, N. K.; Upama, M. B.; Wang, D.; Soufiani, A. M.; Wright, M.; Xu, C.; Haque, F.; Uddin, A., Solution-Processed Lithium-Doped ZnO Electron Transport Layer for Efficient Triple Cation (Rb, MA, FA) Perovskite Solar Cells. *ACS Appl. Mater. Inter.* **2017,** *9* (39), 33841-33854.

253. Liu, D.; Li, S.; Zhang, P.; Wang, Y.; Zhang, R.; Sarvari, H.; Wang, F.; Wu, J.; Wang, Z.; Chen, Z. D., Efficient planar heterojunction perovskite solar cells with Li-doped compact TiO2 layer. *Nano Energy* **2017,** *31*, 462-468.

254. Giordano, F.; Abate, A.; Correa Baena, J. P.; Saliba, M.; Matsui, T.; Im, S. H.; Zakeeruddin, S. M.; Nazeeruddin, M. K.; Hagfeldt, A.; Graetzel, M., Enhanced electronic properties in mesoporous TiO2 via lithium doping for high-efficiency perovskite solar cells. *Nat. Commun.* **2016,** *7*, 10379.

255. Azmi, R.; Hadmojo, W. T.; Sinaga, S.; Lee, C.-L.; Yoon, S. C.; Jung, I. H.; Jang, S.-Y., High-Efficiency Low-Temperature ZnO Based Perovskite Solar Cells Based on Highly Polar, Nonwetting Self-Assembled Molecular Layers. *Adv. Energy Mater.*, 1701683-n/a.

256. Kim, J.; Kim, G.; Kim, T. K.; Kwon, S.; Back, H.; Lee, J.; Lee, S. H.; Kang, H.; Lee, K., Efficient planar-heterojunction perovskite solar cells achieved via interfacial modification of a sol-gel ZnO electron collection layer. *Journal of Materials Chemistry A* **2014,** *2* (41), 17291-17296.

257. Huang, X.; Zeng, Z.; Fan, Z.; Liu, J.; Zhang, H., Graphene-Based Electrodes. *Adv. Mater.* **2012,** *24* (45), 5979-6004.

258. Wang, J. T.-W.; Ball, J. M.; Barea, E. M.; Abate, A.; Alexander-Webber, J. A.; Huang, J.; Saliba, M.; Mora-Sero, I.; Bisquert, J.; Snaith, H. J.; Nicholas, R. J., Low-Temperature Processed Electron Collection Layers of Graphene/TiO2 Nanocomposites in Thin Film Perovskite Solar Cells.

Nano Lett. **2014,** *14* (2), 724-730.

259. Barbero, D. R.; Stranks, S. D., Functional Single-Walled Carbon Nanotubes and Nanoengineered Networks for Organic- and Perovskite-Solar-Cell Applications. *Adv. Mater.* **2016,** *28* (44), 9668-9685.

260. Minemoto, T.; Matsui, T.; Takakura, H.; Hamakawa, Y.; Negami, T.; Hashimoto, Y.; Uenoyama, T.; Kitagawa, M., Theoretical analysis of the effect of conduction band offset of window/CIS layers on performance of CIS solar cells using device simulation. *Sol. Energy Mater. Sol. Cells* **2001,** *67* (1), 83-88.

261. Gloeckler, M.; Sites, J. R., Efficiency limitations for wide-band-gap chalcopyrite solar cells. *Thin Solid Films* **2005,** *480-481*, 241-245.

262. Knutsen, K. E.; Schifano, R.; Marstein, E. S.; Svensson, B. G.; Kuznetsov, A. Y., Prediction of high efficiency ZnMgO/Si solar cells suppressing carrier recombination by conduction band engineering. *physica status solidi (a)* **2013,** *210* (3), 585-588.

263. Ding, C.; Zhang, Y.; Liu, F.; Kitabatake, Y.; Hayase, S.; Toyoda, T.; Wang, R.; Yoshino, K.; Minemoto, T.; Shen, Q., Understanding charge transfer and recombination by interface engineering for improving the efficiency of PbS quantum dot solar cells. *Nanoscale Horizons* **2018**.

264. Minemoto, T.; Murata, M., Theoretical analysis on effect of band offsets in perovskite solar cells. *Sol. Energy Mater. Sol. Cells* **2015,** *133*, 8-14.

265. Im, J.-H.; Jang, I.-H.; Pellet, N.; Grätzel, M.; Park, N.-G., Growth of CH3NH3PbI3 cuboids with controlled size for high-efficiency perovskite solar cells. *Nature Nanotechnology* **2014,** *9*, 927.

266. Son, D.-Y.; Lee, J.-W.; Choi, Y. J.; Jang, I.-H.; Lee, S.; Yoo, P. J.; Shin, H.; Ahn, N.; Choi, M.; Kim, D.; Park, N.-G., Self-formed grain boundary healing layer for highly efficient CH3 NH3 PbI3 perovskite solar cells. *Nature Energy* **2016,** *1*, 16081.

267. Shen, Q.; Ogomi, Y.; Park, B.-w.; Inoue, T.; Pandey, S. S.; Miyamoto, A.; Fujita, S.; Katayama, K.; Toyoda, T.; Hayase, S., Multiple electron injection dynamics in linearly-linked two dye co-sensitized nanocrystalline metal oxide electrodes for dye-sensitized solar cells. *Phys. Chem. Chem. Phys.* **2012,** *14* (13), 4605-4613.

268. Shen, Q.; Ogomi, Y.; Das, S. K.; Pandey, S. S.; Yoshino, K.; Katayama, K.; Momose, H.; Toyoda, T.; Hayase, S., Huge suppression of charge recombination in P3HT-ZnO organic-inorganic hybrid solar cells by locating dyes at the ZnO/P3HT interfaces. *Phys. Chem. Chem. Phys.* **2013,** *15* (34), 14370-14376.

269. Osada, N.; Oshima, T.; Kuwahara, S.; Toyoda, T.; Shen, Q.; Katayama, K., Photoexcited carrier dynamics of double-layered CdS/CdSe quantum dot sensitized solar cells measured by heterodyne transient grating and transient absorption methods. *Phys. Chem. Chem. Phys.* **2014,** *16* (12), 5774-5778.

270. Shen, Q.; Ogomi, Y.; Chang, J.; Toyoda, T.; Fujiwara, K.; Yoshino, K.; Sato, K.; Yamazaki, K.; Akimoto, M.; Kuga, Y.; Katayama, K.; Hayase, S., Optical absorption, charge separation and

recombination dynamics in Sn/Pb cocktail perovskite solar cells and their relationships to photovoltaic performances. *Journal of Materials Chemistry A* **2015,** *3* (17), 9308-9316.

271. Lu, Y. F.; Ni, H. Q.; Mai, Z. H.; Ren, Z. M., The effects of thermal annealing on ZnO thin films grown by pulsed laser deposition. *J. Appl. Phys.* **2000,** *88* (1), 498-502.

272. Szörényi, T.; Laude, L. D.; Bertóti, I.; Kántor, Z.; Geretovszky, Z., Excimer laser processing of indium-tin-oxide films: An optical investigation. *J. Appl. Phys.* **1995,** *78* (10), 6211-6219.

273. Hsieh, P.-T.; Chen, Y.-C.; Kao, K.-S.; Wang, C.-M., Luminescence mechanism of ZnO thin film investigated by XPS measurement. *Appl. Phys. A* **2008,** *90* (2), 317-321.

274. Jung, Y.; Yang, W.; Koo, C. Y.; Song, K.; Moon, J., High performance and high stability low temperature aqueous solution-derived Li-Zr co-doped ZnO thin film transistors. *J. Mater. Chem.* **2012,** *22* (12), 5390-5397.

275. Gao, P.; Gratzel, M.; Nazeeruddin, M. K., Organohalide lead perovskites for photovoltaic applications. *Energy & Environmental Science* **2014,** *7* (8), 2448-2463.

276. Sheng, J.; Wang, D.; Wu, S.; Yang, X.; Ding, L.; Zhu, J.; Fang, J.; Gao, P.; Ye, J., Ideal rear contact formed via employing a conjugated polymer for Si/PEDOT:PSS hybrid solar cells. *RSC Advances* **2016,** *6* (19), 16010-16017.

277. Ross, R. T., Some Thermodynamics of Photochemical Systems. *The Journal of Chemical Physics* **1967,** *46* (12), 4590-4593.

278. Wang, J.; Wang, Z.; Huang, B.; Ma, Y.; Liu, Y.; Qin, X.; Zhang, X.; Dai, Y., Oxygen Vacancy Induced Band-Gap Narrowing and Enhanced Visible Light Photocatalytic Activity of ZnO. *ACS Appl. Mater. Inter.* **2012,** *4* (8), 4024-4030.

279. Reish, M. E.; Zhang, Z.; Ma, S.; Harrison, I.; Everitt, H. O., How Annealing and Charge Scavengers Affect Visible Emission from ZnO Nanocrystals. *J. Phys. Chem. C* **2016,** *120* (9), 5108-5113.

280. Shen, Q.; Ogomi, Y.; Chang, J.; Tsukamoto, S.; Kukihara, K.; Oshima, T.; Osada, N.; Yoshino, K.; Katayama, K.; Toyoda, T.; Hayase, S., Charge transfer and recombination at the metal oxide/CH3NH3PbClI2/spiro-OMeTAD interfaces: uncovering the detailed mechanism behind high efficiency solar cells. *Phys. Chem. Chem. Phys.* **2014,** *16* (37), 19984-19992.

281. Salim, T.; Sun, S.; Abe, Y.; Krishna, A.; Grimsdale, A. C.; Lam, Y. M., Perovskite-based solar cells: impact of morphology and device architecture on device performance. *Journal of Materials Chemistry A* **2015,** *3* (17), 8943-8969.

282. Rudolph, M.; Ratcliff, E. L., Normal and inverted regimes of charge transfer controlled by density of states at polymer electrodes. *Nat. Commun.* **2017,** *8* (1), 1048.

Acknowledgements

The completion of the course of my doctoral research and the thesis has benefited from the support and encouragement of many people.

Firstly, I would like to extend my sincere thanks and admiration for my advisor, Professor Qing Shen. I greatly appreciate her dedication to research, her conscientious academic spirit and modest, and her scientific instinct and patient guidance helped me finish a very efficient PhD. She gives me much help and advice both in research and life during the whole process of my doctoral course, which has made my accomplishments possible. The past more than three years in the Shen laboratory have been the most impactful of my life.

I also thank Professor Toyoda, Professor Abe, Professor Okuno, and Professor Hirano for their inputs and advice to make this thesis clearer and better.

I would specifically like to thank Professor Hayase and Doctor Ogomi for their measurement and analysis of PYS; Professor Yoshino for their measurement and analysis of Hall effect; Professor Minemoto for their measurement and analysis of AFM. To Professor Hayase, Professor Yoshino and Professor Minemoto, I am very pleasant cooperation with you, and very grateful for the insights you provided through discussions.

I would like to thank all members of the Shen laboratory, I have been very fortunate to work with outstanding people over the years. A big thanks to Dr. Chang, Dr. Zhang and Dr. Liu for collaboration on synthesis of quantum dots, and preparation of solar cell, and related publications. I also would like to thank Mr.Yamazaki, Mr.Ono, Mr.Hironaka, Mr. Kaji, Mr. Kobayasi, Mr.Izushi, Mr. Nakazawa, Mr. Fujino, Miss Hori, Mr. Ozu, Miss Kitabatake, Mr.Yoshida, Mr.Yasuda, Mr. Huang, Miss Yoshihara for their continuous help in the key aspects of my research over the years. Finally, I am grateful to my beloved parents and wife for their devotion and wholehearted support. I dedicate this paper to them in their trust and company.

List of Publications

Papers

1. **Ding Chao**, Zhang Yaohong, Liu Feng, Nakazawa Naoki, Huang Qingxun, Hayase Shuzi, Ogomi Yuhei, Toyoda Taro, Wang Ruixiang and Shen Qing. Recombination Suppression in PbS Quantum Dot Heterojunction Solar Cells by Energy-Level Alignment in the Quantum Dot Active Layers. ACS Applied Materials & Interfaces **2018**,10(31), 26142-26152. (content of Chapter 3)
2. **Ding Chao**, Zhang Yaohong, Liu Feng, Kitabatake Yukiko, Hayase Shuzi, Toyoda Taro, Wang Ruixiang, Yoshino Kenji, Minemoto Takashi and Shen Qing. Understanding charge transfer and recombination by interface engineering for improving the efficiency of PbS quantum dot solar cells. *Nanoscale Horizons* **2018**, 3, 417-429 (content of Chapter 4)
3. **Ding Chao**, Zhang Yaohong, Liu Feng, Kitabatake Yukiko, Hayase Shuzi, Toyoda Taro, Yoshino Kenji, Minemoto Takashi, Katayama Kenji and Shen Qing. Effect of the conduction band offset on interfacial recombination behavior of the planar perovskite solar cells. *Nano Energy* **2018**, 53, 17-26. (content of Chapter 5)
4. Liu Feng, **Ding Chao**, Zhang Yaohong, Ripolles Teresa S., Kamisaka Taichi, Toyoda Taro, Hayase Shuzi, Minemoto Takashi, Yoshino Kenji, Dai Songyuan, Yanagida Masatoshi, Noguchi Hidenori and Shen, Qing. Colloidal Synthesis of Air-Stable Alloyed $CsSn_{1-x}Pb_xI_3$ Perovskite Nanocrystals for Use in Solar Cells. *Journal of the American Chemical Society*, vol. 139 (46), pp. 16708-16719, **2017**.
5. Zhang Yaohong, **Ding Chao**, Wu Guohua, Nakazawa Naoki, Chang Jin, Ogomi Yuhei, Toyoda Taro, Hayase Shuzi, Katayama Kenji, and Shen Qing. Air stable PbSe colloidal quantum dot heterojunction solar cells: ligand dependent exciton dissociation, recombination, photovoltaic property and stability. *The Journal of Physical Chemistry C*, vol. 120, pp. 28509-28518, **2016**.
6. Zhang Yaohong, Wu Guohua, **Ding Chao**, Liu Feng, Yao Yingfang, Zhou Yong, Wu Congping, Nakazawa Naoki, Huang Qingxun, Toyoda Taro, Wang Ruixiang, Hayase Shuzi, Zou Zhigang and Shen Qing. Lead Selenide Colloidal Quantum Dot Solar Cells Achieving High Open-Circuit Voltage with One-Step Deposition Strategy. *The Journal of Physical Chemistry Letters* **2018**, 9 (13), 3598-3603.
7. Liu Feng, Zhang Yaohong, **Ding Chao**, Toyoda Taro, Ogomi Yuhei, Ripolles Teresa S., Hayase Shuzi, Minemoto Takashi, Yoshino Kenji, Dai Songyuan and Shen Qing. Ultrafast Electron Injection from Photoexcited Perovskite CsPbI3 QDs into TiO_2 Nanoparticles with Injection Efficiency near 99%. *The Journal of Physical Chemistry Letters*, vol. 9 (2), pp. 294-297, **2018**.
8. Chang Jin, Ogomi Yuhei, **Ding Chao**, Zhang Yao Hong, Toyoda Taro, Hayase Shuzi, Katayama Kenji and Shen Qing. Ligand-dependent exciton dynamics and photovoltaic properties of PbS quantum dot heterojunction solar cells. *Physical Chemistry Chemical Physics*, vol. 19 (9), pp. 6358-6367, **2017**.

9. Septina Wilman, Sugimoto Minori, **Chao Ding**, Shen Qing, Nakatsuka, Shigeru, Nose, Yoshitaro, Harada, Takashi and Ikeda, Shigeru. Photoelectrochemical water reduction over wide gap (Ag,Cu)(In,Ga)S2 thin film photocathodes. *Physical Chemistry Chemical Physics*, vol. 19 (19), pp. 12502-12508, **2017**.

Conference Presentations

1. Poster: ○**Chao Ding**, Yaohong Zhang, Shuzi Hayase, Yuhei Ogomi, Taro Toyoda, Kenji Yoshino, Takashi Minemoto, Qing Shen. Preventing of charge recombination in Colloidal Quantum Dot Solar Cells and Perovskite Solar Cells by doping the metal oxide. International Symposium on Novel Energy Nanomaterials, Catalysts and Surfaces for Future Earth (NENCS 2017 UEC 100th Anniversary Commemorative Event), Tokyo, Japan, 28-30 October, 2017.

2. Oral：○**Chao Ding**, Yaohong Zhang, Shuzi Hayase, Yuhei Ogomi, Taro Toyoda, Kenji Yoshino, Takashi Minemoto, Qing Shen. Properties of $Zn_{1-x}Mg_xO$ films and their enhanced PbS Quantum Dot Solar Cells performance. The 15th International conference on Advanced Materials (IUMRS-ICAM 2017), Kyoto, Japan, August 27 - September 1, 2017.

3. Oral：○**Chao Ding**, Yaohong Zhang, Shuzi Hayase, Yuhei Ogomi, Taro Toyoda and Qing Shen. Interface Engineering of Perovskite Solar Cells using Mg-doped ZnO as Electron Selective Layers. The 78th JSAP Autumn Meeting, Fukuoka, Japan, 05-08 September, 2017.

4. Oral：○**Chao Ding**, Yaohong Zhang, Shuzi Hayase, Yuhei Ogomi, Taro Toyoda and Qing Shen. Bandgap Engineering of Sol-Gel Synthesized $Zn_{1-x}Mg_xO$ films as Electron-Transporting Layers for PbS Colloidal Quantum Dot Solar Cells. The 64th JSAP Spring Meeting, City of Yokohama, Japan, 14-17 March, 2017.

5. Oral：○**Chao Ding**, Yaohong Zhang, Shuzi Hayase, Yuhei Ogomi, Taro Toyoda, Kenji Yoshino, Takashi Minemoto, Qing Shen. Bandgap engineering of Magnesium-doped Zinc Oxide as Electron-Transporting Layers for PbS Colloidal Quantum Dot Solar Cells and Perovskite Solar Cells. Asia-Pacific International Conference on Hybrid and Organic Photovoltaics (AP-HOPV17), Yokohama City, Japan, 02-04 February, 2017.

6. Oral：○**Chao Ding**, Yaohong Zhang, Shuzi Hayase, Yuhei Ogomi, Taro Toyoda and Qing Shen. Controllable ZnMgO Thin Films as Highly Transparent Electron-Transporting Layers for PbS Colloidal Quantum Dot Photovoltaics. The 26th

Annual Meeting of MRS-J, Yokohama City, 19-22 December 2016.

7. Poster: ○**Chao Ding**, Yaohong Zhang, Shuzi Hayase, Yuhei Ogomi, Taro Toyoda, Kenji Yoshino, Takashi Minemoto, Qing Shen. Bandgap engineering using quantum-size-effect-tuned heterojunctions. Interdisciplinary Research and Global Outlook (The Irago Conference 2016), Tokyo, Japan, 01-02 November, 2016.

8. Oral：○**Chao Ding**, Yaohong Zhang, Shuzi Hayase, Yuhei Ogomi,Taro Toyoda, and Qing Shen. Bandgap engineering for enhancing photovoltaic properties of PbS quantum dot solar cells. The 77th JSAP Autumn Meeting, Niigata City, 13-16 September 2016.

9. Poster: ○**Chao Ding**, Jin Chang, Yaohong Zhang, Naotaka Fujikawa, Shuzi Hayase, Kenji Yoshino, Taro Toyoda, Qing Shen. Bandgap Tunable ZnMgO Electron-Transporting Layers for Stable PbS Colloidal Quantum Dot Photovoltaics. Annual Meeting on Photochemistry 2016, Tokyo, 06-08 September 2016.

10. Poster: ○**Chao Ding**, Jin Chang, Yaohong Zhang, Naotaka Fujikawa, Shuzi Hayase, Kenji Yoshino, Taro Toyoda, Qing Shen. One-step deposition of PbS Quantum Dot harvesting layer with new-ligand for solid state heterojunction solar cells. The 63rd JSAP Spring Meeting, Tokyo, 19-22 March 2016.

11. Poster: ○**Chao Ding**, Hiloki Takahashi, Jin Chang, Shuzi Hayase, Kenji Yoshino, Taro Toyoda, Qing Shen. Tunning the photovoltaic and carrier dynamics of PbS QDs by tailoring the architecture of bulk heterojunction quantum dot solar cells. The 76th JSAP Autumn Meeting, Nagoya, 13-16 September 2015.